# Influence of Calcium Phosphate Composition and Design on Bone Regeneration, Degradation and Mechanical Function

by

Alisha Bernadette Diggs

A dissertation submitted in partial fulfillment

of the requirements for the degree of

Doctor of Philosophy

(Biomedical Engineering)

in The University of Michigan

2013

Dissertation Committee:

Professor Scott J. Hollister, Research Chair

Professor John Hallaron, Research Co-Advisor

Professor Paul H. Krebsbach

Professor Brian J. Love

©Alisha Bernadette Diggs

---

2013

# DEDICATION

***Two roads diverged in a yellow wood,***
***And sorry I could not travel both***
***And be one traveler, long I stood***
***And looked down one as far as I could***
***To where it bent in the undergrowth;***

***Then took the other, as just as fair,***
***And having perhaps the better claim,***
***Because it was grassy and wanted wear;***
***Though as for that passing there***
***Had worn them really about the same,***

***And both that morning equally lay***
***In leaves no step had trodden black.***
***Oh, I kept the first for another day!***
***Yet knowing how way leads on to way,***
***I doubted if I should ever come back.***

***I shall be telling this with a sigh***
***Somewhere ages and ages hence:***
***Two roads diverged in a wood, and I—***
***I took the one less traveled by,***
***And that has made all the difference.***

*-Robert Frost, "The Road Not Taken"*

This work is dedicated to the ancestors who have come before me, as well as to my family, especially my mother, who was the first in her family to graduate high school, attain an undergraduate degree, and a master's degree: ***Thank you for clearing a path to higher education. It has been an honor to walk in your footsteps.***

# ACKNOWLEDGEMENTS

*"We are like dwarfs on the shoulders of giants, so that we can see more than they, and things at a greater distance, not by virtue of any sharpness of sight on our part, or any physical distinction, but because we are carried high and raised up by their giant size"*

*-John of Salisbury (1159) comments on Bernard of Chartes' quotation*

I offer my sincere gratitude and appreciation to my research advisors, Professors Scott Hollister and John Halloran. You have guided me and my research and offered an enormous amout of direction to me, in work and in life. I would especially like to thank both of you, your labs, and your families, for being so supportive of me; both after Hurrican Katrina when my family lost everything, and after medical leave. These were times when the completion of this degree seemed out of reach.

Thanks and appreciation also goes to the remainder of my dissertation committee, Professors Paul Krebsbach and Brian Love; for your guidance and research advice; with an additional thank you to Professor Love for giving me my first teaching opportunity and teaching me so much about the task of teaching.

Thank you to Colleen Flanagan; for all of our discussions and your assistance with data management, training, and logistics

I would like to thank the graduate students of Hollister (STEG lab) and Halloran lab, who have been available to scientific discussions and crazy fun, with the same enthusiasm: Shelley Brown, Marta Dias, Claire Jeong, Heesuk Hang, Jessica Kemppainen, Elly Liao,

Francesco Migneco, Erin Moffit, Eiji Saito , Auresa Thomas, Weijut Tseng, Frank Winterroth, Darice Wong, Leenaporn Jongpaiboonkit; Chang-Jun Bae; Nefertiti Patrick-Jackson, Angela Dixon…and a host of other students too many to list.

Thank you to Shelton Manley, Jr…..not only for all of the IT support, but for hanging in the trenches with me and encouragement when I was not sure I could get through.

Thank you to Dr. Alec Gallimore, Derrick Scott, and Dr. Phillip Bowman.

Finally thank you to my family and friends for all of your support, especially my mother and my sister—for always being a constant reminder of the importance of family.

Love,

Alisha

# TABLE OF CONTENTS

DEDICATION ..... ii

ACKNOWLEDGEMENTS ..... iii

List of Figures ..... xii

LIST OF TABLES ..... xxvii

CHAPTER 1 GENERAL INTRODUCTION ..... 1

1.1 Bone grafting: then and now ..... 1

1.2 New frontiers of research ..... 4

1.3 Problem Statement ..... 5

1.4 Research objectives ..... 9

1.5 Strategy for investigation ..... 11

1.5.1 Specific Aims ..... 11

1.6 Summary of thesis contents ..... 12

CHAPTER 2 BIOLOGICAL AND MATERIALS CHARACTERISTICS OF BONE AND THEIR IMPENDING INFLUENCES ON TISSUE ENGINEERING STRATEGIES FOR ITS REPAIR AND REGENERATION ..... 14

2.1 The Need to Imitate Structure and Function ..... 14

2.2 The Biology of Bone ..... 16

2.2.1 The Cellular Components of Bone ..... 16

2.2.2 Bone Formation and Modeling ..... 22

2.2.3 Bone Remodeling ..... 25

2.2.4 Biomineralization ..... 26

2.3 The Structure and Material Properties of Bone ..... 28

2.3.1 Bone Composition, Organization, and Morphology ..... 28

2.3.2 Bone as a Material ..... 32

2.4 Chapter Summary ..... 34

2.5 Figures ..... 35

CHAPTER 3 CHARACTERIZATION OF PHYSICAL PROPERTIES OF CALCIUM PHOSPHATE BULK MATERIALS ..... 43

3.1 Significance of Materials Properties Characterization of Calcium Phosphate Biomaterials ..... 43

3.2 Characterization of Powders and Their Sinterability ..... 50

3.2.1 Powder Characterization ..... 50
3.2.2 Phase Stability ..... 50
3.2.3 Densification ..... 51
3.3 Characterization of Mechanical Strength ..... 52
3.3.1 Diametral Compression ..... 52
3.4 Visualization of Grain Distribution ..... 53
3.5 Results and Discussion ..... 54
3.5.1 Powder Characterization and Maintenance of Phase Purity ..... 54
3.5.2 Effect of β-TCP Phase Amount and Sintering Temperature on Densification and Microporosity ..... 57
3.5.3 Effect of β-TCP Phase Amount and Microporosity on Mechanical Properties 61
3.5.4 Method for Visualization of Grain Distribution in Biphasic Compositions ... 63
3.6 Chapter Summary and Conclusions ..... 66
3.7 Figures ..... 68
CHAPTER 4 ARCHITECTURAL DESIGN AND CHARACTERIZATION OF CALCIUM PHOSPHATE SCAFFOLDS ..... 100
4.1 Scaffold Architectural Influence on Bone Regeneration ..... 100
4.2 Scaffold Design and Manufacturing ..... 106

4.3 Scaffold Characterization ..... 109
4.3.1 Porosity and Pore size ..... 109
4.3.2 Surface Area ..... 113
4.3.3 Permeability ..... 115
4.4 Figures ..... 118
CHAPTER 5 CHARACTERIZATION OF *IN VIVO* MECHANICAL PROPERTY DEGRADATION OF CALCIUM PHOSPHATE SCAFFOLDS ..... 128
5.1 Understanding Mechanical Property Degradation *A Priori* ..... 128
5.2 Materials and Methods ..... 133
5.2.1 Porous Sample Fabrication ..... 133
5.2.2 *In vivo* Degradation Study ..... 133
5.2.3 Mechanical Testing ..... 134
5.2.4 Percent Retention ..... 135
5.2.5 Statistical methods ..... 135
5.3 Results ..... 136
5.3.1 *In vivo* degradation ..... 136
5.4 Discussion ..... 142
5.5 Figures ..... 149

CHAPTER 6 INFLUENCE OF COMPOSITION, SINTERING TEMPERATURE, AND MACROPOROSITY ON BONE REGENERATION VIA CALCIUM PHOSPHATE SCAFFOLDS 173

6.1 Enhancing Bone Regeneration Through the Design of Scaffold Properties ... 173

6.2 Materials and Methods ... 177

6.2.1 Biomaterial fabrication ... 177

6.2.2 Ex vivo gene therapy and ectopic bone formation assay in SCID mice ... 178

6.2.3 Histology and Post-surgical processing ... 179

6.2.4 Microcomputed tomography image analysis ... 180

6.2.5 Statistical analysis ... 183

6.3 Results ... 184

6.3.1 Histological Evaluation of Bone Formation ... 184

6.3.2 Quantifying Bone Formation: Mineral Quality Indices ... 186

6.3.3 Quantifying quality: Indices of Bone Structural Quality ... 190

6.4 Discussion ... 191

6.5 Chapter summary and conclusions ... 203

6.6 Figures ... 205

CHAPTER 7 A POST-HOC ANALYSIS OF THE INFLUENCE OF SURFACE AREA AND PERMEABILITY ON BONE REGENERATION AND MINERAL AND STRUCTURAL BONE QUALITY ..... 221

7.1 The Need for a *Post Hoc* Consideration of Surface Area ..... 221

7.2 Materials and Methods ..... 225

7.2.1 In vivo surgical procedures and post-surgical evaluation ..... 225

7.2.2 Surface Area and Permeability ..... 225

7.2.3 Statistical analysis ..... 226

7.3 Results ..... 227

7.3.1 Surface Area and Permeability ..... 227

7.3.2 Effect on Regeneration and Bone Quality ..... 228

7.4 Discussion ..... 230

7.5 Chapter Summary and Conclusion ..... 235

CHAPTER 8 CONCLUSIONS AND FUTURE WORK ..... 237

8.1 General Discussion and Thesis Summary ..... 237

8.2 Future Directions ..... 243

8.2.1 Understanding degradation mechanics ..... 244

8.2.2 Understanding degradation kinetics ..... 247

Appendix 1: Data Tables ..... 248

REFERENCES..... 269

# List of Figures

Figure 2.1: Bone cell lineage.[77] ..... 35

Figure 2.2: Bone formation via intramembraneous ossification. [78] ..... 36

Figure 2.3: Bone Formation via endochondral ossification.[79] ..... 37

Figure 2.4: Bone Modeling and Remodeling[80] ..... 38

Figure 2.5: Gross Anatomy of Long Bone[81] ..... 39

Figure 2.6: Structure of Trabecular Bone.[82] ..... 40

Figure 2.7: Structure of Cortical Bone.[83] ..... 41

Figure 2.8: Structural hierarchy of bone. The microstructure of cortical bone consists of osteons and Haversian systems formed of lamella. Collagen fibers composed of collagen fibrils and bone mineral form the nanostructure.[56, 74] ..... 42

Figure 3.1 SEM of as-received HA powder, consisting of ~10 micron agglomerates composed of ~0.5 micron-sized primary particles; Magnification 1000x. Image courtesy of Plasma Biotal, Ltd. ..... 68

Figure 3.2: SEM. Enlarged view of as-received HA agglomerate particles; 0.5 micron primary particles are strongly bonded. (Plasma Biotal, Ltd.); Magnification 20000x ..... 69

Figure 3.3: SEM image of as-received β-TCP powder (Plasma Biotal Ltd) consisting of round agglomerates 20-30 microns in size; Magnification 700x. ..... 70

Figure 3.4: SEM of enlarged view of as-received β-TCP agglomerate. The round agglomerate is formed by round primary particles 0.2-0.8 microns in size and tightly bound; Magnification 30000x. ..... 71

Figure 3.5: Calculated XRD pattern of Hydroxyapatite. $P6_3/m$, a = 9.4176 (1), c = 6.8814 (1) Å .[129] ..... 72

Figure 3.6: Calculated XRD pattern of β-TCP. R3c, a = 10.439(1), c = 37.375(6) Å (hexagonal setting).[129] ..... 73

Figure 3.7: Diffraction pattern of as-received HA powder, 2θ equals 25°-35°. Pattern shows significant line broadening and is indicative of a well-crystallized powder. All peaks can be indexed to hydroxyapatite. ..... 74

Figure 3.8: Diffraction pattern of as-received β-TCP powder, with 2Theta between 25 and 35 degrees. Powder is well crystallized and demonstrates line broadening consistent with particles ~30 microns in size. All peaks can be indexed to β-TCP. ..... 75

Figure 3.9: Phase amount of β-TCP after sintering at 1100°C; based on relative intensity of primary HA and β-TCP diffraction peaks. After sintering, compositions high in HA, specifically 100% HA and 75% HA/25% TCP, underwent a phase transformation in which hydroxyapatite decomposed to β-TCP, forming 12-16% β-TCP in the final compositions. ..... 76

Figure 3.10: : Effect of composition on apparent porosity of sintered compacts at 1100°C. There is an inverse relationship between apparent porosity and phase amount of TCP, with higher TCP compositions having less porosity than lower compositions. HA, 25BCP: n=5; 50BCP, 75BCP, TCP: n=20. ..... 78

Figure 3.11: Relative density of sintered discs with respect to sintering temperature and phase amount of β-TCP present. Densification occurs at a faster rate for the higher temperature, and increases with increasing amounts of β-TCP..... 79

Figure 3.12: Comparison of mean apparent porosity of as-received and ball-milled powders, sintered at 1100$^{o}$C. For HA, 25% TCP, and 75% TCP, there is a statistically significant difference in porosity ($p<0.01$); n=20 for each group. ..... 80

Figure 3.13: Comparison of mean apparent porosity for wet-ball milled powders. Agglomerates were ball milled for 20 hours and sintered at various temperatures. TCP experiences a faster densification than HA at temperature range of interest, 1100 and 1150$^{o}$C; densification rates for 75% TCP and 100% TCP are similar, 25% TCP and 50% TCP favor behavior of HA. Moreover, densification rate of HA is highest at 1200 and 1250$^{o}$C, falling outside of the temperature range inhibiting the $\beta \rightarrow \alpha$ transition of β-TCP; making HA a constraining variable to densification of the biphasic compositions. 81

Figure 3.14: SEM of as-fired [A,B] and fracture [C] surface microstructure of biphasic compositions. Each composition shows necking of powder particles and an open pore network. Microstructure of 25BCP [A] and 50BCP [ B] are similar in mean pore size, measuring an average value of 1.08 μm, with larger pores on the order of 2.01 μm. These pores appear to be consistently shaped, and evenly spaced within the microstructure, with smaller pores outnumbering the larger. By contrast, microstructure of the 75BCP [C] composition consists of measuring 1.20 μm in size, but often coalescing to form lengthy pore channels measuring, on average, nearly 5 μm; these

pores appear to dominate the microstructure. Magnification 5000X; scale bars measure 5 μm. ..... 82

Figure 3.15 Microstructure of HA [A] and β-TCP [B] after sintering at 1300°C. HA shows no residual porosity. β-TCP, however, demonstrates a comparatively substantial residual porosity, thereby illustrating the limitation on densification of β-TCP. HA photo taken from Chu, et. al.[52] ..... 83

Figure 3.16: Weibull plots for CaP pellets fractured by diametral compression, where pellets differed according to composition and relative density, P. Weibull moduli is highest for the 50/50 biphasic composition, but and generally increases with increasing density. ..... 84

Figure 3.17: Probability of survival for dense calcium phosphate pellets sintered at 1100°C..... 85

Figure 3.18: Weibull modulus as a function of relative density, depicting high variability for relative densities near 60%, with values approaching steady-state at densities greater than 63%. The 75% TCP composition (dashed red rectangle) is not within trend; a result that may be a consequence of the microstructure. HA (gray); 25BCP (light blue); 50 BCP (red); 75 BCP (orange); TCP (dark blue)..... 88

Figure 3.19: Mean characteristic ( $\sigma_o$) and fracture ($\sigma_{avg}$) strength as a function of compositional changes and relative density. Both characteristic strength and fracture strength showed a steady increase with increasing amounts of TCP and relative density, demonstrating that high TCP constructs are generally stronger. The 75% TCP composition (dashed blue box) is not within trend, and indicates the significance of

relative density in the strength of material. HA (gray); 25BCP (light blue); 50 BCP (red); 75 BCP (tan); TCP (dark blue) ..... 89

Figure 3.20: Weibull modulus and characteristic strength as a function of relative density. Both demonstrate a steady increase with increasing amounts of TCP. The 75% TCP composition (dashed blue box) is out of trend, and indicates a dependency of strength on relative density. ..... 90

Figure 3.21: Back-scattered SEM images (A-E) of three biphasic compositions: 25BCP (B), 50BCP (C), 75BCP (D) and their calcium phosphate components--HA (A) and β-TCP (E). Images show no distinction across compositions. The lighter contrast of the 75BCP composition (D) is due to a change in imaging settings and not to compositional differences. Within a given image, lighter grayscale spots may correspond to agglomerated particles, but no determination can be made of its local composition. All images have a 600 micron field of view. ..... 91

Figure 3.22: Comparison of 25% TCP biphasic back-scattered SEM (A) and CL (B) images. SEM image overall shows gray shadings that are not distinguishable (comparison of circle, square, and triangle in A). CL image depicts the same region in high contrast, with areas within the image distinguishable and distinct from one another due to grayscale contrast. Furthermore, a comparison of shapes in A to corresponding shapes in B shows regions in the CL image that go unnoticed in the SEM image. Image analysis of the bright areas of contrast within the CL image is determined to be 0.25 volume fraction (of the image area). ..... 92

Figure 3.23: Comparison of 50% TCP biphasic back-scattered SEM (A) and CL (B) images. CL regions in high contrast (red square vs. yellow circle vs. blue triangle) are distinctive, displaying various shadings of grayscale. In the comparable SEM image, these regions are not distinctive. Additionally, a comparison of squares, circles, and triangles between the two images reveals distinct differences in each imaging modality's ability to distinguish between TCP grains. Image analysis of the bright areas of contrast within the CL image is determined to be 0.505 ± 0.010 (n=4) volume fraction (of the image area). ..... 93

Figure 3.24: Comparison of 75% TCP biphasic back-scattered SEM (A) and CL (B) images.SEM image overall shows washed-out gray shadings that are not distinguishable. CL image is in high contrast, with areas within the image distinguishable and distinct from one another due to grayscale contrast. Furthermore, a comparison of black shading (yellow square) and bright gray shading (red circle) in the CL image lack the same vivid contrast in corresponding regions (yellow square and red circle respectively) of the SEM image. Image analysis of the bright areas of contrast within the CL image is determined to be 0.754 ± 0.003 volume fraction (of the image area). ..... 94

Figure 3.25: Comparison of 100% β-TCP back-scattered SEM (A) and CL (B) images. SEM image shows minimal contrast as compared to the CL image, with no discernible features. The CL image is in higher contrast, with a relatively homogeneous bright gray region. ..... 95

Figure 3.26: Comparison of 100% HA back-scattered SEM (A) and CL (B) images. SEM image overall shows washed-out gray background with no distinguishable features. Conversely, CL image is in high contrast, with uniform salt and pepper appearance. Moreover, the high-contrasting gray regions comprise 10.81 ± 2.83 % (n=6) volume fraction of the image, comparable to the demonstrated 14% conversion of HA to β-TCP under 1100$^{o}$C sintering conditions. ..... 96

Figure 3.27: EDS analysis at various grayscale regions within the 50% β-TCP cathodoluminescence image. Grayscale regions are numbered (1-3) and relative Ca:P ratio is presented. Ca:P for stoichiometric HA and β-TCP are 1.67 and 1.5 respectively. Ca:P ratio for grayscale regions 1, 2, and 3 is 1. 5, 2.0, and 2.2 respectively. ..... 97

Figure 3.28: EPMA analysis at various grayscale regions within the 50% β-TCP cathodoluminescence image. Grayscale regions are numbered (1-5) and corresponding Calcium and Phosphorus atomic percent as determined by cathodoluminescence microprobe is presented. The relative Ca:P ratio is also determined. Ratios for stoichiometric HA and β-TCP are included for reference. Mean Ca:P ratio for various gray regions (1, 2, 4, and 5) is 1. 51 ± 0.03, closely matched to known Ca:P for β-TCP. Ca:P ratio for the black region (3) is 1.76, slightly higher than that of stoichiometric HA. ..... 98

Figure 3.29: CL image of biphasic calcium phosphate containing 25% β-TCP (A) and corresponding bimodal histogram of voxel values (B). Values corresponding to β-TCP are highlighted in the histogram (D) (voxel value vs frequency) and colored in the CL

image (C). Image analysis reveals the volume fraction in the red region (β-TCP) is 0.25 and is confirmed by xray diffraction. ..... 99

Figure 4.1: Fabrication technique for calcium phosphate ceramic scaffolds. This process occurs in three stages: mold design and fabrication [A], ceramic casting [B], and ceramic processing [C]; and is derived from image-based designs..... 118

Figure 4.2: Pore and strut size measurement using microCT datasets. A slice in the central region was evaluated. Pore and strut sizes were measured by selecting the edges of the struts (white) and calculating the distance between points. Pores correspond to the spaces between struts. This measurement technique is an improvement on manual measurement methods in that aligning the centers of the pores and struts with the plane edge (red and green lines) ensures parallel points, and possibly more accurate and repeatable data..... 120

Figure 4.3: Permeability set-up . ..... 125

Figure 4.4: Comparative permeability for subq scaffolds sintered at 1100$^{o}$C. There were significant differences between macroporosity designs; no significance in regard to composition. **p<0.001; n=6 for all groups; 5 measurements per scaffold, performed in triplicate..... 126

Figure 4.5: Permeability of macroporous designs are distinctly and significantly different. ..... 127

Figure 5.1: Schematic of uniaxial stress-strain curves for an elastic-brittle foam, showing the three regimes: linear elasticity (bending), plateau (brittle crushing), and densification.[230, 232] ..... 149

Figure 5.2: Stress-strain curve of time zero scaffold under uniaxial compression [A; 50BCP-low macroporosity-1150$^{o}$]. Scaffold failed in a manner characteristic of a brittle cellular solid, with each of the three failure regimes present: linear elastic bending [I], brittle crushing [II], and densification [III]. The modulus of the sample was taken at the slope of the linear region between points B and M [red line; A]. Curves are also shown for multiple samples of the time zero [B; HA-high macroporosity-1150$^{o}$], four week [C; TCP-high macroporosity-1100$^{o}$], and eight week [D; 50BCP-high macroporosity-1150$^{o}$] groups. ..... 150

Figure 5.3: Compressive strength as a function of composition, at baseline, 4 week, and 8 week time points..... 154

Figure 5.4: Compressive strength as a function of sintering temperature, at baseline, 4 week, and 8 week time points. ..... 155

Figure 5.5 : Compressive strength as a function of macroporosity design, at baseline, 4 week, and 8 week time points. ..... 156

Figure 5.6 Modulus as a function of composition, at baseline, 4 week, and 8 week time points..... 157

Figure 5.7 Modulus as a function of sintering temperature, at baseline, 4 week, and 8 week time points. ..... 158

Figure 5.8**:** Modulus as a function of macroporosity design, at baseline, 4 week, and 8 week time points. ..... 159

Figure 5.9 : Strength retention as a function of composition, at baseline-4 week, 4-8 week, and 0-8 week intervals. ..... 160

Figure 5.10: Strength retention as a function of sintering temperature, at baseline-4 week, 4-8 week, and 0-8 week intervals..... 161
Figure 5.11: Strength retention as a function of macroporosity design, at baseline-4 week, 4-8 week, and 0-8 week intervals..... 162
Figure 5.12: Change in modulus as a function of composition, at baseline-4 week, 4-8 week, and 0-8 week intervals. ..... 163
Figure 5.13: Change in modulus as a function of composition, at baseline-4 week, 4-8 week, and 0-8 week intervals. ..... 164
Figure 5.14: Change in modulus as a function of macroporosity design, at baseline-4 week, 4-8 week, and 0-8 week intervals..... 165
Figure 6.1: Micro-CT rendering of a low-macroporosity design scaffold, post-implantation. At 4 weeks, bone growth occurs both internally and externally to the scaffold boundaries. In panel [B], the scaffold has been removed from the dataset for ease of analysis of bone mineral indices. ..... 206
Figure 6.2: Cylindrical ROIs used in the analysis of regenerated bone. The original dataset [A] showing a low macroporosity design post-implantation with bone growth and scaffold removed. The initial region of interest (ROI) [B, orange highlight] encompasses all regenerate bone, internal and external to the scaffold boundaries. $C_0$, the infiltration ROI, is bound by the boundaries of the scaffold [C]. Lesser concentric ROIs are generated [D, E, F] by reducing $C_0$ by a fixed amount, 0.71 mm from the outer edge of the scaffold, with $C_1$ residing 0.71 mm from the scaffold edge [D], $C_2$ , 1.42mm [E], and $C_3$ , 2.13mm [F]. All ROIs are shown in panel [G]. ..... 207

Figure 6.3: Ring ROIs used in the analysis of regenerated bone to determine the level of scaffold penetration. The original dataset [A] showing a low macroporosity design post-implantation with scaffold removed. Each ring region of interest (ROI) is the difference between successive cylindrical ROIs previously described in Figure 6.2. Ring1 [C, green highlight] is the difference between $C_0$ and $C_1$, and encompasses 0-0.71mm into the scaffold center; Ring2 [D, red highlight] is the difference between $C_1$ and $C_2$, and encompasses 0.071-1.42mm into the scaffold center; Ring3 [E, black highlight] is the difference between $C_2$ and $C_3$, and encompasses 1.42-2.13mm into the scaffold center. All ROIs are shown in panel [B]..... 208

Figure 6.4: Micro-CT rendering of low macroporosity design 4 weeks post-implantation. Bone (red highlight) regeneration is both internal and external to the scaffold (white) boundaries, and is seen aligning the pore spaces [A1-3] and strut walls [B1-3]. A-1,B-1: x-y plane; A-2,B-2: x-z plane; A-3,B-3: y-z plane..... 209

Figure 6.5: Persistence of a boney cortical shell in all histology sections. H&E [A] and Masson's Trichrome blue [B] stained histology section showing bone formation surrounding the scaffold [S]. In all cases, a boney cortical shell was seen surrounding the outer scaffold surface. Although the distance of the shell from the scaffold differed among samples, there did not seem to be any dependency on any of the factors tested in this model. H&E: bone stains pinkish-purple; Masson's trichrome: remodeled and lamellar bone is indicated by red, whereas blue indicates immature and freshly deposited bone..... 210

Figure 6.6: Bone regeneration occurred internal to the scaffold pores as well as external to the scaffold surface. H&E [A, B, C] and trichrome blue [D, E, F] stained histology sections showing bone formation within a high macroporosity design scaffold. In all cases, bone regeneration was both internal and external to the scaffold boundaries, with the formation of an outer cortical shell surrounding the scaffold surface; the distance of which, varied. Bone regeneration was also found aligning the scaffold pores [B,C, E,F]. H&E: bone stains pinkish-purple; Masson's trichrome: remodeled and lamellar bone is indicated by red, whereas blue indicates immature and freshly deposited bone. ..... 211

Figure 6.7: Bone regeneration within scaffold pores. H&E [A] and trichrome blue [B] stained histology section showing bone formation within the scaffold pores. In many cases, bone was seen aligning the pore surface. H&E: bone stains pinkish-purple; Masson's trichrome: remodeled and lamellar bone is indicated by red, whereas blue indicates immature and freshly deposited bone. ..... 212

Figure 6.8: Regenerate bone is normal in appearance and demonstrates cellular markers for bone tissue; 4 week timepoint. H&E stained histology section of low macroporosity [A; 50BCP, 1100$^{o}$C, 2X magnification] and high macroporosity [B; TCP,1150$^{o}$C, 2X magnification ] design scaffolds, showing bone formation surrounding the scaffold perimeter. Bone ingrowth is also seen inside the pores aligning the scaffold surface [C: HA, low macroporosity design, 1150$^{o}$C, 10X magnification; D: TCP, low macroporosity, 1100$^{o}$C, 10X magnification]. The morphology of the neobone is normal in appearance, indicating the presence of osteoblasts, osteoid, osteocytes, marrow space,

and mineralized bone tissue [E: BCP, high macroporosity design, 1100$^{o}$C, 40X magnification; F: TCP, low macroporosity design, 1150$^{o}$C, 10X magnification]. ..... 213
Figure 6.9: Total bone volume regenerated internal and external to scaffold boundaries. Total volume of bone (TBV; mm$^3$) regenerated internal and external to the scaffold boundaries at 4 weeks implantation; data is presented as a function of composition, macroporosity, and sintering temperature. Composition and sintering temperature had no effect on the TBV of bone produced, whereas macroporosity effects were significant for the low and high macroporosity designs. Values are expressed as arithmetic mean ± standard error. Statistical significance was at the $\alpha$<0.05 (*); $\alpha$<0.01 (**); $\alpha$<0.001 (***). Data tables are presented in Appendix 1. ..... 214
Figure 6.10: Tissue mineral content of regenerated bone internal and external to the scaffold boundaries Tissue mineral content (TMC; mg) of regenerated bone internal and external to the scaffold boundaries at 4 weeks implantation; data is presented as a function of composition, macroporosity, and sintering temperature. There was no effect of composition, macroporosity, or sintering temperature on the TMC of bone produced. Values are expressed as arithmetic mean ± standard error. Data tables are presented in Appendix 1. ..... 215
Figure 6.11: Tissue mineral density of regenerated bone internal and external to the scaffold boundaries. Tissue mineral density (TMD; mg/mm$^3$) of regenerated bone internal and external to the scaffold boundaries at 4 weeks implantation; data is presented as a function of composition, macroporosity, and sintering temperature. Macroporosity and sintering temperature had no effect on the TMD, whereas

composition effects were significant for TCP and the 50/50 biphasic compositions. TMD values obtained were within the range for TMD values of human trabecular bone (500-800 mg/mm$^3$). Values are expressed as arithmetic mean ± standard error. Statistical significance was at the $\alpha$<0.05 (*); $\alpha$<0.01 (**); $\alpha$<0.001 (***). Data tables are presented in Appendix 1. ..... 216

Figure 6.12: Assessment of penetration depth of internal bone volume as a function of macroporosity. At 4 weeks, the significance of macroporosity to penetration depth of regenerate bone is most evident in Ring 2. For the outer ring regions of interest, the high macroporosity scaffold design regenerated more bone than the low macroporosity design. Statistical significance was at the $\alpha$<0.05 (*); $\alpha$<0.01 (**); $\alpha$<0.001 (***). $Ring_1$: 0 - 0.71mm into the interior of scaffold; $Ring_2$: 0.71 - 1.42 mm into the interior of scaffold; $Ring_3$: 1.42 - 2.13 mm into the interior of scaffold. ..... 217

Figure 6.13: Assessment of internal tissue mineral content of bone volume within ring regions of interest as a function of composition. At 4 weeks, the significance of composition to internal tissue mineral content of regenerate bone is evident in all ring regions of interest, with TCP generating more mineral in the outer 1.42 mm of the scaffold. Statistical significance was at the $\alpha$<0.05 (*); $\alpha$<0.01 (**); $\alpha$<0.001 (***). $Ring_1$: 0 - 0.71mm into the interior of scaffold; $Ring_2$: 0.71 - 1.42 mm into the interior of scaffold; $Ring_3$: 1.42 - 2.13 mm into the interior of scaffold. ..... 218

Figure 6.14: Assessment of internal tissue mineral content of bone volume within ring regions of interest as a function of macroporosity. At 4 weeks, data suggests a macroporosity dependence on internal tissue mineral content of regenerate bone: high

macroporosity designs produce more mineral content in ring regions 1 and 2, with ring 2 demonstrating significance. TMC for region 3 is nearly identical. Statistical significance was at the $\alpha$<0.05 (*); $\alpha$<0.01 (**); $\alpha$<0.001 (***). $Ring_1$: 0 - 0.71mm into the interior of scaffold; $Ring_2$: 0.71 - 1.42 mm into the interior of scaffold; $Ring_3$: 1.42 - 2.13 mm into the interior of scaffold. ..... 219

Figure 6.15 : Assessment of penetration depth of internal bone volume as a function of macroporosity. At 4 weeks, the significance of macroporosity to penetration depth of regenerate bone is most evident in Ring 2. For the outer ring regions of interest, the high macroporosity scaffold design regenerated more bone than the low macroporosity design. Statistical significance was at the $\alpha$<0.05 (*); $\alpha$<0.01 (**); $\alpha$<0.001 (***). $Ring_1$: 0 - 0.71mm into the interior of scaffold; $Ring_2$: 0.71 - 1.42 mm into the interior of scaffold; $Ring_3$: 1.42 - 2.13 mm into the interior of scaffold. ..... 220

# LIST OF TABLES

Table 3.1 Geometric and Relative Densities of CaP materials after sintering. As % TCP and sintering temperature increase, density increases. The higher density of the 50/50 biphasic composition, as compared to the 75/25 biphasic material, is most likely the result of more efficient particle packing of large and small agglomerated particles. ..... 77

Table 3.2: Weibull analysis depicting the probability for survival at the 90%, 50%, and 10% levels for calcium phosphate pellets sintered at 1100$^{o}$C. ..... 86

Table 3.3: Relative density, Weibull modulus, characteristic strength and mean fracture strength (± standard deviation) for various compositions of calcium phosphate densely sintered discs. ..... 87

Table 4.1: Scaffold design specifications for full-sized (FS) and subqsized (subq) scaffolds. ..... 119

Table 4.2: Measured pore and strut sizes of fabricated CaP scaffolds. As designed, strut sizes of the lower porosity group are smaller than those of the higher porosity group. Differences in pore sizes are the result of shrinkage due to composition and temperature. Pore size differences were statistically different for designs ($p<0.0001$) and sintering temperature ($p<0.0005$), but did not differ according to composition. For both designs, macroporosity was maintained..... 121

Table 4.3: Range of total porosity of fabricated scaffolds. Ranges of total porosity for fabricated scaffolds were dependent on macroporosity design [30% or 50%] and microporosity due to sintering temperature and composition. Images show representative microstructures of the solid struts of fabricated scaffolds. The 30%

macroporosity design was fabricated within the range of 49-72% porosity. 50% macroporosity designs were fabricated with 69-92% porosity, where macropores were on the order of 800 ± 50 μm, and micropores < 10 μm. ..... 122

Table 4.4: Overview of structural and mechanical properties of porous calcium phosphate ceramic scaffolds for bone tissue engineering. Citations[86, 118, 121, 173, 175, 178-180, 184-191] ..... 123

Table 4.5: Surface areas of as-fabricated scaffold groups. Images are microCT renderings of design isosurface. ..... 124

Table 5.1: Mean compressive strength and modulus of various groups at baseline (time zero). Values are reported as means ±standard deviation. Data for properties of human trabecular and cortical bone are referenced.[48] ..... 151

Table 5.2: Mean compressive strength of scaffolds as a function of experimental factor. Data is presented as means + standard deviations. Low and high macroporous scaffolds had 30% and 50% porosity respectively. Sintering temperatures were 1100$^{o}$C (low) and 1150$^{o}$C (high)..... 152

Table 5.3: Mean stiffness of implanted scaffolds as a function of experimental factor.153

Table 5.4: Regress model coefficients: Peak Stress at time zero ..... 166

Table 5.5: Regress model coefficients: Modulus at time zero..... 167

Table 5.6: Regress model coefficients: Peak Stress at eight weeks..... 168

Table 5.7: Regress model coefficients: Modulus at four weeks ..... 169

Table 5.8: Regress model coefficients: Modulus at time zero..... 170

Table 5.9: Regress model coefficients: Modulus at four weeks ..... 171

Table 5.10: Regress model coefficients: Modulus at eight weeks..... 172

Table 6.1: Summary of Experimental Groups. Twelve permutations of composition, macroporosity, and sintering temperature were utilized. All groups were implanted with an *n*-value corresponding to four. With complications due to surgery (1 animal lost), replicate numbers for some groups were reduced. ..... 205

# CHAPTER 1
# GENERAL INTRODUCTION

*"And the Lord God caused a deep sleep to fall upon Adam, and he slept: and he took one of his ribs, and closed up the flesh instead thereof. And the rib, which the Lord God had taken from man, made he a woman, and brought her unto the man".*
*-Genesis 2:21-22*

## 1.1 Bone grafting: then and now

The prevalence or persistence of major bone or bone-related injuries has always been the impetus for the discovery of surgical procedures or methodologies that resulted in the tissue's repair and eventual return to function. In the distant past, the solution for bone injuries and defects were often based on the implantation of readily-available materials with desired mechanical and structural function, examples of which are evident in medical history as well as in literature. Evidence dating back to the Neolithic age reveal a Peruvian tribal chief whose frontal bone defect had been repaired by a gold plate applied with a hammer; [1] anthropologic artifacts of the Khurits people of Ishtkunui, dating to 2000 BCE, demonstrate skulls with animal bone insertions and other remnants of surgical interventions to repair defects resulting from injury.[1] Literary

accounts supporting the notion of implantation and prosthesis include the Vedas, ancient Hindu texts written between 3500 and 1800 BCE, which chronicle Queen Vishpla, the warrior who loses her leg in battle and has it replaced with an iron limb before returning to battle;[2] in tales of Greek mythology in which Zeus orders the construction of an ivory shoulder for Pelops to replace the one eaten by Demeter at the feast for the Gods;[1, 3] and finally, in the Holy Bible, with the removal of Adam's rib to create Eve.[4]

Modern medicine also documents the use of bone grafts throughout history. The first documented bone graft, xenogenic in nature, derived from canine skull and used in the repair of a soldier's cranium, dates to 1668; [1, 5] while modern grafting is said to have its beginnings with the 1674 description of bone anatomy and physiology,[1] with the subsequent implantation of auto-, allo-, and heterogenic grafts.[6] More important than the detailing of the documented grafting procedures of the past are the landmark discoveries that resulted from their studies. As a result of these endeavors and many like them, scientists have come to understand the three physiological functions attributed to bone grafts: osteoconduction, osteogenicity, and osteoinduction.[5-7] These terms refer to the graft's ability to utilize the three-dimensional porous structure to facilitate cell and nutrient infiltration, to supply bone-forming cells through the bone marrow, and to initiate the differentiation of stem cells present in the graft towards the osteogenic lineage, respectively. [7-12]

To date, the gold standard for osseous reconstruction remains the bone graft, autologous or homologous, yet it is still riddled with disadvantages that prevent widespread usage. Autogenic grafts are marred with limited availability for transplantation, lack the ability to withstand functional loads[13] and can be associated with donor-site morbidity resulting from invasive surgical procedures,[8, 10, 12-14] post-operative chronic pain,[12, 15] and infection.[10, 14, 16] Although the allogenic graft is more readily available and can provide the necessary structural stability, the processing associated with its use (for example, freeze-drying, irradiation, or lyophilization) oftentimes reduces the osteoconductive and osteoinductive potential in an effort to reduce any adverse immunological reactions that may be incurred.[17-18] Additionally, the reduced bioactivity results in the failure to sufficiently revascularize and remodel, resulting in refractures 1-2 years post-implantation, with most recent research attributing its poor clinical success rate to its absence of viable cells.[13, 19] Moreover, due to strict regulations on their usage, allografts are only used in countries where donor-recipient are correctly matched, and where which fresh frozen grafts are stored.[14] Xenografts are rarely considered for grafting due to its high antigenicity. In these cases, processing procedures to reduce the immune response, e. g. partial deproteination and defatting, usually eliminates the osteoinductive proteins necessary for successful grafting, and the absence thereof consistently results in a lack of osteogenic response when used in hard or soft tissue applications.[12] The limited availability and heightened antigenicity of auto- and allografts respectively have spurred the search for new solutions for the repair of

large bone defects. Additionally, with technological advances and the transition of the goal of modern medicine from the reparative to the regenerative, there is a need to find solutions for organ replacement and repair that go beyond the “plug-and-chug” solution of implanting inert materials to stabilize and hide defects to a more holistic approach that seeks to augment and repair lost tissue and function.

## 1.2 New frontiers of research

The search for answers to address this challenge have been enhanced by the development and progression of new fields of integrated, interdisciplinary science, specifically with the evolution of tissue engineering and regenerative medicine as an offshoot of biomedical engineering. In the case of the latter, in its infancy, contributions to clinical practice have been in terms of medical instrumentation for the diagnosis and treatment of disease.[20] Yet after the 1950s and 1960s, its activities have expanded to consist of a breadth of activities, including the creation of new biologic products[21] via the incorporation of biological strategies to address its engineering objectives. This paradigm shift from merely substituting materials for assisted function to discovering solutions that encourage the natural development and regeneration of lost tissue and its function is the defining umbrella under which tissue engineering and regenerative medicine reside. In its simplest form, tissue engineering involves the modification of

artificial materials to not only assist cells in reconstruction, regeneration, and repair of damaged tissue but also to restore lost function.[22] A term often used interchangeably with *tissue engineering*, *regenerative medicine* denotes the addition of stem cells and other cell-based approaches. R. E. Guldberg comments, " the transformation from bone grafting to bone tissue engineering began with the introduction of osteoconductive bone graft substitutes or scaffolds and is rapidly evolving to include local delivery of osteogenic cells -and bioactive factors." [13]

## 1.3 Problem Statement

To date, the fields have helped us understand that the engineering and regeneration of tissue is highly dependent upon the utilization of the tissue engineering triad: matrix, cells, and support. The matrix and support components are virtually inextricable. Realization of these functions, arguably the most critical for large defects,[23] is accomplished through the use of synthetic grafting and scaffolding. Biomaterials used in its construction serve to recapitulate the biological and mechanical function of nascent extracellular matrix (ECM). From the biological standpoint, the ECM directs cell adhesion, proliferation, and differentiation;[24] from the mechanical perspective, it not only serves as a point of support in the maintenance of mechanical integrity, but also directs cellular behavior via its intrinsic mechanical properties.[25-26] Aside from the clear requirement of biocompatibility, scaffolds used for the purpose of osseous regeneration

are obliged to be osteoconductive and demonstrate resorption rates commensurate with rates of bone formation such that the mechanical load may be transferred from scaffold to growing tissue with the progression of time. Additionally, they should allow for the eventual removal of the degradation products through metabolic pathways.[27] Furthermore, scaffolds should be easily and repeatably manufactured and sterilized, cost effective, and uncomplicated to handle in a clinical environment, where preparatory procedures can increase the risk of contamination and infection.[25] Radiolucency has also been identified as an optimal feature, for the ease of distinction between scaffold and neo-tissue.[25]

It is well-accepted that the design specifications of scaffolds include considerations for porosity, fenestration, permeability, and geometry, i.e., dimensionality and configuration that may be specific to anatomic location of defect site.[28-42] Research has elucidated a need for minimal pore sizes of 100 microns, but the range of 200-900 microns has been highly investigated and touted for its ability to encourage both bone growth and neo-tissue vascularization.[25, 29, 35-36, 40] Pore size, however, is not nearly the sole determinant of a successful scaffold construct. Pores must be plentiful and interconnected, while the scaffold geometry is such that the diffusion of nutrients and the removal of cellular metabolic products occurs in a way that promotes healthy tissue ingrowth.

Several biomaterials have been used in the development of scaffolds for bone tissue applications: natural ECM,[13, 24, 36, 43-47] polymers,[13, 24, 28, 31, 40-41] metals,[40] and ceramic materials,[40, 48-52] each with its own set of advantages and limitations. Natural ECM materials are advantageous in that they are biocompatible, yet their use is limited in that they have been shown to have uncontrolled degradation, lack mechanical stability, and induce inflammatory and other immunogenic responses.[13] Synthetic polymers can circumvent the limitations associated with immunogenicity, mechanical instability, and degradation of natural ECM materials, but often introduce the problem of lack of cellular adhesion and hydrophobicity.[13] Metallic biomaterials have excellent mechanical properties, and are commonly used in load-bearing applications. However, high stiffness not commensurate with that of bone often leads to stress-shielding, bone resorption, and loosening or inadequate fixation of the implant, largely due to the material's inability to form sufficient bonds with bone tissue. Finally, ceramic biomaterials based on calcium-phosphate have demonstrated sufficient bone-bonding capabilities due to the presence of hydroxyapatite, but the brittleness of the materials and the high degree of chemical instability for several compositions prevents them from being used in load-bearing applications.

Few limitations, however, have prevented the use of these respective biomaterials in scaffold technology: synthetic hydrophobic polymers are coated with (RGD sequences) to encourage the adsorption and retention of cellular adhesion proteins such as fibrinogen and fibronectin; ingrowth and bond strength of metallic implants and scaffolds

are enhanced with the advent and use of porous constructs, or surface treatments and coatings to improve surface roughness and introduce microporosity--thereby enhancing bond strength by creating nucleation sites for calcium-phosphate crystals present in the milieu. Chemical instability of CaP compositions can be minimized through the use of composite materials, e.g. biphasic calcium phosphates in which the degree of resorption depends on the phase amount of hydroxyapatite and tricalcium phosphate used; or composites of CaP and polymers that reduce the material's brittleness, but allow for the exploitation of its bone bonding capabilities.[14, 19, 53-55]

The cellular component of the triad is necessary for the realization of regeneration, as in the case of many congenital or acquired conditions, or in cases of traumatic injury, when the degree of bone damage exceeds the body's intrinsic capabilities of regeneration. In tandem with support structures, biologics in the form of stem cells or growth factors have been used to leverage existing endogenous mechanisms for the repair or restoration of tissue and function.

The combination of the three triad components defines the scaffold- and cell-based approaches conceptualized with tissue engineering and regenerative medicine. Through their investigations, the field has not only been able to establish effective biomaterials for its uses, but has also established and demonstrated repeatable methods to encourage tissue growth *in vitro* and *in vivo*. With the myriad of advances

the research has afforded us, one limitation encountered by the clinician and researcher intending to utilize this technology is in knowing where to begin with its implementation; specifically, when faced with the limitation or boundary of a fixed variable, a CaP ceramic material type for example. The question beckons: how do we balance the inherent material properties due to composition and fabrication with the architectural augmentations necessary to encourage positive boney expression? Put more simply, ***how does one derive, or design, a scaffolding construct suitable for the production of the "best quality" bone?***

## 1.4 Research objectives

The current research targets the identification of the critical scaffold properties (materials vs. designed) that drive performance in terms of tissue regeneration within the calcium phosphate ceramic construct. **The principle hypothesis governing this work is that successful bone tissue engineering critically depends on design parameters, and marginally on materials properties in the instance of achieving maximum volume of regenerated tissue. Conversely, we assert that the quality of regeneration is highly dependent on the materials parameters of the ceramic construct, namely the composition and the microstructure.** The objective of the proposed research, therefore, is to elucidate the dependency of bone tissue

regeneration via a calcium phosphate ceramic scaffold on the scaffold's inherent materials properties (ceramic composition and microporosity) and compare it with its dependence on designed scaffold properties (macroporosity, permeability, and surface area). In doing so, the degree and quality of tissue regrowth will be quantified, and an "optimum or minimum" macroporosity for a given composition-microporosity profile will be suggested. We are, however, not attempting an optimization effort, but rather attempting to highlight the regeneration expectations of a particular group. We are specifically seeking to advance the understanding of synergy between ceramic biomaterials and the designed scaffold fabrication parameters which result in the ability to direct regeneration of tissue. In order to address these goals, several questions should be addressed:

- *How do the chemical composition and microstructure influence the regeneration potential of our scaffolds?*
- *How is the regeneration potential influenced by the design parameter, macroporosity?*
- *Of the parameters under consideration, i.e., microporosity, macroporosity, and composition, which is most important?*
- *Is there a difference in bone quality as a result of any parameters investigated?*
- *Is there a traceable pattern of materials mechanical property degradation to be expected for each group?*
- *Lastly, for a given composition, is there an ideal parameter cocktail that produces better bone?*

## 1.5 Strategy for investigation

The investigation into these questions utilized one material model: sintered porous ceramics based on hydroxyapatite, though the composition of the material was a primary variable. The *in vitro* model characterized the material microstructure and mechanical properties of bulk and scaffold materials. Additionally, a simulated body fluid (SBF) model was employed to study the mechanical property degradation associated with each material type. Degradation was also studied *in vivo*. The model used for this portion mirrors the *in vivo* regeneration model: subcutaneous implantation of SCID mice; the regeneration study with the addition of human gingival fibroblasts (HGFs) infected with an adenovirus producing bone morphogenic protein (BMP-7) under a CMV promoter. This *in vivo* model was used to characterize material degradation via micro-computed tomography, characterize mechanical degradation as a function of time, as well as study regeneration of each aforementioned group.

### 1.5.1 Specific Aims

The specific aims of this thesis are to:

1. Characterize the microstructure of the bulk material constructs, and identify a technique that allows for the distinction of hydroxyapatite and tricalcium

phosphate grains and confirmation of a characteristic microstructure for biphasic groups.

2. Determine the effect of chemical composition on the mechanical property degradation.

3. Determine the influence of scaffold materials and design parameters, composition, microporosity, and macroporosity, on tissue regeneration.

## 1.6 Summary of thesis contents

We address these aims in the following manner: Chapter 2 introduces the background and current state of literature. Here you will find a discussion of bone as a biological material, calcium phosphate ceramics in bone tissue engineering applications, biomineralization and related biomarkers, and essential materials and design parameters as consideration for scaffolding. Chapter 3 characterizes the material properties of the bulk material; specifically we assess the powder sinterability, densification and microstructure development, as well as the bulk mechanical properties of sintered pellets. Chapter 4 focuses on the design architecture of the scaffolds utilized in the current study. Here, a baseline characterization that addresses design parameters and differences in final structure due to fabrication and processing is presented. Chapter 4 addresses specific aim one by characterizing the material properties of the scaffolds, specifically the composition and microstructure of each

group utilized. Chapter 5 addresses specific aim two by characterizing the degradation of the mechanical properties, includes a discussion of the *in vivo* degradation of the material as assessed using micro-computed tomography. Specific aim three is addressed in chapters 6 and 7: chapter 6 investigates the influence of composition, sintering temperature, and macrostructure on the regeneration of osseous tissue via fabricated CaP scaffolds; chapter 7 re-evaluates data presented in chapter 6 to assess the relative contributions of design parameters, macroporosity, surface area, and permeability, to the regeneration of bone. Chapter 8 concludes with a discussion of how all the pieces fit together and how effective we can expect to be in realizing *a priori* a favorable degree of regeneration based on scaffold parameters modeled in this study, as well as a discussion of proposed future work.

# CHAPTER 2
# BIOLOGICAL AND MATERIALS CHARACTERISTICS OF BONE AND THEIR IMPENDING INFLUENCES ON TISSUE ENGINEERING STRATEGIES FOR ITS REPAIR AND REGENERATION

*"The tendency of old age, say the physiologists, is to form bone. It is as rare as it is pleasant to meet an old man whose opinions are not ossified".*
*-Bob Wells, quoting Dr. John F. Boyse*

## 2.1 The Need to Imitate Structure and Function

When we consider bone and its physiological uses, we are reminded of its functions: support, protection, movement, mineral storage and blood cell formation. The framework provided by our bones provides structural support that not only allows us to stand, but also protects viable internal soft tissue organs of the cranial and thoracic cavities. Additionally, this support structure provides a site for muscle attachment thereby enabling locomotion and respiration, while mineral homeostasis and hematopoiesis constitute bone's primary regulatory functions.

The structure and properties of a given biological material are dependent on the chemical and physical nature of the components present and their relative amounts. Therefore, if we are to employ the use of biomaterials to augment and improve tissue or organ function, an understanding of the exact role played by a tissue and its interrelationship with the function of the entire living organism is essential.[56] Thus, the design of a bone prosthesis or other replacement structure has to be based on the understanding of not only the property-structure relationship of bone but also its systemic function: not only is it a source of mechanical support, but also a reserve of ions, especially calcium and phosphate, for the maintenance of serum homestasis.

This chapter seeks to provide an overview of bone structure and function, as well as discuss the interaction between structure and function and the resulting physical and physiological changes. First, bone is reviewed from the biological perspective, with the discussion focused on the cellular components and their respective divisions of labor, biomineralization, and bone formation and modeling. Second, bone is viewed from the materials perspective, with inspection of the mineral content and resulting biomechanical properties. This section begins with a discussion of mechanically-mediated adaptation: the feedback interaction between remodeling and mechanical properties imparted as a function of physiological loading, and follows with a discussion of the calcium phosphate ceramic materials utilized in bone tissue engineering

applications, as well as the essential materials and design parameters under consideration for scaffolding applications.

## 2.2 The Biology of Bone

### 2.2.1 The Cellular Components of Bone

Four cell types comprise bone: osteoblasts, osteoclasts, bone-lining cells, and osteocytes. These cells not only differ in anatomical function and location but also in lineage and morphology (Figure 2.1). Of this group, the latter reside in the mineralized interior of bone and functions to maintain bone, while the former three (osteoblasts, osteoclasts, and bone-lining cells) reside on its surfaces and function in bone formation or resorption. Their respective lineages can be traced to either osteoprogenitor cells or to cells originating in hemopoietic tissues.

#### 2.2.1.1 Cells of Mesenchymal Origin

Osteoprogenitor cells, also referred to as preosteoblasts, are the differentiated progeny of local mesenchymal stem cells, originating from bone marrow stromal cells or connective tissue mesenchymal stem cells, transformed under the influence of various growth factors, bone morphogenic proteins, Wnt proteins and the transcription factors Runx2 and Osterix. These preosteoblasts are the inactive precursors to osteoblasts,

and are located on the periosteal and endosteal surfaces of bone as well as in bone's microvasculature. [57-59] They have the ability to proliferate and are responsive to molecular stimuli that further facilitate their differentiation into one of the three maturational stages of osteoblast development: osteoblast, osteocyte, and bone lining cell. "The fidelity of bone structure and metabolic function relies on the exchange of regulatory signals among these cell populations." [60]

#### *2.2.1.1.1 Osteoblasts*

Triggered by core binding factor alpha-1 (CBFA1), as well as a host of other proteins and growth factors, preosteoblasts acquire the phenotype of osteoblasts, hence differentiating into the bone-forming cells of the mesenchymal line. Osteoblasts are considered the fully-differentiated bone formers and have the ability to produce and secrete bone matrix and regulate its mineralization. More specifically, osteoblasts have been credited with the ability "to effect calcification in three primary ways: firstly, as the origin of matrix vesicles; secondly, by controlling, to some degree, the movement of calcium ions into and out of bone fluid, and thirdly, by its ability to store calcium in its mitochondria and possibly pass it into the matrix." [61] This is achieved, directly or indirectly, via its ability to synthesize collagen type I, various glycoproteins and proteoglycans of the ground substance, as well as osteocalcin, osteonectin, osteopontin, and osteoprotegrin. Additionally, the osteoblast membrane contains

receptors for various hormones, vitamins, and cytokines that control the activity of the cell.[59]

Actively secreting osteoblasts are cuboidal in shape and aligned on bone surfaces. They do not present themselves as a typical epithelium in that they are spaced a short distance apart, but maintain contact with neighboring osteoblasts via short lateral processes. "The nucleus is near the rounded upper end of the cell and the underlying cytoplasm is basophilic and contains abundant rough endoplasmic reticulum and free ribosomes. Osteoblasts appear to be polarized towards the surface that is in contact with the underlying bone, but their release of matrix components is not confined to that surface. On a growing bony surface, some of the osteoblasts become enveloped by their own secretions, and are imprisoned in lacunae within the newly synthesized bone matrix and are transformed into osteocytes."[59] Once inactive, osteoblasts are flattened against the underlying bone and their basophilia and content of endoplasmic reticulum are reduced, thus transformed into bone lining cells.

#### *2.2.1.1.2 Bone Lining Cells*

Bone lining cells, or *resting osteoblasts,*[61] are found on the surface of adult bone undergoing neither formation nor resorption, and differ morphologically from the active osteoblasts previously described. These cells have been said to resemble fibroblasts in

that they are long and flat, possessing long flat dense nuclei, few internal organelles, and long processes extending into the osteoid and mineralized bone. Bone lining cells often occur as a single layer adjacent to the mineralized surface or to the separated marrow[61] of cancellous and endocortical bone surfaces. The function of bone lining cells is subject to controversy: although many researchers often consider them inactive, some investigators have demonstrated their ability to synthesize DNA, and therefore proliferate,[61] while others postulate a role in the localization and initialization of the remodeling process[62] or possibly as precursors for osteoblasts. [18]

#### *2.2.1.1.3 Osteocytes*

The osteocyte, the most abundant cell type of bone,[63] is the terminally differentiated stage of osteoblast development. Mature osteoblasts are distinguished from their surface precursors in that they are embedded within the calcified bone matrix, residing within tiny lacunae (25,000 per $mm^3$ of bone).[57] Osteocytes are ultimately responsible for matrix maintenance. These cells have the capacity to not only synthesize, but may also possess a limited ability to resorb matrix, although this too is disputatious. [57, 61, 63-64] Additionally, osteocytes have been hypothesized to play a role in blood-calcium homeostasis as well as the functional adaptation in the regulation of bone mass and structure.

Osteocytic morphology, though still similar to that of the osteoblast, varies with the cell's age and functional activity. Young osteocytes retain decreased cell volume and reduced importance of organelles involved in protein synthesis [57] when compared to functional osteoblasts. Older osteocytes are located deeper within the calcified bone and demonstrate further decreases in cell volume as well as an accumulation of glycogen within the cytoplasm. Osteocytes of either age group have numerous long filapodial cell processes that not only connect, via gap junctions, with those of other osteocytes but also with those of surface-residing osteoblasts and bone lining cells. This network *connexon* of thin canalaculi permeates the total bone matrix and assists in the osteocytic function of mechanotransduction and regulation of metabolic activity. To this end, cell-matrix adhesion assists in the translation of biomechanical signals due to bone loading into chemical signals that facilitate the synthesis of matrix molecules essential in the regulation of mineral deposition and resorption.

#### 2.2.1.2 Cells of Hematopoietic Tissue Origin

##### *2.2.1.2.1 Osteoclasts*

Unlike osteoblasts and its progeny, osteoclasts differentiate from the fusion of precursor cells with similarities to mononuclear blood cells, thought to be the mononuclear cell from the hemopoietic marrow.[61, 65] The defining characteristics of osteoclast morphology

are characterized by its multinucleation, ruffled and brushed borders[i], and clear zone. These giant cells can have as many as 100 nuclei, or as few as two, though most have roughly 10-20; yet there is no direct evidence of a correlation between resorption capacity and number of nuclei.[61, 66] The active osteoclast can be found resting directly on the bone surface, and functions in the resorption of hydroxyapatite, bone's mineral phase. Its cytoplasm is highly vacuous, with the zone of bone contact marked by the presence of a central ruffled border surrounded by a ring of actin (sealing zone); functioning, along with adhesion integrins, to anchor the cell to the bone surface, thus isolating the subosteoclastic bone-resorbing compartment. The mechanism by which bone resorption is facilitated is best described as local acidification. Protons are secreted across the ruffled border membrane, creating a highly acidic milieu in which the hydroxyapatite crystals are released from their collagen links and dissolved; additionally, the digestion of residual collagen fibrils and degradation of matrix components ensues, and the resulting residues are internalized and transported across the cell and released to the central area of basal membrane. [57, 64, 66]

[i] There is a distinction to be made between the ruffled border and the brush border: the former has been described as a cause of resorption, composed of finger-like processes that extend into the cytoplasm, fanning out from the cell and terminating on the bony surface, while the latter has been described as an effect of resorption: the straight collagenic fibrils of calcified bone (or cartilage) freed from mineral during resorption, and occurring at right angles to a resorption surface. [**61.** Vaughan J. *The Physiology of Bone*. Third ed. Oxford: Clarendon Press; 1981.]

### 2.2.2 Bone Formation and Modeling

During embryonic development, osteogenesis occurs via one of two mechanisms: *intramembranous* ossification or *endochondral* ossification. The two processes differ in their starting soft tissue base and the presence of a cartilage precursor. Intramembranous ossification (Figure 2.2) is the direct transformation of connective tissue, fibrous tissue, into bone. It is the process by which the flat bones of the face and skull, as well as the mandible and clavicle are formed. This mode of bone formation begins with the condensation of cells within the mesenchyme, followed by the differentiation into osteoprogenitor cells expressing the *Cbfa1* transcription factor. The process initiates vascularization at the bone site and changes in cell morphology and cytoplasmic milieu lead to the differentiated osteoblast and secretion of collagen, bone sialoproteins, osteocalcin, and other components of the osteoid. This bone matrix first appears as trabeculae, or thin strands of eosinophilic material,[67] but soon mineralizes and gives rise to osteocytes. At the periphery, the differentiation of mesenchymal cells into osteoblasts persists, and bone formation proceeds on the surface of the trabeculae, thereby creating primary spongiosa (woven bone). Cortical bone forms if the trabeculae continues to thicken; cancellous bone develops where trabecular thickening halts and vascular connective tissue space is gradually transformed into hematopoietic tissue.[67] In both instances, the primary, woven bone, is remodeled and progressively replaced by mature lamellar bone.

By contrast, endochondral ossification begins with a hyaline cartilage precursor established during embryonic development (Figure 2.3). In this process, fibroblastic growth factors (FGFs) and BMPs encourage the expression of collagen type II and chondroblastic differentiation, and therefore the production of the cartilage matrix. The newly established cartilage model grows interstitially and appositionally (whereas new bone apposes on the surface) and is advantageous for the rapid longitudinal growth of long bones. With the establishment of a primary center of ossification in the center of the diaphyseal portion of the cartilage model, three events occur simultaneously:

> *1.) Under the existing perichondrium, newly differentiated osteoblasts create the periosteal collar by secreting a type I collagen-rich osteoid that later becomes mineralized;*
>
> *2.) chondrocytes in the central portion of the model undergo hypertrophy, cease the production of proteoglycans aggregates and type II collagen, and begin to produce alkaline phosphatase, matrix vesicles, and type X collagen. This matrix intervenes, is compressed into thin septa, and calcifies, leading to the degeneration of chondrocytes and the presence of a calcified cartilage scaffold;*
>
> *3.) blood vessels invade and penetrate the cartilage core accompanied by hematopoietic cells, osteoprogenitor cells and osteoclasts, ultimately forming the periosteum and bone marrow.*[67]

In the interior of the cartilage model, osteoblasts deposit bone onto the thin calcified cartilage septa. These trabeculae are either remodeled and replaced by secondary lamellae of trabecular bone or by marrow.[67] With the creation of the bony collar, no

interstitial growth of the diaphysis can occur. Instead, growth in the diameter and shape of the bone occurs via intramembranous ossification, i.e., appositional growth, due to apposition on the periosteal surface and resorption on the endosteal surface. Secondary centers of ossification occur, post-birth, in the epiphyses of the long bones; growth occurs in a sequence that is similar to that of the primary centers, without the subperichondral deposition of bone.[61, 67] Instead, the rapid and continuous longitudinal growth depends on endochondral growth at the epiphysial growth plate, and continues until the bone has reached its final length and the growth plates fuse.

These processes of longitudinal growth and modeling, two phases in the development and turnover of bone, see a continuous adaptation of bone's macroscopic shape. With boney surfaces experiencing resorption and formation in tandem, the size and geometric shaping of bone is achieved. Modeling plays its major role during growth, but becomes relatively ineffective around and after skeletal maturity; after which any changes in bone's structure and shape are due to remodeling.[67]

### 2.2.3 Bone Remodeling

Remodeling, the third stage in the development and turnover of bone, results in the turnover in lamellar bone; and, unlike modeling, does not result in large changes in the size, shape, or quantity of bone. Instead, its occurrence is to "adjust the skeleton to changes in mechanical demands, to prevent accumulation of fatigue damage, to repair micro fractures, to ensure viability of the osteocytes, and to allow the skeleton to participate in calcium homeostasis."[67] Remodeling occurs in discrete packets throughout the skeleton, and is completed within a finite period of time,[ii] with time differences between the remodeling of cortical vs. cancellous bone; cancellous bone turnover being longer in duration.[57, 68] Bone remodeling differs from the other two stages of bone turnover in that osteoblasts and osteoclasts do not act independently, but are coupled; that is, in the normal remodeling process, resorption and formation are closely associated both temporally and spatially, and, resorption will always be followed by formation, and formation will always be preceded by resorption.[67]

As first described by H. Frost, [57, 69] remodeling occurs via the activation-resorption-formation (ARF) sequence[iii] (Figure 2.4), where after activation, osteoclasts erode and

[ii] The complete remodeling cycle at each BSU, bone structural unit, site takes roughly 3-4 months (also cited as 3-6 months).

[iii] Remodeling has also been described in 5 stages: 1.) Quiescence, referring to the resting state of (all) bone surfaces; 2.) Activation, the recruitment of osteoclasts to a bone surface and signal coupling of osteoblasts; 3.) Resorption, the removal of bone by osteoclasts; 4.) Reversal, the process by which

resorb bone. At a particular depth, mononuclear cells replace osteoclasts and complete the resorption phase. Upon the completion of resorption, preosteoblasts infiltrate the area, differentiate into osteoblasts, and begin bone matrix formation.

### 2.2.4 Biomineralization

Physiological mineralization of the matrix is the hallmark of bony connective tissue, and the process by which cells deposit mineral within or outside of its matrix is called biomineralization. The presence of these mineral constituents in some tissues and not others leads to much uncertainty regarding the precise reason mineralization occurs. Yet, even in the face of such uncertainty, there are several points that are accepted regarding this phenomenon: (a) the organized formation of mineral does not occur without the presence of a matrix; (b) the matrix differs from tissue to tissue; (c) the site of initial mineral deposit may differ; and, (d) the roles of matrix proteins are varied.[70]

For any matrix upon which mineralization occurs, in bones and teeth for example, oriented support for the deposition of mineral is essential. For bone specifically, this is achieved via the osteoid's collagen I foundation, and assisted by noncollagenous elements of the matrix, although it is unclear whether the collagen participates directly in

---

osteoclasts stop removing bone and osteoblasts fill the deficit; and 5.) Formation, the laying down of bone by osteoblasts.

mineralization by serving as a nucleator or indirectly via the attachment or orientation of ions for incorporation into the crystal lattice.[70] In either regard, the mineralization of osteoid occurs in an orderly and controlled manner, with its mineral deposition being highly regulated.

The multi-step process of mineral formation begins with the facilitation of nucleation by the increased concentration of $Ca^{2+}$ and $PO_4^{2-}$ thereby increasing the probability of association, allowing the ions to form oriented stable structures resembling the phases deposited. Nucleation can also be facilitated by providing surfaces resembling that of the nucleus crystal for the templating of ion attachment.[71] These similar surfaces may arise through the use of foreign molecules which, through their crystal binding, may also serve to regulate mineral size and shape through the retardation of mineral proliferation by blocking growth sites.[71]

The three-dimensional spaces within the collagen structure, i.e., the gaps between the ends of two collagen molecules, also called hole zones, serve as the site of initial deposition, and occurs without disrupting the fibrils' orientation. Other matrix components also contribute to the mineralization process: ground substance proteoglycans, for example, may be involved in regulating the formation of collagen fibers in a form appropriate for subsequent matrix mineralization; osteocalcin, a Gla

protein, is involved in binding calcium during mineralization; and osteonectin may serve to bridge collagen and mineral, and sialoproteins and other proteins.[72]

## 2.3 The Structure and Material Properties of Bone

### 2.3.1 Bone Composition, Organization, and Morphology

Bone is a highly specialized and complex form of connective tissue, distinctive from others due to the mineralization of the extracellular matrix, conferring rigidity and strength, and at the same time, maintaining a degree of elasticity.[64] Aside from its cellular components, bone's primary organic constituents lie in its organic matrix, of which 95% is Type I collagen, and the remaining 5% is comprised of proteoglycans and other noncollagenous proteins. This matrix is strengthened by inorganic crystalline salts (roughly 69 wt% of cortical bone), primarily calcium and phosphate in the form of a nonstoichiometric carbonate-substituted hydroxyapatite[73] [$Ca_{10}(PO_4)_6(OH)_2$], though other mineral ions such as citrate [$C_6H_5O_7^{4-}$], carbonate [$CO_3^{2-}$], and fluoride [$F^-$] are present. Apatite crystals are small and morphologically characterized as thin needles 20-40 nm long and 1.5-3 nm thick and are organized in and around collagen fibers in the extracellular matrix.[56] The exact composition of bone depends on several factors, including the species, age, sex, and location from where the sample was taken, as

significant variability in the composition can be correlated with the structural variety of bone.[61, 73]

The structural organization of bone is most often discussed in terms of its macroscopic and microscopic arrangement.[iv] Macroscopic descriptions of bones are often in reference to long bones (Figure 2.5) and characterize its gross anatomy: the diaphysis, or tubular-shaped shaft, of the bone constitutes its long axis; the two wider extremities, the epiphyses, are located at the ends and are more expanded; and a transitional or developmental zone, the metaphysis, housed between the epiphysis and diaphysis. The epiphysis and metaphysis originate from two independent ossification centers, and in a growing bone, are separated by a layer of proliferating and expanding epiphyseal cartilage, also referred to as the growth plate, responsible for the bone's longitudinal growth. There are three boney surfaces of consequence: 1.) the surfaces at the epiphysis associated with the joint, covered with a layer of articular cartilage; 2.) the periosteum and 3.) endosteum, external and internal bone surfaces, both in contact with nearby soft tissues and lined with osteogenic cells organized in layers. The cortex of the long bone, comprised of a thick, dense layer of compact, or cortical bone, occupies

[iv] The hierarchical structural organization of bone has been characterized on (as many as) five levels: 1.) Macroscopic (whole bone organization, comprised of cortical and cancellous bone); 2.) Microscopic (10-500 μm, composed of osteons, Haversian systems, and trabeculae); 3.) Sub-microscopic (1-10 μm, composed of lamellae); 4.) Nanostructure (a few hundred nanometers-1 μm, composed of collagen fibers and embedded mineral); and 5.) Sub-nanostructure (less than a few hundred nanometers, composed of matrix constituents such as collagen, proteins, and individual mineral crystals). [ **74.** Rho J-Y, Kuhn-Spearing L, Zioupos P. Mechanical properties and the hierarchical structure of bone. *Medical Engineering & Physics.* 1998;20(2):92-102.]

bone's externus and, in the diaphysis, encloses the medullary cavity where the hemapoietic bone marrow resides. Toward the metaphysis and epiphysis, the cortex becomes progressively thinner, and the internal space is filled with a network of thin interlacing partitions--calcified trabeculae referred to as cancellous, spongy, or trabecular bone. Counter to cortical bone, cancellous bone is nearly equal in length and diameter[61] and has a loosely organized porous matrix enclosing cavities containing red or yellow, fatty marrow, and is continuous with the medullary cavity of the diaphysis.

The appearance of a loosely and poorly organized cellular structure (Figure 2.6) is the hallmark of trabecular bone, and yet the seemingly arbitrary orientation of the microarchitecture is not random. The mineralized collagen within this infrastructure, produces a webbing of the small, thin calcified tissue, arranged in a high porosity-low density structure in which the trabeculae align themselves along stress directions.[75] This interconnecting framework can organize in any number of combinations comprised of basic cellular structures, rod-rod, rod-plate, or plate-plate,[74] where rods and plates refer to the relative densities of the cell wall as well as the degree of openness of the entire cellular structure.[76]

Conversely, compact cortical bone is less porous; having the appearance of a more organized and extremely dense structure (Figure 2.7). Although the organization of this bone form is also preferential, the pattern conferred by the mineral-attached collagen

fibrils allows for the highest density of collagen per unit volume of tissue.[57] Here, the tightly compacted fibrils orient themselves in layers with alternating directions, attributing to its lamellar form. Lamellar sheets (3-7 μm) are oriented helically with respect to the long axis of the cylindrical *osteons,* with concentric rings surrounding a Haversian canal.[v] The osteon itself is comprised of 4 to 20 lamellae and 150-200 μm in diameter. Interstitial osteons are sharply divided by the *cement lines*, and metabolic substances are transported via interconnecting pore systems known as *canaliculi, lacunae, and Volkmann's canals*.[56-57]

The structural and functional differences that distinguish cortical and cancellous bone are based on the degree of calcification of their matrices: 80-90% of the volume of compact bone is calcified compared to 15-25% of that in trabecular bone. As a result, 70-85% of the interface with soft tissues is at the endosteal bone surface. Cortical bone functionality is primarily mechanical and protective, while the function of trabecular bone is metabolic.[57]

Morphologically, bone is classified according to its shape (long, short, flat, or irregular), each differing in its proportions of osseous tissue type, i.e., cortical or cancellous bone. Long bones, the elongated bones of our skeletal system such as the humerous, tibia, or fibula, contain primarily cortical bone, but may also contain significant amounts of

[v] In trabecular bone and periosteum, lamellae are parallel to each other and deposited on a flat surface.

cancellous bone within its interior. Short bones tend to be cuboidal in shape, for example, the patella, and are primarily cancellous bone, with compact bone limited to its thin surface layer. Flat bones (thin, flattened, and curved; the sternum and most bones of the skull, for example) have a layer of cancellous bone sandwiched in between two roughly parallel thick compact bone surfaces; while irregular bones, i.e., vertebral and hip bones, are more complicated in shape and are mainly spongy bone enclosed by thin layers of compact bone, not necessarily parallel in orientation.[58, 75] It is the coupling of morphology and composition, due to both organic and inorganic components, that accounts for the mechanical properties for which bone is notorious: exceptional hardness and ability to withstand compressive forces, as well as the ability to maintain some elasticity without being brittle.

### 2.3.2 Bone as a Material

From a materials science perspective, bone is considered a composite material in several senses of the term; its structure, intricate and complex on several levels of development. On (one) the microscopic level, it is considered a hydroxyapatite-reinforced collagen composite, analogous to a dual-phase composite with collagen as the continuous phase, or matrix, and HA as the reinforcing particulate with preferred orientation. This (initial composite material) can be considered bone's basic building block. On (another microscopic level) we can consider it to be a different 2- (or possibly

3-) phase composite with the continuous phase being the (goop of fluids, proteoglycans and other biological macromolecules) with collagen fibrils functioning as the fiber reinforcement with random orientation. As we progress to higher macroscopic levels, the orientation of the collagen fibers changes and gives rise to several composite types, defining the structural differences in the macroscopic classifications of bone. For example, woven bone can be considered a single-layer discontinuous fiber-reinforced composite with random orientation, while lamellar bone a multi-layered composite with locally-oriented fibers arranged in lamellar sheets. This end product, bone, with its multi-level composite structure forms a most complicated structure difficult to emulate in synthetic form.

As with any composite material, the mechanical properties of bone are dictated by the constituents from which it is made, being strongly influenced by the proportions and properties of the matrix and its reinforcement. In this manner, bone's hardness is attributed to its mineral deposition while toughness and viscoelasticity are due to the collagen fiber network. Collagen has a Young's modulus of 1-2 GPa and an ultimate tensile strength of 50-1000 MPa. Hydroxyapatite, on the other hand, has a Young's modulus of about 130 GPa and an ultimate tensile strength of nearly 100 MPa. The mechanical properties of compact bone, with its closely packed Haversian systems surrounded by concentric rings of matrix, differs greatly from that of cancellous bone, having loosely organized porous matrix with collagen fibrils forming concentric lamellae. The mechanical properties of cancellous bone have been reported to depend on age

and are related to the changes in bone density. At the microstructural levels, mechanical properties also differ, mainly as a function of cortical bone maturation, which may alter mechanical properties on this level.

## 2.4 Chapter Summary

This chapter presented an overview of bone, from the biological and engineering perspectives. We discussed bone's cellular components, its physical make-up, and biological functionality; and we attempted to draw parallels between bone's structural organization and the resulting materials properties, and therefore, the subsequent alternatives available for the repair of inefficient osseous function. It is with the understanding of these points that we can begin to investigate the use of calcium-based ceramics and their influence on the regeneration of bone.

## 2.5 Figures

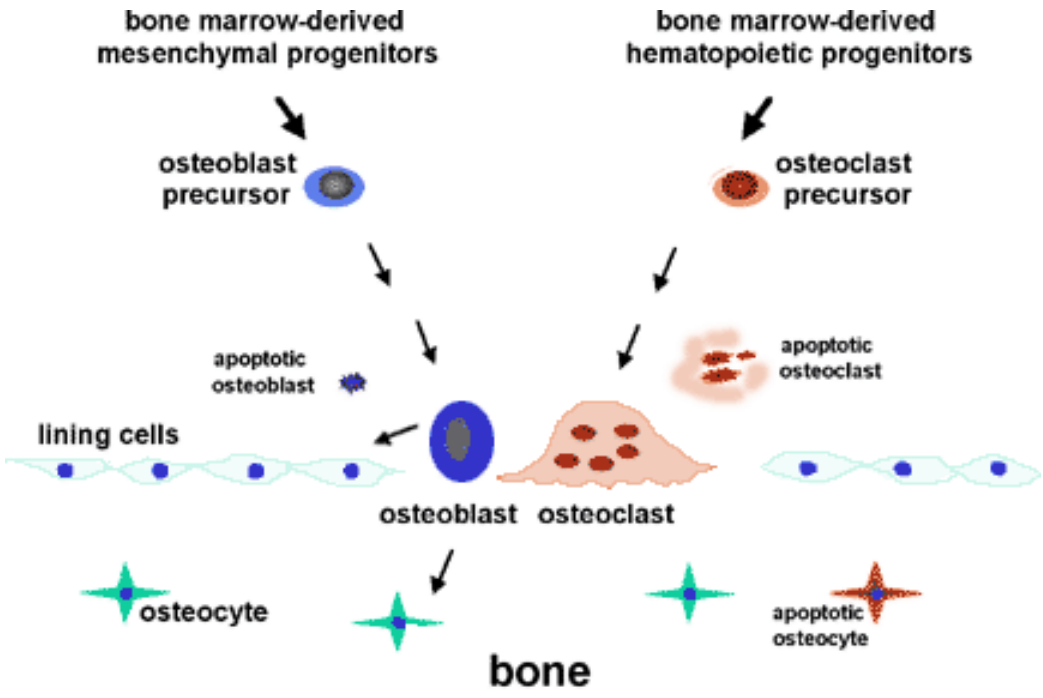


Figure 2.1: Bone cell lineage.[77]

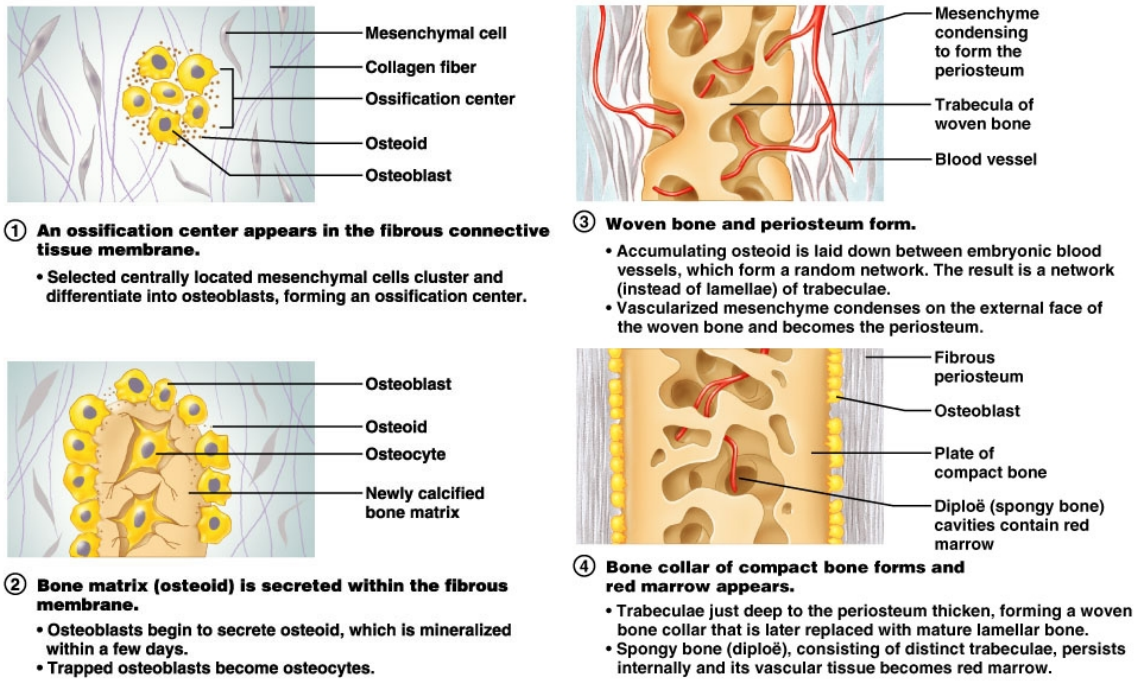


Figure 2.2: Bone formation via intramembraneous ossification. [78]

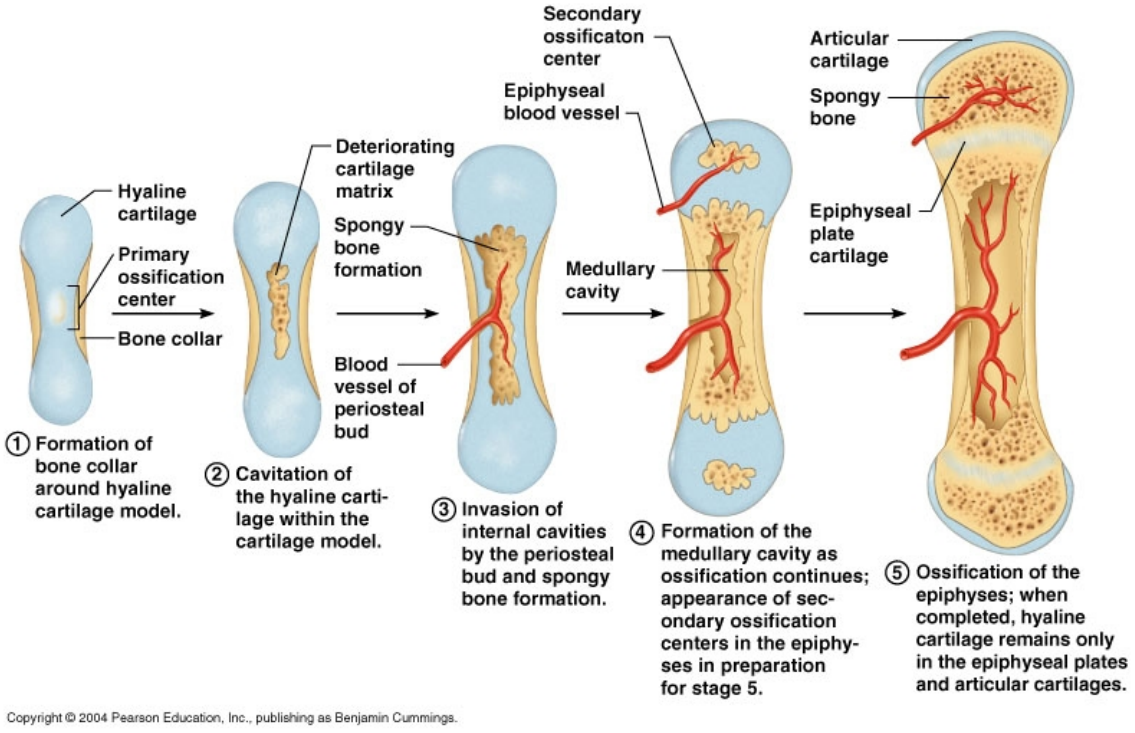


Figure 2.3: Bone Formation via endochondral ossification.[79]

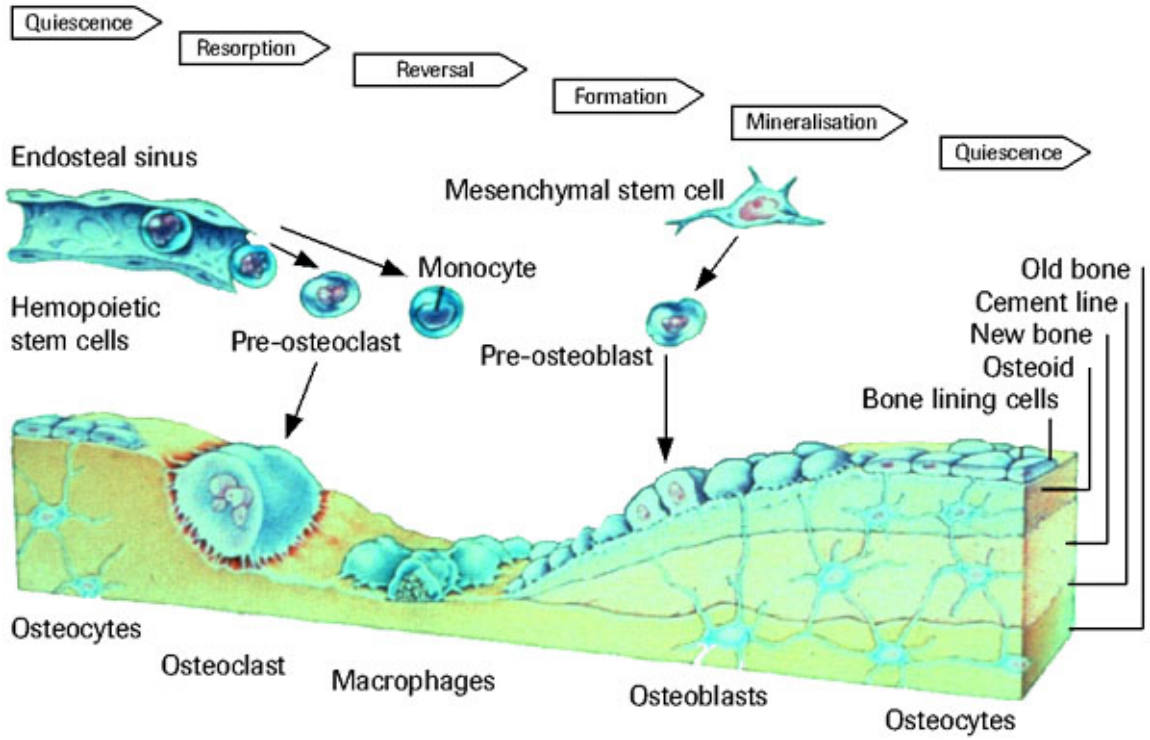


Figure 2.4: Bone Modeling and Remodeling[80]

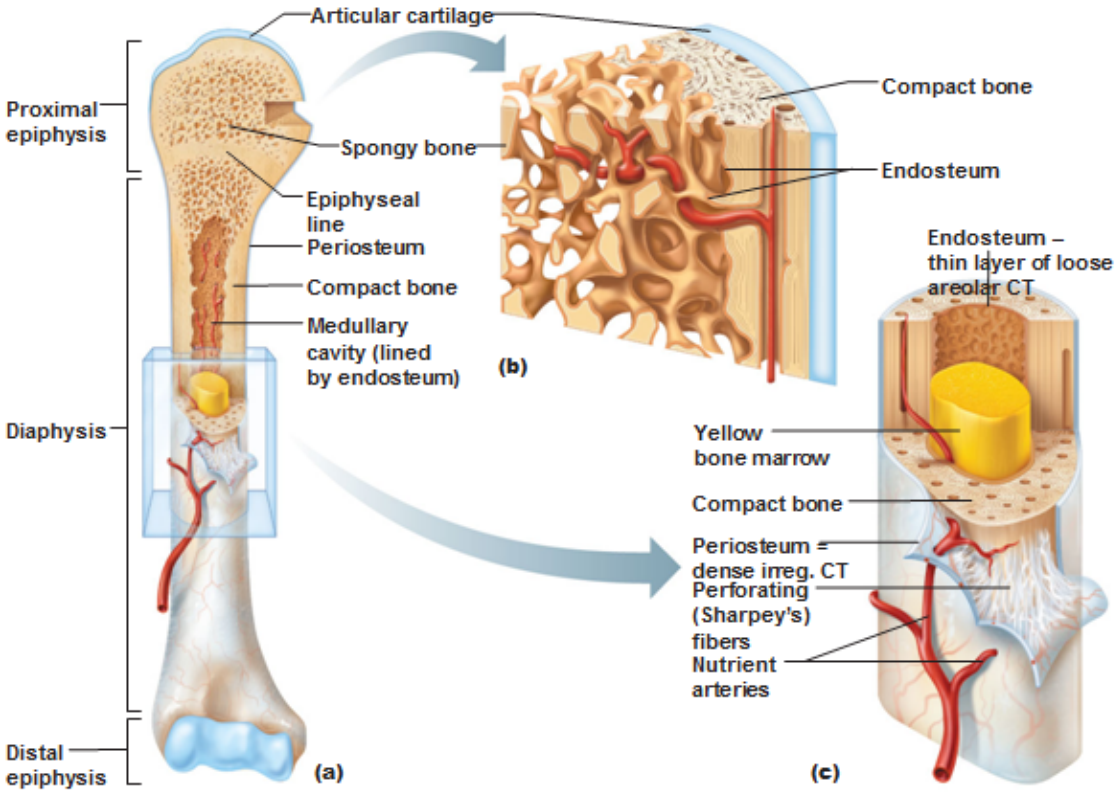


Figure 2.5: Gross Anatomy of Long Bone[81]

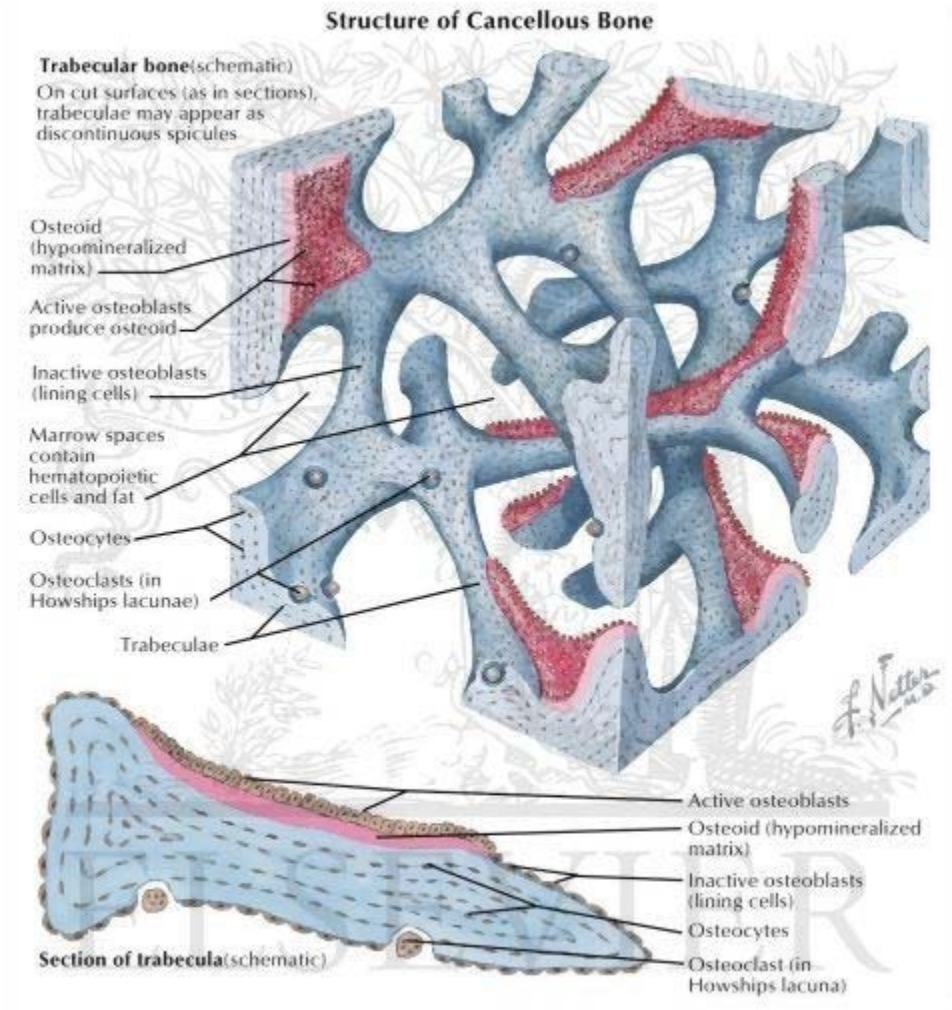


Figure 2.6: Structure of Trabecular Bone.[82]

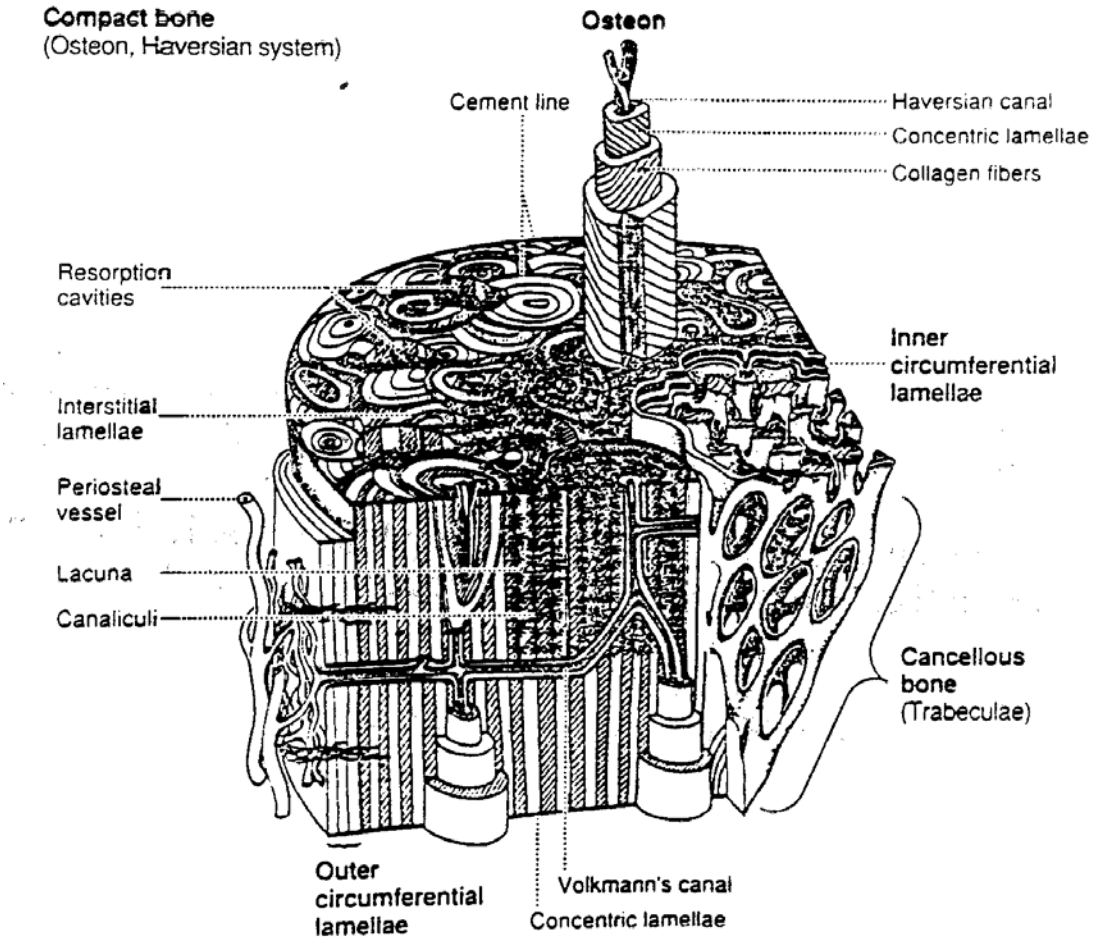


Figure 2.7: Structure of Cortical Bone.[83]

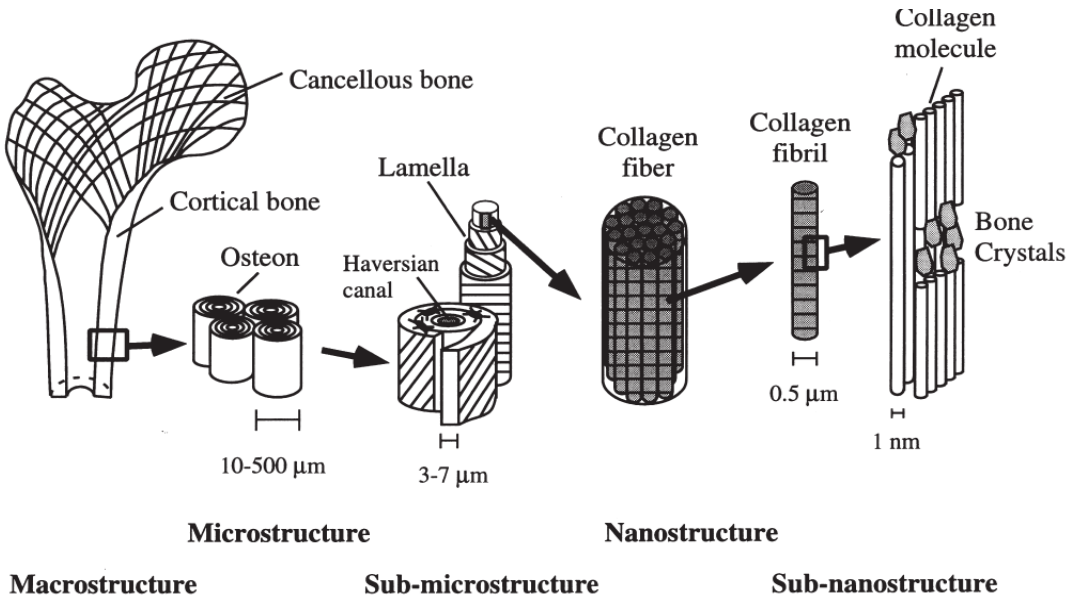


Figure 2.8: Structural hierarchy of bone. The microstructure of cortical bone consists of osteons and Haversian systems formed of lamella. Collagen fibers composed of collagen fibrils and bone mineral form the nanostructure.[56, 74]

# CHAPTER 3
# CHARACTERIZATION OF PHYSICAL PROPERTIES OF CALCIUM PHOSPHATE BULK MATERIALS

*"Nature will bear the closest inspection. She invites us to lay our eye level with her smallest leaf, and take an insect view of its plain".*
*-Henry David Thoreau*

## 3.1 Significance of Materials Properties Characterization of Calcium Phosphate Biomaterials

Since its establishment as a suitable materials construct for bone tissue engineering applications, much research has been devoted to understanding the material properties characteristics of calcium phosphate materials and how those properties impact bone regeneration. Elucidated in the literature is the effect of fabrication methodologies such as powder preparation,[84] sintering profile,[85-87] and presence of various inorganics[85, 88-89] on chemical and physical properties and subsequently, biological behavior.[90-92] LeGeros, et al. demonstrated that the firing temperature of calcium-deficient apatite affects the final phase amounts of HA and β-TCP as well as the crystallinity of the

powder.[93] Boulsma, et al. determined that the addition of fluorapatite to tricalcium phosphate resulted in ceramic constructs with increased mechanical properties.[94] In a series of short-term implantation experiments, Winter, et al.[95] demonstrated the variability in histological response to hydroxyapatites obtained from various commercial sources and sintered using different processes and temperatures; thus implying that biological behavior changes considerably for the same nominal material—that behavior for a particular material depends on processing variables such as sintering temperature, and that that behavior is different between different commercial sources. These inconstancies are surprising, and more importantly, stress the significance of processing parameters and sintering temperatures to the success of calcium phosphate ceramics for biological use.

It is well understood that for ceramic materials, sintering temperature is a major determinant in microstructure evolution and microporosity, the degree of void space due to pores <10 microns in size. A starting ceramic powder of fine particle size and absence of agglomeration (also referred to as its *sinterability*), formed to a particular starting density before sintering (also referred to as its *green density*), is expected to develop an average grain size and residual microporosity upon sintering (collectively referred to as its *microstructure*) that is highly dependent on the sintering temperature and duration of the sintering treatment. And, as a matter of consequence, sintering behavior can vary widely from one source of powder to the next. To further complicate

matters, HA and β-TCP are known to have different sintering requirements to reach full densification (95%-98% theoretical density), as well as to have limitations on sintering temperature to maintain its composition, thereby making the processing of biphasic compositions containing both HA and β-TCP more difficult. HA has been shown to initiate rapid densification at temperatures near 1100°C-1200°C[84, 96] with density plateaus reached at 1200°C-1350°C;[52, 84, 96-98] implying that full densification can be achieved at any temperature within this range given an appropriate dwell time. However, although grain growth tends to occur at temperatures greater than 1100°C, temperatures higher than 1150°C may lead HA to decompose into the α or β phase of tricalcium phosphate;[99] if cooled appropriately, this transition becomes irreversible. Additionally, the densification of β–TCP plateaus within the range of 1200°C-1250°C,[100-101] but maintenance of the β-TCP phase is restricted to sintering temperatures below that of a critical temperature, generally 1180°C,[102] to prohibit phase transformation to α-TCP, a phase of calcium phosphate having substantially higher solubility and considerably less strength than the beta phase. The disparity in the literature regarding the critical phase transition temperature for β-TCP,[85, 97, 103-105] densification behavior for both constituent powders,[106-107] and microstructure development[92, 104, 107] further emphasizes the dependency of sintering temperature on powder history, preparation, and fabrication.

The need for microstructure characterization of ceramic biomaterials is well established. Traditional methods of characterization include, but are not limited to, characterization of surface features, grain size and morphology, and specific surface. Several studies have noted the influence and importance of these characterizations as it pertains to biocompatibility and interaction with cellular milieu, both *in vitro* and *in vivo*.[108-111] In a 2007 study conducted by Okuda et al. it was shown that rod-shaped β-TCP constructs demonstrated adequate resorption and bone formation 24 weeks post-implantation as compared to similar constructs of conventional globular shape, in which materials were more quickly resorbed and demonstrated significantly less bone formation after 12 weeks.[112] Li, et al. demonstrated that inductive bone formation is due largely to the specific surface area, not surface roughness, of CaP sintered discs, and that larger surfaces allow for the concentration of more proteins that lead to the differentiation of cells down an osteogenic lineage forming inductive bone.[109] Gross et al. showed that particle size had the greatest influence on surface roughness and topography of HA thermal sprayed coatings,[vi] and that osteoclasts demonstrated a clear preference to topographical features.[113]

Specific surface area increases and decreases with the number and size of micropores respectively, and has been linked to a materials' osteoinduction; though it is unclear

[vi] With thermally sprayed coatings, fine powders typically between 10 and 150 microns injected into a hot gas, partially melted and sprayed with a torch—creating a deposit of "splats" with a surface roughness that depends upon the size of the starting powder and heat treatment.

whether the benefits of higher specific surface are the result of increases in microporosity due to size or number of micropores. As with specific surface area and other surface features, microporosity has been demonstrated to influence cellular attachment, proliferation, and subsequently, regeneration. However, even with microporosity, higher void space is not necessarily better (than lesser void space), as there are limitations to its benefit. Isaac, et al.[114] determined that the attachment of serum protein is proportional to the level of microporosity of the construct, and that the highest microporosities do not facilitate the differentiation and proliferation of human bone marrow stromal cells in vitro. This study examined β-TCP structures with 0%, 25%, and 45% microporosity, and concluded that the comparatively high levels of microporosity[vii] negatively affected the ceramic's ability to facilitate osteoblastic differentiation in vitro.

Even within the lower microporosity ranges, there is some degree of inconsistency with bone induction. In a study conducted by Rouahi et al.,[111] there was a three-fold increase in the quantity of adsorbed proteins on a 12% microporous structure compared to a 2% version. The initial 30 minutes saw the largest difference in adsorption (15 times higher) with subsequent decreases in the differences over a 24 hour period. After 4 days, however, the less porous structures demonstrated the presence of more cells than the higher porosity version. The data from these studies, and those like them, suggest

[vii] The authors site the success of several other investigations in facilitating bone growth via microporosity. In these cases, the microporosity levels that successfully induced boney growth were below 20%.

there may be an effective range of microporosity, beyond which bone regeneration is not enhanced.

The microstructure of any biomaterial not only affects its ability to modify or elicit cellular response but also its mechanical properties. For calcium orthophosphate bioceramics, the mechanical properties are affected by the material's crystallinity, its composition, grain size and boundaries, as well as porosity and crack growth.[115-117] In the case of dense ceramics, strength is a function of grain size, with finer grain-sized materials having smaller flaws at grain boundaries and therefore more strength than materials with larger grain sizes. Additionally, several researchers have commented on the intimate relationship between composition, i.e., HA/TCP ratio, and strength[115] and degradation showing that rising fractions of β-TCP impart proportionally low mechanical strength and high dissolution,[86-87] while others have demonstrated that the strength of the ceramic is strongly dependent on the porosity and weakly dependent on its composition.[118] While many studies have been conducted relating to the dissolution and mechanical behavior of these materials separately, few have discussed the relationship between microporosity and solubility,[87, 119-120] or microporosity and regeneration;[9, 111] and fewer still have addressed changes in mechanical properties via dissolution,[121] or attempted to quantify the relationship between microporosity, macroporosity, composition, and regeneration.

The goal of work presented in this chapter is to characterize the CaP materials on which the reviewed body of research is based. An understanding of powder sinterability and bulk microstructures assists in the *a priori* scaffold design for bone tissue applications. We demonstrate that the resulting microstructures and mechanical properties are influenced by composition and firing temperature, and we introduce a methodology by which grains of HA and β-TCP can be distinguished within the microstructure. Characterizing the microstructure of the biphasic calcium phosphate ceramic construct in this manner may be instrumental in understanding its *in vivo* degradative properties, thereby making the changing design of a biodegradable scaffold of the same material more predictable. Conventional methods of microstructure imaging, such as SEM using secondary electron (SE) and back scattered electron (BSE) modes, have proven ineffective in observing the spatial distribution of the two phases due to a lack of contrast between them. Moreover, the Ca/P ratio for HA and β-TCP is 1.67 and 1.5 respectively, also making Energy Dispersive Spectroscopy (EDS) ineffective in establishing distinctions between the two phases at local composition levels. An alternative method may be cathodoluminescence (CL). This method examines light emitted from features in the sample when excited by an electron beam. It has traditionally been used in the geosciences to detect and identify rare earth element impurities in apatites[122-123] as well as to determine information on rock formation and mineralization processes.[123-124] In the field of biomaterials, it has been investigated as a method of identifying the presence of amorphous phases in plasma-sprayed HA coatings,[125] of differentiating the degree of carbonation in apatites,[126] and in

microstructural characterization of plasma-sprayed HA coatings.[127] In this work, we investigate the effectiveness of using cathodoluminescence to distinguish between the two calcium phosphate phases.

## 3.2 Characterization of Powders and Their Sinterability

### 3.2.1 Powder Characterization

Commercially available hydroxyapatite ($Ca_{10}(PO_4)_6(OH)_2$; HA) and β-tricalcium phosphate ($Ca_3(PO_4)_2$; β-TCP) powders (Plasma Biotal, Ltd., North Derbyshire UK) were used in this work. As-received powders were analyzed using benchtop X-ray diffraction (XRD; Rigaku MiniFlex, Woodlands, TX). The x-ray radiance was produced using CuKα radiation, $\gamma$ = 1.54056 Å. The crystalline phases were identified from standard powder diffraction files (PDF) of the International Center for Diffraction Data (ICDD). Scanning electron microscopy (SEM, Phillips XL30 FEG) was used to assess the morphology of the powder particulates. Powder density (g/cm$^3$), as determined by the manufacturer, was 3.14 and 3.05 for HA and TCP powders respectively. The specific surface area (SSA) was determined by the BET method using nitrogen ($N_2$) as an adsorbate. Powders were degassed overnight at 300$^o$C.

.

### 3.2.2 Phase Stability

Various compositions of biphasic calcium phosphate (BCP) ceramics based on HA and β-TCP ratios were prepared by mechanically mixing as-received powders in the desired

proportions: 0% TCP/100% HA (HA), 20% TCP/80% HA (20 BCP), 25% TCP/75% HA (25 BCP), 40% TCP/60% HA (40 BCP), 50% TCP/50% HA (50 BCP), 60% TCP/40% HA (60 BCP), 75% TCP/25% HA (75BCP), 80% TCP/20% HA (80 BCP), and 100% TCP/0% HA (TCP). Cylindrical pellets were formed by uniaxially dry-pressing approximately 1.2 g powder in a 13-mm diameter stainless steel die at 87 MPa. Pellets were then sintered in a high temperature furnace at 1100$^{o}$C with a sintering rate of 10$^{o}$C/min. The phase purity of as-received and sintered specimens was assessed using an XRD: samples were scanned from a 2$\theta$ angle of 25$^{o}$ to 35$^{o}$ with a scanning speed of 1$^{o}$/minute. The phase contents were measured by the relative intensities, $\rho$, of the main diffraction peaks for HA (2$\Theta$ = 31.8$^{o}$) and $\beta$-TCP (2$\Theta$ = 31$^{o}$) according to Yang, et. al[107]:

$$\rho = \frac{I_{HA}}{I_{HA} + I_{TCP}}$$

The microstructures of compacts sintered at 1100$^{o}$C and 1150$^{o}$C were investigated by SEM; compacts were coated with Pt under a vacuum to reduce the amount of charging on the surface.

### 3.2.3 Densification

Geometric density was calculated by dividing the mass of the sintered compacts by the volume. The apparent porosity was measured by the water immersion method after boiling samples in deionized water for 2 hours and cooling to room temperature. This

was done to prewet samples and remove air trapped within the micropores. Apparent porosity,[107] $P_a$, was calculated according to

$$P_a = \frac{W_{cw} - W_{AIR}}{W_{cw} - W_{H2O}}$$

where $W_{cw}$ is the weight containing water, $W_{H2O}$ is the weight submerged in water, and $W_{AIR}$ is the dry weight.

## 3.3 Characterization of Mechanical Strength

### 3.3.1 Diametral Compression

The diametral compression test, also known as the Brazilian test or indirect tensile test, is an accepted method of testing tensile strength in brittle materials, and has been extensively used in the characterization of ceramic materials, rocks, polymers, pharmaceuticals, i.e., tablets, coal, and cemented carbides.[128] The test was performed at room temperature using an Instron (MTS RT30) testing machine in uniaxial compression. A cross-head speed of 2.54 mm/min was selected. In this testing scheme, compacts approximately ⌀12mm x 5mm are placed on their circumferential edge between compression platens. The stress calculated is derived in the following manner:

$$\sigma = \frac{dF}{dA}$$

$$\sigma dA = dF$$

$$dA = d\theta rt$$

$$\therefore dF = \sigma rtd\theta$$

$$\int F = \int_0^{\pi} \sigma rtd\theta$$

$$F = \sigma rt \int_0^{\pi} d\theta$$

$$F = \sigma rt\pi$$

$$\sigma = \frac{F}{\pi rt}$$

and rewritten according to:

$$\sigma_f = \frac{2P}{\pi Dt}$$

where $\sigma_f$ is the diametric strength, $P$ is the peak load, $D$ is the diameter of the disk, and $t$ is the thickness.

## 3.4 Visualization of Grain Distribution

As-fired samples of sintered BCP (0BCP, 25BCP, 50BCP, 75BCP, and 100BCP) were imbedded in an epoxy resin and polished to a flat finish. A panchromatic

cathodoluminescence microscopy detector was attached to a Cameca SX100 Electron Microprobe Analyzer (EPMA). SEM-CL was performed using an accelerating voltage ranging from 10-15 keV, with a beam current of 5-10 nA. Back scattered electron images were used for comparison. EDS, EPMA, and image analysis using GEMS MicroView were employed to detect phase differences across the samples as well as to determine the effectiveness of CL in distinguishing between the phases of the calcium phosphate ceramic.

## 3.5 Results and Discussion

### 3.5.1 Powder Characterization and Maintenance of Phase Purity

SEM images reveal a HA powder morphology (Figures 3.1-3.2) composed of agglomerates of particles acicular in shape with an average particle size range of 0.3-0.6 μm. β-TCP particles are spherical agglomerates with an average agglomerate size of 10-30 μm. The agglomerates are composed of round particles, 1-2 μm in size, bonded via sintering (Figures 3.3-3.4). Calculated x-ray diffraction spectra[129] of HA (Fig. 3.5) shows primary peaks at the (2 1 1), (1 1 2), and (3 0 0) planes corresponding to 2Θ values of 31.77°, 32.196°, and 32.902° respectively; β-TCP (Fig 3.6) exhibits primary peaks at (0 2 10), (2 2 0), and (2 1 4) planes corresponding to the 2Θ values of 31.03°,

34.37°, and 27.77° respectively. All peaks were observed from the as-received HA and β-TCP powder samples (Fig 3.7-3.8), and demonstrate no presence of additional phases. Upon sintering, TCP and the upper biphasic compositions (50BCP and 75BCP) were shown to maintain their phase purity (Fig 3.9) in the appropriate proportions. HA and 25BCP, however, demonstrated a 12-14% increase in phase amount of β-TCP, accompanied with deficits in the pre-sintered amount of HA.

HA has been shown to decompose to β-TCP according to the pathway,[130]

$$Ca_{10}(PO_4)_6(OH)_2 \rightarrow 3Ca_3(PO_4)_2 + CaO + H_2O$$

or, as an alternative[131-132]

$$Ca_{10}(PO_4)_6(OH)_2 \rightarrow 2Ca_3(PO_4)_2 + Ca_4P_2O_9 + H_2O$$

where CaO is calcium oxide, and $Ca_4P_2O_9$ is tetracalcium phosphate (TTCP). This transformation is due to the gradual dehydroxylation of HA at elevated temperatures, leading to the release of $OH^-$ ions and subsequent transformation into the intermediary phase of oxyhydroxyapatite (OHA), denoted as $Ca_{10}(PO_4)_6(OH)_{2-2x}O_x\square_x$ , where□ denotes a vacancy. At its vacancy maximum, where x = 1, OHA transforms to oxyapatite (OA, $Ca_{10}(PO_4)_6O$ ), and upon further heating transforms to tricalcium and tetracalcium phosphates via dehydration.[132]

The temperatures at which these phase transitions occur have been shown to depend on processing parameters. In air, with short dwell times (on the order of 1-2 hours), the onset of dehydroxylation occurs at 1400$^{o}$C, with decomposition to $\alpha$-TCP at 1450$^{o}$C.[131-132] While the current work is not in agreement with these findings, it is supported by the findings of Wang and Chaki,[133] where for longer dwell times, the decomposition of HA to $\beta$-TCP is initiated at 1100$^{o}$C, while the dehydroxylation begins much earlier. Furthermore, Wang and Chaki determined that sintering in moisture will prevent both dehydroxylation and dehydration, and sintering under pressure commencement is much earlier than occurring in air.

In the current work, it was also demonstrated that decomposition occurred within biphasic compositions composed of $\beta$-TCP phase amounts less than 50%. HA transformed to $\beta$-TCP by 14% for the HA and 25BCP compositions, whereas biphasic compositions greater than 50% were able to maintain phase proportions. Nilen and Richter[130] report a similar post-sintering trend of the reduction of HA intensity, as seen in XRD measurements, " relative to known HA pre-sinter contents, and always associated with an increase in $\beta$-TCP intensity." As in the current work, no other crystalline phases were detected in these post-sintered groups. However, contrary to what was found in

this study, they determined that the extent of decomposition was greater for greater phase amounts of β-TCP.[viii]

### 3.5.2 Effect of β-TCP Phase Amount and Sintering Temperature on Densification and Microporosity

The resulting densities of the compacts after sintering are presented in Table 3.1. Relative densities of the sintered compacts vary as a function of sintering temperature and composition. For samples sintered at 1100$^{o}$C, mean values are 76.16 (TCP), 62.76 (75BCP), 63.72 (50BCP), 59.61 (25BCP), and 58.24 (0BCP); for samples sintered at 1150$^{o}$C, 81.13 (TCP), 76.98 (50BCP), 68.86 (25BCP), and 63.17(0BCP), with no statistical significance between 0BCP and 25BCP, or 50BCP and 75BCP as determined by an unpaired t-test.

Further illustrating the densification behaviors of these materials is the apparent porosity achieved (Figure 3.10). Apparent porosity measurements reveal variable microporosity among the sintered samples as a function of sintering temperature and composition.

[viii] Nilen and Richter also determined that the extent of decomposition was greater at higher temperatures, and in the cases of presinter β-TCP contents below 60%, that the β-α transition occurring above 1125$^{o}$C is not completely reversible upon gradual cooling as expected. Furthermore, there appears to be a critical content of HA, above which the transformation is retarded.

For samples sintered at 1100$^{o}$C, mean apparent porosity is 24.2% (100BCP), 36.3% (75BCP), 37.8% (50BCP), 39.0% (25BCP), and 39.4% (0BCP), with no statistical significance between 0BCP and 25BCP, or 50BCP and 75BCP as determined by an unpaired t-test. Significance between all other compositions is demonstrated by $p \leq 0.005$.[100, 134]

The relative densities of all materials were greater than 50%, with the highest values for TCP at both temperatures (Figure 3.11). Temperature is proportional to densification, in that the higher temperature group experienced higher densification than the low temperature group. Furthermore, increases in phase amount of TCP results in increases in relative densities for both thermal treatments. The 75BCP composition is the exception to the rule: its relative density lies between that of 25TCP and 50TCP (59.6% and 63.7% respectively). This may be a function of the packing of agglomerates within this powder composition. TCP (SSA = 1.9872 $m^2/g$) appears to pack more efficiently with HA (SSA=14.0173 $m^2/g$) in the 50-50 matrix than in the 75-25 matrix composition. This is supported by shrinkage values of the as-received powder (compacts) compared to that of the milled powders from the aforementioned ball-milling study, in which 75BCP milled compacts experienced a 23.65% and 34.98% shrinkage compared to 10.96% and 21.12% for 50BCP at 1100$^{o}$C and 1150$^{o}$C respectively. In this case, the reduced particle sizes of the milled particles may have allowed for a better packing efficiency, and therefore, a more complete sintering.

Further powder processing as a means to improve densification of HA was investigated; details of the previously mentioned ball-milling study follow. As-received HA and TCP powders were wet ball-milled 20 hours prior to compaction and sintering. The results indicated that although milling significantly improved the apparent porosity of HA, 25BCP and 75BCP sintered at 1100$^{o}$C ($p < 0.01$; Figure 3.12), there was no significant difference in HA porosity sintered within the relevant temperature range (Figure 3.13). Furthermore, the slower densification rate demonstrates that, for these temperature-composition groups, phase amount of HA will be the constraining variable on densification[ix] and, therefore, the limiting element in microstructure development. This may be, in part, due to the dehydroxylation of HA; in that dehydroxylation is known to impair or hinder densification.

During solid state sintering of powder compacts, the pore size and morphology, and ultimately, density, evolves through three stages: 1.) an initial stage, characterized by the increase in interparticle contact area via neck growth and increases in relative density from 60 to 65 percent; 2.) an intermediate stage, characterized by the presence of continuous, or tubular pores, along the grain boundaries and increases in relative density from 65 to about 90 percent; and 3.) a final stage, characterized by the lack of the continuous pore network of stage two. In this final stage, tubular pores are broken

[ix] The degree of densification is determined by the sintering temperature and duration of processing. For the temperature range utilized, HA's sintering is minimal, and therefore considered a limiting factor.

up or pinched off, producing new pores either lenticular or round in shape (depending on location) and relative density approaches theoretical density.[135-136]

Stages one and two within this typical microstructural evolution were observed for the various compositions sintered in this study. At 1100$^{o}$C, most groups were within stage one, having relative densities less than 65 percent. 100% TCP, however, achieved a relative density in access of 75%, a hallmark of stage two microstructures. When sintering temperature was increased to 1150$^{o}$C, the biphasic compositions experienced stage two sintering, and groups demonstrated an increase in shrinkage, accompanied with an increase in grain size and reduction in pore size. A comparison of the resulting biphasic microstructures at 1100$^{o}$C is illustrated in Figure 3.14 A-C. Each composition shows necking of powder particles and an open pore network. Differences in apparent pore size and shape, however, are clear. The average pore size for the 25% and 50% TCP groups are similar, measuring an average value of 1.08 μm, with larger pores on the order of 2.01 μm. These pores appear to be consistently shaped, and evenly spaced within the microstructure, with smaller pores outnumbering the larger. By contrast, pores within the 75% TCP group present a much more complicated microstructure, with *base* pores measuring 1.20 μm in size, but often coalescing to form lengthy pore channels measuring, on average, nearly 5 μm; these pores appear to dominate the microstructure. As an aside, an increase in temperature to 1300$^{o}$C, well outside of the range of temperatures used in this study, demonstrates the ability of

these compacts to reach higher levels of densification. Figure 3.15 illustrates the microstructure of 100% HA and 100% TCP sintered at 1300$^{o}$C. HA shows no residual porosity, characteristic of stage three sintering. β-TCP, however, even at the higher temperature, continues to demonstrate a comparatively substantial residual porosity, although pores have begun to migrate toward the grain boundaries. This limitation on densification at this temperature may be a function of the α-β transformation experienced by TCP at temperatures above 1180$^{o}$C, or general particle coalescence due to sintering.[105] Collectively, these data suggest that near theoretical density, cannot be achieved for any of the compositions evaluated, when sintered within the range of 1100-1150$^{o}$C. Furthermore, at these temperatures, sintered compacts will maintain microporosities within the range of 20-40%, with micropores well within the range of 0-10 μm in size.

### 3.5.3 Effect of β-TCP Phase Amount and Microporosity on Mechanical Properties

For the five compositions of calcium phosphate materials analyzed in this work, a total of 98 disks, a two-parameter Weibull distribution analysis was applied to the fracture strength data according to the equation

$$\ln \ln \left( \frac{1}{1 - P_f} \right) = m \ln \sigma_f - m \ln \sigma_c$$

where $P_f$ is the probability of failure, $m$ is the Weibull modulus, $\sigma_f$ is the fracture strength and $\sigma_c$ is the characteristic strength. Weibull plots of the five compositions are shown in Figure 3.16. Probability of survival for all groups are shown in Figure 3.17 and Table 3.2; while details regarding the average fracture strength, the characteristic strength, and the Weibull modulus are summarized in Table 3.3.

There was a nearly monotonic decrease in both $\sigma_f$ and $\sigma_c$ with decreasing phase amounts of β-TCP and increasing microporosity, while $m$ varied from 1.01 to 3.66. Both Weibull modulus and characteristic strength showed a steady increase with increasing amounts of TCP (Figure 3.20); with a high variability in Weibull modulus for relative densities near 60%, values seeming to level off at densities greater than 63% (Figure 3.18). Moreover, a plot of strength vs. relative density shows increases in characteristic and fracture strengths with increases in β-TCP, demonstrating that constructs high in volume fraction of β-TCP are stronger (Figure 3.19).

In each of these instances (Figures 3.18-3.20), however, the 75% TCP composition does not comply with the noted patterns. This composition consistently presents strength parameters less than its 50% TCP counterpart. The aforementioned variation of Weibull modulus with porosity has been noted,[136] but variation may also be due to

presence of agglomerates;[136-137] processing techniques and microstructure, pore size and shape, and strength testing techniques.[138] While parameters relating to processing and testing were kept consistent in this work, the resulting microstructures for the 75% group differ greatly in pore size and shape, and agglomeration, as noted previously.

### 3.5.4 Method for Visualization of Grain Distribution in Biphasic Compositions

Back scattered SEM (SEM-BSE) images for the various compositions are indistinguishable from one another and illustrate no distinction between the HA and β-TCP phases (Figure 3.21 A-E).[139] This imaging technique may highlight agglomerated particles (lighter grayscale color; Figure 3.21 B-D) or void spaces (darker grayscale color; Figure 3.21 D-E), but no determination can be made concerning the local compositions of these regions with variations in grayscale. Conversely, CL images indicate visible differences in the biphasic microstructure for each of the compositions investigated (Figures 3.22-3.26, B-panel for each). In these images, particularly figures 3.22-3.24, overall indistinguishable gray shadings in Panel A demonstrate high contrast for the same regions in Panel B. Furthermore, some visible regions within CL images go unnoticed in SEM-BSE images.[139]

Each CL image was considered to consist of a combination of black, white, light gray, and dark gray areas, with patterns in the arrangement consistent with the previous description. HA (Figure 3.26 B) exhibits a pattern best described as primarily dark with a distribution of light-colored specks scattered throughout; whereas β-TCP (Figure 3.25 B) samples produce an image that is primarily light in color with patches of varying gray shades throughout. Biphasic samples produced images that lie between the two phases (Figures 3.22-3.24, Panel B for each). Areas of high contrast were subjected to elemental dispersive spectroscopy (EDS), a technique often utilized in conjunction with SEM for the determination of elemental composition. EDS identifies and quantifies elemental composition via the use of a detector that counts all x-rays simultaneously. In doing so, it provides a rough proportionality of elements within a composition, but its limitations are defined by the corrections needed for overlapping peaks, and high background noise which can limit sensitivity. Regions analyzed using EDS (Figure 3.27, regions 1-3) show that the white regions were lower in calcium, the gray was intermediate, as compared to the black regions, with Ca:P ratios of 1.5, 2.0, and 2.2 respectively.

By contrast, an alternative elemental analysis technique was performed to produce more quantitative data. Electron microprobe analysis (EPMA), sometimes used in conjunction with CL, utilizes a wavelength dispersive spectrometer (WDS) to tune in to the characteristic X-ray energies of a single element. It counts the number of X-rays

emitted from a sample, and compares that number with the number emitted from a standard. By doing so, the concentration of the element of interest may be determined, and an accurate assessment chemical difference within the grayscale contrast can be achieved. We looked at distinct locations within the biphasic construct; shown in Figure 3.28. Regions of lightest contrast (light gray) demonstrated a Ca:P 1.49-1.52. Regions of darker contrast (dk. gray) exhibited a ratio of 1.54, and regions of darkest contrast (black) 1.76. Both regions of light contrast are comparable in Ca:P to that of β-TCP (Ca:P = 1.50), suggesting that the grayscale contrast evident in the biphasic images correlate to the β-TCP phase within the construct.

For further verification, CL images were also subject to image analysis using GEMS MicroView, in which a bimodal histogram depicting the range of voxel values present within each image was generated; with one mode representing HA and the other, β-TCP (Figure 3.29 B). Voxel values corresponding to the β-TCP phase were highlighted on the histogram (Figure 3.29 D), and corresponding contrast highlighted red in the new image (Figure 3.29 C). For all compositions, the volume fraction of the highlighted voxel values were, consistently, in accordance with the known phase amount of β-TCP as confirmed by x-ray diffraction. In the instances of compositions with high HA phase amounts, the tranformation of HA to β-TCP was also confirmed.

## 3.6 Chapter Summary and Conclusions

In this chapter, we have established a relationship between powder sinterability, percent of β-TCP, and sintering temperature. Constructs high in β-TCP (> 50%) are able to maintain composition, whereas those low in TCP (100% HA and 75/25 HA/TCP) demonstrated a phase shift to roughly 12-14% increase in β-TCP, most likely the result of dehydroxylation of HA at low sintering temperatures, i.e., 1100$^{o}$C-1150$^{o}$C. Furthermore, the densification of these constructs also varied with % β-TCP and temperature. Increases in TCP correlated with higher densities, and density increased with sintering temperature. This means that for compositions tested, the highest relative densities (lowest microporosities) were achieved for 100% TCP disks sintered at 1150$^{o}$C and 1100$^{o}$C, and highest microporosities were obtained in the HA constructs.

Fracture strength of sintered disks were also evaluated for compositional and porosity influence. At the upper ranges of survival probability (>90%), compositions high in β-TCP are stronger than compositions low in β-TCP, with the mean fracture strength for 100% TCP disks in the range of 13MPa (characteristic strength at the 90% level is on the order of 8MPa). This behavior (stronger TCP than HA) is due to the early-stage sintering of HA at low temperatures, 1100$^{o}$C and 1150$^{o}$C, where, at these temperatures TCP reaches near full-density, while HA maintains microporosity on the order of 40%. Data demonstrates a porosity dependence of Weibull modulus, *m*, characteristic

strength, $\sigma_o$, and fracture strength $\sigma_f$, where compositions low in porosity are weaker. Also suggested is the significance of pore size and shape on the strength parameters, as demonstrated by the microstructure of the 75 percent TCP composition.

Finally, we were able to establish CL as an important technique for the visualization of differences between HA and $\beta$-TCP grains. When compared to more conventional methods of microstructure visualization, e.g. SEM, CL was best at highlighting surface topography and, with the use of EPMA, produced more quantitative readings for elemental X-ray energies, and therefore better estimations for element concentrations within a given sample.

## 3.7 Figures

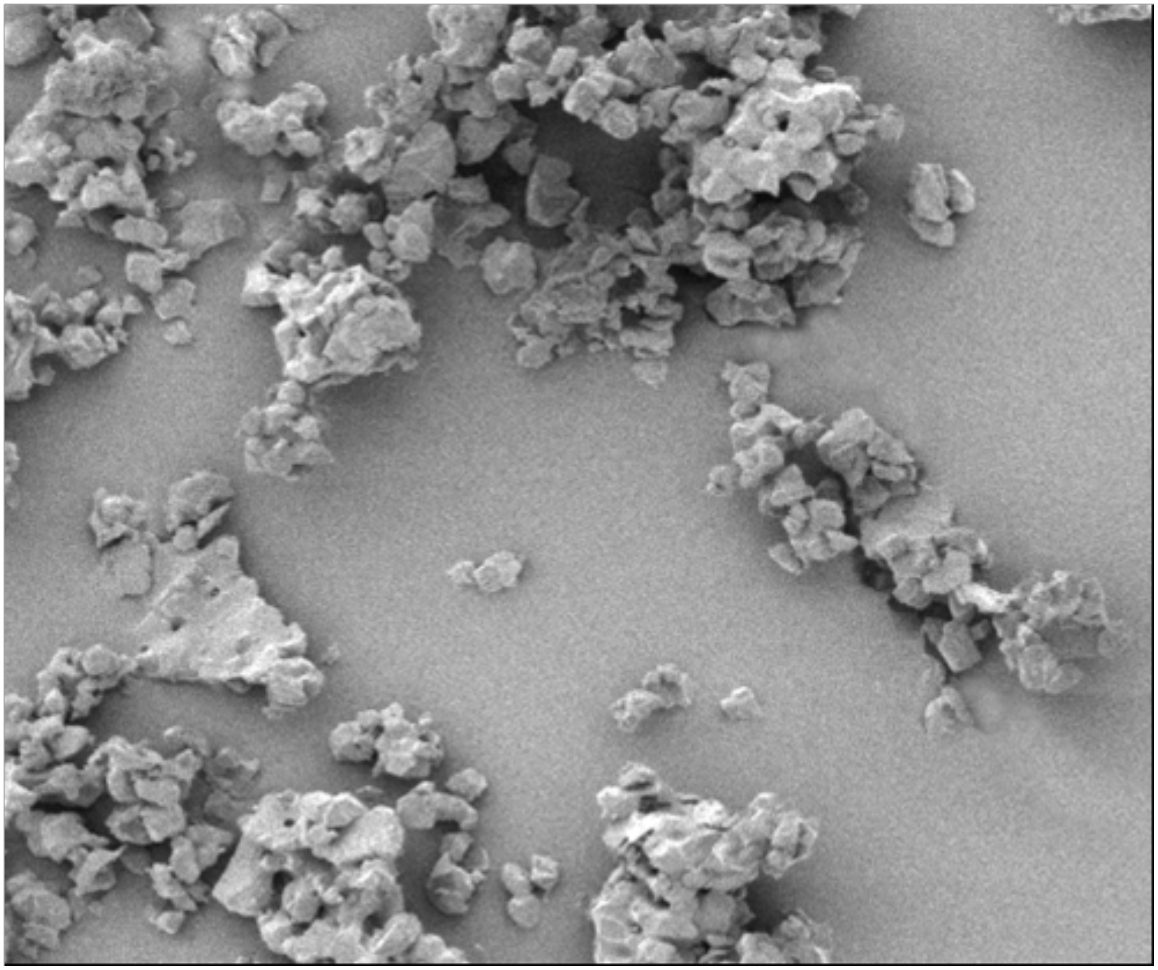

Figure 3.1 SEM of as-received HA powder, consisting of ~10 micron agglomerates composed of ~0.5 micron-sized primary particles; Magnification 1000x. Image courtesy of Plasma Biotal, Ltd.

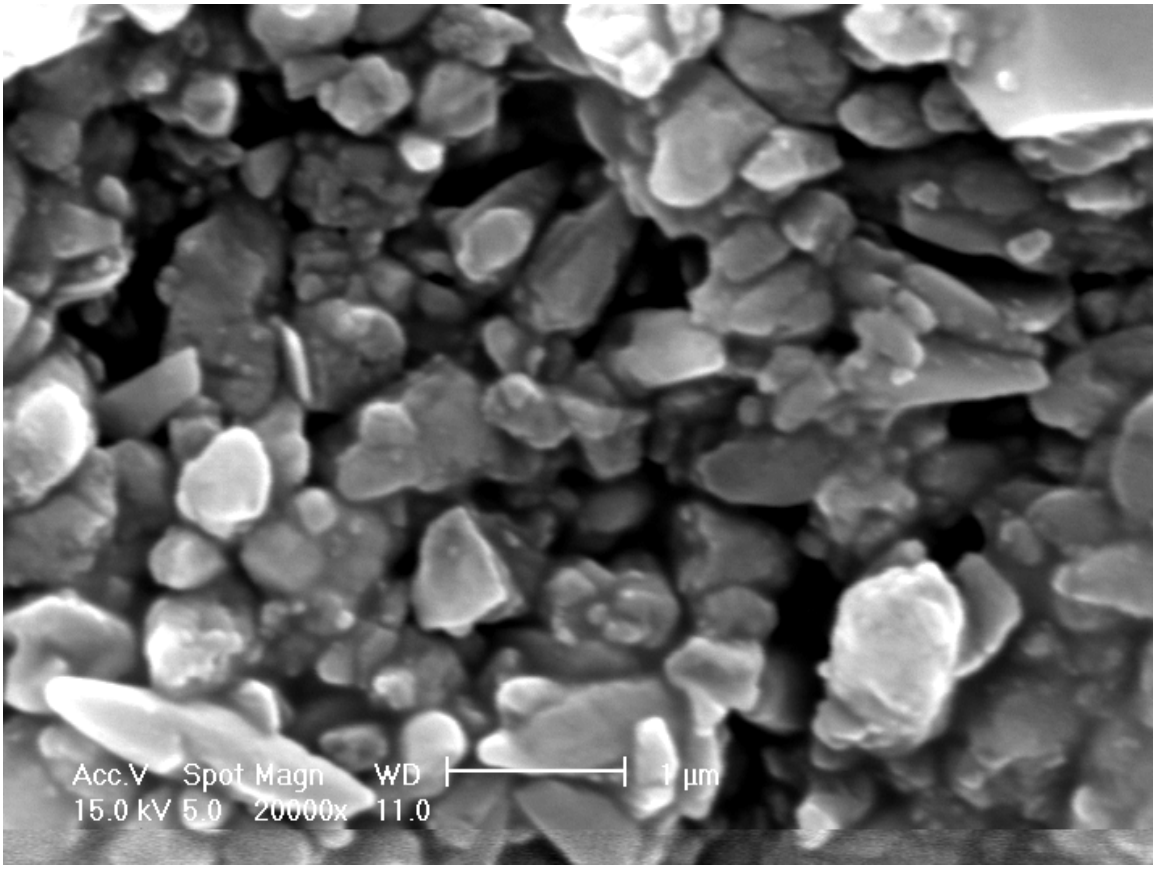


Figure 3.2: SEM. Enlarged view of as-received HA agglomerate particles; 0.5 micron primary particles are strongly bonded. (Plasma Biotal, Ltd.); Magnification 20000x

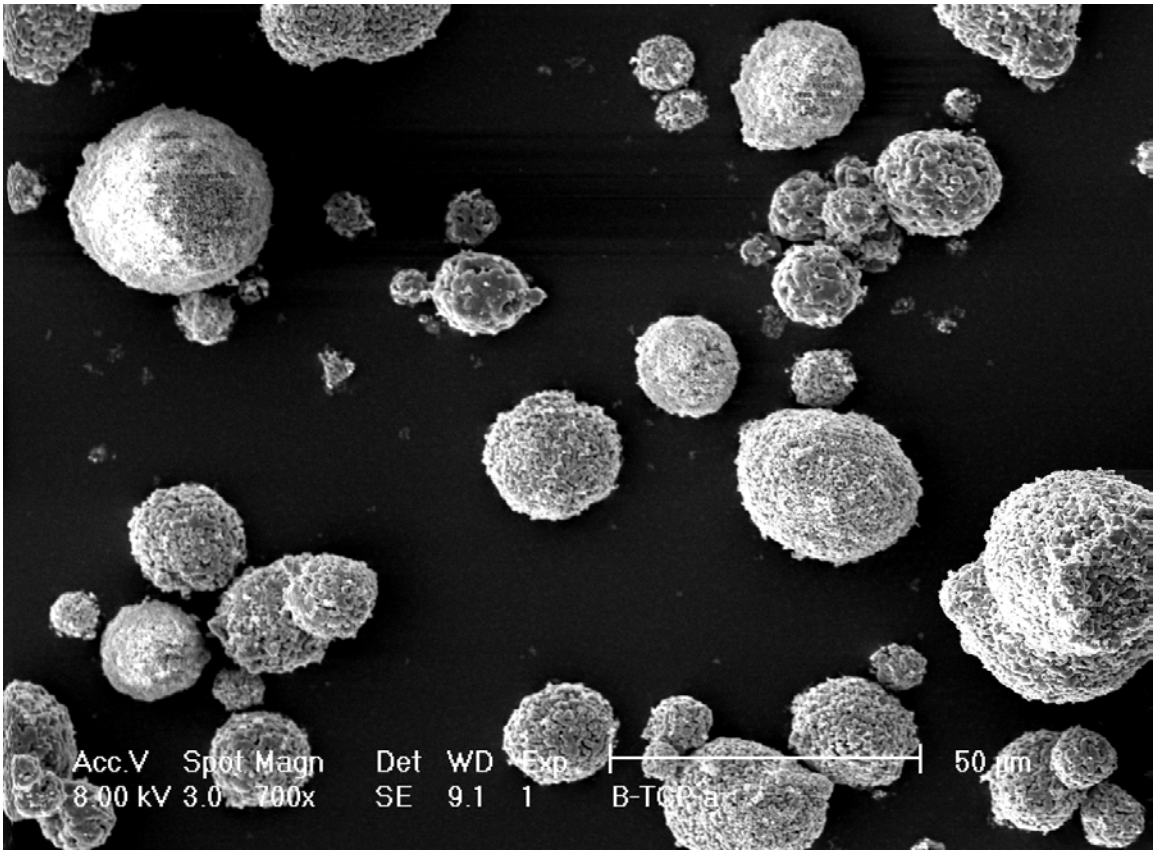


Figure 3.3: SEM image of as-received β-TCP powder (Plasma Biotal Ltd) consisting of round agglomerates 20-30 microns in size; Magnification 700x.

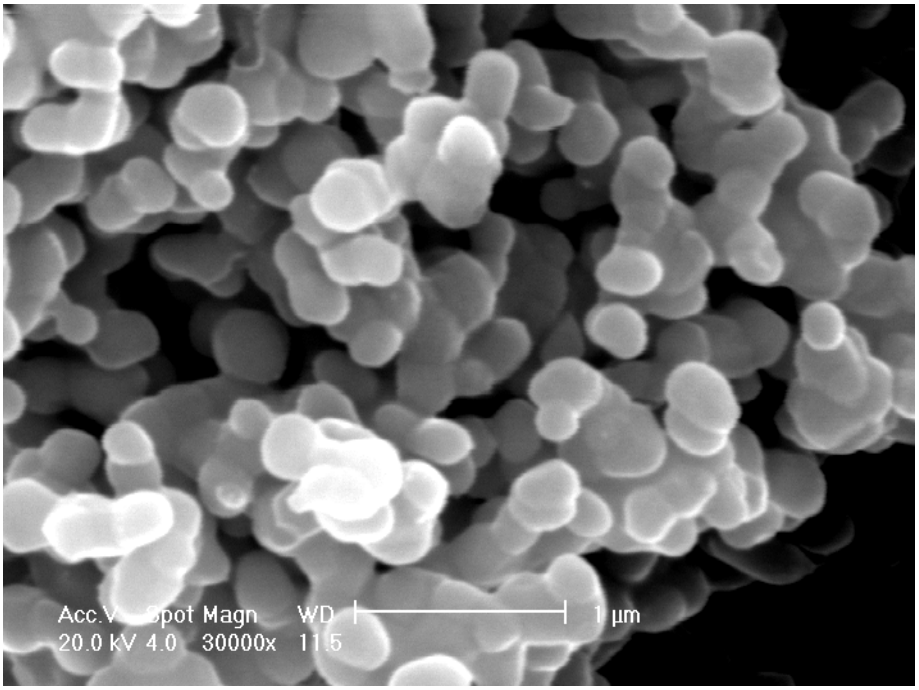


Figure 3.4: SEM of enlarged view of as-received β-TCP agglomerate. The round agglomerate is formed by round primary particles 0.2-0.8 microns in size and tightly bound; Magnification 30000x.

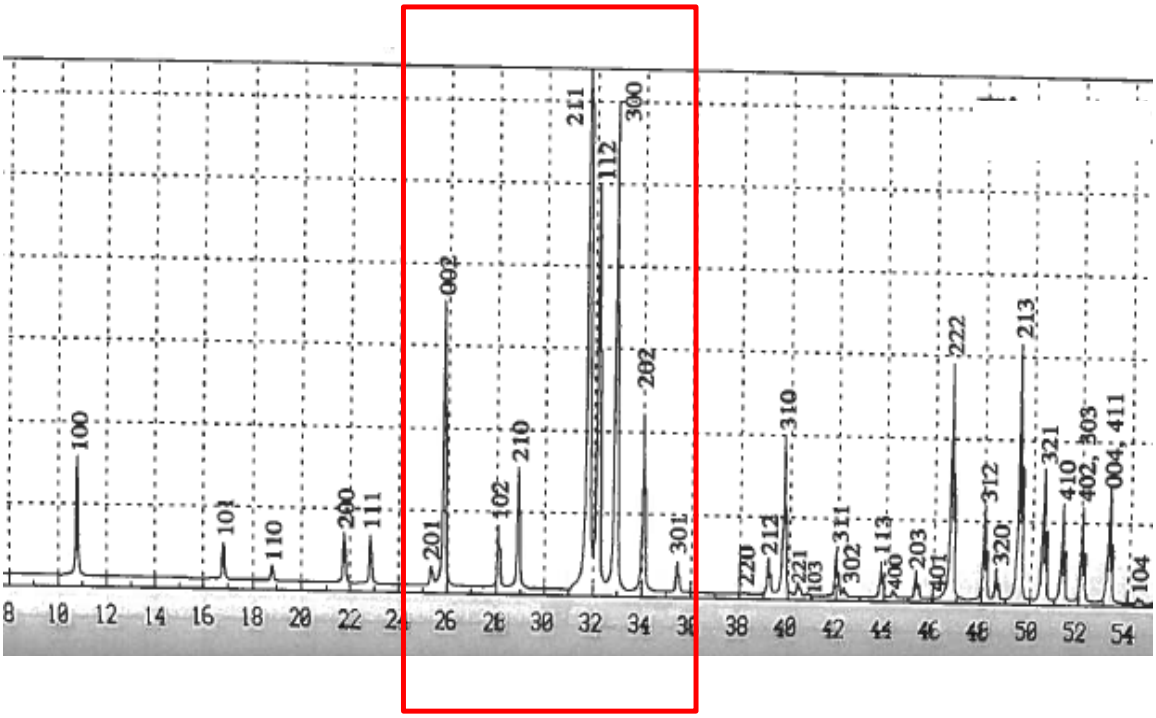


Figure 3.5: Calculated XRD pattern of Hydroxyapatite. $P6_3/m$, a = 9.4176 (1), c = 6.8814 (1) Å .[129]

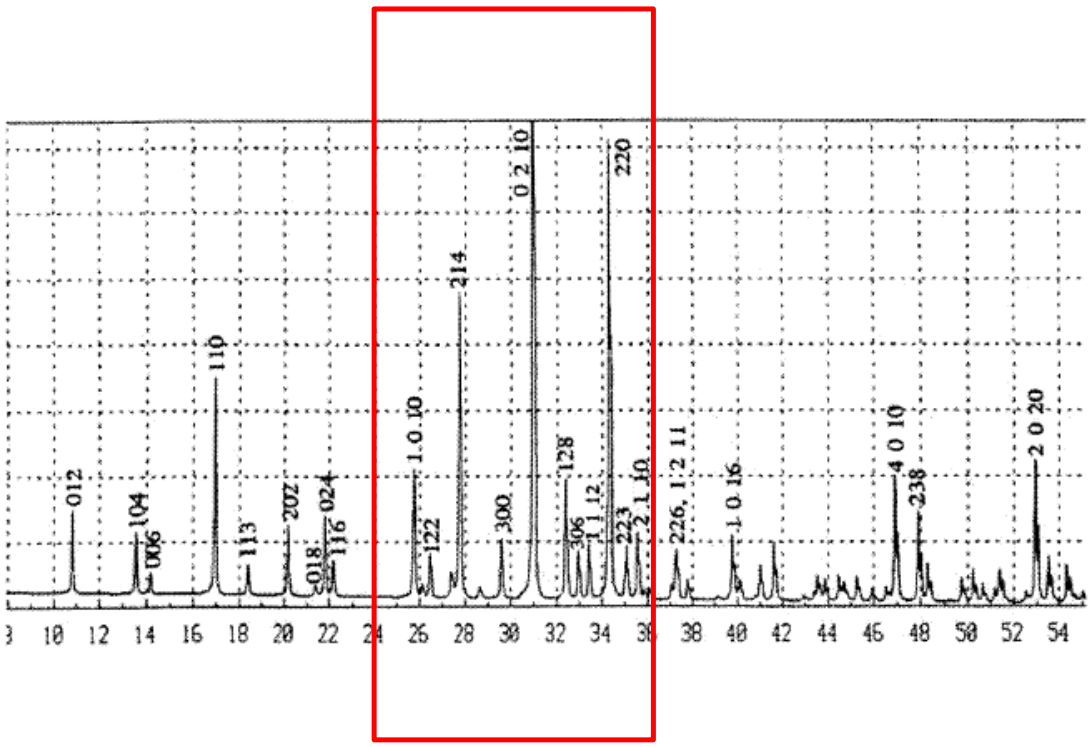


Figure 3.6: Calculated XRD pattern of β-TCP. R3c, a = 10.439(1), c = 37.375(6) Å (hexagonal setting).[129]

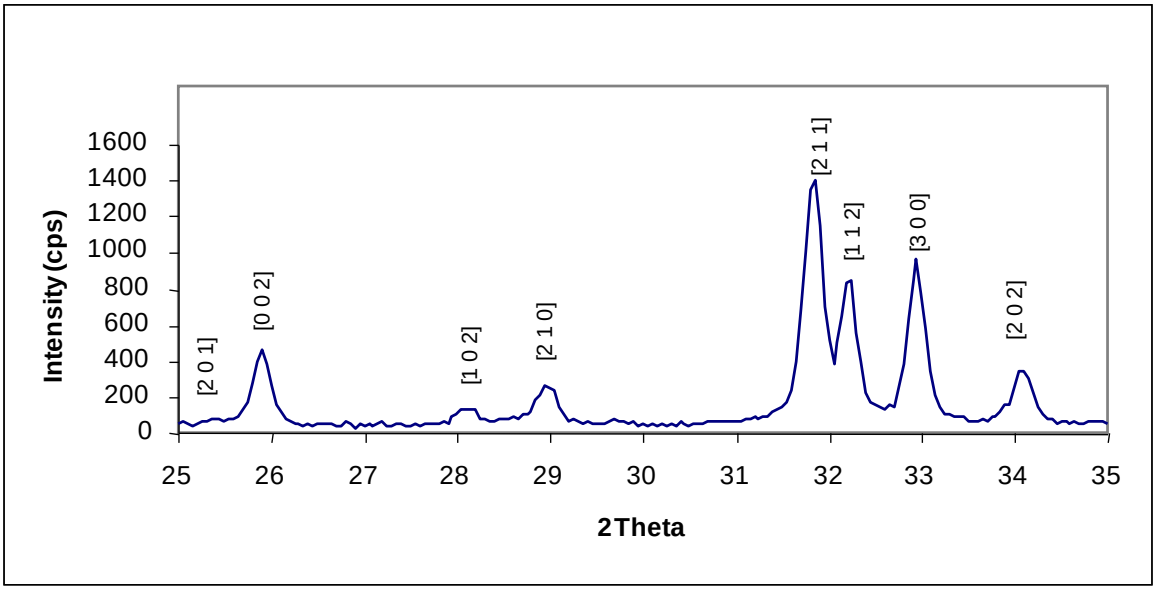


Figure 3.7: Diffraction pattern of as-received HA powder, $2\theta$ equals $25^{o}$-$35^{o}$. Pattern shows significant line broadening and is indicative of a well-crystallized powder. All peaks can be indexed to hydroxyapatite.

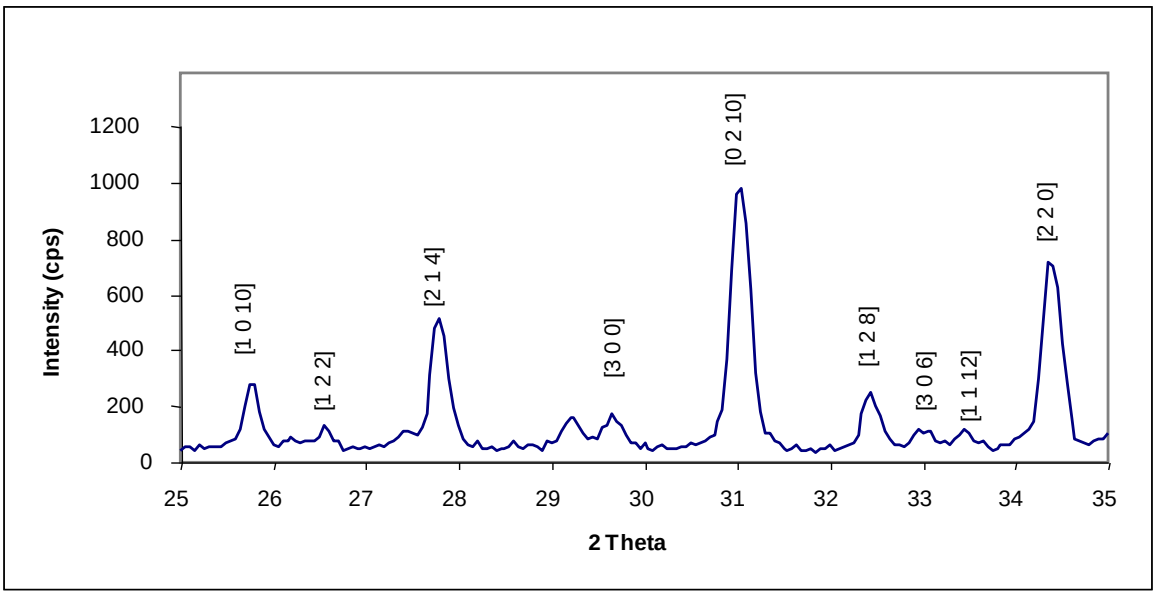


Figure 3.8: Diffraction pattern of as-received β-TCP powder, with 2Theta between 25 and 35 degrees. Powder is well crystallized and demonstrates line broadening consistent with particles ~30 microns in size. All peaks can be indexed to β-TCP.

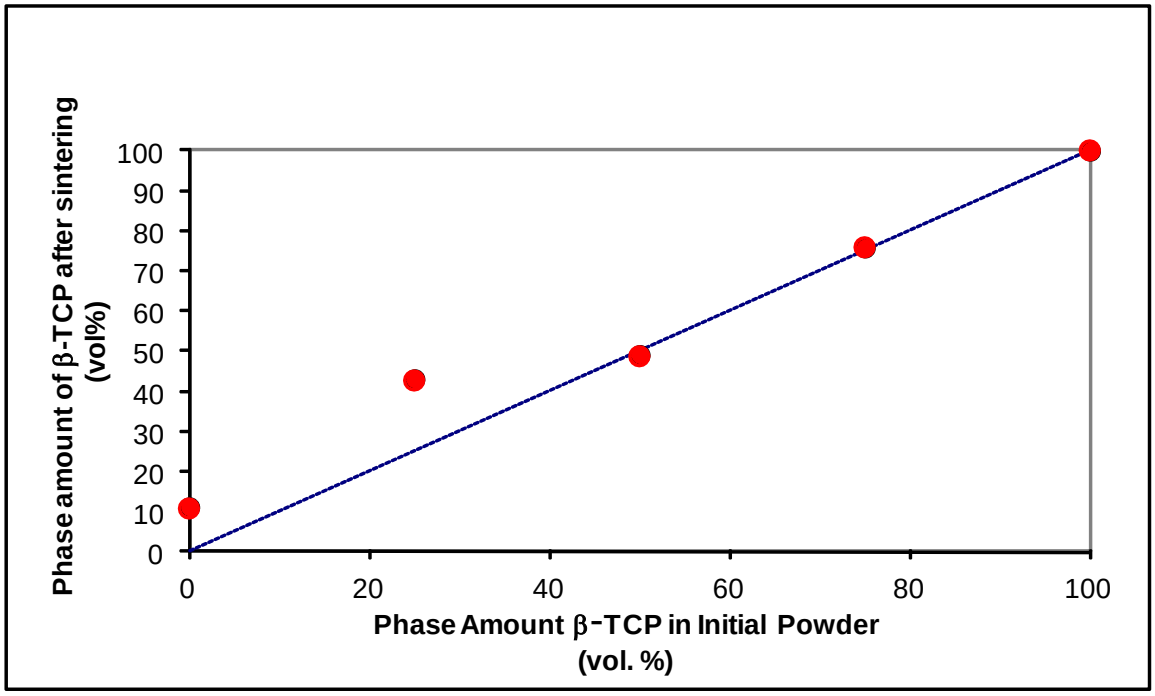


Figure 3.9: Phase amount of β-TCP after sintering at 1100°C; based on relative intensity of primary HA and β-TCP diffraction peaks. After sintering, compositions high in HA, specifically 100% HA and 75% HA/25% TCP, underwent a phase transformation in which hydroxyapatite decomposed to β-TCP, forming 12-16% β-TCP in the final compositions.

| | 1100°C | | 1150°C | |
|---|---|---|---|---|
| Composition (% TCP/HA) | Geometric Density ($g/cm^3$) | Relative Density (%) | Geometric Density ($g/cm^3$) | Relative Density (%) |
| 100/0 | 2.34 | 76.16 | 2.49 | 81.13 |
| 75/25 | 1.94 | 62.76 | | -------- |
| 50/50 | 1.98 | 63.72 | 2.40 | 76.98 |
| 25/75 | 1.87 | 59.61 | 2.16 | 68.86 |
| 0/100 | 1.84 | 58.24 | 1.99 | 63.17 |

Table 3.1 Geometric and Relative Densities of CaP materials after sintering. As % TCP and sintering temperature increase, density increases. The higher density of the 50/50 biphasic composition, as compared to the 75/25 biphasic material, is most likely the result of more efficient particle packing of large and small agglomerated particles.

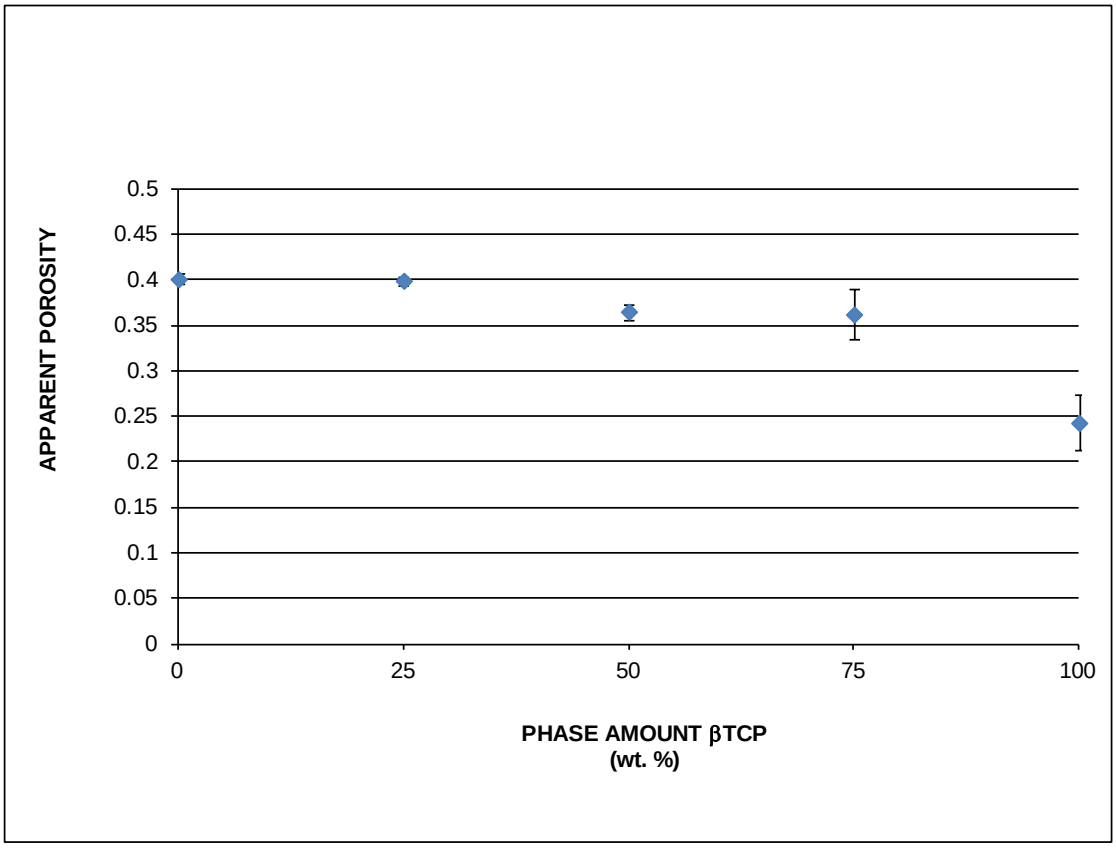


Figure 3.10: : Effect of composition on apparent porosity of sintered compacts at 1100$^{o}$C. There is an inverse relationship between apparent porosity and phase amount of TCP, with higher TCP compositions having less porosity than lower compositions. HA, 25BCP: n=5; 50BCP, 75BCP, TCP: n=20.

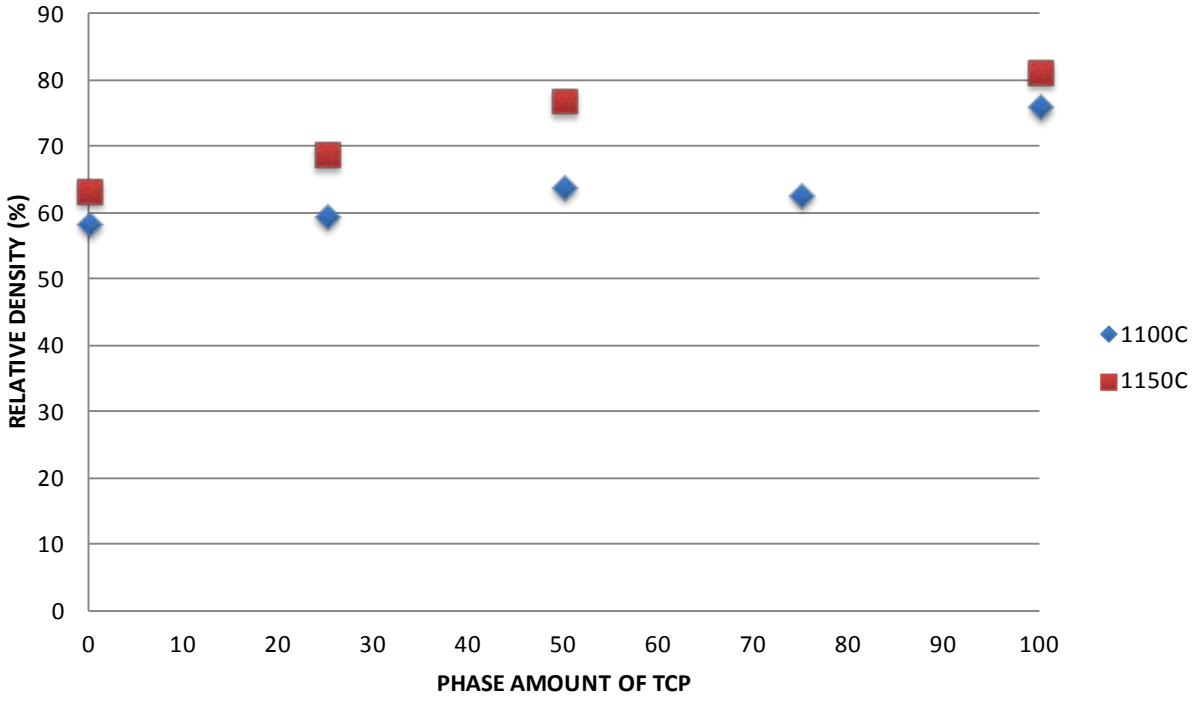


Figure 3.11: Relative density of sintered discs with respect to sintering temperature and phase amount of β-TCP present. Densification occurs at a faster rate for the higher temperature, and increases with increasing amounts of β-TCP.

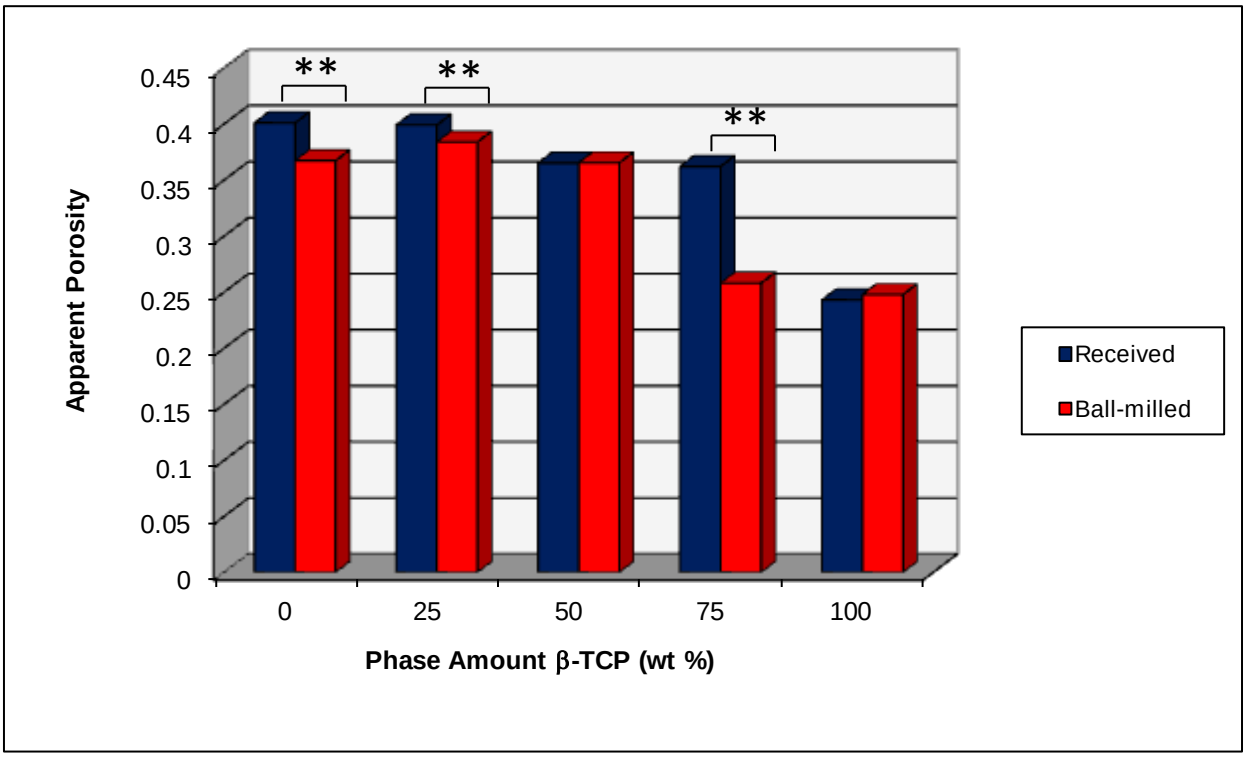


Figure 3.12: Comparison of mean apparent porosity of as-received and ball-milled powders, sintered at 1100°C. For HA, 25% TCP, and 75% TCP, there is a statistically significant difference in porosity ($p<0.01$); n=20 for each group.

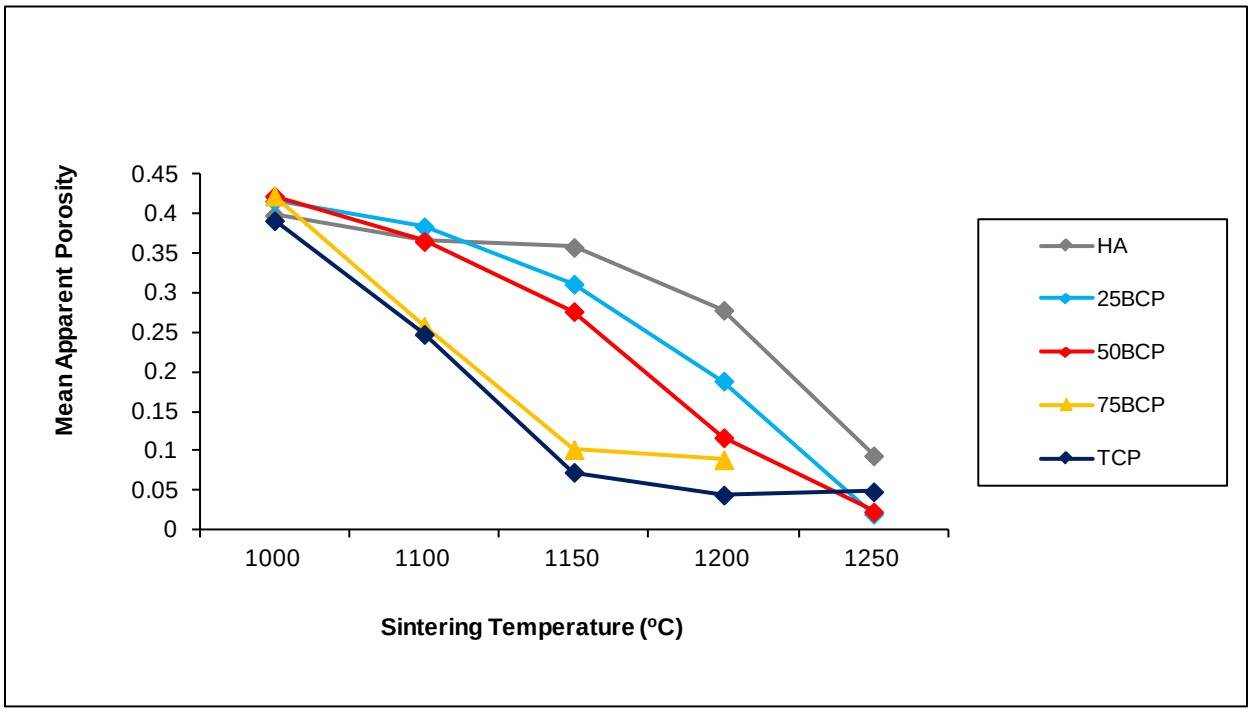


Figure 3.13: Comparison of mean apparent porosity for wet-ball milled powders. Agglomerates were ball milled for 20 hours and sintered at various temperatures. TCP experiences a faster densification than HA at temperature range of interest, 1100 and 1150$^{o}$C; densification rates for 75% TCP and 100% TCP are similar, 25% TCP and 50% TCP favor behavior of HA. Moreover, densification rate of HA is highest at 1200 and 1250$^{o}$C, falling outside of the temperature range inhibiting the $\beta \rightarrow \alpha$ transition of $\beta$-TCP; making HA a constraining variable to densification of the biphasic compositions.

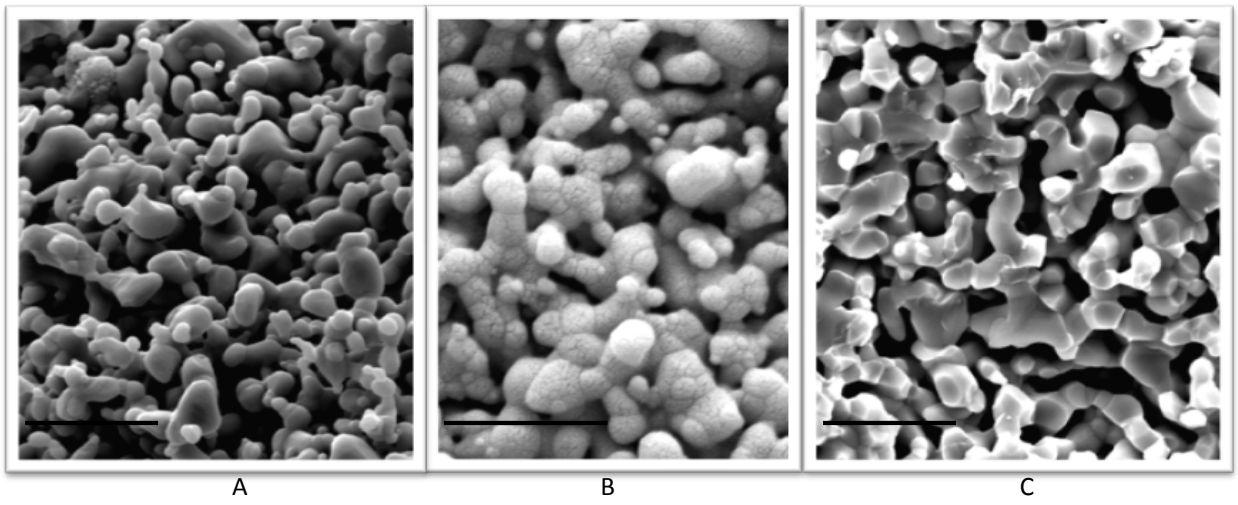


Figure 3.14: SEM of as-fired [A,B] and fracture [C] surface microstructure of biphasic compositions. Each composition shows necking of powder particles and an open pore network. Microstructure of 25BCP [A] and 50BCP [ B] are similar in mean pore size, measuring an average value of 1.08 μm, with larger pores on the order of 2.01 μm. These pores appear to be consistently shaped, and evenly spaced within the microstructure, with smaller pores outnumbering the larger. By contrast, microstructure of the 75BCP [C] composition consists of measuring 1.20 μm in size, but often coalescing to form lengthy pore channels measuring, on average, nearly 5 μm; these pores appear to dominate the microstructure. Magnification 5000X; scale bars measure 5 μm.

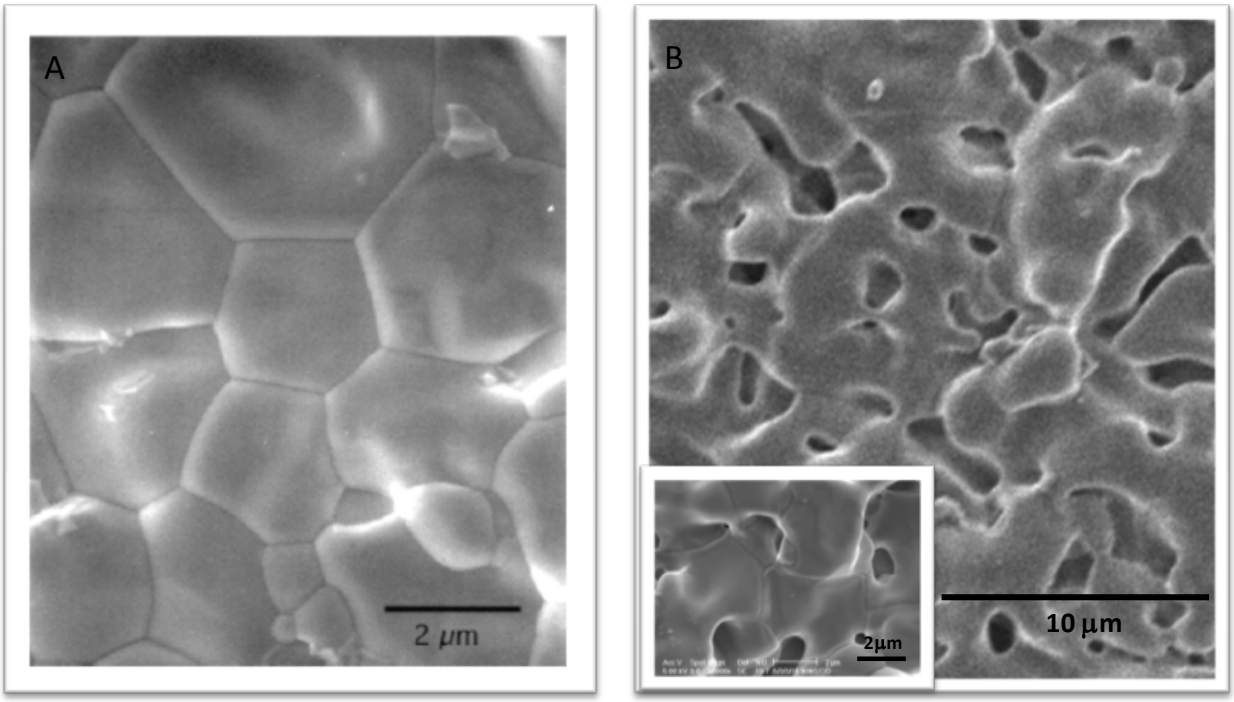


Figure 3.15 Microstructure of HA [A] and β-TCP [B] after sintering at 1300°C. HA shows no residual porosity. β-TCP, however, demonstrates a comparatively substantial residual porosity, thereby illustrating the limitation on densification of β-TCP. HA photo taken from Chu, et. al.[52]

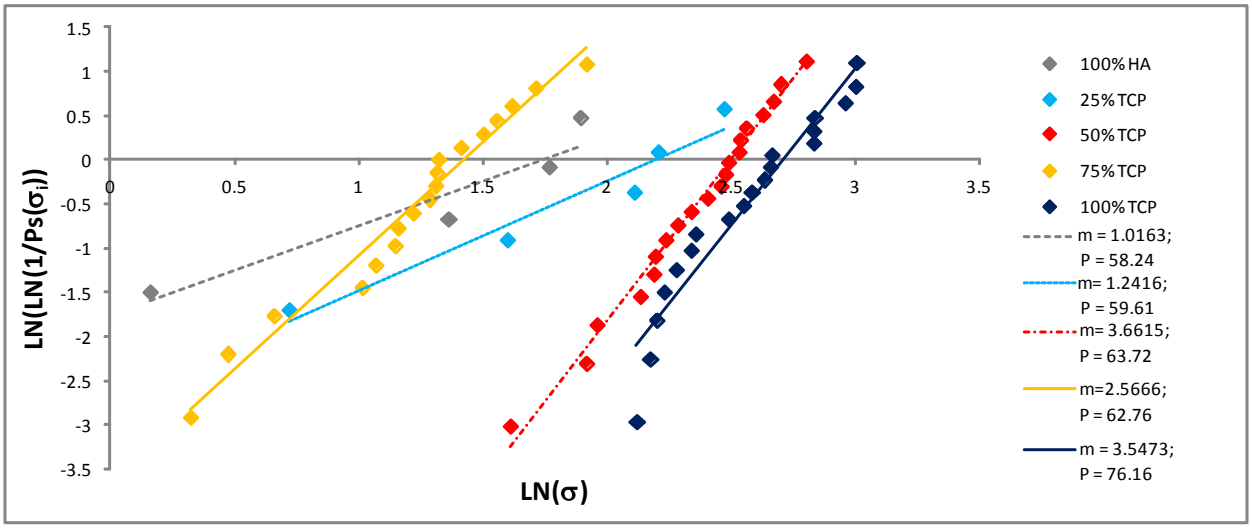


Figure 3.16: Weibull plots for CaP pellets fractured by diametral compression, where pellets differed according to composition and relative density, P. Weibull moduli is highest for the 50/50 biphasic composition, but and generally increases with increasing density.

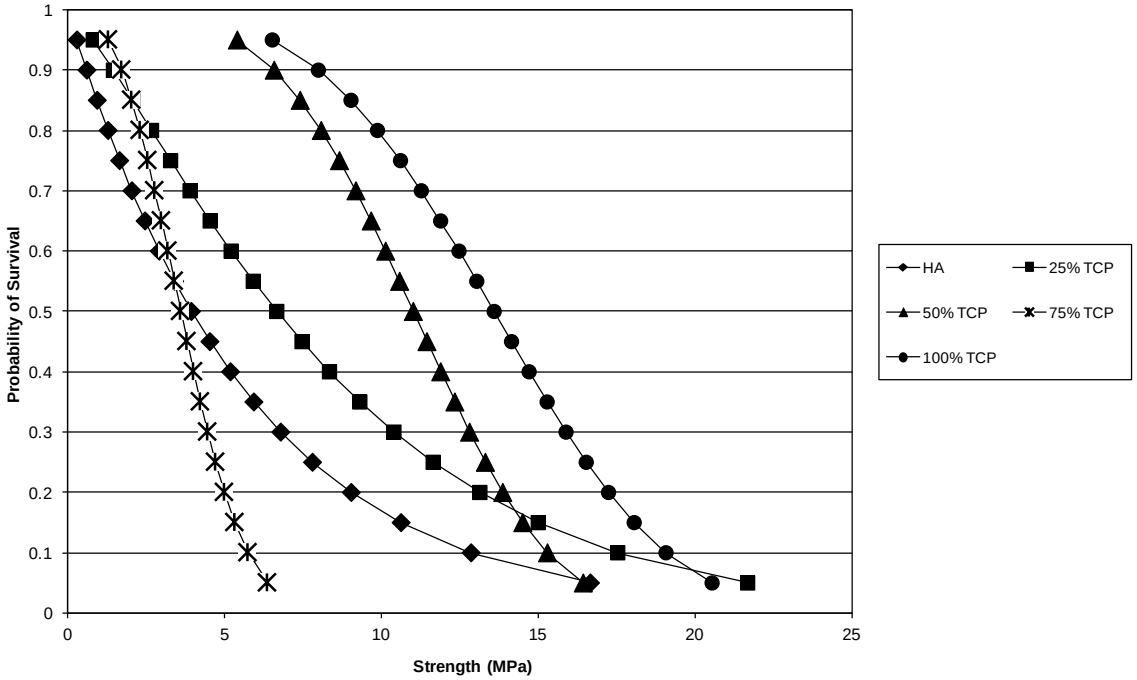


Figure 3.17: Probability of survival for dense calcium phosphate pellets sintered at 1100$^{o}$C.

| | Survival Rate | | |
|---|---|---|---|
| Composition (% TCP/HA) | 90% ($\sigma$, MPa) | 50% ($\sigma$, MPa) | 10% ($\sigma$, MPa) |
| 100/0 | 7.99 | 13.59 | 19.07 |
| 75/25 | 1.73 | 3.60 | 5.75 |
| 50/50 | 6.59 | 11.02 | 15.29 |
| 25/75 | 1.46 | 6.67 | 17.53 |
| 0/100 | 0.62 | 3.95 | 12.86 |

Table 3.2: Weibull analysis depicting the probability for survival at the 90%, 50%, and 10% levels for calcium phosphate pellets sintered at 1100$^{o}$C.

| Composition (% TCP/HA) | Relative Density (%) | Weibull Modulus | Characteristic Strength (MPa) | Mean Fracture Strength (MPa) |
|---|---|---|---|---|
| 100/0 | 76.16 | 3.55 | 15.07 | 13.55 ± 3.97 |
| 75/25 | 62.76 | 2.57 | 4.16 | 3.65 ± 1.37 |
| 50/50 | 63.72 | 3.66 | 12.18 | 10.97 ± 2.94 |
| 25/75 | 59.61 | 1.24 | 8.96 | 7.25 ± 3.81 |
| 0/100 | 58.24 | 1.02 | 5.66 | 4.39 ± 2.43 |

Table 3.3: Relative density, Weibull modulus, characteristic strength and mean fracture strength (± standard deviation) for various compositions of calcium phosphate densely sintered discs.

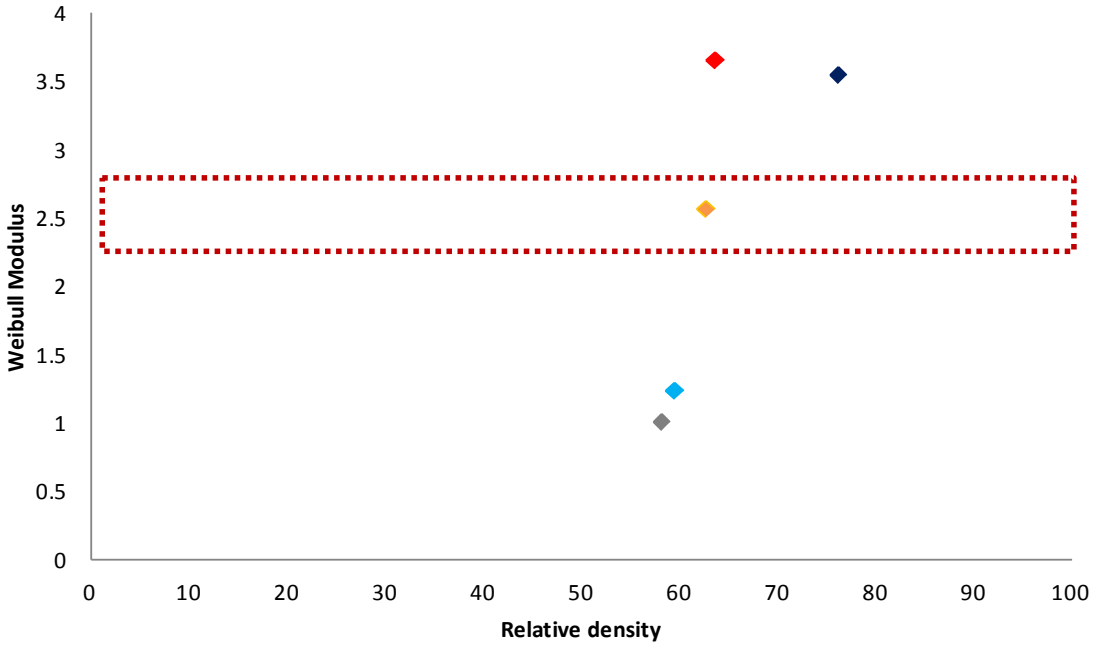


Figure 3.18: Weibull modulus as a function of relative density, depicting high variability for relative densities near 60%, with values approaching steady-state at densities greater than 63%. The 75% TCP composition (dashed red rectangle) is not within trend; a result that may be a consequence of the microstructure. HA (gray); 25BCP (light blue); 50 BCP (red); 75 BCP (orange); TCP (dark blue).

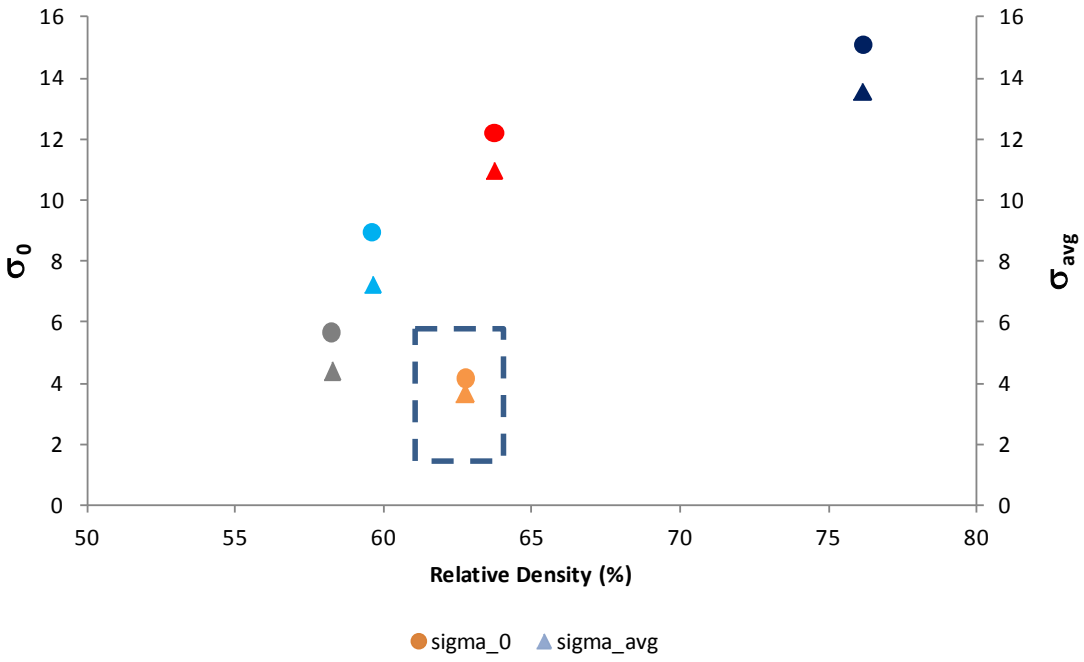


.

Figure 3.19: Mean characteristic ( $\sigma_o$) and fracture ($\sigma_{avg}$) strength as a function of compositional changes and relative density. Both characteristic strength and fracture strength showed a steady increase with increasing amounts of TCP and relative density, demonstrating that high TCP constructs are generally stronger. The 75% TCP composition (dashed blue box) is not within trend, and indicates the significance of relative density in the strength of material. HA (gray); 25BCP (light blue); 50 BCP (red); 75 BCP (tan); TCP (dark blue)

.

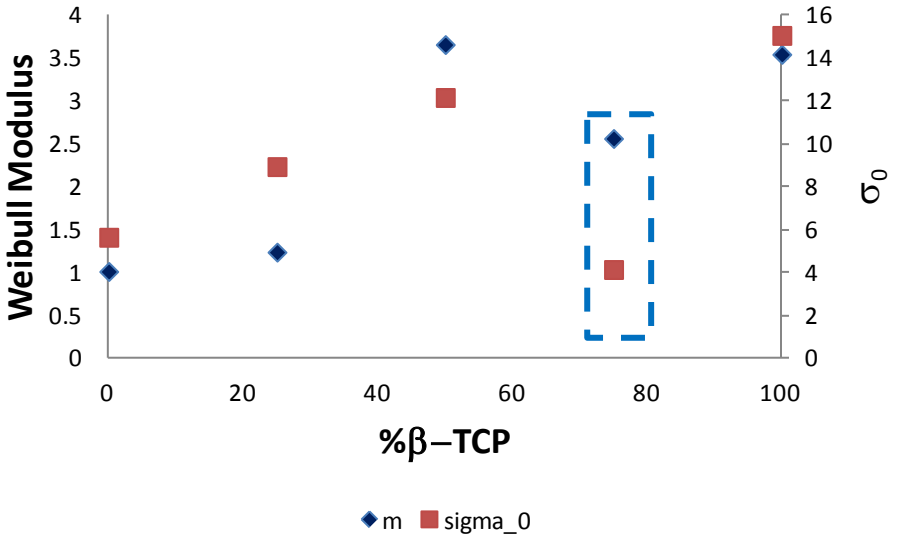


Figure 3.20: Weibull modulus and characteristic strength as a function of relative density. Both demonstrate a steady increase with increasing amounts of TCP. The 75% TCP composition (dashed blue box) is out of trend, and indicates a dependency of strength on relative density.

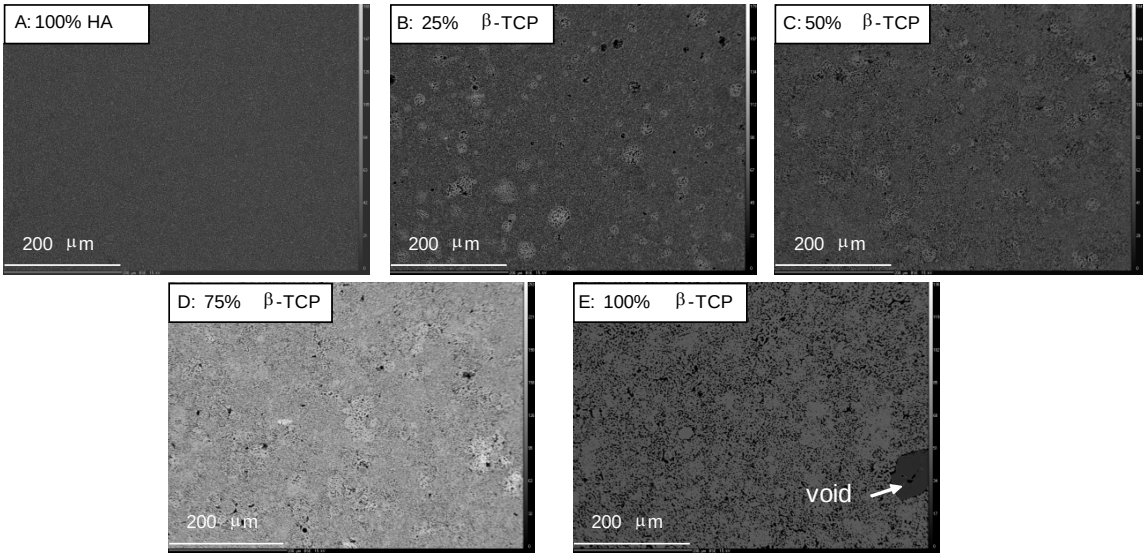


Figure 3.21: Back-scattered SEM images (A-E) of three biphasic compositions: 25BCP (B), 50BCP (C), 75BCP (D) and their calcium phosphate components--HA (A) and β-TCP (E). Images show no distinction across compositions. The lighter contrast of the 75BCP composition (D) is due to a change in imaging settings and not to compositional differences. Within a given image, lighter grayscale spots may correspond to agglomerated particles, but no determination can be made of its local composition. All images have a 600 micron field of view.

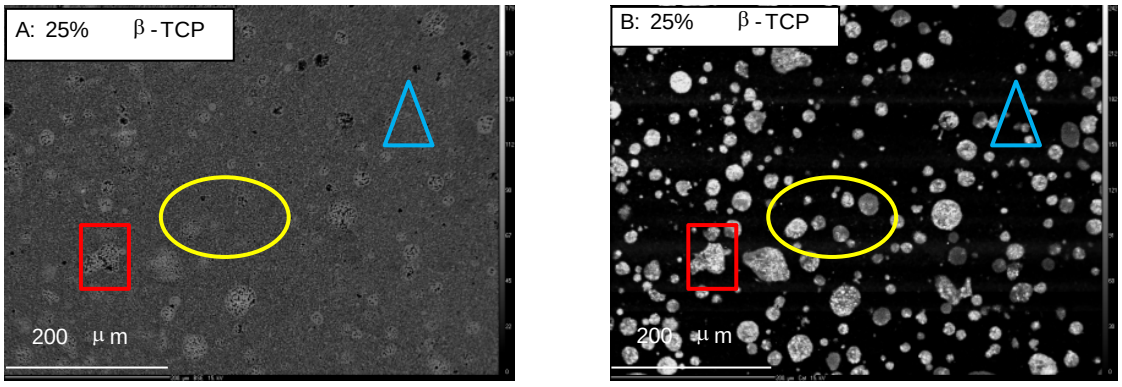


Figure 3.22: Comparison of 25% TCP biphasic back-scattered SEM (A) and CL (B) images. SEM image overall shows gray shadings that are not distinguishable (comparison of circle, square, and triangle in A). CL image depicts the same region in high contrast, with areas within the image distinguishable and distinct from one another due to grayscale contrast. Furthermore, a comparison of shapes in A to corresponding shapes in B shows regions in the CL image that go unnoticed in the SEM image. Image analysis of the bright areas of contrast within the CL image is determined to be 0.25 volume fraction (of the image area).

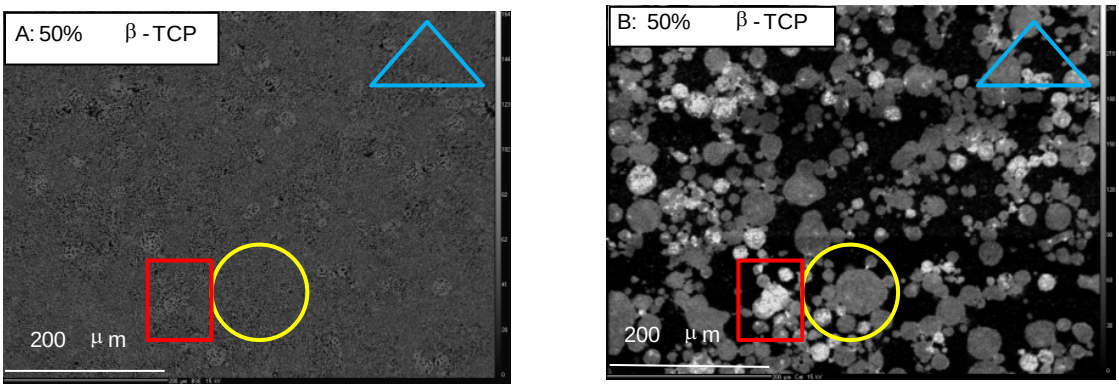


Figure 3.23: Comparison of 50% TCP biphasic back-scattered SEM (A) and CL (B) images. CL regions in high contrast (red square vs. yellow circle vs. blue triangle) are distinctive, displaying various shadings of grayscale. In the comparable SEM image, these regions are not distinctive. Additionally, a comparison of squares, circles, and triangles between the two images reveals distinct differences in each imaging modality's ability to distinguish between TCP grains. Image analysis of the bright areas of contrast within the CL image is determined to be 0.505 ± 0.010 (n=4) volume fraction (of the image area).

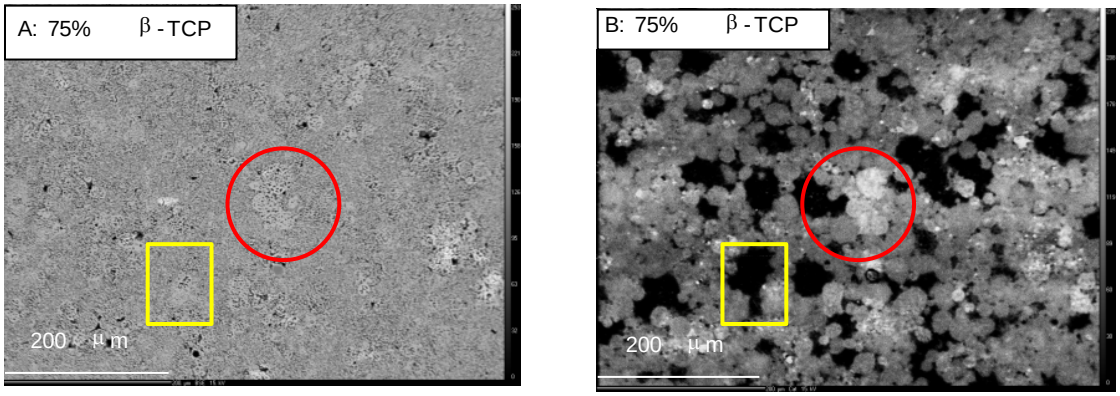


Figure 3.24: Comparison of 75% TCP biphasic back-scattered SEM (A) and CL (B) images.SEM image overall shows washed-out gray shadings that are not distinguishable. CL image is in high contrast, with areas within the image distinguishable and distinct from one another due to grayscale contrast. Furthermore, a comparison of black shading (yellow square) and bright gray shading (red circle) in the CL image lack the same vivid contrast in corresponding regions (yellow square and red circle respectively) of the SEM image. Image analysis of the bright areas of contrast within the CL image is determined to be 0.754 ± 0.003 volume fraction (of the image area).

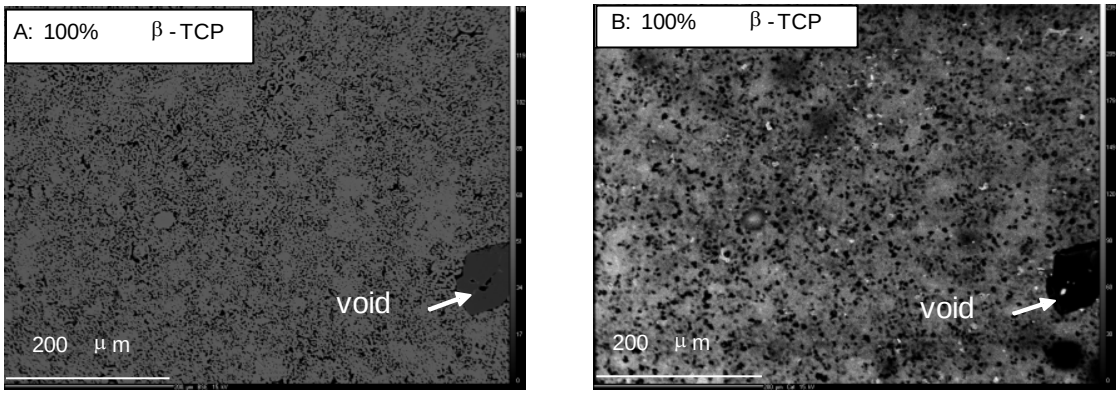


Figure 3.25: Comparison of 100% β-TCP back-scattered SEM (A) and CL (B) images. SEM image shows minimal contrast as compared to the CL image, with no discernible features. The CL image is in higher contrast, with a relatively homogeneous bright gray region.

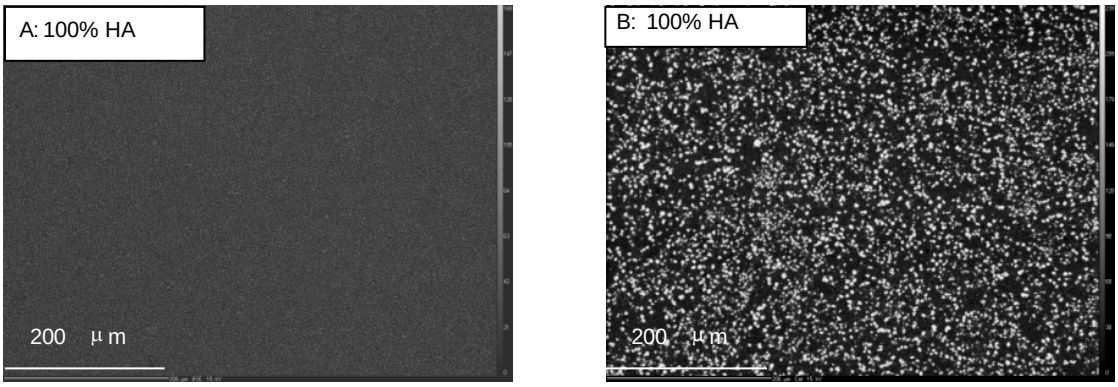


Figure 3.26: Comparison of 100% HA back-scattered SEM (A) and CL (B) images. SEM image overall shows washed-out gray background with no distinguishable features. Conversely, CL image is in high contrast, with uniform salt and pepper appearance. Moreover, the high-contrasting gray regions comprise 10.81 ± 2.83 % (n=6) volume fraction of the image, comparable to the demonstrated 14% conversion of HA to β-TCP under 1100$^{o}$C sintering conditions.

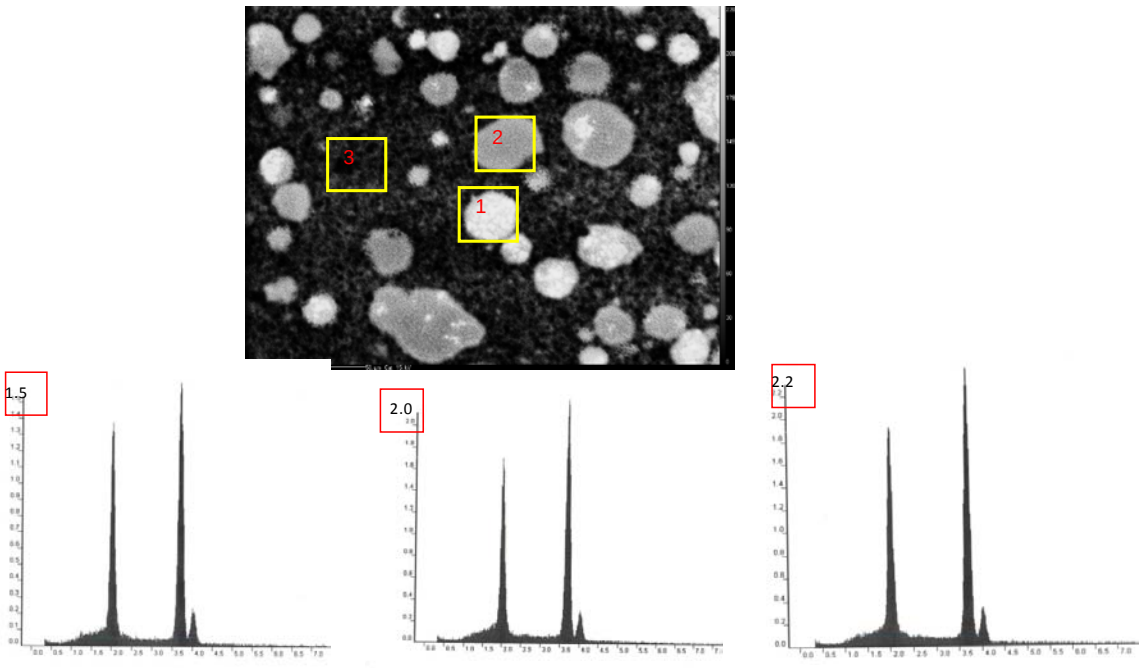


Figure 3.27: EDS analysis at various grayscale regions within the 50% β-TCP cathodoluminescence image. Grayscale regions are numbered (1-3) and relative Ca:P ratio is presented. Ca:P for stoichiometric HA and β-TCP are 1.67 and 1.5 respectively. Ca:P ratio for grayscale regions 1, 2, and 3 is 1. 5, 2.0, and 2.2 respectively.

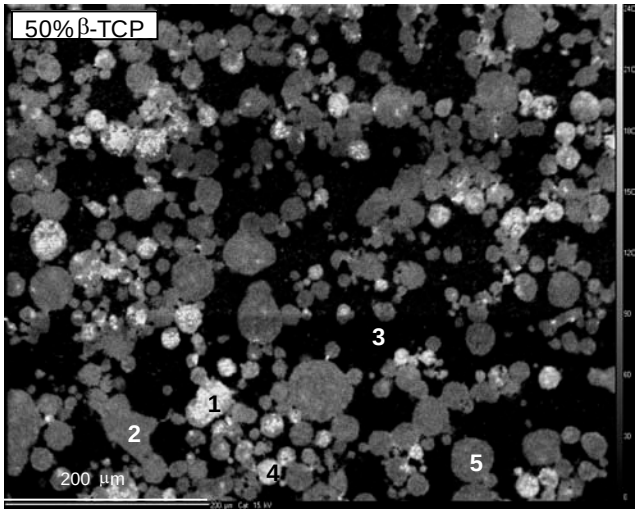


| Known Standard | Hydroxyapatite (HA) Ca: P = 1.667 | | β-Tricalcium Phosphate (β-TCP) Ca: P = 1.50 |
|---|---|---|---|
| Point # (Region color) | Amount Ca (atomic %) | Amount P (atomic %) | Ca: P |
| 1 (Lt. Gray) | 22.934 | 15.397 | 1.49 |
| 2 (Dk. Gray) | 23.434 | 15.182 | 1.54 |
| 3 (Black) | 24.935 | 14.191 | 1.76 |
| 4 (Lt. Gray) | 23.291 | 15.225 | 1.52 |
| 5 (Dk. Gray) | 23.348 | 15.165 | 1.54 |

Figure 3.28: EPMA analysis at various grayscale regions within the 50% β-TCP cathodoluminescence image. Grayscale regions are numbered (1-5) and corresponding Calcium and Phosphorus atomic percent as determined by cathodoluminescence microprobe is presented. The relative Ca:P ratio is also determined. Ratios for stoichiometric HA and β-TCP are included for reference. Mean Ca:P ratio for various gray regions (1, 2, 4, and 5) is 1. 51 ± 0.03, closely matched to known Ca:P for β-TCP. Ca:P ratio for the black region (3) is 1.76, slightly higher than that of stoichiometric HA.

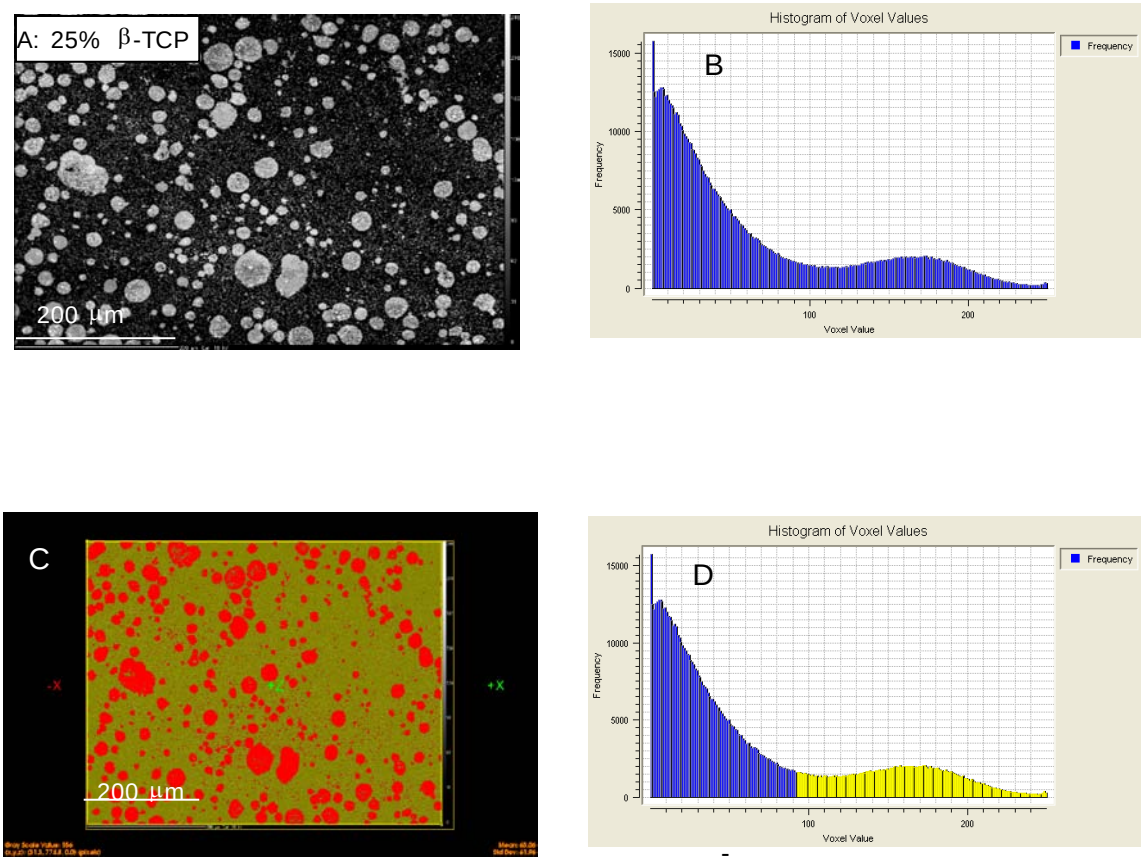


Figure 3.29: CL image of biphasic calcium phosphate containing 25% β-TCP (A) and corresponding bimodal histogram of voxel values (B). Values corresponding to β-TCP are highlighted in the histogram (D) (voxel value vs frequency) and colored in the CL image (C). Image analysis reveals the volume fraction in the red region (β-TCP) is 0.25 and is confirmed by xray diffraction.

# CHAPTER 4
# ARCHITECTURAL DESIGN AND CHARACTERIZATION OF CALCIUM PHOSPHATE SCAFFOLDS

*"All architecture is shelter, all great architecture is the design of space that contains, cuddles, exhalts, or stimulates the persons in that space".*
*-Philip Johnson, designer of The Glass House (1949)*

## 4.1 Scaffold Architectural Influence on Bone Regeneration

Tissue engineering and regenerative medicine allow for the effective engineering of several tissue types; bone, cartilage, and nerve tissues are the only tip of the iceberg. The paradigm for the successful tissue regeneration often depends on the usage of porous scaffolds coupled with relevant biologics, e.g., growth factors, stem cells, and other biological macromolecules, that induce tissue ingrowth. The architectural features of the inductive scaffold have been shown to direct cellular migration, attachment, and proliferation, as well as provide a conduit for oxygen and nutrient transport.[37, 42, 140-141] Important architectural features include, but are not limited to, porosity and pore size, permeability, degree of fenestration, and mechanical stiffness. The inherent function of the scaffold is not only to provide a structure onto which tissue growth may pattern itself, but also to provide the mechanical strength and support necessary to sustain the regenerating tissue. Rendering constructs that meet the needs of neo-tissue can be

challenging in that several requirements are contradictory if optimized. For example, in order to provide the highest permeability and opportunity for tissue ingrowth a scaffold with a high void space is necessary; yet, high void space is detrimental to the strength of the scaffold, in that high void fractions generally do not provide the requisite structural support. Similarly, limitations exist for materials chemistry-dictated and fabrication-dictated characteristics. Furthermore, the regeneration potential of tissue engineering scaffolds is not only dependent on the fabrication modality and material choice, but also on its processing parameters and inherent tissue specificity.

Specificity for tissue application defines the end architecture and design parameters of the scaffold construct.[142-146] While the requirements of three-dimensionality, interconnected porosity, facilitation of mass transport and mechanical support are universal, the specifics of these requirements differ according to the anatomical location and material choice.[26, 147-150] Bone is highly regenerative and possesses unique properties: 1.) the ability to repair small fractures or defects; 2.) the ability to undergo skeletal growth and maturation via cycles of regeneration; and 3.) the ability to sustain load and retain optimal shape, structure, and function.[151] Given these biological capabilities, several architectural features are paramount for scaffolds intended for the repair of bone tissue: 1.) they must have adequate macroporosity and permeability to accommodate the infiltration of cells and the establishment and support of vascularity within the tissue; 2.) the implant material must be able to encourage bonding at the

implant-bone interface in order to promote implant fixation; and 3.) the material must be able to support loading without deformation. Inasmuch, scaffolds for this biological tissue target tend to make use of calcium phosphate (CaP) materials, either as bulk materials or as coatings, to exploit the surface chemistry and microporosity shown to bond well with nascent tissue, elicit favorable cellular responses similar to wound healing, and encourage the differentiation of osteoblasts. However, scaffolds intended for the repair of loaded bone must have sufficient strength and stiffness to sustain load. For this reason, the brittle nature of calcium phosphate materials limits the use of the bulk material to non-load bearing applications. Consequently, as a means to overcome these limitations, CaP is often thermally coated on materials more mechanically suited to meet bone's mechanical requirements.[152-155] Other materials used for bone applications include metals,[156-158] polymers,[159-160] and composite materials,[54, 161] each of which has its own limitations or challenges regarding fabrication.

Fabrication generates matrix architectures that can be characterized on several length-scales: the nanoscale (molecular level), the microscale (cellular level), or the macroscale (tissue level). Scaffolds can have various shapes and forms including fibers, granules, blocks, discs, and foams; morphologies can include geometric blocks and pellets or the anatomical replica of a mandibular condyle or the highly interconnected porous structure of cancellous bone (macroscale); architectures can present roughened textures or guided pathways that aid or enhance cellular attachment,

fluid flow, or cellular migration (microscale); and functionalized surfaces that exploit matrix adhesions and selectively encourage or discourage the attachment of specific ions (nanoscale). Scaffold fabrication technologies, in general, can be categorized in one of two ways: 1.) those methods that produce random architectures;[162-164] and 2.) those that generate designed, controlled architectures.[35, 41-42, 162, 165]

Non-designed, or conventional random architecture fabrication methods, such as solvent casting and particle-leaching, gas infusion, phase separation, and hydrocarbon templating, tend to produce cellular structures with a range of pore sizes and sometimes ranges of pore shapes. These isotropically distributed pores and channels are often created through the use of porogens. While adequate porosity and interconnections can be achieved through these methods, a major limitation is that conventional methods of scaffold fabrication offer little control over scaffold mechanical properties; additionally, architectures offer little control in terms of repeatability. Another disadvantage is that highly porous structures are necessary to ensure pore connectivity in porogen leached methods, creating drastically inferior mechanical properties. Conversely, designed architecture fabrication methods, particularly solid freeform fabrication (SFF) techniques such as three-dimensional printing and stereolithography, allow for precision in hierarchical microstructures by enabling the strategic orientation of channels and pores, thereby imparting tremendous control over macroporosity, geometry, and pore interconnectedness.[165-167] Several subsets of SFF exist, each with its own set of

advantages and limitations. For example, laser sintering (SLS) methods can offer a variety of materials choices and higher part strength, but are associated with the difficulty of removing materials trapped in small holes; droplet deposition does not produce parts with materials trapped within, but are limited by anisotropy between the XY and Z direction; and achieving scaffold features of 100 μm or smaller can be done with ease for 3-dimensional printing, but the high heat affects the raw material and materials are difficult to change without the manufacturer's cooperation.[165-166] Furthermore, there is a greater appeal for the use of SFF techniques for the hope that mechanical properties are better controlled than through the use of conventional techniques. And, although the ability to control mechanical properties such as the interplay of stiffness and porosity is not imparted on all modes of SFF, it can be overcome by image-based optimization design approaches.[167-172]

The merit of SFF is not only that it allows for the fabrication of scaffolds with controlled architecture, but also that it allows for the reproducibility of those scaffolds. Through the use of design, it eliminates the randomness associated with conventional fabrication techniques and allows for specificity in tissue application and in geometry, relevant to anatomical location. As such, the fidelity of geometric intricacies can be critical to the performance of the scaffolds, and therefore, must be maintained throughout the entire fabrication process; repeatedly.

In chapter 3 we characterized the bulk materials used in this body of work. We demonstrated that differences in microstructure and mechanical properties were heavily influenced by the thermal treatment and porosity respectively, and equally influenced by composition. In the current chapter we seek to characterize the architectural features of the scaffold constructs utilized throughout this study. We believe that a detailed understanding of the starting structures is necessary, and that the composition-dependent and processing-dependent characteristics of CaP materials may result in scaffolds with varying physical properties. It is our intention, therefore, to (1.) document differences in structure between experimental groups utilized in this work; and (2.) determine if those differences are due to variation in composition and heat treatment, or if they are a function of fabrication defects; and (3.) determine the effect of architecture (design plus heat treatment) on initial scaffold properties. In making such characterizations, the feasibility and repeatability of fabricating these scaffolds will be addressed. We discuss the architectural details of the IDL designs as well as the STL interpretations of those designs and resulting manufactured molds. We use micro-computed tomography to determine scaffold structural dimensions, porosity, and surface area. Finally, scaffold permeability is characterized.

## 4.2 Scaffold Design and Manufacturing

The design parameters chosen in this work aid in the production of bone tissue engineered scaffolds that comply with universally accepted requirements for effective bone tissue engineering scaffolds: 1.) they are osteoconductive, having high porosity and adequate interconnections to ensure nutrient delivery and removal of metabolic waste; 2.) they are biocompatible and biodegradable, providing surface chemistries conducive to cellular attachment, proliferation, and differentiation; and 3.) they have sufficient mechanical properties matching those of native tissues at the site of implantation. We use simple geometries with designed macroporous architectures, pore size and shape, and interconnections. The unit cells are such that the strut size and porosity are able to produce effective mechanical properties within the range of trabecular bone. Our processing parameters, composition and sintering temperatures, allow for the control of microporosity and degradation.

Four architectures are utilized throughout this work, and therefore assessed in this study: two “full-size architectures” used primarily in the mechanical property and materials degradation characterization of the materials, and two subcutaneous (subq) architectures, smaller versions of the full-size scaffolds, sized appropriately for in vivo studies. The subq designs are not direct reductions of the full-size designs but are similar in total porosity, pore size, and pore orientation. Image-based design (IBD) and Indirect solid freeform fabrication (ISFF) techniques were utilized in the scaffold design

and fabrication process. These techniques were introduced by Hollister, et al.,[167, 169-170] and Chu, et al.,[173] respectively, and involve the manufacturing of scaffolds based on the image data for the production of constructs with external geometries matching anatomical requirements of the implant site. This process, from initial design to end fabricated scaffolds, occurs in three stages: stage 1, mold design and fabrication; stage 2, ceramic casting; and stage 3, ceramic processing (Figure 4.1 A-C).

In stage one, mold design and fabrication, design files generated from Computer-Aided Design (CAD) or Interactive Design Language (IDL) image files are imported into ModelWorks software (Solidscape, Inc., Merrimack, NH) and converted into input files comprised of sliced, or layered, data usable by 3D printing technologies. The result of this process is a mold generated from the negative of the desired scaffolds. Rapid prototyping devices, in this case the ModelMaker II (Solidscape Inc.), are used to build molds via the deposition of two different waxes serving as either build material or support material. The sliced design is laid down in a series of layers comprised of both wax materials, and maintained by a rotary cutting blade used to control layer thickness and smooth the wax surface before deposition of the next layer. This process proceeds in the layer-by-layer fashion until all layers (layer number specified in the STL sliced file) are completed. For designs used in this body of work, a layer thickness of 0.0508 mm in all designs, with layer number varying according to overall design size; 80 layers for subq and 157 layers for the full-size groups. In the final step of this processing stage, usable molds are created after heating the dual-wax constructs in a benchtop oven to

melt the support wax, melting temperature in the range of $50^{o}$-$75^{o}$C; build wax melts in the range $95^{o}$-$105^{o}$C. Residual support wax is removed by washing the molds in BioAct, heated and stirred with a stir bar. Molds are then left overnight for solvent evaporation in fume hood.

For all designs, scaffolds with controlled architecture were created with square orthogonal 100% interconnected pores, 900 ± 20 μm in size. Strut thickness was varied to maintain the desired porosities; full-size low porosity scaffolds had a strut thickness of 1718 μm; high porosity scaffolds were designed with 754 μm struts. Pores and struts are equidistant. Scaffolds were of cylindrical geometry with full size dimensions of ⌀8.85 x 6.65 mm. Two levels of macroporosity were targeted: a low macroporosity of 29%, and a high macroporosity of 59%. Subq-sized designs were comparable in pore size and wall thickness ranges, with cylindrical geometry, square-shaped pores, and targeted macroporosities (27% and 58% respectively), but differed in overall dimensions, having measurements of ⌀6.503 x 3.00 mm. Details of the design specifications for all groups are outlined in Table 4.1. Throughout this work, we refer to these macroporosities as “low; or 30%” and “high; or 50%” designs.

Ceramic casting processes, stage two (Fig. 4.1B), lead to the fabrication of the ceramic scaffold: casting the slip into the molds, curing the newly formed scaffolds, and removal of the wax molds. 40 vol % ceramic slips were prepared by separately mixing as-

received commercially available HA and β-TCP powders with 5 wt% Variquat 55 (Goldschmidt, Janesville, WI) and 5 wt% Emphos CS-1361 (Witco, Houston, TX) as deflocculants and 50 wt% Proxylated Neopentyl Glycol (PNPGDA) (Sartomer, West Chester, PA) and 50 wt% Isoburnyl Acrylate Esters (IBA) (Sartomer, West Chester, PA) as acrylate binders (suspension vehicle). Biphasic slurry was achieved by mixing the desired vol% of each of the phase-pure preparations. Prior to casting, benzoyl peroxide was mixed into the suspension (0.15% monomer weight) as a thermal initiator. The slurry was cast into the designed wax molds, and after curing in a nitrogen-rich environment, the wax molds were dissolved in acetone, leaving the ceramic scaffolds. Stage three (Fig 4.1C) commences after acetone evaporation (usually 24 hours under a fume hood): scaffolds are pyrolyzed in a furnace, producing green bodies with the desired architectural features. Green bodies were subsequently sintered in a furnace at 1100$^{o}$C or 1150$^{o}$C at a rate of 10$^{o}$C/min from room temperature, for 5 hours and furnace cooled.

## 4.3 Scaffold Characterization

### 4.3.1 Porosity and Pore size

A morphological property independent of material selection, porosity is defined as the percentage of void space within a solid material. The scaffold requirement of high porosity in order to achieve cellular migration, vascular ingrowth, and osteoconduction has prompted a vast amount of research on the subject of the effect of pores and porosity on bone regeneration. The knowledge gained from this multitude of works has been varied, with little consensus on the details. To summarize, a distinction can be made between types of porosity, microporosity (pores < 10μm) and macroporosity (pores > 50μm); the presence of both are essential for in vitro and in vivo regeneration. Furthermore, while the idea of an optimal pore size is still debatable, researchers have postulated that bone ingrowth is most successful when pore sizes are within the range of 200-900 μm;[29, 40, 174] and although pore shape is not influential, the orientation of pores in specific directions or arrangements has demonstrated favorable results in terms of guided regeneration.

In order to accurately assess and discuss bone regeneration due to specific scaffold architectural features, an understanding of the final fabricated scaffold architecture needs to be ascertained. To this point, we have discussed the overall goal of determining necessary architectural features for bone regeneration via this class of biomaterials, as well as determining if these features can be realized. Micro-computed tomography (μCT) was used to determine how well the goal of controlled architecture could be achieved. μCT is an accepted modality for the assessment of internal scaffold

architecture. Its appeal and benefit lie in its ability to perform non-destructive characterizations; allowing for sample preservation and at times, in vivo monitoring of tissue regeneration. Moreover, 3D datasets generated from its use allow for the determination and prediction of mechanical properties through finite element analysis (FEA).

A commercial μCT system using a micro-focus cone-field beam X-ray source was used to assess the solid void fraction of the wax molds and post-fabricated scaffolds, as well as the pore size, strut size, and overall geometrical dimensions. Data was acquired with an isotropic voxel size of 16 μm, for sub-q groups, or 27 μm, for the full-size groups. Hounsfield unit calibration was performed with a phantom containing water, air, and a cortical bone mimic. Using a Feldkamp cone beam reconstruction algorithm, a 3-dimensional representation of the image was used to constructs. Analysis was conducted using MicroView 2.1.2 software (www.microview.sourceforge.net) from which a uniform threshold value (T=1700) and region of interest (ROI) were used to detect the construct. Three-dimensional datasets were analyzed using the measurement tool. For analyses of scaffold measurements, a slice in the central region was evaluated (Figure 4.2). Pore and strut sizes were measured by selecting the edges and calculating the distance between points. This is an improvement on manual measurement methods in that aligning the centers of the pores and struts with the plane edge ensures parallel points, and possibly more accurate and repeatable data. For porosity measurements,

the ROI was bound by the dimensions of the scaffold. Because scaffold dimensions differ due to differences in shrinkage, a function of composition and thermal treatment combinations, a consistently sized ROI could not be used, and therefore consistent penetration ROIs could not be utilized.

Pore sizes of fabricated scaffolds differed according to design and temperature. In general, the pores of the low-porosity architecture were smaller in size as compared to the high-porosity architectures. As a result of differences in shrinkage due to composition and temperature, variability exists in end-fabricated pore size, expected and measured values (Table 4.2). Differences in pore sizes were significant in regard to architecture designs ($p<0.001$) and sintering temperature ($p<0.005$) but did not differ according to composition ($p=0.448$). Macroporosity of each architectural design were within 5% of the target values, with each design differing significantly from each other. This means that the inherent shrinkage imparted on the scaffolds did not affect overall porosity.

Total porosity of fabricated scaffolds is detailed in Table 4.3. Porosities for the low macroporosity design range from 49-72%; porosities of the high macroporosity design range from 69-92%. These values are inclusive of the designed macroporosity and the microporosity achieved due to sintering, as outlined in Chapter 3. Several studies have demonstrated the ability to, as well as the utility of, fabricate such high porosity CaP-

based scaffolds for bone regeneration;[175-180] some have postulated the need for porosity on the order of 90%.[37, 181] Scaffolds used in this study, then, are well-within the appropriate range and suitable for the determination of porosity influences on bone regeneration (Table 4.4).

### 4.3.2 Surface Area

The significance of surface area to scaffold osteoconductivity has not gone overlooked. In fact, “the differences between structure and function of cortical and cancellous bone suggest osteoconduction requires porosity, and that substances with greater porosity and surface area allow osteoconduction to proceed more completely and quickly.”[11] A primary path to increased surface area is obviously via increases in macroporosity; however, increases in macroporosity will lead to sharper decreases in mechanical stiffness. Other methods, and oftentimes less detrimental to the structural integrity of the scaffold, to increase surface area is through the manipulation of microstructure and surface topology. The addition of micropores and added surface roughness, either via thermal treatment or surface patterning or etching, for example, has been shown to provide enough topology to influence the attachment and proliferation of bone cells.

Surface areas of fabricated scaffolds were obtained from μCT scans (MicroView 2.1.2). This analysis was performed with regard to the subq-sized implants used in *in vivo* studies, as the influence of surface area on bone regeneration is considered later in this

work, in Chapters 6 and 7. A uniform threshold value (T=2500) and ROI were used to detect the surface area and volume of pre-implanted scaffolds at time t= 0. The ROI was cylindrical in geometry and encompassed the entire scaffold region. Values were acquired with a no smoothing algorithm, surface quality factor (SQF) of 1.0, and decimation value equal to 0. Consideration of surface area without smoothing allows for the consideration of total surface area due to designed macroporosity as well as microporosity due to fabrication.

Surface areas of fabricated scaffold groups are detailed in Table 4.5, illustrating differences in surface areas of designed and manufactured scaffolds as a function of architecture, composition, and temperature. End-fabricated scaffold surface area of sub-q scaffolds was not influenced by macroporosity ($p=0.6846$) or composition ($p= 0.5647$, 0.5231, and 0.0533), but was heavily influenced by sintering temperature, p-value equal to 0.0001; furthermore, the temperature-induced surface areas are distinguishable and statistically different from one another (student's t-test). With this consideration, we may refer to these characterizations as "high" and "low" surface area.

This assessment demonstrates that the larger determinant of end surface area was not the architectural design of the scaffolds, but the thermal treatment. In other words, the differences in design were not great enough to overcome the large changes in final dimensions as a result of sintering. In light of this fact, the surface areas of the final

scaffolds is an important characterization that may later lend itself to understanding the regeneration dynamics of this materials group, and more importantly, may be a necessary design consideration for scaffolds generated from these materials.

### 4.3.3 Permeability

Scaffold (and graft) osteoconductivity not only rests in the high porosity and surface area of the construct, but also in its three-dimensional architecture, considered a primary determinant of vascular invasion, and therefore, (graft) incorporation.[11] This concept is well-supported by the notion that scaffolds should, ideally, have high porosity with interconnected pore networks for cellular growth and transport of nutrients and metabolic waste, i.e., scaffolds should be permeable. Permeability is defined as the physical property that dictates the efficiency with which fluid flows into and out of the construct. Not a single-property characterization, this mass transport phenomenon has been shown to depend on porosity and pore size, pore orientation, and fenestration. For this reason, the primary manner in which permeability has been studied in the past attests to the difficulty of isolating permeability from any of the aforementioned cofactors for rigorous study. In these instances, SFF and ISFF techniques can, once again, provide a viable solution, as Hollister et al. has shown that control of the effective permeability, through its use as a design factor, allows for a more comprehensive study of architectural effects on biological behavior. () () () While permeability was not considered a design criterion in the current work, the assessment of scaffold

permeability is an important characterization; the understanding of which may assist in determining influential contributors to bone regeneration.

The experimental protocol used for the assessment of scaffold permeability has been previously described[145, 182] and utilized in our lab (Figure 4.3). Briefly, we utilize a reservoir in which the water level is held in equilibrium by a continuous water flow proceeding from the reservoir, through an acrylic chamber where the scaffold is housed, to a collector. The collector resides on a scale and the mass is recorded using LabView (National Instruments, Austin, TX). Water mass is read at variable time points and allows for the calculation of mass flow, and after achieving stability, average mass flow is used for the calculation of permeability based on a formulation derived from Bernoulli's equation and Darcy's Law:[183]

$$k = \frac{\Delta x}{A.M_s} \cdot \frac{2\pi^2 r^4}{\left(M_0/M_s\right)^2 - 1}$$

where $\Delta x$ corresponds to the scaffold's height, $A$ the scaffold's cross-sectional area, $r$ is the outlet radius and $M_s$ and $M_0$ are the mass flow rate with and without the scaffold, respectively.

Scaffold permeabilities are illustrated in Figures 4.4-4.5. Fabricated scaffold permeability differed significantly between macroporosity designs ($p<0.001$); it did not differ according to composition, sintering temperature, or composition-temperature interaction (upaired student's t-test; GraphPad.com). This means that the inherent shrinkage imparted on the scaffolds did not affect overall permeability and scaffolds were able to maintain interconnections in light of slight fabrication anomalies.

## 4.4 Figures

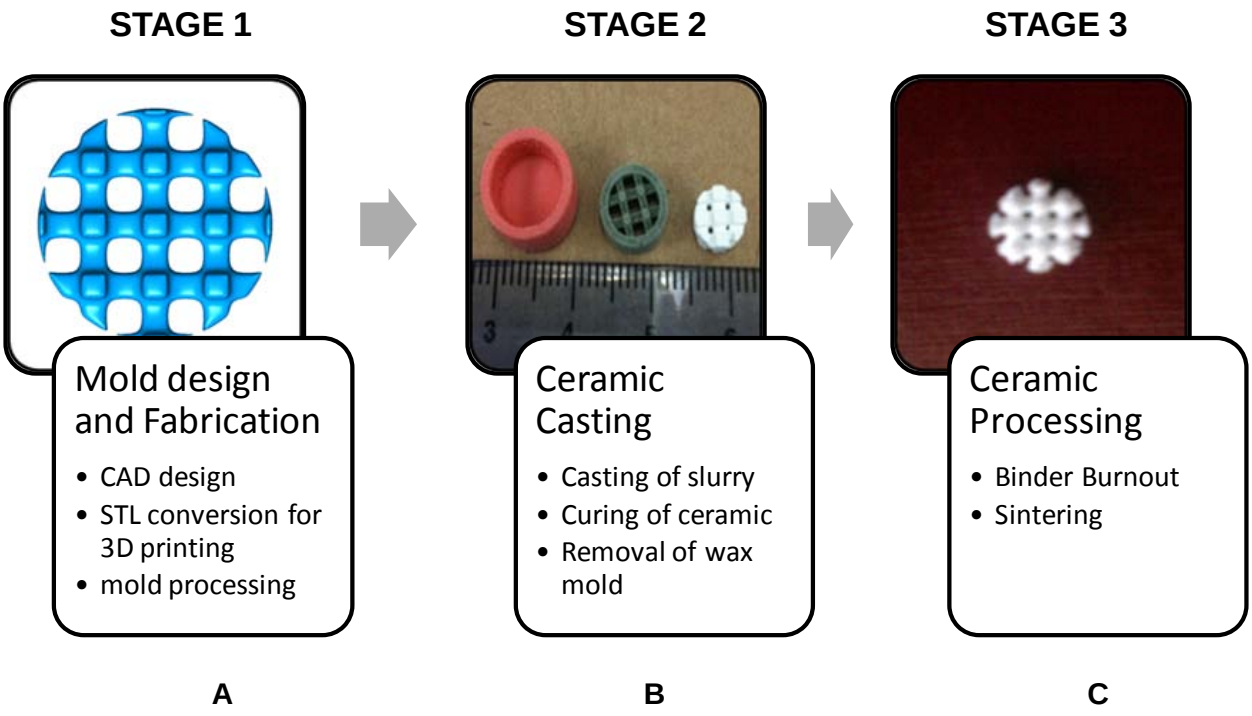


Figure 4.1: Fabrication technique for calcium phosphate ceramic scaffolds. This process occurs in three stages: mold design and fabrication [A], ceramic casting [B], and ceramic processing [C]; and is derived from image-based designs.

| Scaffold Design (% Macroporosity) | Geometry; Scale | Scaffold Porosity (%) | Pore Size (μm) | Strut Size (μm) |
|---|---|---|---|---|
| 30 | Cylindrical; FS | 28.9 | 904 | 1718 |
| | Cylindrical; subq | 26.7 | 879 | 1671 |
| 50 | Cylindrical; FS | 58.8 | 891 | 754 |
| | Cylindrical; subq | 58 | 918 | 904 |

[†]estimated value

Table 4.1: Scaffold design specifications for full-sized (FS) and subqsized (subq) scaffolds.

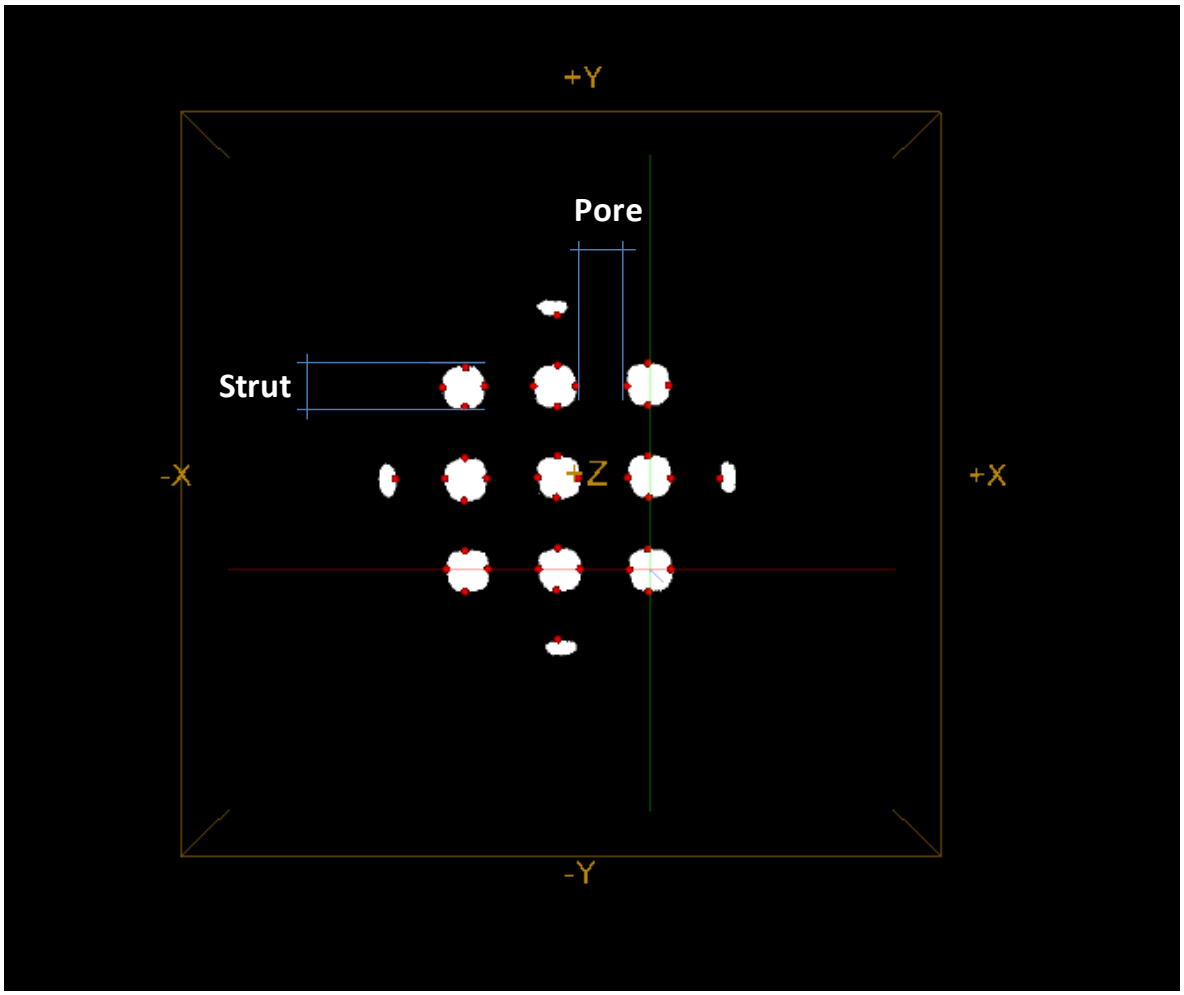


Figure 4.2: Pore and strut size measurement using microCT datasets. A slice in the central region was evaluated. Pore and strut sizes were measured by selecting the edges of the struts (white) and calculating the distance between points. Pores correspond to the spaces between struts. This measurement technique is an improvement on manual measurement methods in that aligning the centers of the pores and struts with the plane edge (red and green lines) ensures parallel points, and possibly more accurate and repeatable data.

| Group | Design | Pore Size (μm) | n-value | Strut size (μm) | n-value |
|---|---|---|---|---|---|
| TCP-1100 | 30% | 753 | 24 | 1443 | 12 |
| TCP-1150 | 30% | 733 | 24 | 1365 | 12 |
| TCP-1100 | 50% | 862 | 46 | 695 | 52 |
| TCP-1150 | 50% | 816 | 46 | 683 | 53 |
| 50BCP-1100 | 30% | 759 | 24 | 1416 | 12 |
| 50BCP-1150 | 30% | 717 | 24 | 1396 | 12 |
| 50BCP-1100 | 50% | 847 | 47 | 688 | 54 |
| 50BCP-1150 | 50% | 837 | 47 | 668 | 54 |
| HA-1100 | 30% | 754 | 24 | 1448 | 12 |
| HA-1150 | 30% | 735 | 24 | 1407 | 12 |
| HA-1100 | 50% | 858 | 48 | 696 | 54 |
| HA-1150 | 50% | 825 | 48 | 693 | 54 |

Table 4.2: Measured pore and strut sizes of fabricated CaP scaffolds. As designed, strut sizes of the lower porosity group are smaller than those of the higher porosity group. Differences in pore sizes are the result of shrinkage due to composition and temperature. Pore size differences were statistically different for designs ($p<0.0001$) and sintering temperature ($p<0.0005$), but did not differ according to composition. For both designs, macroporosity was maintained.

| Macroporosity | Composition-Sintering Temperature | Microporosity (Pore volume, %) | Total Porosity | Total Porosity Range (%) |
|---|---|---|---|---|
| 30% Design 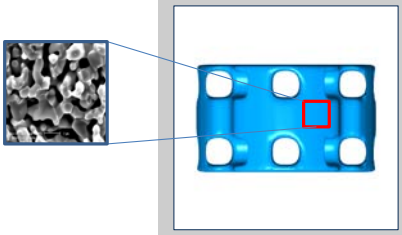 | TCP-1100 | 24 | 54; 74 | For 30% Design, 49-72% |
| | TCP-1150 | 19 | 49; 69 | |
| | 75BCP-1100 | 37 | 67; 87 | |
| | 75BCP-1150 | ---------- | ---------- | |
| | 50BCP-1100 | 36 | 66; 86 | |
| 50% Design 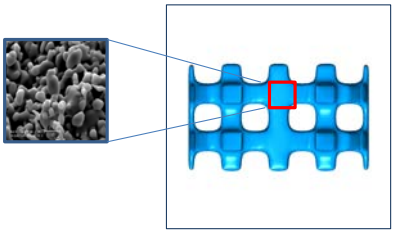 | 50BCP-1150 | 23 | 53; 73 | For 50% Design, 69-92% |
| | 25TCP-1100 | 40 | 70; 90 | |
| | 25TCP-1150 | 31 | 61; 81 | |
| | HA-1100 | 42 | 72; 92 | |
| | HA-1150 | 37 | 67; 87 | |

Table 4.3: Range of total porosity of fabricated scaffolds. Ranges of total porosity for fabricated scaffolds were dependent on macroporosity design [30% or 50%] and microporosity due to sintering temperature and composition. Images show representative microstructures of the solid struts of fabricated scaffolds. The 30% macroporosity design was fabricated within the range of 49-72% porosity. 50% macroporosity designs were fabricated with 69-92% porosity, where macropores were on the order of 800 ± 50 μm, and micropores < 10 μm.

| | Material | Pore Size (μm) | Porosity (%) | Compressive Strength† (MPa) | Group |
|---|---|---|---|---|---|
| Indirect SFF | HA, TCP, Biphasic CaP | 730-865 | 49-92 | 0.8-5.62 | [This work] |
| Robocasting | HA | 100-600 | ---------- | ---------- | Dellinger, et. al.,2006; 2007 |
| Indirect SFF | HA | 469 x 334 | 39% | 30 ±8 | Chu, et. Al., 2002 |
| Stereolithography | Calcium Polyphosphate Cement | -------- | 22.9-27.7% | Bending: 19-31 | Porter, 2001 |
| Theriform | HA | 15 | 45% | ---------- | Roy, 2003 |
| Indirect SFF | Biphasic HA/TCP | 600 | 60-70 | 3.3-5.8 | Guo, 2008 |
| Indirect SFF | DCPD Cement | 900 | 33% | 0.3-0.9 | Jongpaiboonkit, 2006 |
| Polymer sponge | HA | 450-560 | 86% | 0.21 | Kian, 2005 |
| Gel-casting/foaming | HA | 200-1000 | 76-80% | 4.4-7.4 | Sepulveda, 2000 |
| Polymer Sponge | Biphasic: HA/ZrO2 | -------- | 72-91% | 0.3-13.8 | An, 2012 |
| Hot Pressing | Biphasic: HA/TCP | ---------- | 2-17 | 3 pt. bending: ~50-150 | Raynaud, 2002 |
| Pressure Casting | Biphasic: HA/TCP | 300-1250 | 53-73% | 1.5-22 | Bignon, 2003 |
| Polymer Sponge | Biphasic: HA/TCP; HA | 200-400 | 70-77% 73% | 0.55-5 9.8 | Ramay, 2003; 2004 |
| Polyurethane Sponge | HA; TCP; HA/TCP | 600 | 60-90 | 0.02-3.3 | Kwon, 2002 |

Table 4.4: Overview of structural and mechanical properties of porous calcium phosphate ceramic scaffolds for bone tissue engineering. Citations[86, 118, 121, 173, 175, 178-180, 184-191]

| | Group | N-value | Surface Area ($mm^2$) |
|---|---|---|---|
|  | TCP-1100 | 3 | 258.28 ± 16.69 |
| | TCP-1150 | -------- | -------- |
| | 50BCP-1100 | 2 | 312.25 ± 51.87 |
| | 50BCP-1150 | 3 | 170.33 ± 2.08 |
| 30% Design | HA-1100 | 3 | 264.77 ± 16.09 |
| Surface Area: 199.57 | HA-1150 | 2 | 175.25 ± 6.27 |
| | TCP-1100 | 4 | 299.88 ± 42.11 |
|  | TCP-1150 | 2 | 203.85 ± 14.99 |
| | 50BCP-1100 | 3 | 314.32 ± 147.54 |
| | 50BCP-1150 | 4 | 207.83 ± 32.84 |
| 50% Design | HA-1100 | 3 | 223.53 ± 13.66 |
| Surface Area: 161.62 | HA-1150 | 2 | 196.52 ± 19.83 |

Table 4.5: Surface areas of as-fabricated scaffold groups. Images are microCT renderings of design isosurface.

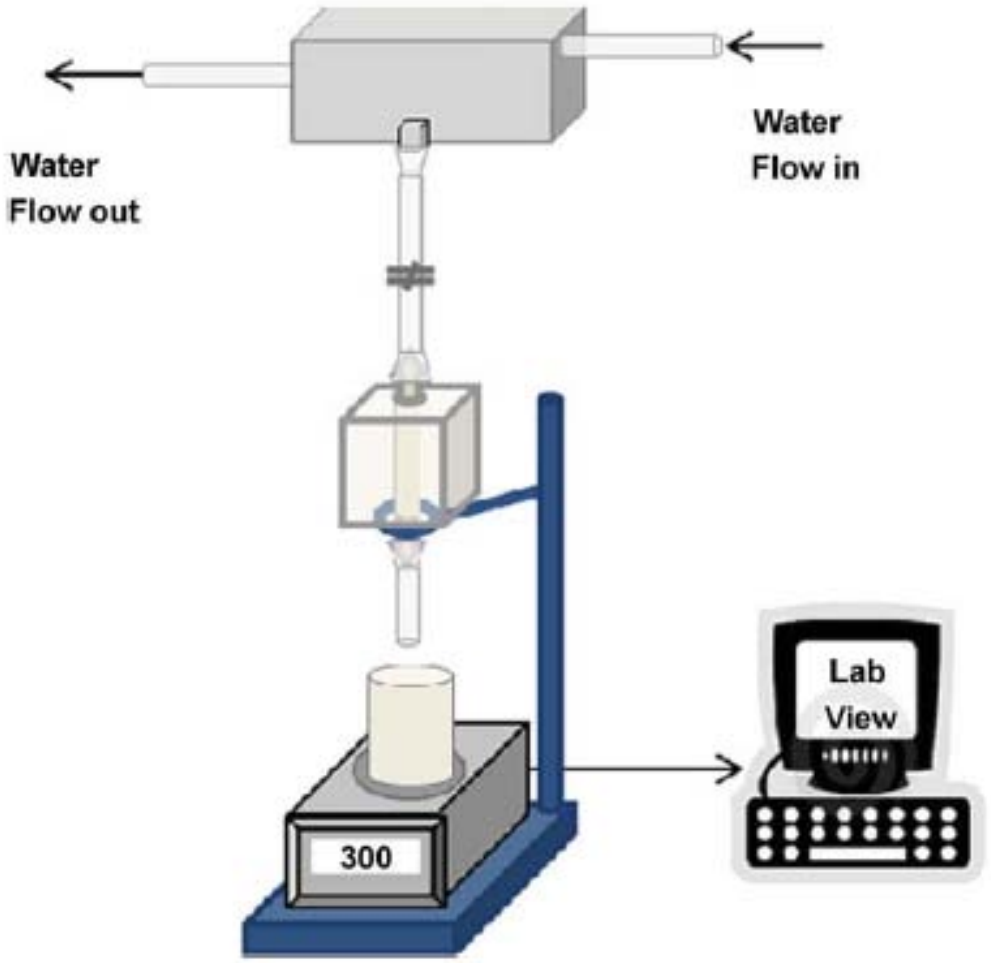


Figure 4.3: Permeability set-up .

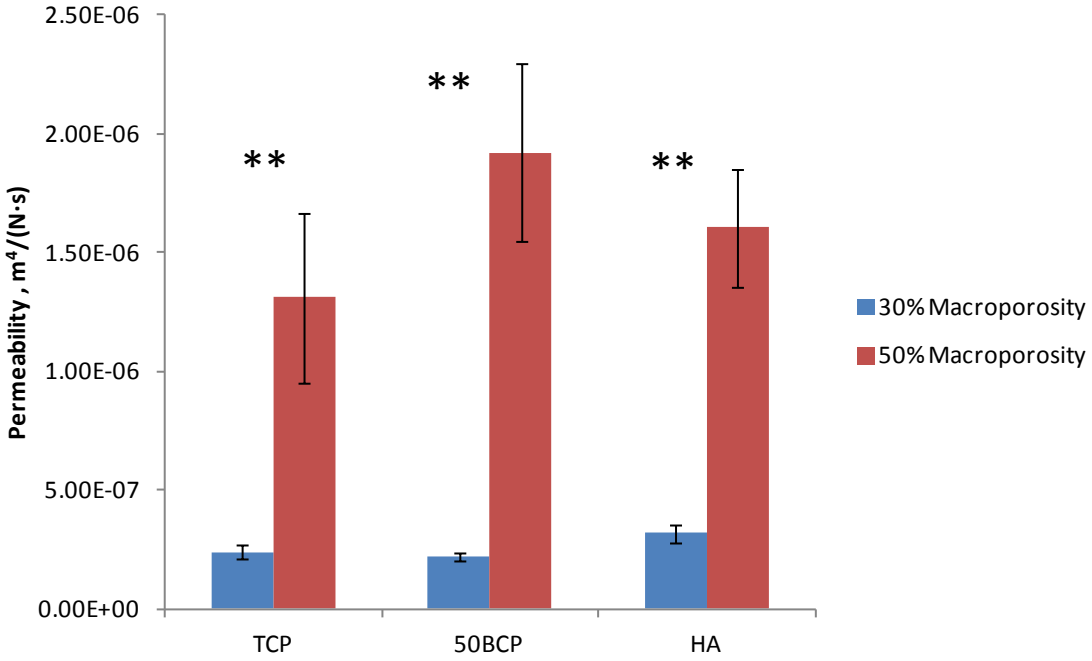


Figure 4.4: Comparative permeability for subq scaffolds sintered at 1100°C. There were significant differences between macroporosity designs; no significance in regard to composition. **p<0.001; n=6 for all groups; 5 measurements per scaffold, performed in triplicate.

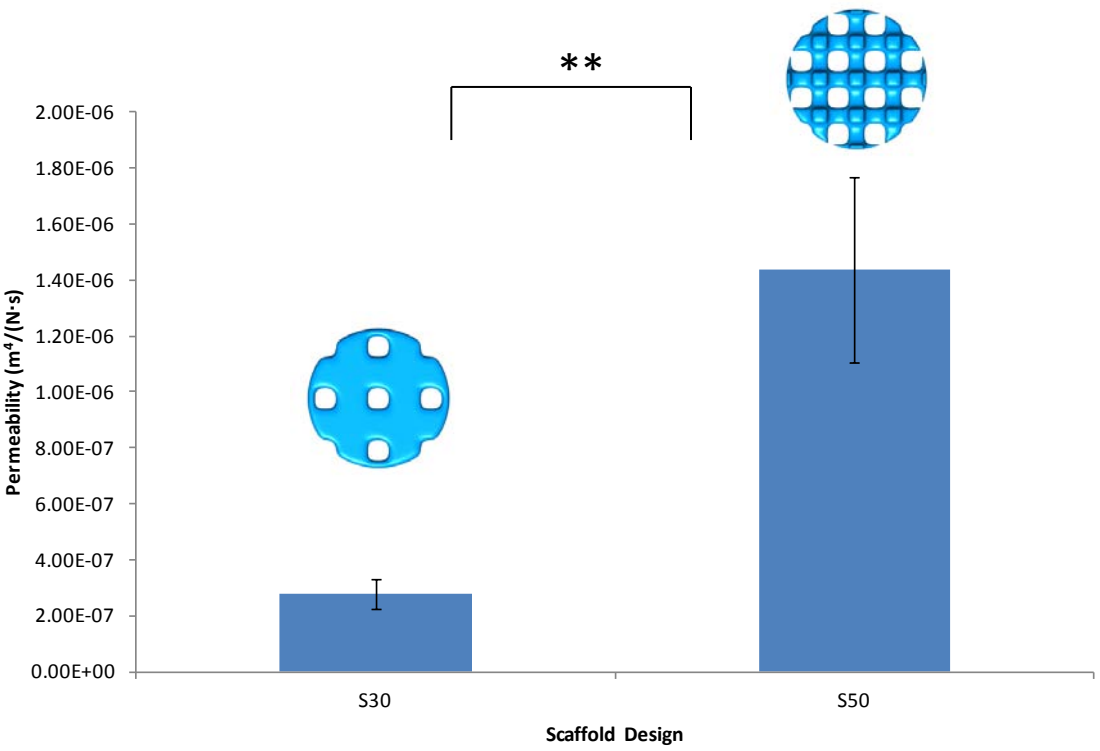


Figure 4.5: Permeability of macroporous designs are distinctly and significantly different.

# CHAPTER 5
# CHARACTERIZATION OF *IN VIVO* MECHANICAL PROPERTY DEGRADATION OF CALCIUM PHOSPHATE SCAFFOLDS

*"No amount of experimentation can ever prove me right; a single experiment can prove me wrong".*
*-Albert Einstein*

## 5.1 Understanding Mechanical Property Degradation *A Priori*

Scaffolds composed of synthetic and natural porous ceramic materials have been widely used in bone tissue engineering applications. Although effective material constructs of this nature may vary in composition, chemistry, and architecture, they must all comply with the chief requirements of scaffolding: demonstrating biocompatibility, osteoconductivity, and requisite mechanical stability and support. As a requirement of osteoconductivity, ideal scaffolds are to be biodegradable. Moreover, degradation rates should be commensurate with rates of bone formation and tissue infiltration; such that newly formed tissue may adopt mechanical demands of the degrading scaffold. That is, the reduction in strength due to degradation should closely match the increasing strength of the neotissue. Important considerations for all scaffolds, then, are condensed to chemistry, geometry, architecture, and mechanics; and the successful marriage between these components may lead to the evolution of an ideal scaffold structure.

As a class of ceramic biomaterials, calcium phosphates (CaP) have long been used to address bone tissue engineering challenges. Research over the past 40 years has offered materials characterizations[129, 192-194] and investigations into the *in vitro*[51, 195] and *in vivo*[90-91, 195-197] performance of this group, and as a result, has provided an understanding for its utility. Considered ideal for bone applications from the perspective of chemistry, the mineral component of calcium phosphates, hydroxyapatite (HA), closely resembles the mineral component of bone, a non-stoichiometric HA. Because of this similarity, CaPs are easily bonded with nascent tissue and able to provide stable implant fixation. Moreover, bone has a greater affinity for implants containing high percentages of HA than it does for those containing only trace amounts.[48, 198] For this reason, scaffolds utilized for the repair of bone have been composed of solely HA,[52, 173] β-Tricalcium phosphate (β-TCP),[199-201] biphasic combinations of HA and β-TCP (BCP),[90, 107, 202-203] HA and other ceramics,[189, 204-205] and HA with various polymers.[161, 166, 206-211] An extensive amount of early work with CaP materials investigated the biocompatibility and solubility of CaP phases, determining that the exploitation of phase solubility imparts a degree of control over dissolution rates. More plainly, control over the fast degradation rate of β-TCP, for example, may be had via the addition of more stable phases such as HA; hence giving rise to the extensive study of BCP compositions.[90, 97, 107, 118, 197, 212-218]

While CaPs are well suited for integration with bone and demonstrate excellent biocompatibility and osteoconductivity, they generally possess low mechanical properties and are appropriate for load-bearing applications. They are, however, well-suited for the repair of craniofacial defects, and as coatings for femoral components of hip replacements in humans,[48] for example. Moreover, improvements in mechanical, and at times, degradation, properties are observed through variations in fabrication methods as well as with the use of composite materials; thereby fostering renewed interest in CaP use for bone augmentation.

A first step in the development of scaffolds that display tissue specificity entails understanding the material's initial mechanical properties and the retention thereof. Such an understanding would allow for the development of methods for the control of property loss during the lifetime of the implant. One possibility to achieve this may be through the design of scaffold architectures. The goal of this chapter, then, is to determine the effect of composition on loss of mechanical property due to *in vivo* degradation of CaP scaffolds. We hypothesize that the degradation of mechanical properties is commensurate with the degradation of material, but the rate of mechanical property degradation may be modulated via the design of porosity. More specifically, for high β-TCP constructs, the balance of strength and scaffold retention is maintained by low overall scaffold porosity, the combination of both macro- and microporosity, in order to accommodate for fast degradation times. The null hypotheses follow:

*$H_{0\text{-}1}$: There is no difference in strength retention across phase amounts of $\beta$-TCP.*

*$H_{0\text{-}2}$: There is no relationship between strength retention and overall porosity, i.e., designed macroporosity and microporosity due to sintering.*

*$H_{0\text{-}3}$: There is no difference in the retention of mechanical properties across composition profiles.*

Work conducted here and in previous chapters will provide the basis for the acceptance or rejection of the aforementioned null hypotheses. Chapter 3 established the bulk mechanical property dependency on thermal treatment and microporosity, and demonstrated that starting composition was a factor in overall mechanical strength. We demonstrated that in dense compacts, compositions with higher fractions of $\beta$-TCP were stronger and that constructs high in microporosity were weaker. The 75/25 TCP/HA composition was an anomaly in that its densification and strength (fracture strength, characteristic strength, and Weibull modulus) were unusually weak and out of trend from all other compositions evaluated. This behavior may have been due to in inefficient packing of agglomerated particles, thereby leading to larger voids in the green bodies, and subsequently larger (than that of other compositions) voids differing in size and shape after sintering. We showed a porosity dependence of Weibull modulus and

highlighted a trend of high variability in Weibull modulus for microporosities greater than 37% and the achievement of a near-steady state for lesser microporosities. Similarly, Chapter 4 extended the discussion as it relates to fabricated scaffolds, and demonstrated that the initial baseline mechanical properties were also correlated to macroporosity and composition. 50/50 HA/TCP biphasic compositions had higher overall fracture strengths as compared to single-phase HA and TCP. Constructs highest in porosity were weakest.

With this knowledge, we progress to evaluate the mechanical performance due to *in vivo* degradation of three compositions of calcium-based scaffolds differing in architecture and microporosity. We address this chapter's goals through the pursuit of answers to the questions:

> *How is material degradation correlated to degradation of mechanical properties for each composition studied?*

> *Do changes in scaffold architecture impart changes in degradation rate?*

> *Is there a pattern of mechanical property degradation for a given scaffold profile, i.e., composition-temperature combination?*

## 5.2 Materials and Methods

### 5.2.1 Porous Sample Fabrication

HA and β-TCP powders (Plasma Biotal Ltd.) were used as-received. As described in section 4.2, ceramic suspensions of the three compositions were used with image-based design and indirect solid freeform fabrication techniques to produce subq-sized constructs with designed architecture and macroporosity. Molds were fabricated using the Model Maker II (Solidscape Inc., Merrimack, NH). Sintering was performed at 1100$^{o}$C and 1150$^{o}$C at a rate of 10$^{o}$C/min with a 5 hour holding time. Final dimensions of the fabricated scaffolds differed according to composition and sintering temperature, as discussed in 4.3.1 and 4.3.2.

### 5.2.2 *In vivo* Degradation Study

Subq-sized scaffolds of various compositions and porosities were used in the *in vivo* degradation study. Prior to implantation, scaffolds were sterilized in 70% ethanol and sterile distilled water for 24 hours respectively. After sterilization, scaffolds were immersed in serum-containing alpha-minimum essential medium (α-MEM) media for a minimum of three hours. Fibrin gel was used as a carrier, though no cells were used in this study. Scaffolds were loaded according to their volume. Ninety-six scaffolds were used, varying according to composition, macroporosiy, and sintering temperatures, comprising a total of 12 groups, over 2 timepoints, 4 and 8 weeks. Scaffold locations randomized. Twenty-four five-to-eight-week-old immunocompromised mice (N: NIH-bg-nu-xid; Charles River, Willington, MA) were anesthetized with intraperitoneal injections of 80μL of ketamine/xylazine in HBSS (0.3mL ketamine, 0.2 mL xylazine, 0.5 mL

HBSS). Midline longitudinal skin incisions, roughly 1 cm in length, were made on the dorsal surface of each mouse and four subcutaneous pockets were created laterally using blunt dissection. One scaffold was placed into each pocket, for a total of four scaffolds per mouse. The incision sites were closed using surgical staples. Four and eight weeks post-implantation, mice were euthanized by inhalation of carbon dioxide, in accordance with institutional guidelines for animal use of the University of Michigan. Transplants with surrounding tissue were explanted by sharp dissection and fixed in a formaldehyde solution (ZFix; Anatech, Ltd, Battlecreek, MI) for 24 hours, rinsed in distilled water for 24 hours, and stored in 70% ethanol.

### 5.2.3 Mechanical Testing

Compression tests were performed on *n = 2-10* scaffolds from each of the twelve sample groups: three compositions, two macroporosities, and two sintering temperatures. Neo-tissue was well-integrated with post-implanted samples, with tissue infiltration occupying much of the scaffold's pore space, macropores as well as micropores. In order to accommodate for this, prior to testing implanted samples, as much of the soft tissue as possible was trimmed away without damaging the scaffolds. All tests were conducted using an Instron MTS RT30 (Instron Corp, Norwood, MA) in uniaxial compression, with a crosshead speed of 2.54 mm/min. Load and displacement data were used to generate engineering stress-strain curves and to determine the compressive strength and stiffness for each sample. Compressive strength refers to the local stress maximum after the linear elastic region of the curve. Stiffness was

calculated as the direct slope of the linear elastic region of the curve taken between two marker points identifying the peak slope region.

### 5.2.4 Percent Retention

Percent retention was calculated as the percent change in modulus or compressive strength between successive time points, *Ra:if,* where *a* is *M* or *S* (modulus or strength) and *i* and *f* are the initial and final time points under consideration. Using this nomenclature, RM: 48 denotes the percent change in modulus between 4 and 8 weeks, for example. Percent retention was analyzed as a function of composition, macroporosity, sintering temperature, and microporosity.

### 5.2.5 Statistical methods

Individual values are reported as mean ± standard deviation (SD). Statistical analyses were performed using SPSS (SPSS for Windows, Rel 19.0, 2011; SPSS, Inc., Chicago, Illinois). To assess the correlation between strength retention, microporosity, and total porosity, Kendall's $\tau$ correlation was applied. In addition, comparison of levels of composition, macroporosity, and sintering temperature across the three time points (0, 4, and 8 weeks) was performed using the Kruskal-Wallis test, the non-parametric equivalent of the one-way ANOVA, better suited for small sample sizes and data not demonstrating normality. In cases of significance, posthoc pairwise comparisons were performed using Dunn's (1964) procedure with a Bonferonni correction for multiple

comparisons. Statistical significance was accepted at the $p < 0.05$ level. Reported p-values are asymptotic. Comparisons between two-level factors at each time point were conducted using Mann-Whitney statistic, a non-parametric equivalent of the independent t-test, to assess differences in scaffold performance. A multiple linear regression was performed to assess how much of the amount of variation in strength (or modulus) can be explained by variation in composition, macroporosity, and sintering temperature; and also, to understand the relative unique contribution of each factor to this total.

## 5.3 Results

### 5.3.1 *In vivo* degradation

**Influence of factors:** A schematic representation of failure behavior of brittle cellular solids is presented in Figure 5.1. Implanted scaffolds demonstrated stress-strain curves characteristic of cellular solids and trabecular bone subjected to compressive loading, possessing a region of linear elastic deformation followed by a failure stress (I), a plateau with nearly constant stress (II), and densification (III), a region of increasing stress (Fig 5.1-5.2); regions attributed to cell wall bending, the collapse of cells due to brittle crushing, and further compression after near complete wall collapse, respectively.[48, 76] The mechanical behavior of a representative sample of specimens at each time point is presented (Figure 5.2 B-D), with differences primarily in the initiation

and duration of regions I, II, and III. Scaffolds at the time zero [Figure 5.2 B] exhibit a shorter interval of stage I, and a longer interval of stage II at lower stresses than the four and eight week groups [C,D]. The plateau stage is shortest at eight weeks, and the initiation of densification occurs earlier with implantation time, occurring at 0.2, 0.3, and 0.45 strain for eight, four, and baseline, respectively. Finally, there appears to be a decrease (zero weeks vs. four weeks) and then an increase (four weeks vs eight weeks) in peak stress. These differences in mechanical behavior, with the exception of the difference in peak stress, are most likely attributed to the incorporation of soft tissue within the scaffold's porosity. The presence of soft tissue would allow load to be transferred from the scaffold to the surrounding tissue; a consequence thereof being a decrease in the amount of brittle crushing of struts, an increase in the stress accommodated by the scaffold at plateau and densification stages, and a faster approach to densification. In the case of peak stress, differences may be a function of composition and degradation, minimal tissue incorporation within scaffold porosity, or some combination thereof. The likelihood of it being due primarily to porosity is small in that this behavior is taken from a low macroporosity-high microporosity group, with comparatively little tissue ingrowth to the eight week group and lower porosity than both zero and eight week groups; a porosity-dominated effect would, in the least, produce peak stress higher than those of the baseline group.

The compressive strength values for all scaffold groups fall within the lower range of that of human trabecular bone,[48, 219-220] and are on par with those of similar calcium phosphate scaffolds reported in literature.[175, 221-223]

The mean compressive strength and modulus of scaffolds at time zero is presented in Table 5.1; also presented is the stiffness and strength for human cortical and trabecular bone. Tables 5.2 and 5.3 present compressive strength and stiffness as a function of composition, macroporosity design, and sintering temperature for each time point observed. At baseline, statistically significantly differences were found between two levels of composition (TCP vs. BCP) and both levels of macroporosity and sintering temperature for both strength and stiffness as determined by Mann-Whitney and Kruskal-Wallis statistic calculations. For macroporosity and sintering temperature, these statistical differences were mostly maintained for the 4 and 8 week time points. Compositional differences were not maintained (Figure 5.3-5.8).

A Kruskal—Wallis test showed that the differences in stiffness across time points for the three compositions studied were not statistically significant (TCP: $\chi^2$ (2) = 1.909, $p$ = .385; BCP: $\chi^2$ (2) = 5.810, $p$ = .055; HA: $\chi^2$ (2) = 1.185, $p$ = .553). Statistically significant differences in compressive strength were present for the 4 and 8 week groups and 0 and 8 week groups of TCP and HA (TCP: 4 and 8 weeks, $p$ = .031, 0 and

8 weeks, $p$ = .001; HA: 0 and 8 weeks, $p$ = .000). No statistical significance was present for the BCP groups ($\chi 2$ (2) = 5.381, $p$ = .068).

Comparable tests examining the differences in modulus and strength across time points for macroporosity and sintering temperature were conducted. Statistically significant differences in modulus were present for the 0 and 4 week low macroporosity groups (p = .011) but no significant differences for the high macroporosity group ($\chi 2$ (2) = 0.173, $p$ = .917). Statistically significant differences in compressive strength were present for the 4 and 8 week groups and 0 and 8 week groups for both macroporosity levels (Low: 4 and 8 weeks, $p$ < .0005, 0 and 8 weeks, $p$ < .0005; High: 4 and 8 weeks, $p$ < .0005, 0 and 8 weeks, $p$ < .0005).

Differences in modulus across time points for sintering temperatures were not statistically significant (Low temp: $\chi^2$ (2) = 4.670, $p$ = .097; High temp: $\chi^2$(2) = 1.495, $p$ = .474). Statistically significant differences in compressive strength were present for the 4 and 8 week groups and 0 and 8 week groups of both temperature levels (Low: 4 and 8 weeks, $p$ = .009, 0 and 8 weeks, $p$ = .002; High: 4 and 8 weeks, $p$ = .022, 0 and 8 weeks, $p$ = .000).

A multiple regression was run to predict peak stress and modulus from composition, macroporosity, sintering temperature, and microporosity, for the three time points evaluated. These variables statistically significantly predicted peak stress and modulus. At T=0, regression models were: $F(4, 113) = 113.523$, $p < .0005$, adj. $R^2 = .794$; and $F(4, 113) = 18.447$, $p < .0005$, adj. $R^2 = .374$, for peak stress and stiffness respectively. At T= 4, and T=8, peak stress models were : $F(4, 35) = 13.017$, $p < .0005$, adj. $R^2 = .552$, and : $F(4, 35) = 10.359$, $p < .0005$, adj. $R^2 = .490$, respectively. Stiffness models were: $F(4, 35) = 1.403$, $p = .243$, adj. $R^2 = .040$;and : $F(4, 35) = 2.426$, $p = .066$, adj. $R^2 = .128$, for the same time points. Macroporosity and sintering temperature were the consistently statistically contributed to the prediction of strength for each time point, $p < 0.003$ in all cases; it did not contribute statistically to modulus. Composition (BCP) demonstrated statistically significant contributions to both models only at the zero time point, $p < 0.005$ and $p = 0.002$ for strength and modulus. Microporosity was not included in any of the regression models due to collinearity with composition and temperature, collinearity coefficients 19.703 and 4.889 respectively. Regression coefficients and standard errors are listed in Table 5.4-5.9.

**Percent retention**: The retained strength of implanted scaffolds is depicted in Figures 5.9-5.11. There was high variability in the strength retention of the implanted scaffolds. Overall, scaffold strength increased over the eight week time period. BCP scaffolds demonstrated the poorest performance when compared to other compositions, losing

11% of its initial strength within the first four weeks of implantation. HA scaffolds demonstrated the better initial retention during the 0-4 week period, while TCP scaffolds maintained the best retention percentages over the entire 8 week timeframe. Most consistent were strength retentions due to sintering temperature and macroporosity. Scaffolds sintered at 1150$^{o}$C were able to maintain strength better than those sintered at 1100$^{o}$C. Similarly, high macroporosity scaffolds performed better than low macroporosity scaffolds for all time frames considered. In all cases, strength remained within the range of human trabecular bone; stiffness was well below, differing by an order of magnitude.

Similar behavior is observed for retention of initial scaffold stiffness, also demonstrating high variability in values (Figures 5.12-5.14). For all factors analyzed, overall stiffness decreased within the first four weeks of implantation, whereas most groups experienced net increases in stiffness over the eight week time period. BCP scaffolds saw the biggest loss in stiffness over each of the time periods, while the margin between TCP and HA remained consistent from 0-4 weeks and 4-8 weeks. Patterns of stiffness retention were comparable to strength retention for macroporosity and temperature, where high temperature and low macroporosity have the most favorable performances.

## 5.4 Discussion

In the present study, scaffolds varying in composition, architectural design and thermal heat treatment were fabricated to study the influence of these factors on strength retention of implanted CaP scaffolds used in bone tissue engineering applications. The experimental design of the work studied the degradation of compressive strength and modulus due to in vivo implantation, and allowed for the inspection of the main effect of composition, macroporosity, and sintering temperature; as well as microporosity, the interaction effect of composition and sintering temperature. As a result of the combination of the three factors mentioned, twelve groups of scaffolds were produced; each demonstrating initial compressive strengths and moduli within the range of 1-6 MPa and 100-300 MPa respectively, corresponding to the lower range of cancellous bone for compressive strength and upper range for elastic modulus.[48, 219-220]

Past research has shown that porous bioceramic scaffolds of various compositions can be produced via several methodologies.[224] For example, Catagne and colleagues fabricated BCP constructs by cold isostatic pressing and conventional sintering, introducing porosity through the use of naphtelen or saccharose particles;[225] while Ramay et al demonstrated the ability to cast HA porous scaffolds using a hybrid technique combining gel-casting methods with polymer sponge casting, capitalizing on the benefit of increased mechanical strength without the disadvantage of inhomogeneous structure, poor interconnections, or thin walls separating pores.[175] In

many cases, pores are formed with varying degrees of control over several architectural features, including pore shape, pore volume, and the associated interconnecting pathways;[186, 202] in other instances, the porosity architecture is much more randomly derived () () (). In contrast, solid freeform fabrication methodologies allow for more direct control of mechanical properties () () (), either through the rigorous design of interconnectivity and pore orientation, or via control over properties such as stiffness () () (). The ability to control for architectural features, such as macroporosity for example, and mechanical properties proves significant for several reasons. Firstly, efficient bone substitute materials that allow for the degradation of material and the subsequent infiltration of bone must demonstrate an adapted, or multi-scaled, porous structure[29, 226] comprised of micropores, on the order of < 10 microns, in the sintered ceramic and macropores, on the order of > 200 microns, in the main body. The presence of both contributes to the overall osteoconductivity of the scaffold, allowing for the infiltration of bone, the vascularization of tissue, and the degradation of construct. Furthermore, microporosity also functions as a drug delivery vehicle, aiding in the diffusion of growth factors and other biologics for the stimulation of bone ingrowth.[48, 227] Secondly, the dependency of mechanical properties on macroporosity is such that optimum strength is achieved via minimum pore volume, and typically, ceramics used successfully in tissue engineering applications possess levels of 40% macroporosity, and at times, higher than 75%.[29, 226] Yet, the significance of macroporosity is undeniable in terms of the scaffold's ability to produce viable functional tissue: higher macroporosity leads to higher osteoconductivity. This paradoxical relationship between macroporosity and

mechanical properties necessitates the understanding of changes in mechanical properties of degrading calcium phosphate materials, where degradation may lead to greater porosity and, subsequently, even less strength. The intent of the current work was to further the understanding in this regard. We utilized solid freeform techniques in the fabrication of porous scaffolds, allowing for the control of pore architecture: pore volume and pore connectivity; choosing to vary pore and strut size in order to maintain constant designed macroporosity. Our initial hypotheses and assumptions regarding the outcome of this study were focused on the β-TCP phase of the CaP materials; postulating that in order to reduce loss of strength, scaffold architecture of TCP compositions needs to be tailored to accommodate for its faster degradation. The key findings and detailed discussion of the results of this study follows:

***Overall retention of mechanical properties was positive, indicating strength gains, and is primarily due to tissue infiltration into the scaffold pores.***

The data presented in this study demonstrates that overall strength retention is positive, i.e., scaffolds appear stronger after implantation than at time zero. Previous studies have shown that *in vitro*, degradable scaffolds of this nature will lose strength and volume with time, and that that the loss can be, to some extent, predicted;[185] others have gone further to say that the loss can be accounted for *a priori* in the design of scaffold architecture using SFF methods.[228] Our own work has demonstrated that CaP

scaffolds lose strength upon in vitro degradation;[229] these preliminary studies were relevant to the full-size scaffold designs discussed in Chapter 4. All of these studies were conducted and evaluated without the consideration of infiltrated tissue. By contrast, *in vivo* studies, and scaffold use in general, are undertaken with the hope to encourage tissue regeneration, and by consequence, tissue infiltration. The hallmark of an ideal scaffold, in fact, is the ability to encourage the infiltration of tissue, and offset the mechanical load through tissue development.

To stay within the parameters of this work, however, we implanted scaffolds without the use of cells so as not to encourage the ingrowth of bone. It was our intention to carry out, as closely as possible, the aforementioned *in vitro* work; the resolution to which was to remove the infiltrated tissue prior to mechanical testing. While most tissue could be removed, there were several instances where residual tissue remained so as not to damage scaffolds. As a result, data presented in this study not only shows reductions in strength properties during the 0-4 week interval, it also demonstrates that at 4 weeks, ingrown tissue begins to offset loads subjected onto scaffolds, and at 8 weeks, the tissue infiltration changes the mechanical behavior of the scaffolds, such that crush strength is higher, crushing is less, and the densification phase is initiated earlier.

***The high variability in mechanical properties is a function of both scaffold architecture and degradation.***

The relationship between strength and porosity, as well as the catastrophic nature in which ceramic materials fail, is well-understood and, as such, high variability in strength is to be expected. In terms of elastic modulus, however, it is customary that the variability is minimal, as this is considered a materials constant. However, in the case of brittle cellular structures, as explained by Gibson and Ashby, " the modulus of rupture of struts varies for brittle materials, as these strength values are dependent on length and location of critical defects and crack propagation", and that low Weibull moduli, as a result, is to be expected.[230] Additionally, for brittle open-cell constructs of the same relative density, crushing strength decreases with increasing pore size. This has several implications for the work presented in this study.

Firstly, as it relates to size of pores: differences in macroporosity were attained through the design of scaffolds having a fixed pore size, achieved through variation in strut thickness. As a result of scaling factors and shrinkage due to sintering, scaffolds were created having a range of pore and strut sizes, while maintaining constant macroporosity per design (the details are discussed in Chapter 4). Secondly, also as a result of sintering, and addressed in detail in Chapter 3, variation in microporosity occurs as a function of both composition and sintering temperature, and dense

constructs produced different microstructures for the compositions and temperatures investigated in the *in vivo* work; six in total. As a result, not only is there a wide range of total porosities in the scaffolds studied, but the microporosity occurs in the scaffold struts, already of variable thicknesses to accommodate macroporosity. Thirdly, as a result of degradation, we can be assume that changes in strut density occurs over implantation time, as is supported by previous work showing that changes in microporosity due to degradation can be on the order of 10-20% over the eight week time period.[231]

And finally, and as an aside, variation in mechanical properties can be expected when we consider how groups were analyzed. As applies to the property of modulus, for example, samples were analyzed according to the influence of one of three factors: composition, macroporosity, and sintering temperature. For the aforementioned reasons, groupings tethered on composition and sintering temperature include large porosity differences mostly due to the inclusion of macroporosity. When constrained by macroporosity, variation in porosity becomes smaller, and is reflected by the comparatively lesser variation in modulus as a function of macroporosity.

***The faster degrading composition, TCP, is not a significant factor in the degrading mechanical strength of scaffolds.***

Scaffolds based on TCP experienced the largest increases in strength, with greatest variability, compared to the BCP and HA compositions, with TCP having the largest increase over the eight week implantation time course. Changes in modulus due to composition are largest for the biphasic composition, and not TCP, although TCP was initially weaker (in terms of both) at baseline measurements; thus implying that these changes are not due to faster degradation. Moreover, if degradation were the highest contributor to retention, we would expect that retention due to microporosity would be highest for the 1100$^{o}$C, or lowest sintering temperature group. In an *in vitro* study using micro-CT to assess changes in materials properties to degradation, Diggs et al. determined that the fast degrading TCP materials showed the highest change in overall material density (later demonstrated to be microporosity) for the 1100$^{o}$-sintered group, a value that was 420% higher than dissolution demonstrated by the 1150$^{o}$-sintered group (lower microporosity) over the same 8-week time period.[231] Therefore the data presented in this work strongly points to macroporosity for changes in mechanical properties, and shows the change to be positive due to the infiltration of local tissue.

***And finally, the relationship between microporosity and strength retention is obfuscated by the larger influence of macroporosity, and cannot be tested for directly in this model.***

## 5.5 Figures

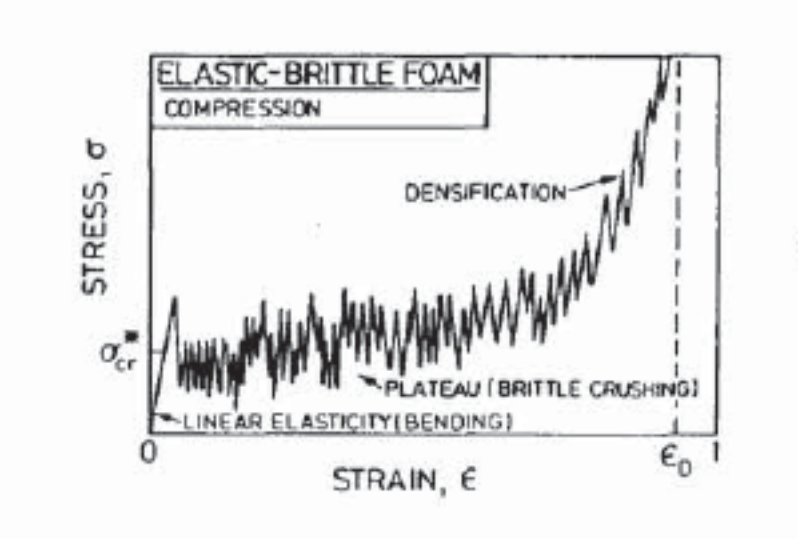


Figure 5.1: Schematic of uniaxial stress-strain curves for an elastic-brittle foam, showing the three regimes: linear elasticity (bending), plateau (brittle crushing), and densification.[230, 232]

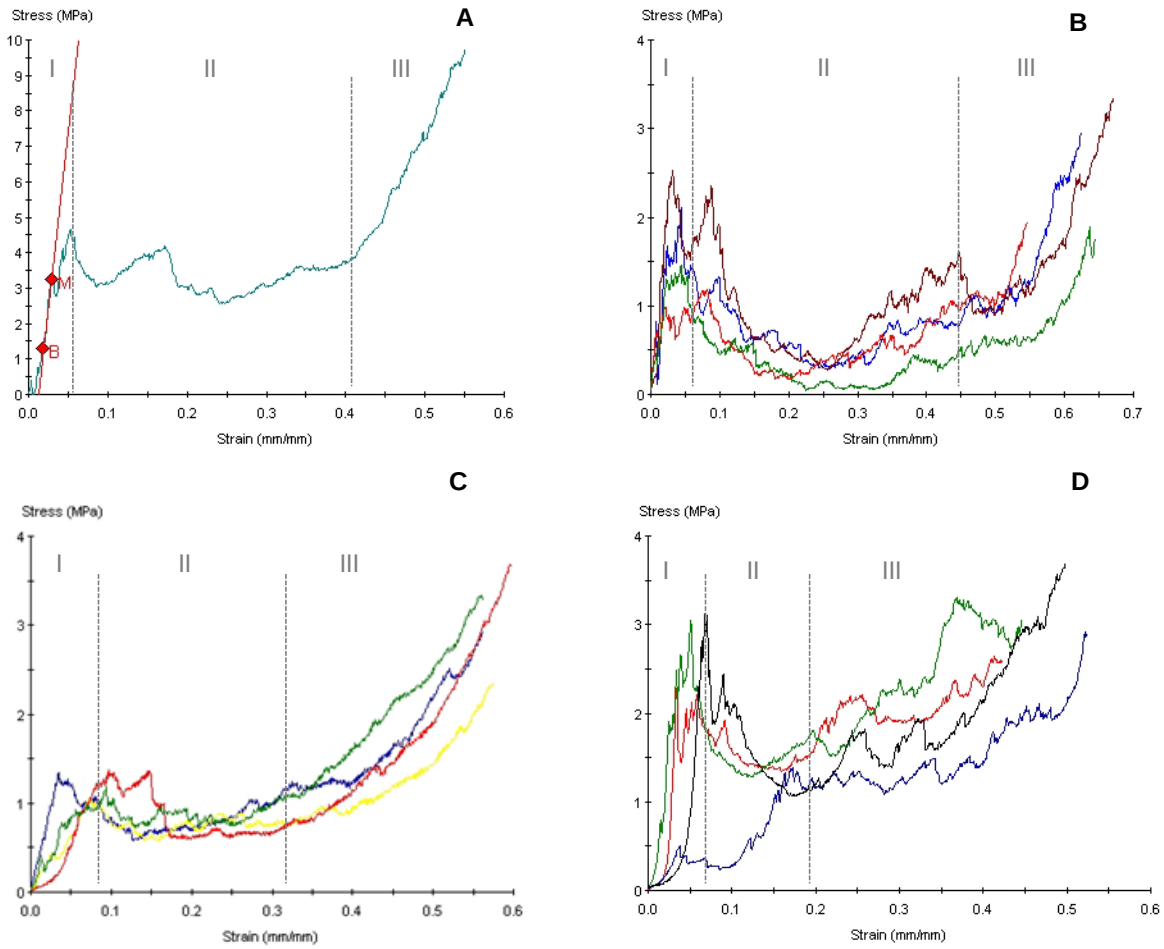


Figure 5.2: Stress-strain curve of time zero scaffold under uniaxial compression [A; 50BCP-low macroporosity-1150$^{o}$]. Scaffold failed in a manner characteristic of a brittle cellular solid, with each of the three failure regimes present: linear elastic bending [I], brittle crushing [II], and densification [III]. The modulus of the sample was taken at the slope of the linear region between points B and M [red line; A]. Curves are also shown for multiple samples of the time zero [B; HA-high macroporosity-1150$^{o}$], four week [C; TCP-high macroporosity-1100$^{o}$], and eight week [D; 50BCP-high macroporosity-1150$^{o}$] groups.

**Mean compressive strength (MPa) and modulus**

| Group (Composition-Macroporosity %-Temperature) | Compressive Strength (MPa) | Modulus (MPa) |
|---|---|---|
| TCP-30-1100 | 3.40 ± 0.87; *n=10* | 180.20 ± 66.66; *n=10* |
| TCP-30-1150 | 5.08 ± 0.82; *n=10* | 270.45 ± 74.72; *n=10* |
| TCP-50-1100 | 1.32 .± .0.29; *n=10* | 107.31 ± 39.31; *n=10* |
| TCP-50-1150 | 1.28 ± 0.35; *n=10* | 143.42 ± 59.20; *n=10* |
| 50BCP-30-1100 | 5.00 ± 1.08; *n=10* | 273.80 ± 94.62; *n=10* |
| 50BCP-30-1150 | 6.08 ± 1.21; *n=10* | 364.30 ± 63.95; *n=10* |
| 50BCP-50-1100 | 1.49 ± 0.25; *n=9* | 100.18 ± 52.36; *n=9* |
| 50BCP-50-1150 | 2.12 ± 0.38; *n=10* | 181.14 ± 60.52; *n=10* |
| HA-30-1100 | 3.15 ± 0.73; *n=10* | 142.24 ± 41.91; *n=10* |
| HA-30-1150 | 5.15 ± 0.88; *n=9* | 212.41 ± 81.53; *n=9* |
| HA-50-1100 | 1.43 ± 0.47; *n=10* | 182.29 ± 74.36; *n=10* |
| HA-50-1150 | 1.86 ± 0.69; *n=10* | 161.75 ± 83.94; *n=10* |
| Trabecular bone, human | 0.7-15 | 12.1-22.2E4 |
| Cortical bone, human | 1.43 ± 0.47; *n=10* | 10-26E4 |

Table 5.1: Mean compressive strength and modulus of various groups at baseline (time zero). Values are reported as means ±standard deviation. Data for properties of human trabecular and cortical bone are referenced.[48]

| **Mean compressive strength (MPa) values** | | | |
|---|---|---|---|
| Composition | Baseline (T=0) | T = 4 weeks | T= 8weeks |
| TCP | 175.34 ± 85.16; *n=40* | 145.64 ± 92.41; *n=14* | 188.14 ± 165.66; *n=13* |
| BCP | 233.69 ± 119.75; *n=39* | 155.92 ± 89.66; *n=13* | 187.97 ± 92.74; *n=14* |
| HA | 173.70 ± 73.93; *n=39* | 169.82 ± 131.93; *n=13* | 248.18 ± 211.31; *n=13* |
| Macroporosity | | | |
| Low | 165.68 ± 84.59; *n=60* | 176.76 ± 117.41; *n=19* | 246.43 ± 176.68; *n=19* |
| High | 222.75 ± 102.39; *n=59* | 143.29 ± 88.69; *n=20* | 168.76 ± 136.75; *n=21* |
| Temperature | | | |
| Low | 175.34 ± 85.16; *n=40* | 128.29 ± 83.22; *n=21* | 148.20 ± 100.26; *n=20* |
| High | 175.34 ± 85.16; *n=40* | 196.11 ± 115.14; *n=18* | 261.34 ± 187.09; *n=20* |

Table 5.2: Mean compressive strength of scaffolds as a function of experimental factor. Data is presented as means + standard deviations. Low and high macroporous scaffolds had 30% and 50% porosity respectively. Sintering temperatures were 1100$^{o}$C (low) and 1150$^{o}$C (high).

| **Mean stiffness (MPa) values** | | | |
|---|---|---|---|
| Composition | Baseline (T=0) | T = 4 weeks | T= 8weeks |
| TCP | 175.34 ± 85.16; *n=40* | 145.64 ± 92.41; *n=14* | 188.14 ± 165.66; *n=13* |
| BCP | 233.69 ± 119.75; *n=39* | 155.92 ± 89.66; *n=13* | 187.97 ± 92.74; *n=14* |
| HA | 173.70 ± 73.93; *n=39* | 169.82 ± 131.93; *n=13* | 248.18 ± 211.31; *n=13* |
| Macroporosity | | | |
| Low | 165.68 ± 84.59; *n=60* | 176.76 ± 117.41; *n=19* | 246.43 ± 176.68; *n=19* |
| High | 222.75 ± 102.39; *n=59* | 143.29 ± 88.69; *n=20* | 168.76 ± 136.75; *n=21* |
| Temperature | | | |
| Low | 175.34 ± 85.16; *n=40* | 128.29 ± 83.22; *n=21* | 148.20 ± 100.26; *n=20* |
| High | 175.34 ± 85.16; *n=40* | 196.11 ± 115.14; *n=18* | 261.34 ± 187.09; *n=20* |

Table 5.3: Mean stiffness of implanted scaffolds as a function of experimental factor.

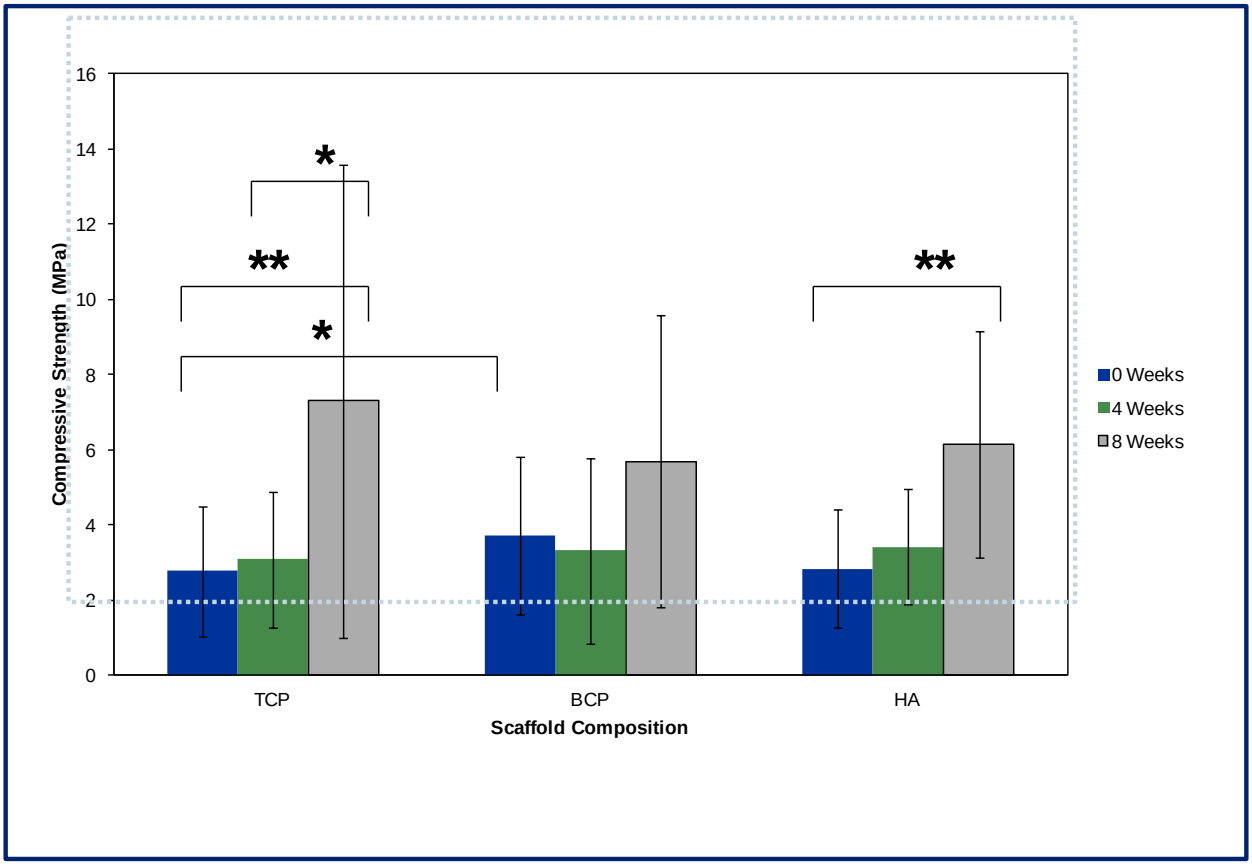


Figure 5.3: Compressive strength as a function of composition, at baseline, 4 week, and 8 week time points.

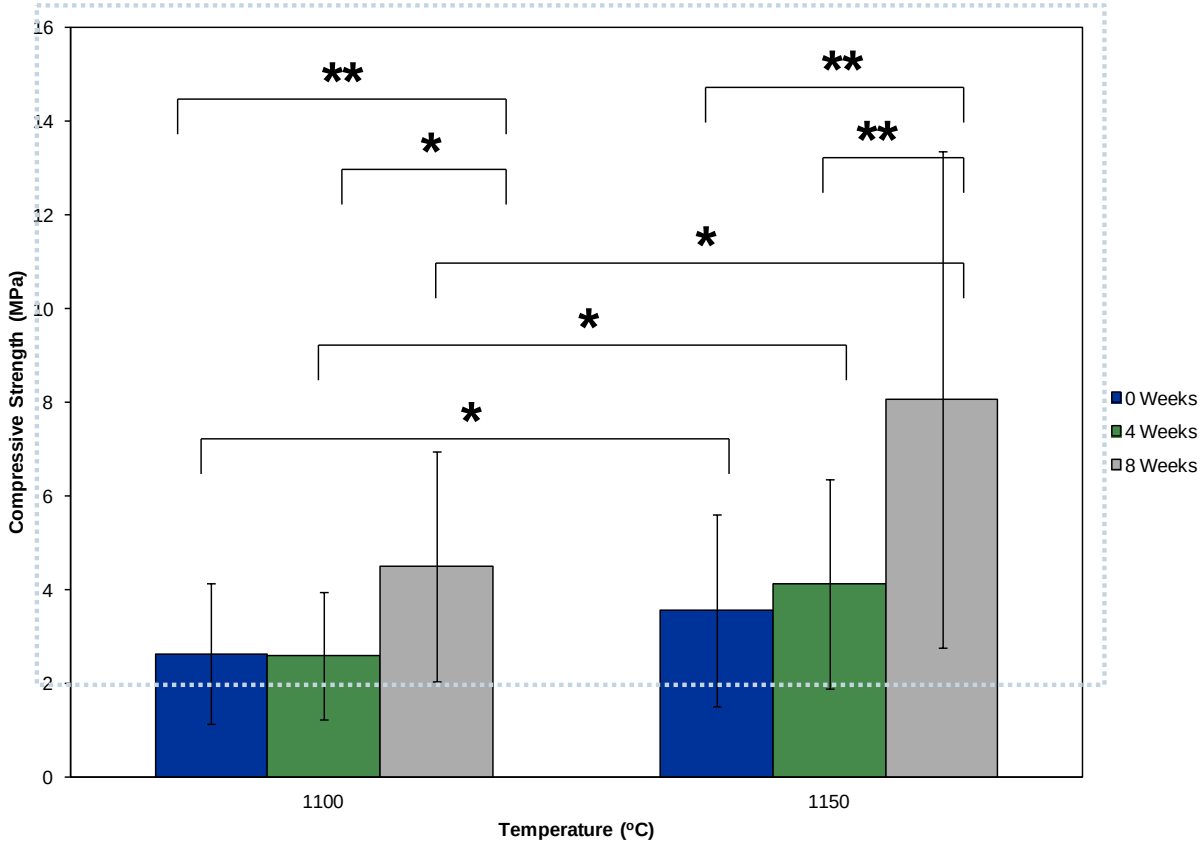


Figure 5.4: Compressive strength as a function of sintering temperature, at baseline, 4 week, and 8 week time points.

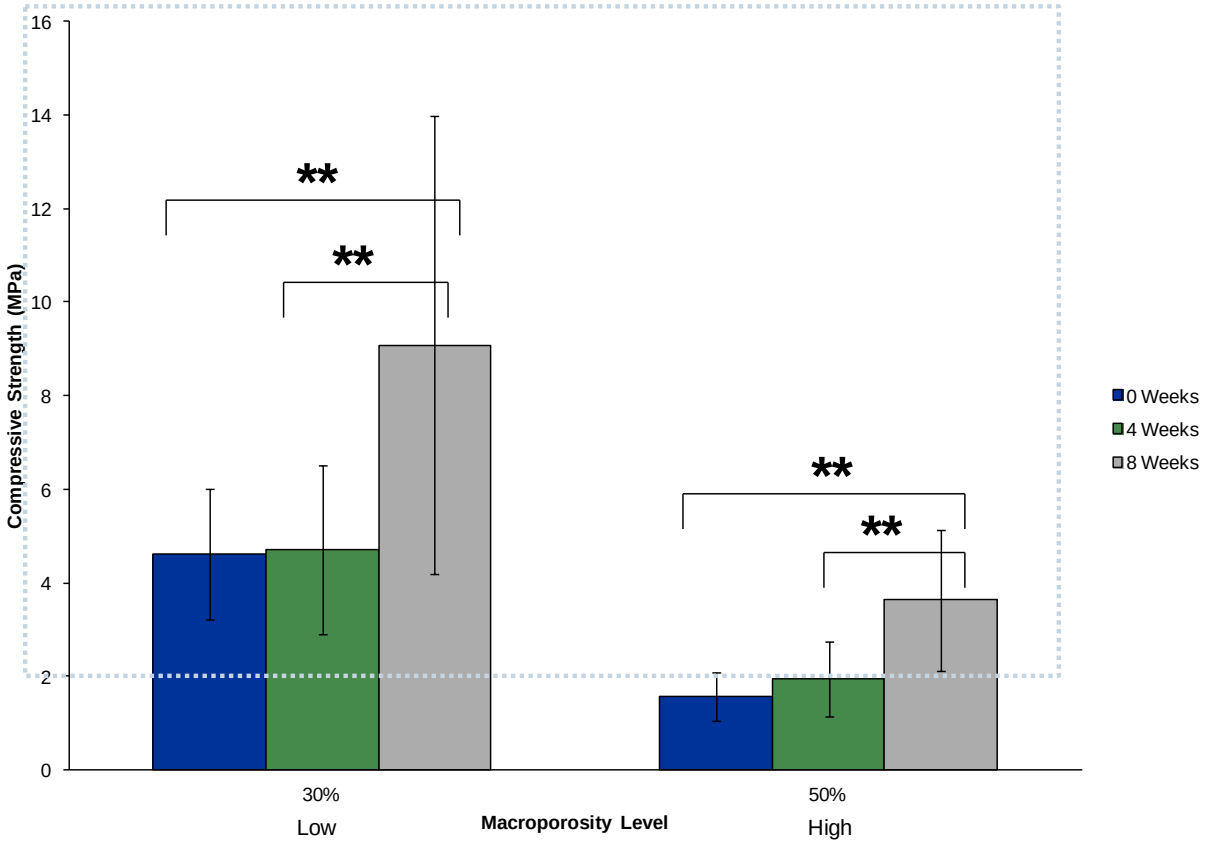


Figure 5.5 : Compressive strength as a function of macroporosity design, at baseline, 4 week, and 8 week time points.

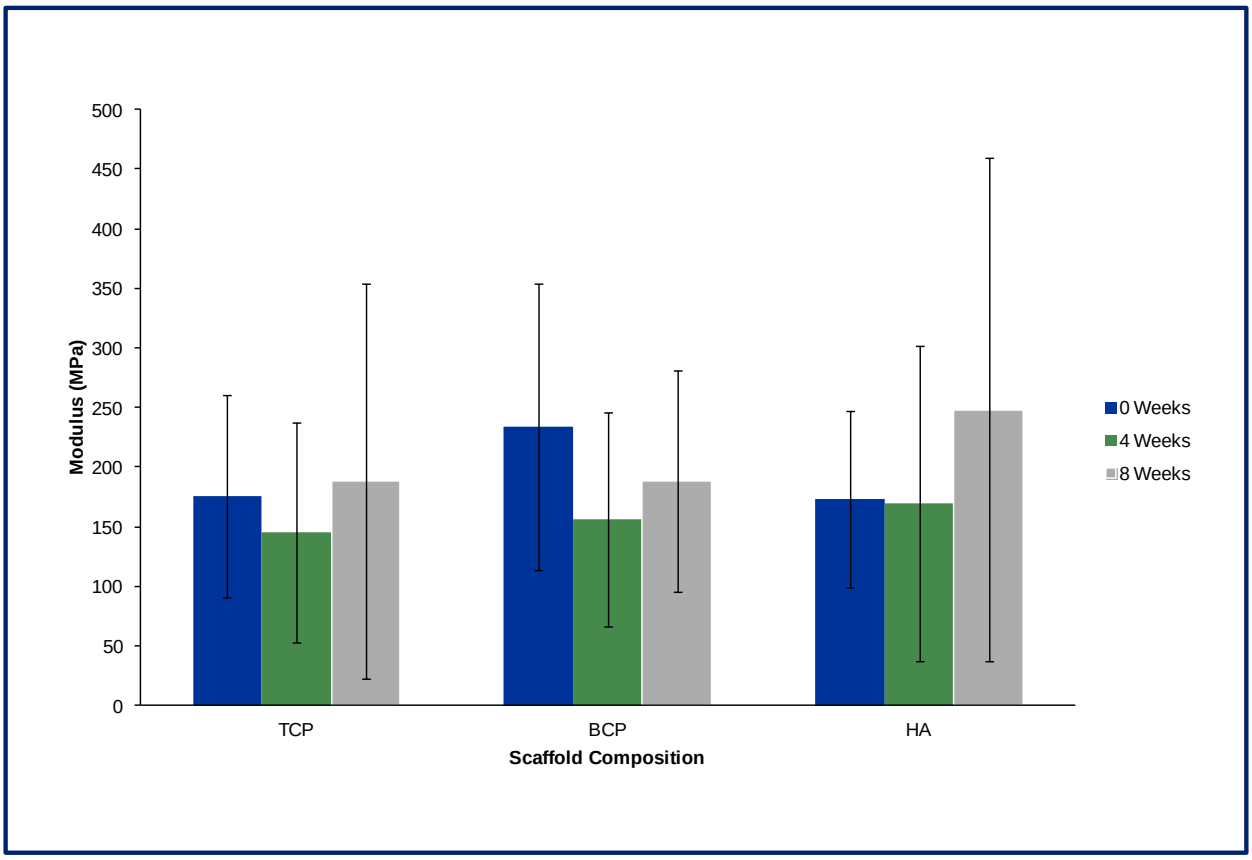


Figure 5.6 Modulus as a function of composition, at baseline, 4 week, and 8 week time points.

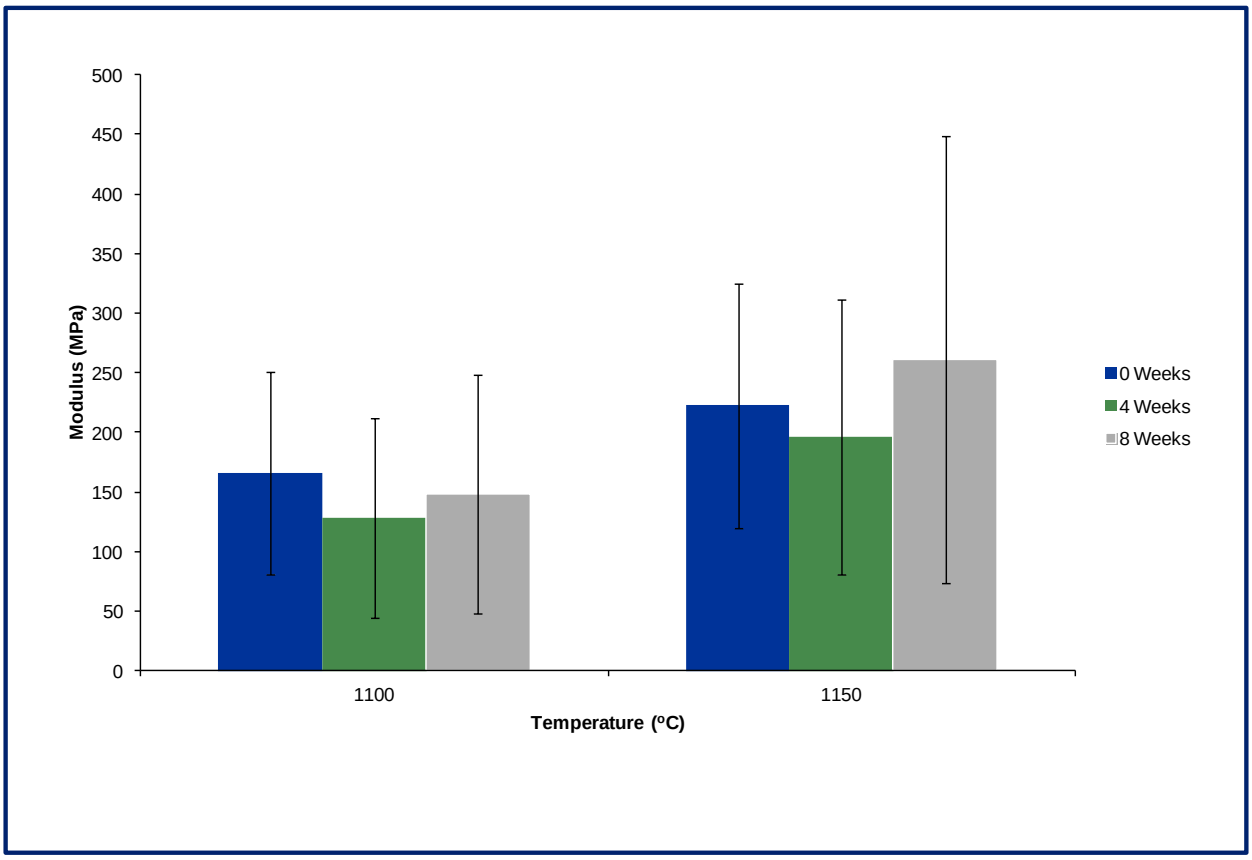


Figure 5.7 Modulus as a function of sintering temperature, at baseline, 4 week, and 8 week time points.

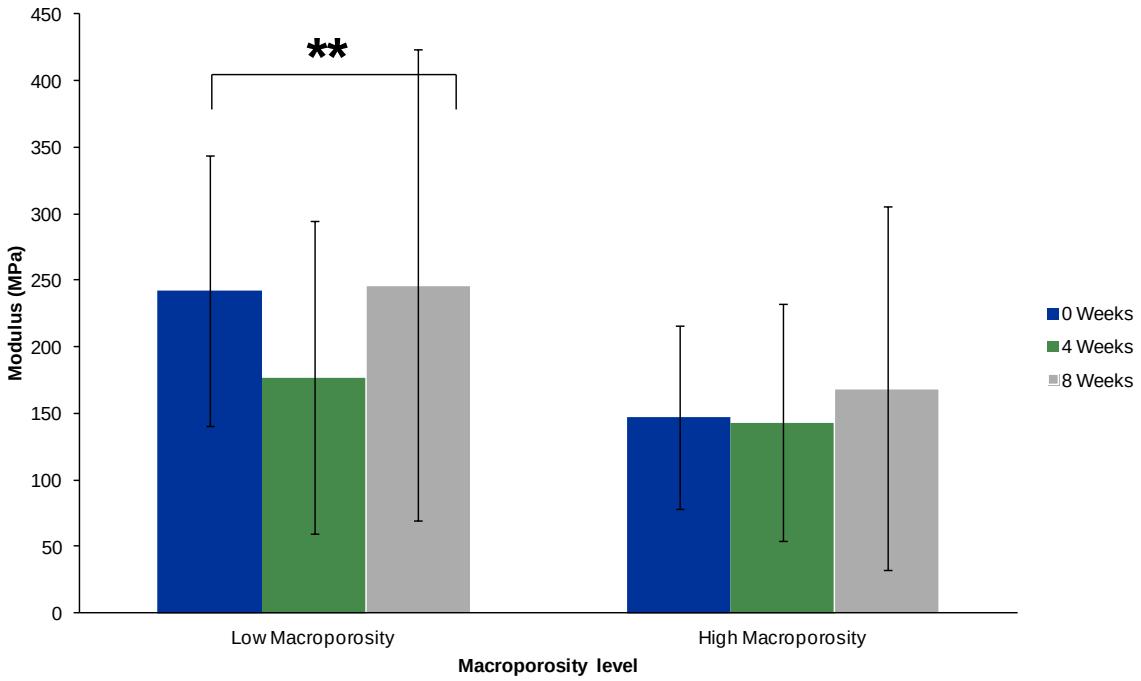


Figure 5.8: Modulus as a function of macroporosity design, at baseline, 4 week, and 8 week time points.

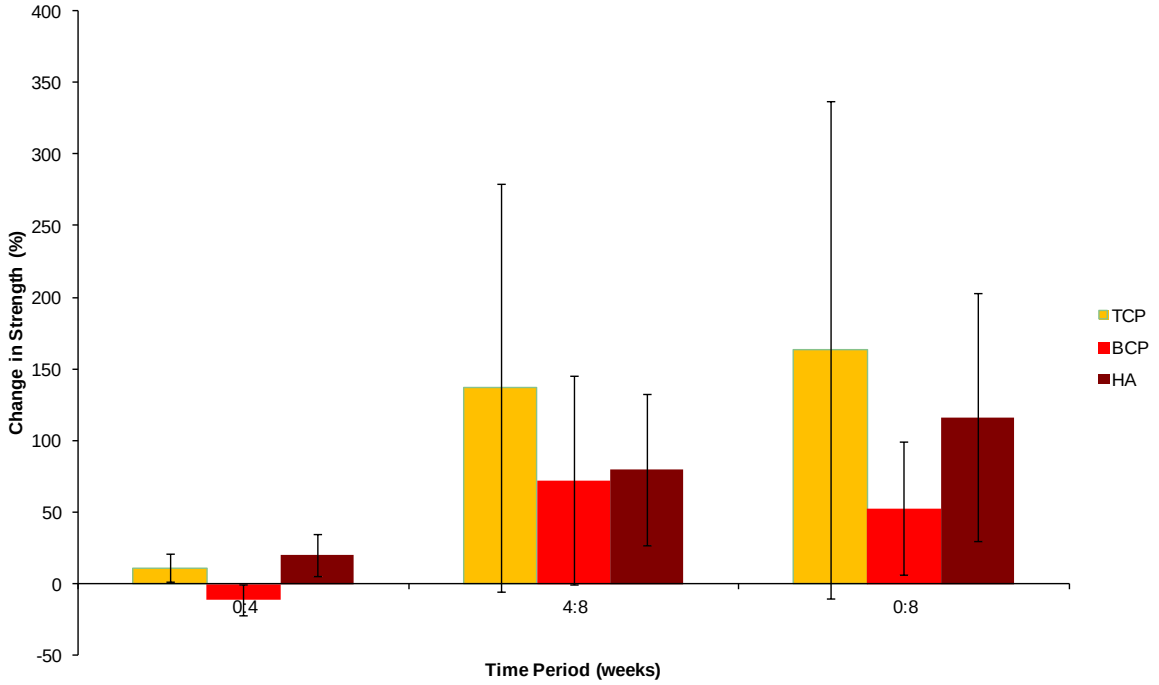


Figure 5.9 : Strength retention as a function of composition, at baseline-4 week, 4-8 week, and 0-8 week intervals.

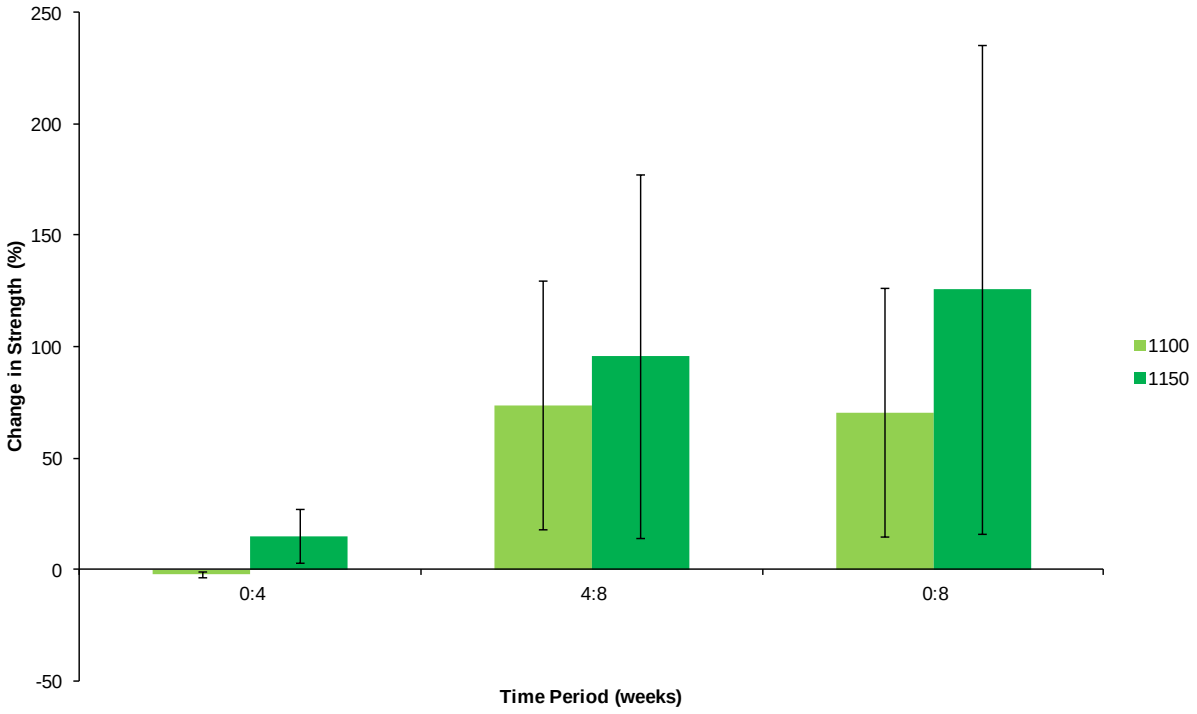


Figure 5.10: Strength retention as a function of sintering temperature, at baseline-4 week, 4-8 week, and 0-8 week intervals.

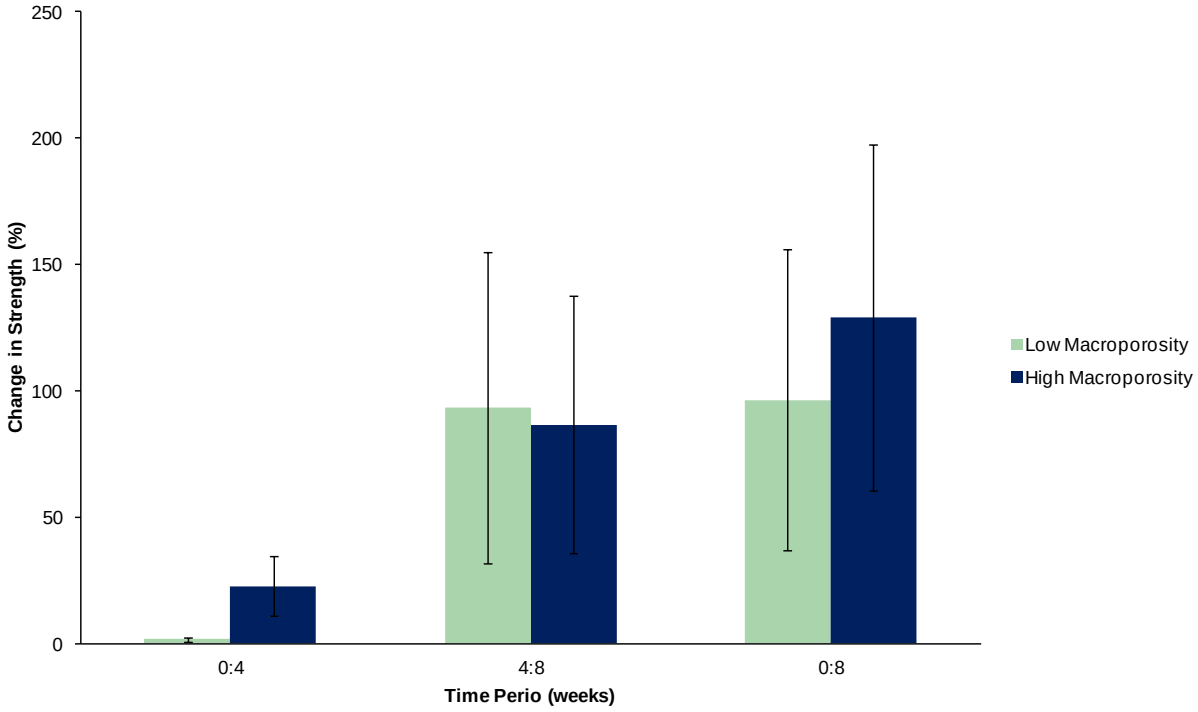


Figure 5.11: Strength retention as a function of macroporosity design, at baseline-4 week, 4-8 week, and 0-8 week intervals.

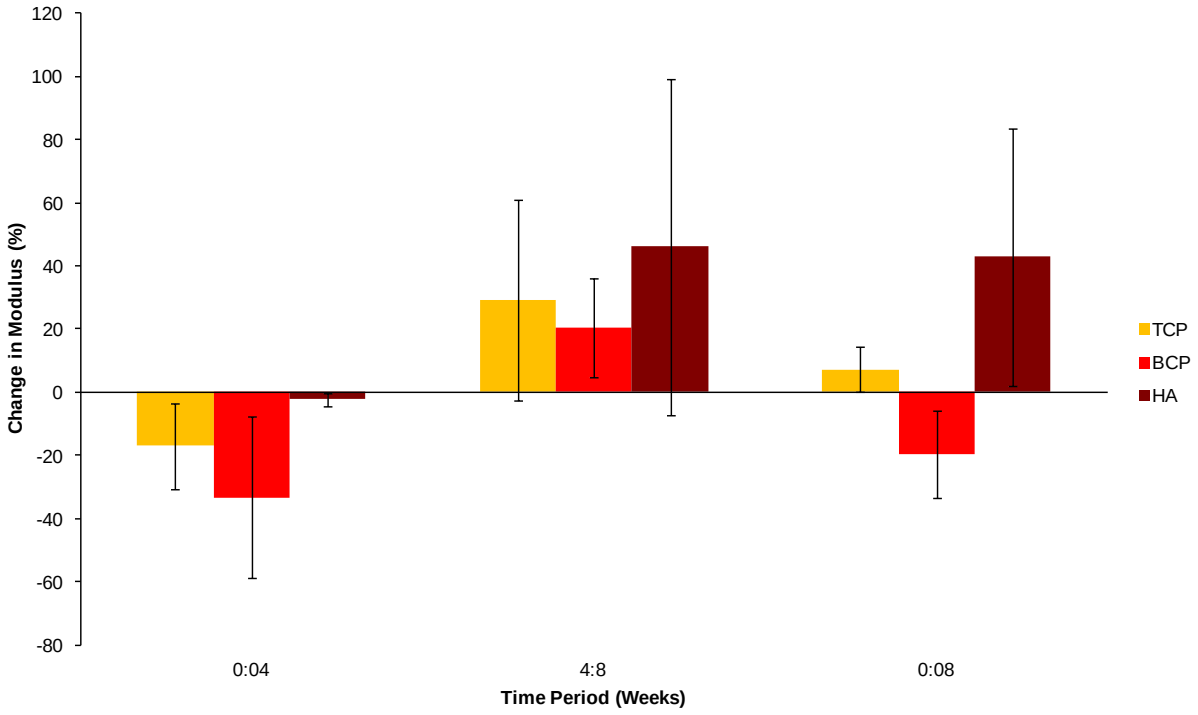


Figure 5.12: Change in modulus as a function of composition, at baseline-4 week, 4-8 week, and 0-8 week intervals.

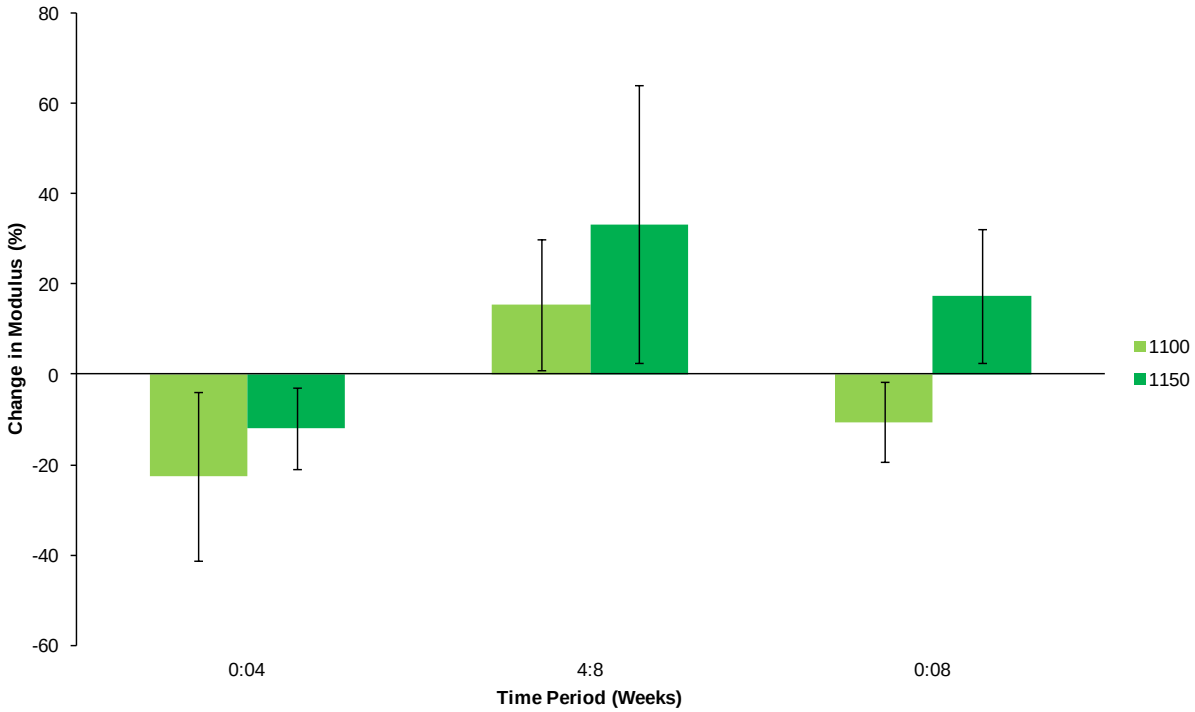


Figure 5.13: Change in modulus as a function of composition, at baseline-4 week, 4-8 week, and 0-8 week intervals.

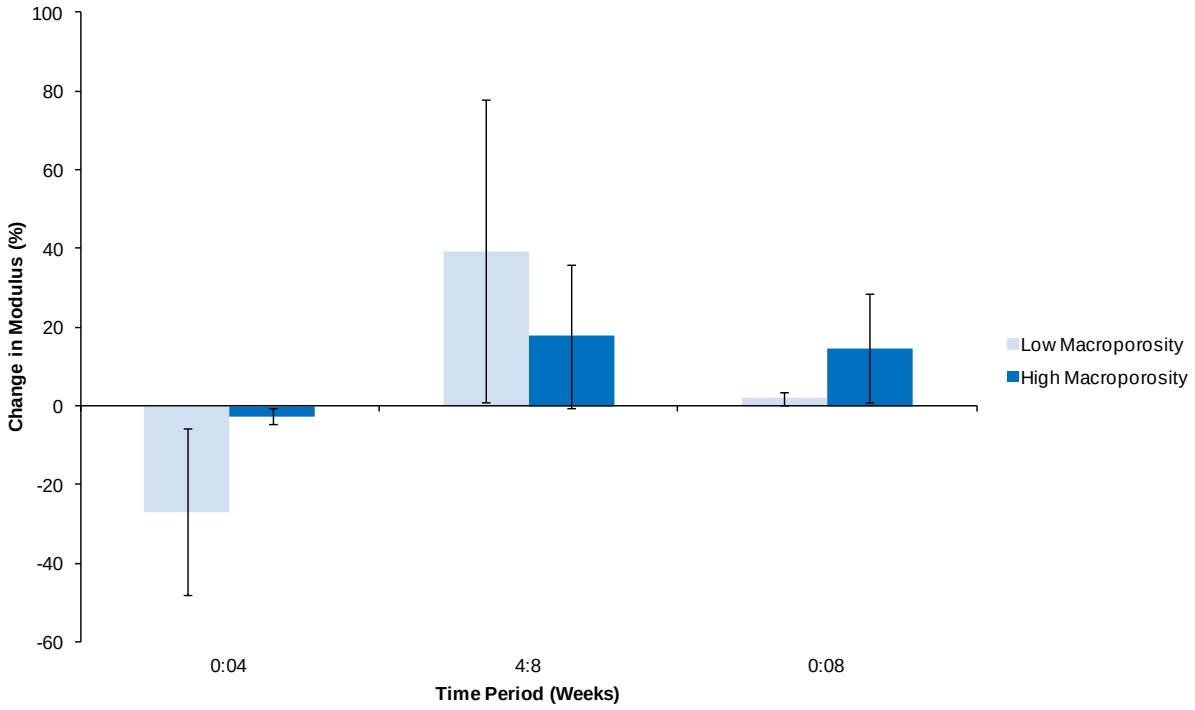


Figure 5.14: Change in modulus as a function of macroporosity design, at baseline-4 week, 4-8 week, and 0-8 week intervals.

| **Regression Model: Peak Stress (MPa) T=0** | | | |
|---|---|---|---|
| Variable | B | $SE_B$ | $\beta$ |
| (Constant) | 0.766 | 0.173 | ---- |
| HA | 0.122 | 0.189 | 0.031 |
| BCP | 0.907 | 0.189 | 0.232* |
| Low Macroporosity | 3.053 | 0.155 | 0.828* |
| High Temperature | 0.954 | 0.155 | 0.259* |

*p < 0.0001; B = unstandardized regression coefficient; $SE_B$ = Standard error of the coefficient; $\beta$ = standardized coefficient

Table 5.4: Regress model coefficients: Peak Stress at time zero

| **Regression Model: Modulus (MPa) T=0** | | | |
|---|---|---|---|
| Variable | B | $SE_B$ | $\beta$ |
| (Constant) | 99.387 | 15.967 | |
| HA | 0.307 | 17.481 | 0.001 |
| BCP | 56.401 | 17.481 | 0.271* |
| Low Macroporosity | 93.945 | 14.306 | 0.481* |
| High Temperature | 57.969 | 14.306 | 0.297* |

Table 5.5: Regress model coefficients: Modulus at time zero

| **Regression Model: Peak Stress (MPa) T=8** | | | |
|---|---|---|---|
| Variable | B | $SE_B$ | $\beta$ |
| (Constant) | 3.040 | 1.141 | ---- |
| HA | -1.311 | 1.270 | -0.138 |
| BCP | -1.914 | 1.243 | -0.205 |
| Low Macroporosity | 5.355 | 1.023 | 0.601* |
| High Temperature | 3.306 | 1.027 | 0.370* |

Table 5.6: Regress model coefficients: Peak Stress at eight weeks

| **Regression Model: Modulus (MPa) T=4** | | | |
|---|---|---|---|
| Variable | B | $SE_B$ | $\beta$ |
| (Constant) | 105.646 | 33.916 | ---- |
| HA | 22.714 | 39.220 | 0.104 |
| BCP | 7.197 | 39.214 | 0.033 |
| Low Macroporosity | 21.000 | 32.397 | 0.102 |
| High Temperature | 68.830 | 32.513 | 0.334* |

Table 5.7: Regress model coefficients: Modulus at four weeks

| **Regression Model: Modulus (MPa) T=0** | | | |
|---|---|---|---|
| Variable | B | $SE_B$ | $\beta$ |
| (Constant) | 99.387 | 15.967 | |
| HA | 0.307 | 17.481 | 0.001 |
| BCP | 56.401 | 17.481 | 0.271* |
| Low Macroporosity | 93.945 | 14.306 | 0.481* |
| High Temperature | 57.969 | 14.306 | 0.297* |

Table 5.8: Regress model coefficients: Modulus at time zero

| **Regression Model: Modulus (MPa) T=4** | | | |
|---|---|---|---|
| Variable | B | $SE_B$ | $\beta$ |
| (Constant) | 105.646 | 33.916 | ---- |
| HA | 22.714 | 39.220 | 0.104 |
| BCP | 7.197 | 39.214 | 0.033 |
| Low Macroporosity | 21.000 | 32.397 | 0.102 |
| High Temperature | 68.830 | 32.513 | 0.334* |

Table 5.9: Regress model coefficients: Modulus at four weeks

| **Regression Model: Modulus (MPa) T=8** | | | |
|---|---|---|---|
| Variable | B | $SE_B$ | $\beta$ |
| (Constant) | 94.298 | 53.118 | ---- |
| HA | 63.628 | 59.159 | 0.188 |
| BCP | -6.618 | 57.904 | -0.020 |
| Low Macroporosity | 68.710 | 47.663 | 0.216 |
| High Temperature | 115.389 | 47.835 | 0.363* |

Table 5.10: Regress model coefficients: Modulus at eight weeks

# CHAPTER 6
# INFLUENCE OF COMPOSITION, SINTERING TEMPERATURE, AND MACROPOROSITY ON BONE REGENERATION VIA CALCIUM PHOSPHATE SCAFFOLDS

*"There are three principle means of acquiring knowledge: observation of nature, reflection, and experimentation. Observation collects facts; reflection combines them; experimentation verifies the result of that combination".*

*-Denis Diderot*

## 6.1 Enhancing Bone Regeneration Through the Design of Scaffold Properties

Engineering effective scaffolds depends on one's ability to identify and control important parameters related to scaffold architecture and its impact on tissue regeneration. Knowledge of a material's structural, mechanical, and degradation bulk properties a priori and the subsequent application of that knowledge to the fabrication of degradable scaffolds that match predetermined requirements would be valuable and is indeed possible. Similarly, knowledge of a tissue's growth rate and changes in mechanical property as a result of regeneration, for example, would aid in the production of a scaffold demonstrating tissue specificity. In this regard, further understandings of the processes through which we may control scaffold properties during degradation and regeneration has clear value and urgency.

Collectively, prior chapters averted to the foundation from which we begin when we speak about biomaterials applications to tissue engineering problems. In addition to providing an understanding of bone's biological and materials properties and their relationship to the functioning bio-system as a whole, chapter two addressed the plethora of biomaterials identified as suitable for scaffold applications. Of these, CaP materials have been favored because of their strong bonding with the mineral phase of bone, and have often been integrated into the chemistry of other materials, as fillers, [233-234] and coatings,[55, 235-239] for example, to ensure adequate material-tissue interfacing and enhance osteogenic potential. The materials properties of this family of ceramics vary according to the chemical composition employed. Chapters three and four characterized the bulk material and scaffold designs used in this study, as well as discussed the important architectural features of scaffolds—well-identified and well-investigated;[28, 35, 37, 40, 42, 142-143] including, but not limited to, pore size, porosity, permeability, interconnectivity, and fenestration; all of which have been investigated in several tissue types including cerebral,[142-143, 240-242] cardiovascular,[243-245] cartilage,[149, 246] and bone.[151, 247-251] For the regeneration of bone, specifically, it has been noted that pore size[219, 252] and surface roughness[110, 253-254] are influential in encouraging the attachment, proliferation, and differentiation of both osteoblasts and progenitor cells. Chapters four and five demonstrated that the mechanical and degradation properties of CaP materials are highly influential in the decisions regarding their use and, hence, are a major consideration in material choice. Resorption proceeds from least to most

resorptive according to HA< Ca-deficient HA< oxyHA< β-TCP< α-TCP < tetraTCP [152, 255] (in other words, HA << β-TCP< α-TCP); and is highly dependent on its processing parameters. Mechanical properties, on the other hand, vary according to material structure, i.e., density, pore size, shape, and interconnectedness; and both dissolution and mechanics are fabrication-dependent.

Given these points of consideration, we assert that the dynamics of CaP scaffolds can change as a function of changing properties, and inductively argue that different requirements, in terms of initial architectural features and properties, may be needed to account for the scaffold's effective properties. That is, the most effective architecture may demonstrate a composition-dependency, and the scaffold architecture that best serves HA may not be the optimal for TCP. Also, we postulate that, given similarities in properties due to composition, there exists a degree of manipulation of scaffold features that can equalize the regeneration potential of various CaP compositions. Such information in the literature, to date, is non-existent. Therefore, the goal of the work presented in this chapter is to elucidate the effect of macroporosity, sintering temperature, and composition on bone regeneration via calcium phosphate scaffolds, and to determine, if possible, the extent to which these scaffold criterions can be manipulated to encourage better bone regeneration. We address these goals through the pursuit of answers to the following questions:

*How do the chemical composition and microstructure influence the regeneration potential of our scaffolds?*

*How is the regeneration potential influenced by the design parameter, macroporosity?*

*Of the parameters under consideration, i.e., microporosity, macroporosity, and composition, which is most important?*

*Is there a difference in bone quality as a result of any parameters investigated?*

We hypothesize that ***favorable bone regeneration can be achieved through optimization of composition, scaffold architecture, and microporosity.*** More specifically, for high β-TCP constructs, the balance of ingrowth and retention of scaffold structure is maintained by low overall scaffold porosity in order to accommodate for fast degradation rates. Additionally, we hypothesize the existence of an ideal composition-porosity relationship that maximizes tissue ingrowth generated from a given calcium phosphate composition.

Micro-computed tomography was used to analyze the influences of these factors on bone volume and structural quality at the early time-point of four weeks. Three compositions of calcium-based ceramics (hydroxyapatite, β-tricalcium phosphate, and a 50/50 biphasic combination of the two) were considered, as well as two designed macroporosities, and two sintering temperatures. Bone regeneration was realized using

an established model of *in vivo* bone formation utilizing *ex vivo* gene therapy in a murine model.

## 6.2 Materials and Methods

### 6.2.1 Biomaterial fabrication

Cylindrical porous implants were produced by solid free-form fabrication methods previously reported in Chapter 4. As stated, scaffolds with controlled architecture were designed with square orthogonal interconnected 600μm pores, and either 1266 or 550 μm struts to produce 30% and 50% macroporosity respectively, and an overall average measurement of 3 mm height x 6 mm diameter. 40 vol % ceramic slips were prepared by methods previously described, also in Chapter 4. The slurry was cast into the designed wax molds; which, after curing in a nitrogen-rich environment, were dissolved in ethanol. After binder burnout, scaffolds were sintered in air at 1100$^{o}$C and 1150$^{o}$C for 5 hours and furnace cooled. Prior to implantation, scaffolds were sterilized in 70% ethanol and sterile distilled water for 24 hours respectively. After sterilization, scaffolds were immersed in serum-containing alpha-minimum essential medium (α-MEM) media for a minimum of three hours.

### 6.2.2 Ex vivo gene therapy and ectopic bone formation assay in SCID mice

Primary human gingival fibroblasts (HGFs) were explanted from human surgical waste in compliance with the University of Michigan Institutional Review Board. HGFs were isolated and cultured in polystyrene flasks containing $\alpha$-MEM media supplemented with 10% fetal bovine serum and 1% penicillin-streptomycin (Gibco, Grand Island NY, USA). Passage-9 cells were infected with a first generation recombinant adenovirus expressing murine bone morphogenic protein 7 (BMP-7) under a CMV promoter, AdCMV-BMP-7. The infection was performed over a 24-hour period using a concentration of 500 plaque-forming units per cell. A fibrin hydrogel was used as a secondary carrier for cell seeding. Transduced HGFs were suspended in a gel made from 5mg/ml fibrinogen dissolved in cell culture medium. Immediately prior to seeding, media-saturated scaffolds were placed into a tight-fitting 96-well culture plate using sterile forceps. 60 $\mu$L and 90 $\mu$L of fibrinogen containing 2 million cells were pipetted onto each 30% and 50% macroporosity scaffold design, respectively. 3$\mu$L and 4.5$\mu$L of thrombin solution (thrombin dissolved in Hanks Balanced Salt Solution at 100U/ml) were added to each porosity design respectively. The difference in the volume of fibrinogen and thrombin used reflects the porosity differences between the two designs. These amounts appropriately filled the volume of the scaffolds with a minimum upper and lower gel layer surrounding each scaffold, thereby ensuring cellular penetration into scaffold pores. Forty-eight scaffolds were used in this study; thirty-six of which were each seeded with 2 million transduced HGFs, twelve remained empty and served as controls. The scaffolds used were combinations of varying compositions,

macroporosities, and sintering temperatures, comprising a total of 12 groups (Table 6.1). The location of each scaffold (upper left, upper right, lower left, lower right) was determined using randomized selection methods but optimized such that the location of the scaffold was not an additional variable for consideration. Twelve five-to-eight-week-old immunocompromised mice (N: NIH-bg-nu-xid; Charles River, Willington, MA) were anesthetized with intraperitoneal injections of 80μL of ketamine/xylazine in HBSS (0.3mL ketamine, 0.2 mL xylazine, 0.5 mL HBSS). Midline longitudinal skin incisions, roughly 1 cm in length, were made on the dorsal surface of each mouse and four subcutaneous pockets were created laterally using blunt dissection. One scaffold was placed into each pocket, for a total of four scaffolds per mouse. The incision sites were closed using surgical staples.

### 6.2.3 Histology and Post-surgical processing

Four weeks post-implantation, mice were euthanized by inhalation of carbon dioxide, in accordance with the institutional guidelines for animal use of the University of Michigan. Transplants with surrounding tissue were explanted by sharp dissection and fixed in a buffered zinc formalin solution (ZFix; Anatech, Ltd, Battlecreek, MI) for 24 hours, rinsed in distilled water for 24 hours, and stored in 70% ethanol. Prior to processing for histological analysis, specimens (scaffolds plus newly formed bone) were imaged using a μCT system (MS-130, GE Healthcare Systems) operated at 100 kVP, 110 μA with 3000 msec integration time. Specimens were later decalcified for histological evaluation.

In short, samples were agitated in a rapid bone decalcifier (RDO, APEX Engineering Products Corporation, Plainfield, IL) for up to 4 hours, stored in ethanol until paraffin embedding. After sectioning, sections were stained with hematoxylin-eosin (H&E) or Masson's trichrome to highlight bony incidence. H&E staining is the most commonly used basic stain for histology sections. The hematoxylin component stains cellular nuclei blue. A counter stain using eosin follows and colors eosinophilic structures various shades of red, orange, and pink. In H&E stained sections, bone appears pinkish-purple. Masson's trichrome is a three-stain protocol used to visualize connective tissue and distinguish it from surrounding cellular components. In this staining methodology, collagen (and other connective tissues) stain blue or green, keratin and muscle fibers stain red, cytoplasm stains pink, and cell nuclei stain dark brown. In bone histology, collagen and newly deposited bone appear blue, while remodeled and lamellar bone appears bright red.

### 6.2.4 Microcomputed tomography image analysis

The aforementioned commercial μCT system utilizes a micro-focus cone beam X-ray source, with data being acquired with an isotropic voxel size of 16 μm. Hounsfield unit calibration was performed with a phantom containing water, air, and a cortical bone mimic. Using a Feldkamp cone beam reconstruction algorithm, a 3-dimensional representation of the image was used to evaluate tissue regeneration. Analysis was conducted using MicroView 2.1.2 software (www.microview.sourceforge.net) from which

a uniform threshold value and region of interest (ROI) were used to detect new bone: threshold values of 2500 and 950 were used for scaffold and neo-bone respectively. In order to assess the degree of new bone formation, the scaffold region was removed (Figure 6.1) from the image datasets using Analyze 8.1 software (Mayo Clinic, AnalyzeDirect.com) prior to the quantitative bone analysis. Three-dimensional datasets were analyzed for several bone mineral density (BMD) indices, including bone volume (BV), tissue mineral content (TMC), tissue mineral density (TMD), and bony ingrowth of the newly formed bone, normalized for the maximum volume[x] of the scaffold. In order to achieve this goal, a cylindrical region of interest (ROI) was used for analyses (Figure 6.2A-G). For analyses of total bone, the ROI exceeded the scaffold boundaries, and included all new bone, internal and external to the scaffold (Figure 6.2B). For infiltrated bone analyses, the ROI was bound by the dimensions of the scaffold (Figure 6.2C). In order to assess the degree to which bone was able to penetrate the scaffold, lesser concentric ROIs were constructed by reducing the initial infiltration ROI by a fixed amount. Because scaffold dimensions differ due to differences in shrinkage, a function of composition and thermal treatment, a consistently sized ROI could not be used, and therefore consistent penetration ROIs could not be utilized. In order to compensate

[x] Maximum volume of the scaffold = $volume\ of\ scaffold \times porosity\ of\ scaffold$. With this methodology, each scaffold's dimensions were considered, rendering 33 possible unique values, and thereby adjusting for any differences due to fabrication defects.

and have all analyses on equal par, the smallest scaffold dimensions were divided into 4 equal parts, determining the step size of decreasing radii. This produced four regions for consideration, progressing from the outside of the scaffold to its center: $C_o$, the initial infiltration radius (Figure 6.2C); region 1 ($C_1$), has a radius one step less than that of $C_o$ (Figure 7.2D); region 2 ($C_2$), has a radius two steps less than $C_o$ (Figure 6.2E); and region 3 ($C_3$), has a radius three steps less than $C_o$ (Figure 6.2F), where the radius step size was 0.714 mm. Scaffolds larger in size also had 1-2 additional regions. For ease of comparison, results are discussed as they apply to $C_1$-$C_3$: $C_1$ resides 0.71 mm from the outer edge of the scaffold; $C_2$, 1.42 mm from the outer edge, and $C_3$, 2.13 mm away.

In order to assess the level of penetration within the scaffold, an analysis of rings was also employed (Figure 6.3 A-E), in which each ring was the difference between successive cylindrical regions: progressing from the outside of the scaffold to its center: $Ring_1$, comprised of the edge of the scaffold through 0.071 mm into the scaffold interior (Figure 6.3 C); $Ring_2$, 0.071-1.42 mm into the scaffold interior (Figure 6.3D); and $Ring_3$, 1.42-2.13 mm into the scaffold interior (Figure 6.3E). Bone mineral density (BMD) indices were calculated for each region according to:

$$BV_{Ring_j} = BV_{C_{j-1}} - BV_{C_j}$$

$$TMC_{Ring_j} = TMC_{C_{j-1}} - TMC_{C_j}$$

$$TMD_{Ring_j} = \frac{TMC_{Ring_j}}{BV_{Ring_j}}$$

When analyzing for penetration depth, the ring ingrowth was calculated according to:

$$Ingrowth_{Ring_j} = \frac{BV_{C_{j-1}} - BV_{C_j}}{MPV_{C_{j-1}} - MPV_{C_j}}$$

where MPV, maximum pore volume, is calculated according to:

$$MPV_{C_i} = Volume\ C_i * Porosity\ C_i$$

Trabecular thickness, trabecular spacing, and structure model index were obtained using the same ROI schema and the advanced bone analysis tool in MicroView.

### 6.2.5 Statistical analysis

Statistical calculations were performed using PASW18. A linear regression model was used to analyze all μCT data. The main effects of composition, macroporosity, and sintering temperature, as well as the interaction effects of composition-macroporosity, composition-temperature, and temperature-macroporosity, were evaluated. Data is

reported as the arithmetic mean ± standard deviation; graphically represented as arithmetic mean ± standard error. Statistical significance was considered for p values ≤ 0.05.

## 6.3 Results

In this study we used two architectures and three compositions of calcium phosphate scaffolds to assess the influence of design and fabrication parameters on bone regeneration in an *in vivo* model. μCT was used to determine the influence of composition, sintering temperature, and macroporosity on (1) overall bone regeneration, and (2) neo-bone quality. The analyses of these parameters were based on traditional μCT indices of bone mineral quality: bone volume (BV), tissue mineral content (TMC), tissue mineral density (TMD); and bone structural quality indices: structure model index (SMI), trabecular thickness (Tb.Th.), and trabecular spacing (Tb.Sp.).

### 6.3.1 Histological Evaluation of Bone Formation

One animal was lost due to complications arising from surgery. As a result, data from three tissue-containing scaffolds were not introduced in this study. Of the remaining animals, no complications were evident and all implants were successfully retrieved. At

retrieval, cell-containing implants were surrounded by well-vascularized tissue boluses reddish-purple in color; empty scaffolds contained thinner tissue with a much lesser degree of vascularization. There was no evidence of an inflammatory response or toxicity toward any of the implants utilized.

All scaffolds implanted with cells produced bone, and there was no evidence of cross-communication between scaffolds with cells and those without. Bony incidence was both internal and external to the scaffold, forming a cortical shell surrounding the outer scaffold surface (Figure 6.4-6.7); distance of the boney shell from the scaffold differed and did not seem to be dependent on any of the factors tested for in this model. Two instances occurred in which cell-containing scaffolds on opposing lateral sides of the anterior end formed a bony bridge across the dorsal area. It was determined that during the time course of the investigation, 4 weeks, the scaffolds may have migrated closer to the dorsal side and cells were in close enough proximity to produce large amounts of connecting bone. In these instances, the bridge was cut in half and processed under each relevant scaffold.

Upon visual inspection, there appeared to be no bone regeneration dependency on composition or sintering temperature. Higher macroporosities seemed to have more bone infiltrating the pores. The morphology of the neobone was normal in appearance, indicating the presence of osteoblasts aligning the implant pore surface, osteoid,

osteocytes, marrow space, and mineralized bone tissue (Figures 6.8). There were also areas of soft tissue constituting muscle, believed to have derived from areas of the scaffolds that were in contact with muscle during implantation; these instances, however were not commonplace. Also, there were no visible signs of scaffold damage or large-scale degradation of any of the samples.

### 6.3.2 Quantifying Bone Formation: Mineral Quality Indices

The analysis of bone regeneration was considered from two perspectives: total bone regeneration, inclusive of all bony growth internal and external to the scaffold, and infiltrated bone regeneration, characterized by the amount of bone growth internal to the scaffold boundaries. Data is presented in Appendix 1.

#### 6.3.2.1 Total Regeneration

The total volume of bone produced, internal and external to the scaffold boundaries, was influenced by the scaffold's macroporosity: the lesser macroporosity design (30%) produced statistically significant more bone than the higher macroporosity design (50%) ($p \leq 0.05$), whereas there was no statistical difference in the volume of bone as a function of composition or sintering temperature. Tissue mineral content did not differ according composition, sintering temperature, or macroporosity. Tissue mineral density,

unaffected by sintering temperature or macroporosity, was influenced by composition: the mineral density of TCP was statistically different from the 50/50 biphasic composition ($p \leq 0.05$), though similar in values to those values produced by HA scaffolds (Figure 6.9-6.11).

### 6.3.2.2 Scaffold Infiltration

The degree of regeneration internal to the scaffold boundaries was analyzed after the removal of the scaffold construct to reduce any interference from the mineralized scaffold. In these cases, the volume of bone was not dependent on the composition or sintering temperature, but was dependent on macroporosity ($p \leq 0.01$), where higher macroporosities supported more internal bone volume. TMC values were higher for high macroporosity scaffolds ($p \leq 0.01$), and TCP compositions compared to the biphasic group ($p \leq 0.05$), but similar in value to the HA groups; TMC was unaffected by microporosity due to sintering temperature. TMD values demonstrated no composition dependency, with the TCP compositions performed on par with HA ($p=0.95$) and better than the 50/50 biphasic groups ($p= 0.65$).

Examination of the concentric ring ROIs reveals similar patterns to the overall internal regeneration (Figure 6.12-6.14). The significant influence of macroporosity on bone volume is most evident in ring 2 (0.71-1.42 mm into the interior of the scaffold). TMC

shows significance due to composition for all ring regions, with TCP generating more mineral in the first 1.42mm of the scaffold. Additionally, TMC may have a dependence on macroporosity as well: high macroporosity scaffolds produce more mineral content in rings 1 and 2, with R2 being significant ($p < 0.001$). Compositional dependency of TMD may suggested, in that TCP produces denser mineral than both HA and biphasic compositions, though not significantly so. R1: p=0.052, p=0.128; R2: p=0.074, p=0.271; R1: p=0.093, p=0.302 for biphasic and HA compositions respectively.

Ring analysis allows for the assessment of neobone penetration into the scaffold, and differs from cylinder analysis in that it allows for inspection within segmented, unrepeated, scaffold regions. As with cylinder analysis, there were decreasing amounts of bone (volume and mineral) with progressive steps into the scaffold, and a seemingly steady-state of mineral density across all ring regions. Other discoveries to be confirmed were the lack of dependency of bone regeneration and mineral density on the composition or microporosity of the scaffold; whereas macroporosity's influence remained evident. Mineral content appears to be influenced by composition, with TCP faring better than the other compositions.

#### 6.3.2.3 Ingrowth

When normalized for maximum available pore volume, infiltrated bone volume can be used to assess total bone ingrowth (%). Ingrowth was significantly influenced by macroporosity: the lesser porosity design had statistically more ingrowth than the higher macroporosity design ($p < 0.001$); a result which is in diametric contradiction to the infiltrated group. Furthermore, ring analysis demonstrates that this behavior persists across all three ring regions ($p \leq 0.001$, $p \leq 0.05$, $p \leq 0.01$ for rings 1 -3 respectively), indicating the scaffold's ability to sustain regeneration within the scaffold interior (Figure 6.15).

Ingrowth due to composition peaks with TCP scaffolds in all three rings, though no significance is achieved; similarly, the lesser microporosity group (high sintering temperature) demonstrates more ingrowth in each region, but, again, no level of significance was seen. These results, consistent ingrowth with composition and sintering temperature, reveal that all levels of both factors had similar influence on bone growth within the scaffold confines.

In regard to either method of analysis, cylindrical or ring, ingrowth was determined to be significantly influenced by macroporosity: the 30% porosity having a statistically higher total bone volume due to ingrowth than the higher 50% macroporosity ($p < 0.001$).

Furthermore, this pattern persists in each progressive region of interest into the scaffold interior. By contrast, composition and sintering temperature demonstrated no difference in its influence on bony ingrowth.

### 6.3.3 Quantifying quality: Indices of Bone Structural Quality

The second objective of analysis was to evaluate the structural quality of the regenerated bone. As before, the evaluation occurred in regard to the total bone regenerated as well as infiltrated bone internal to the scaffold boundaries. The relevant indices, in this instance were directed measure calculations: trabecular thickness (Tb.Th.), trabecular spacing (Tb.Sp.); and structural calculation, structure model index (SMI); all of which are oftentimes used as indications of structural bone quality.

The thickness of trabeculae resulting from the biphasic scaffolds were statistically less than those originating from the HA scaffolds ($p \leq 0.02$); there was no statistical difference in the thicknesses of trabeculae resulting from the biphasic compared to the TCP ($p = .125$), or the HA and TCP scaffolds ($p = .404$). Trabecular spacing was not influenced by composition, temperature, or macroporosity. The structure of neo-bone (SMI) was not affected by temperature or macroporosity, but was influenced by composition: bone due to the TCP scaffolds differed in structure from that of the biphasic ($p = 0.036$) and HA ($p = 0.015$) scaffolds.

For bone internal to the scaffold region, trabeculae thickness was not significantly different according to macroporosity, but was dependent on the composition and sintering temperature: scaffolds sintered at the lower temperature produced thinner trabeculae than those sintered at higher temperatures ($p \leq 0.05$); conversely, TCP produced thicker trabeculae than the biphasic compositions ($p \leq 0.05$) and the HA composition ($p \leq 0.05$). Trabecular spacing, however, was not reliant on composition, but differed according to both temperature and macroporosity: scaffolds sintered at 1100$^{o}$C produced trabeculae closer in proximity than those sintered at 1150$^{o}$C ($p \leq 0.01$) and the lower macroporosity designs produced trabeculae at a greater distance than was produced from scaffolds of higher macroporosity designs ($p \leq 0.001$). There was no statistical difference in the structure model index of internal neo-bone according to any of the factors analyzed.

## 6.4 Discussion

In this present study, we investigated the influence of macroporosity and sintering temperature on bone formation and regeneration in bioceramic scaffolds fabricated from three calcium phosphate compositions. The compositions not only differed in chemical phase amount of HA and TCP, but, as a result, also differed in solubility, and potentially, osteoinductivity. Aside from these chemical compositions, scaffolds were designed and fabricated such that the effect of two macrostructures and two sintering temperatures

could be investigated. All other design parameters were held constant. To examine the occurrence of bony formation, we relied on a previously established model of ectopic bone formation, in which HGFs were infected with an adenovirus to produce BMP-7, seeded unto scaffolds, and subcutaneously implanted in immunocompromised mice. Such studies have shown that HGFs can be modified genetically to produce biologically active BMP-7 and to differentiate into osteoblast-like cells in vivo.[256-257]

Several studies have reported data regarding the macroporosity requirements for scaffolding constructs; some of which are often confusing or conflicting in that the terminology can be redundant and is often used interchangeably. Porosity, itself, refers to the total void fraction of a material, and can be further defined by microporosity (typically, pores <10μm) and macroporosity (typically, pores > 100μm). Macroporosity can vary due to differences in pore size, pore volume fraction, and pore interconnectivity. Several studies support the idea that optimal pore size for bone ingrowth is in the range of 200-900 μm[25, 29, 35-36, 40, 152] and agree that the role of macroporosity is to impart osteoconductivity on the material used, and to allow for the infiltration of relevant cells and the vascularization of newly formed tissue.[38, 40, 151, 258] Additionally, many studies use the term *ingrowth* to signify the ability of the scaffold to regenerate tissue within the confines of its boundaries, more specifically into the medial and central regions, and not limited to the scaffold's periphery, while some studies refer to a normalized value in which the maximum available pore space has been

considered.[259-260] Several studies have also reported on the effect of processing parameters, specifically thermal treatment, on the development of ceramic microstructures and on the subsequent effect on bone regeneration;[261] these studies concluded that the effective thermal ranges for bone regeneration were those temperature ranges which impart some degree of microporosity and increased surface area, and that these temperature ranges were composition-dependent. Temperatures used in this study were chosen because they provide significant sintering and microporosity without initiating the β-α transformation of TCP (occurs at temperatures higher than 1180$^{o}$C). Maintenance of the beta phase is important to maintain chemical stability and mechanical integrity; the α–phase has a higher degradation rate and is weaker.

The current study used scaffold designs that were consistent in pore size (800 ±50 μm) and interconnectivity (100%), resulting in a difference in volume of macropores. Ingrowth was normalized for the maximum available pore space internal to the scaffold—an adjustment that attempts to correct for the fact that the more porous scaffold can hold more tissue. Un-normalized internal new-growth was referred to as *infiltrated*. Thermal treatment occurred at 1100$^{o}$C and 1150$^{o}$C, and produced constructs that demonstrated differences in specific surface area due to shrinkage variances, and overall porosity resulting from the occurrence of residual microporosity due to sintering.

An enumerated discussion of the important findings, as well as answers to the previously posed questions to be addressed in this chapter, follows:

***This study demonstrated that the amount of neo-bone formation is dependent on macroporosity; and of the three parameters tested (composition, macroporosity, and sintering temperature) macroporosity is the most influential in bone regeneration for calcium phosphate ceramic materials.***

Data suggests that, for the animal and experimentation model tested, (1) the significant factor in determining bone regeneration is macroporosity, and (2) the lower porosity prevails over the higher, thus allowing for the rejection of the null hypothesis:

> ***$H_{0\text{-}1a}$: There is no difference in bone regeneration across macroporosities.***

This data, on the outset, seems to contradict what others have reported over the years. Gauthier [29] performed a similar study in rabbits that concluded macropore diameter (not macropore volume or an interaction between the two) was the most influential factor in determining overall bone growth in biphasic (60/40 HA/TCP) scaffolds. The model used predicted, and experimentally confirmed, bone growth on the order of 21 ± 5%, a value that is supported by the current work. In a similar work, Mastrogiacomo,[38] in a study

that examined the interplay between pore size distribution, macroporosity, and interconnection pathway, demonstrated more bony ingrowth for a lower density (higher macroporosity) construct at the 4-week timepoint. In this case, the higher porosity scaffolds generated 35% new bone compared to the 22% of the lower porosity design; the magnitude of these values are also consistent with the current work. Both studies imply the co-dependency of pore size and pore volume, and suggests they may be confounding factors in bone regeneration, attesting to the difficulty with segregating the two in designs that are fabricated via methods that produce random pore size, structure, and orientation : Mastrogiacomo's high porosity design had a higher pore volume, smaller pore size, and smaller pore interconnectivity than the lower porosity design, and Gauthier concludes there may exist a threshold pore size (~500 mm) above which there exists no real difference in *in vivo* performance of the scaffolds. Restated, the effect of macroporosity on bone ingrowth for CaP scaffolds strongly depends on the pore organization or design. This may indicate that a measure incorporating pore organization, like permeability, is an important design factor for scaffolds. The current study eliminates pore size and size of connection pathway as a consideration. In this regard the effect of macroporosity should only be due to the volume of pores available.

We postulate that the lower macroporosity design prevails due to the higher surface area imparted by design; values are 199.57 $cm^2$ and 161.62 $cm^2$ for the 30% and 50% macroporosity designs respectively. This is, ironically, supported by Mastrogiacomo's

aforementioned work—the higher porosity scaffolds were also higher in surface area. This surface area consideration, we think, has implications specific to the osteoinductive nature of CaP materials, as our earlier work has previously implied the inverse relationship of regeneration and surface area with respect to non-osteoinductive materials like PLGA and PCL. The important considerations in this case, it appears that for internal bone volume, higher macroporosity performed best, as with the aforementioned polymer studies. However, once normalized for available pore volume (ingrowth) the lower macroporosity had the better performance, suggesting that surface area with an osteoconductive material may more important than for a non-osteoconductive polymer. To further this discussion, a more rigorous look at the comparative surface area influences is in order, and will be addressed in the chapter that follows

***This study demonstrated that the chemical composition and sintering temperature do not significantly affect the amount of neo-bone formation.***

The linear regression model used in this work not only demonstrates the significance of macroporosity but also demonstrates the lack of a significant contribution to regeneration and ingrowth from composition and sintering temperature respectively. Therefore, we fail to reject the null hypotheses that

***$H_{0\text{-}1a}$: There is no difference in bone regeneration across phase amounts of $\beta$-TCP.***

***$H_{0\text{-}1c}$: There is no difference in bone regeneration across sintering temperatures.***

***$H_{0\text{-}2a}$: There is no difference in tissue ingrowth across composition profiles.***

The data shows no difference in values; instead, it demonstrates the ability of each group to perform similarly without any indication that one group may have slower rates of induction as compared to another's. This is in contrast to several studies examining the osteoinductive ability of pure phase HA and TCP comparatively to biphasic compositions in which the biphasic compositions almost always outperform HA and/or TCP, and in which HA and/or TCP demonstrate comparatively low, or no, capacity for regeneration. More often than not, the better bone-producing biphasic constructs are higher in wt % TCP and microporosity, an effect of thermal conditioning. As such, the resorption properties of TCP, coupled with its higher microporosity (as therefore higher surface area) have been credited with saturating the milieu with calcium ions and maintaining an environment more conducive to bone production.

In a study that used a similar ectopic model to examine the ability of human mesenchymal stem cells (hMSCs) to induce bony formation via various CaP compositions, Arinzeh and coworkers [262] found more bone formation at 6 weeks post-implantation in the 20/80 HA/TCP biphasic composition, with lesser bone for the other biphasic and the least bone in the pure phase HA and TCP compositions; by 12 weeks, the HA and TCP compositions continued to demonstrate the least amount of bone growth among all groups. The implants used (60-70 % total porosity, with pore size ranging 300-600 μm) differed in composition. In 2002, Yuan et al conducted a 12-week study in which ceramics with similar macroporosity (overall porosity not characterized, though 80% of the macropores are in the 100-800 μm size range) were implanted intramuscularly in goats. This work showed a difference in bone induction and credited the difference in the microporosity and dissolution of BCP vs. HA as the reason for bony formation in the biphasic and not HA materials.[263] A later study by this same group in 2006 demonstrates the cross-species dependency of osteoinduction and supports their earlier findings that the greater osteoinductivity of BCP over HA is due to the presence of TCP.[264]

By contrast, the current study indicates that, for the current animal and experimentation model, scaffolds of either CaP composition or sintering temperature have similar probability (predictive influence) to regenerate bone, internally and externally. Additionally, the absence of an interaction effect between composition and temperature

implies that the resulting residual porosities are also indistinguishable in their regenerative potentials as well. This data is in regard to the early timepoint of 4 weeks, and its pertinence may not extrapolate to later time intervals. However, the literature more often than not suggests the reverse behavior in that the slower progression does not extend to the longer time points. More studies are needed to definitively say which applies in this case.

***This study demonstrated that composition was important for mineralization and that the structural quality of the newly formed bone is dependent on both composition and sintering temperature.***

Research on the quality of bone has been dedicated to understanding and identifying fracture risk associated with developed adult bone, with an emphasis on the diagnosis, treatment, and prevention of osteoporosis. Although the term “bone quality” remains unclear and elusive, it has been well-noted that the integrity of bone very much depends on its biomechanical contributors but also on its chemistry and morphology. As such, many studies have focused on the relevance of trabecular thickness, trabecular spacing, trabecular number, and structure model index as indicators of pathogenesis. To this end, not much research has been dedicated to analyzing the trabecular structure of newly formed bone.

TCP and HA are indistinguishable in terms of most indices, though both demonstrate statistical difference in performance from the biphasic composition. Where TCP differs from HA is in terms of structure model index. It is superior to both compositions in that it produces new bone that is organized more in the plate-structure than in the rod-structure. The plate- or rod-like quality of bone has been associated and correlated with its mechanical performance and determined that bone with the plate-like organization has lower fracture risk.

***Taken all together, the data supports the idea that TCP is best for this model in terms of bone growth and mineral and structural integrity.***

Overall, the amount of bone produced by TCP is on par with that produced by HA; yet, the mineral content and density of bone due to TCP is more significant than that of the other compositions. Similarly, TCP performs as well as HA and out-performs the biphasic composition in terms of trabecular thickness and spacing. Finally, the SMI due to TCP implies that its neobone is better organized from a mechanical perspective.

***And, finally, there exists a significant interaction effect that can be considered in design and possibly offset the regenerative limitations demonstrated by this model.***

Interaction effects, composition-temperature, composition-macroporosity, and temperature-macroporosity, were analyzed in order to determine if one or more of the main effects are confounded; thereby indicating or alluding to the existence of another factor worthy of consideration in future analyses and experiments. For example, composition-temperature and composition-macroporosity can arguably indicate contributions due to surface area. The composition-temperature interaction may refer to materials-specificity in that the shrinkage due to thermal treatment can differ according to composition. The composition-macroporosity interaction may refer to design-specificity in that macroporosity may be a larger contributor, and surface area to the lesser degree, since a given composition may demonstrate several ranges of surface area over the temperatures utilized in the experimental design. Since the surface area was not a direct focus of this work, more analysis, either post-hoc or additional experimentation, would be beneficial.

Nevertheless, what can be said regarding the original experimental design is that there exists an interaction effect of composition-macroporosity that warrants consideration in future scaffold design. The HA-low macroporosity design (composition-macroporosity)

interaction has a significant effect on overall bone growth, ingrowth, and tissue mineral content ($p \leq 0.05$, 0.03, and 0.01 respectively). By utilizing the interaction in the design of CaP materials, the model predicts an increase in overall bone regeneration of 40.19%, 21.45%, and 31.82% when we compare the HA-low macroporosity to HA-high macroporosity, all other composition-low porosity groups, and all other composition-high porosity groups, respectively. Similarly, bone ingrowth is expected to increase 54.83% when compared to the HA-high porosity group, 20.23 ± 7.47% compared to the other composition-low porosity groups, and 41.17 ± 8.96% when compared to the other composition-high porosity groups.

We believe the reason for the difference in the behavior of this group, compared to the behavior of the other groups, may, again, be rooted in the surface area differences between groups. Hydroxyapatite, at the sintering temperatures used in this study, experiences the least amount of shrinkage compared to the other compositions. Therefore, across the board, the final volume of the scaffold is larger than that of the rest, regardless of which macroporosity is utilized. Furthermore, the dissolution of TCP is much faster than the dissolution of HA, though it has been shown that HA does demonstrate some dissolution when sintered at 1000$^{o}$C (or 1100$^{o}$C). Though many have attributed the increase in bone growth to the immediate environment due to TCP dissolution, the fact that there is a minor difference in regeneration due to composition (main effect) between HA and TCP may imply that the saturation of the milieu with

calcium and phosphate ions is not the sole determinant of bone regeneration. This interaction effect, therefore, seems to imply that, while the main effect of macroporosity is a strong contributor to the initiation of regeneration, the indirect contribution of composition signifies that there is a synergistic relationship between several factors that may not be explained solely by the main effects the field so often studies. To support this point, we see, even in this case, that the composition-macroporosity interaction may be sufficient enough to override the benefit of higher ionic concentrations and encourage the production of new bone and mineral within the construct, at least for the early timepoint under consideration. Whether this relationship holds true in later timepoints, or whether macroporosity persists as the main effect worthy of consideration, is unclear.

## 6.5 Chapter summary and conclusions

To our understanding, the literature does not report any data that specifically demonstrates, or addresses, the predictive influence of scaffold design parameters on neo-bone regeneration in calcium phosphate materials. In the current study, we evaluated the volume and the mineral and structural quality of newly regenerated osseous tissue for its dependence on scaffold composition, macroporosity, and microporosity generated via sintering temperature.

Data from this study reveals that macroporosity has the most influence on the volume of bone regenerated, while the mineral quality was most influenced by composition and structural quality by sintering temperature. Furthermore, it can be inferred that TCP has the more desirable in vivo performance, but due to interaction effects of composition and macroporosity, HA scaffolds can surpass the regenerative potential of TCP if design modifications are considered.

The successful accomplishment of this work not only provides an important step in the understanding of the scaffolding requirements of a fully functioning degradable calcium phosphate ceramic construct but may also provide a starting point for the fabrication of more complex structures for the regeneration of more complex multi-functional tissues.

## 6.6 Figures

| Summary of Experimental Groups | | |
|---|---|---|
| Composition | Sintering Temperature | Macroporosity |
| TCP | 1100°C | 30%,50% |
| | 1150°C | 30%,50% |
| 50/50 Biphasic | 1100°C | 30%,50% |
| | 1150°C | 30%,50% |
| HA | 1100°C | 30%,50% |
| | 1150°C | 30%,50% |

Table 6.1: Summary of Experimental Groups. Twelve permutations of composition, macroporosity, and sintering temperature were utilized. All groups were implanted with an *n*-value corresponding to four. With complications due to surgery (1 animal lost), replicate numbers for some groups were reduced.

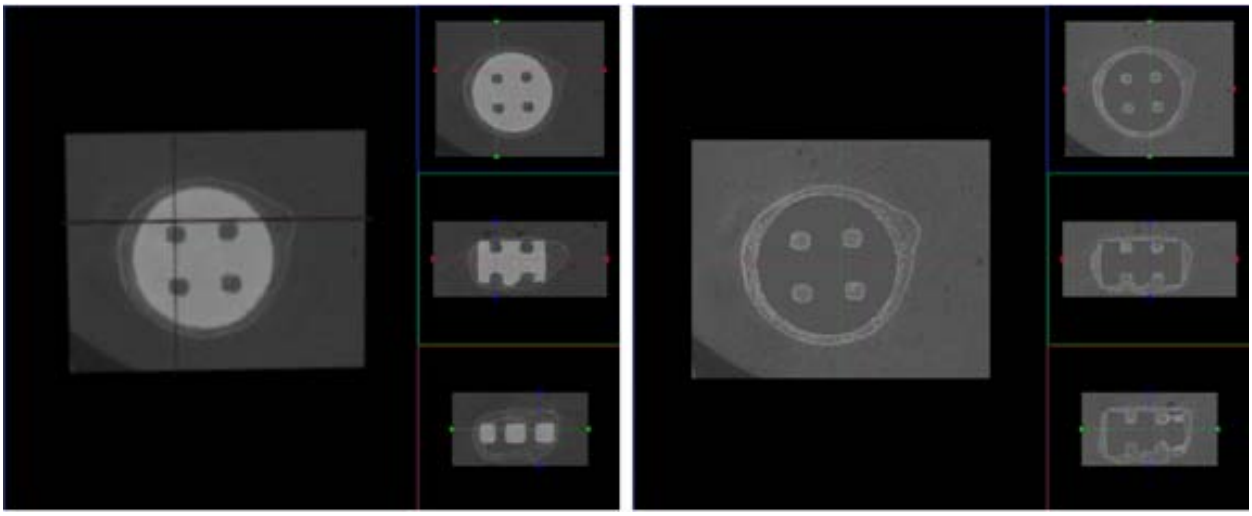

Figure 6.1: Micro-CT rendering of a low-macroporosity design scaffold, post-implantation. At 4 weeks, bone growth occurs both internally and externally to the scaffold boundaries. In panel [B], the scaffold has been removed from the dataset for ease of analysis of bone mineral indices.

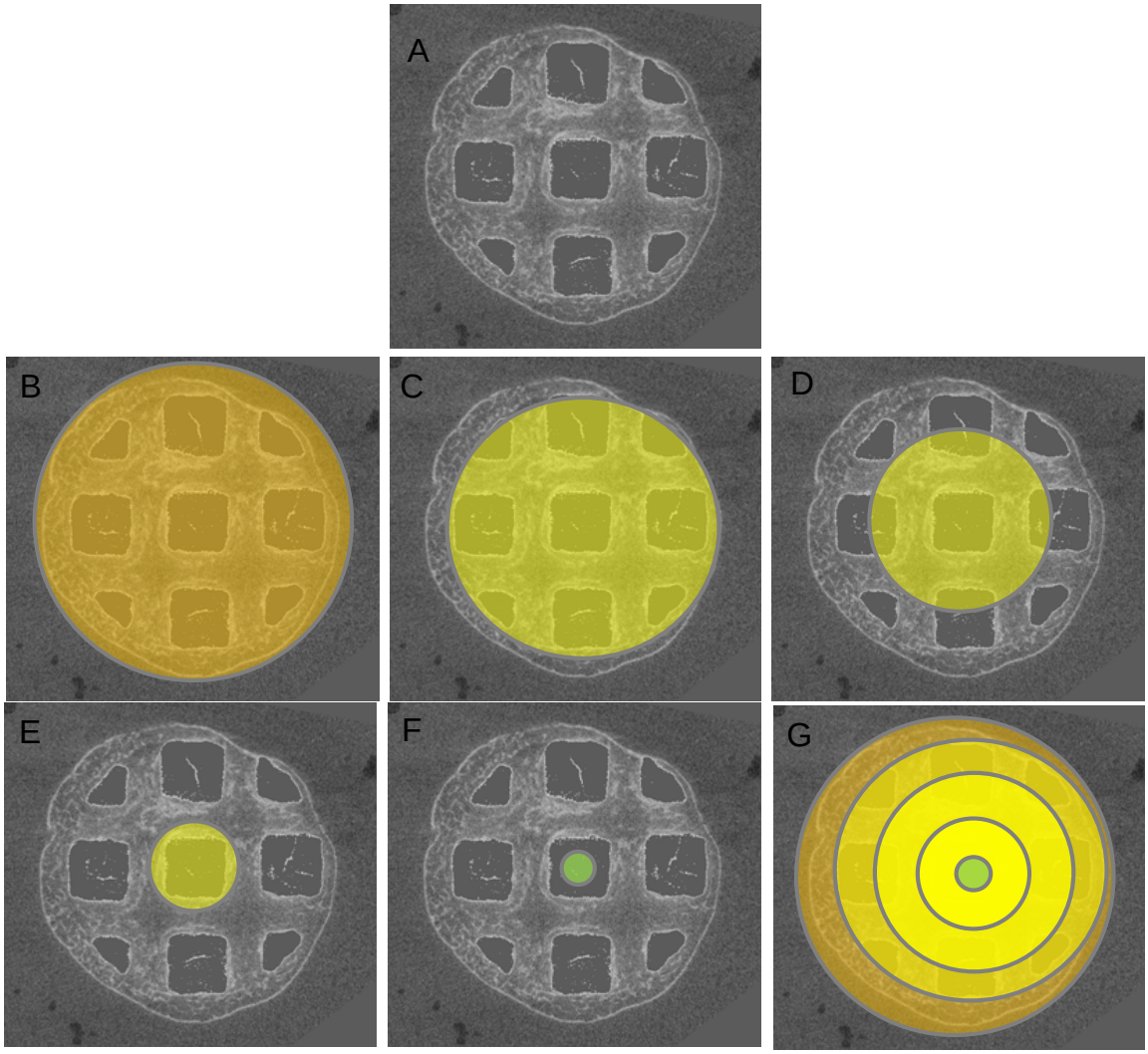


Figure 6.2: Cylindrical ROIs used in the analysis of regenerated bone. The original dataset [A] showing a low macroporosity design post-implantation with bone growth and scaffold removed. The initial region of interest (ROI) [B, orange highlight] encompasses all regenerate bone, internal and external to the scaffold boundaries. $C_0$, the infiltration ROI, is bound by the boundaries of the scaffold [C]. Lesser concentric ROIs are generated [D, E, F] by reducing $C_0$ by a fixed amount, 0.71 mm from the outer edge of the scaffold, with $C_1$ residing 0.71 mm from the scaffold edge [D], $C_2$ , 1.42mm [E], and $C_3$ , 2.13mm [F]. All ROIs are shown in panel [G].

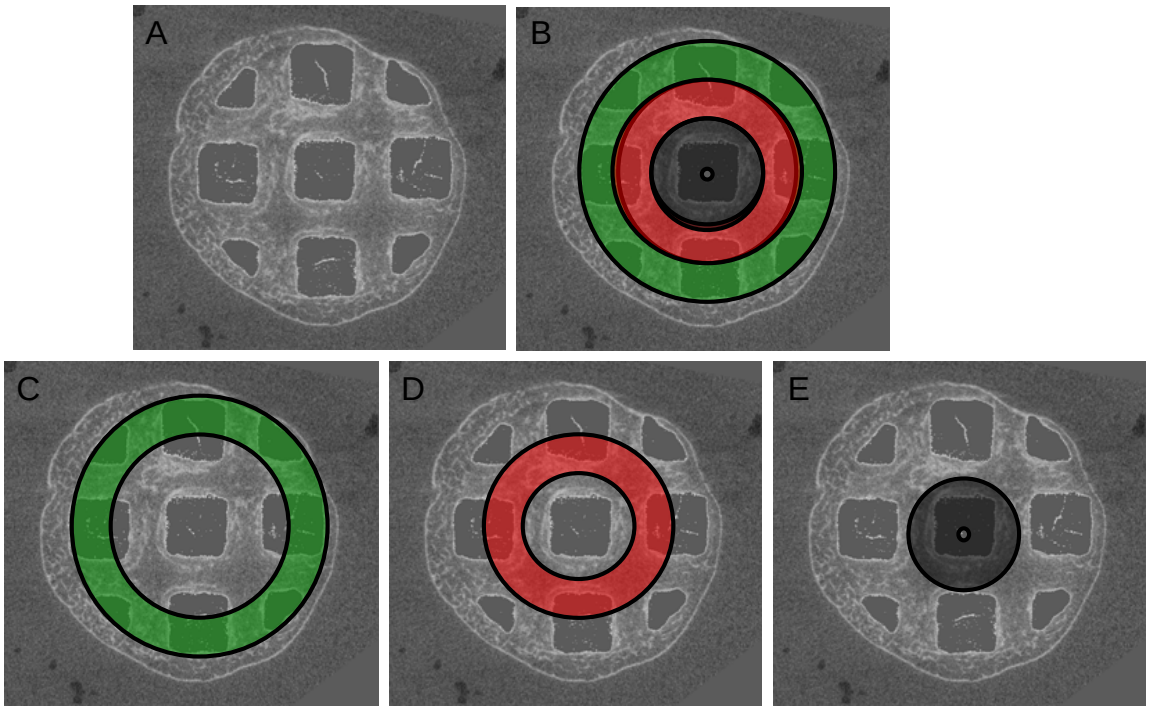


Figure 6.3: Ring ROIs used in the analysis of regenerated bone to determine the level of scaffold penetration. The original dataset [A] showing a low macroporosity design post-implantation with scaffold removed. Each ring region of interest (ROI) is the difference between successive cylindrical ROIs previously described in Figure 6.2. Ring1 [C, green highlight] is the difference between $C_0$ and $C_1$, and encompasses 0-0.71mm into the scaffold center; Ring2 [D, red highlight] is the difference between $C_1$ and $C_2$, and encompasses 0.071-1.42mm into the scaffold center; Ring3 [E, black highlight] is the difference between $C_2$ and $C_3$, and encompasses 1.42-2.13mm into the scaffold center. All ROIs are shown in panel [B].

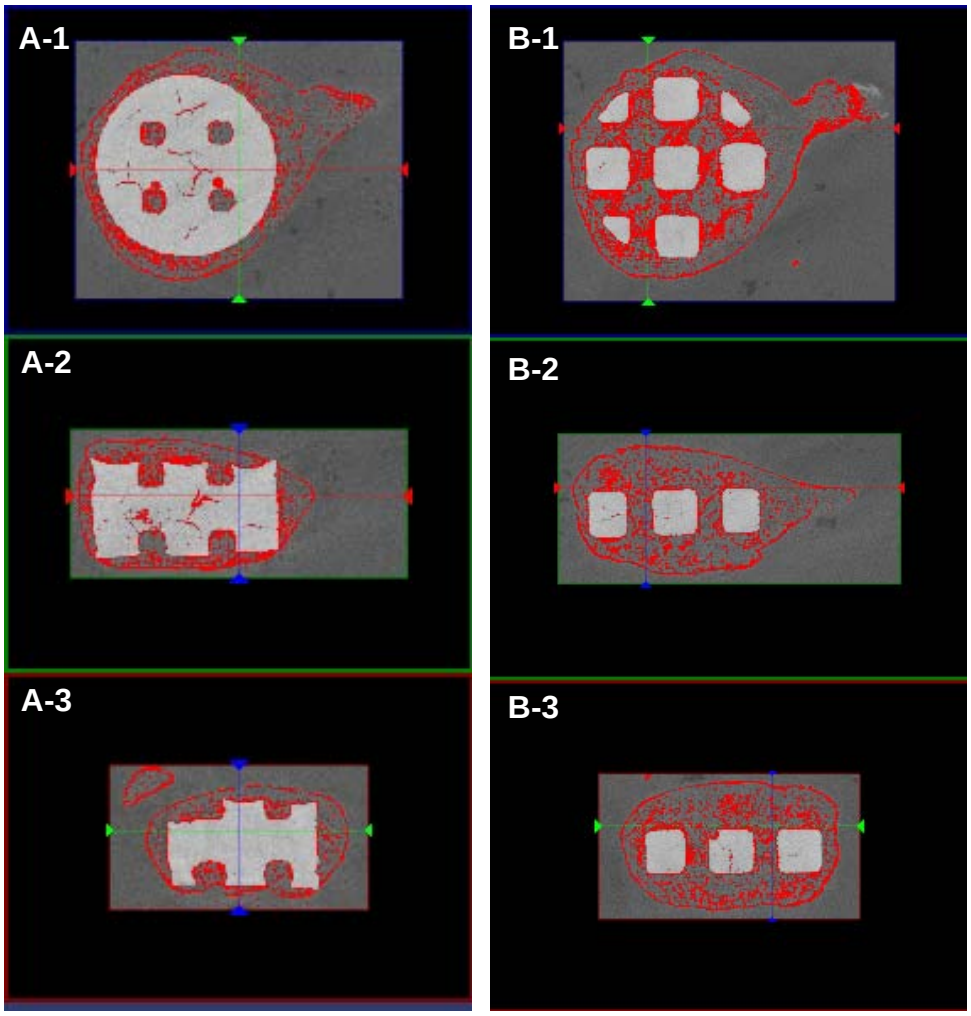


Figure 6.4: Micro-CT rendering of low macroporosity design 4 weeks post-implantation. Bone (red highlight) regeneration is both internal and external to the scaffold (white) boundaries, and is seen aligning the pore spaces [A1-3] and strut walls [B1-3]. A-1,B-1: x-y plane; A-2,B-2: x-z plane; A-3,B-3: y-z plane.

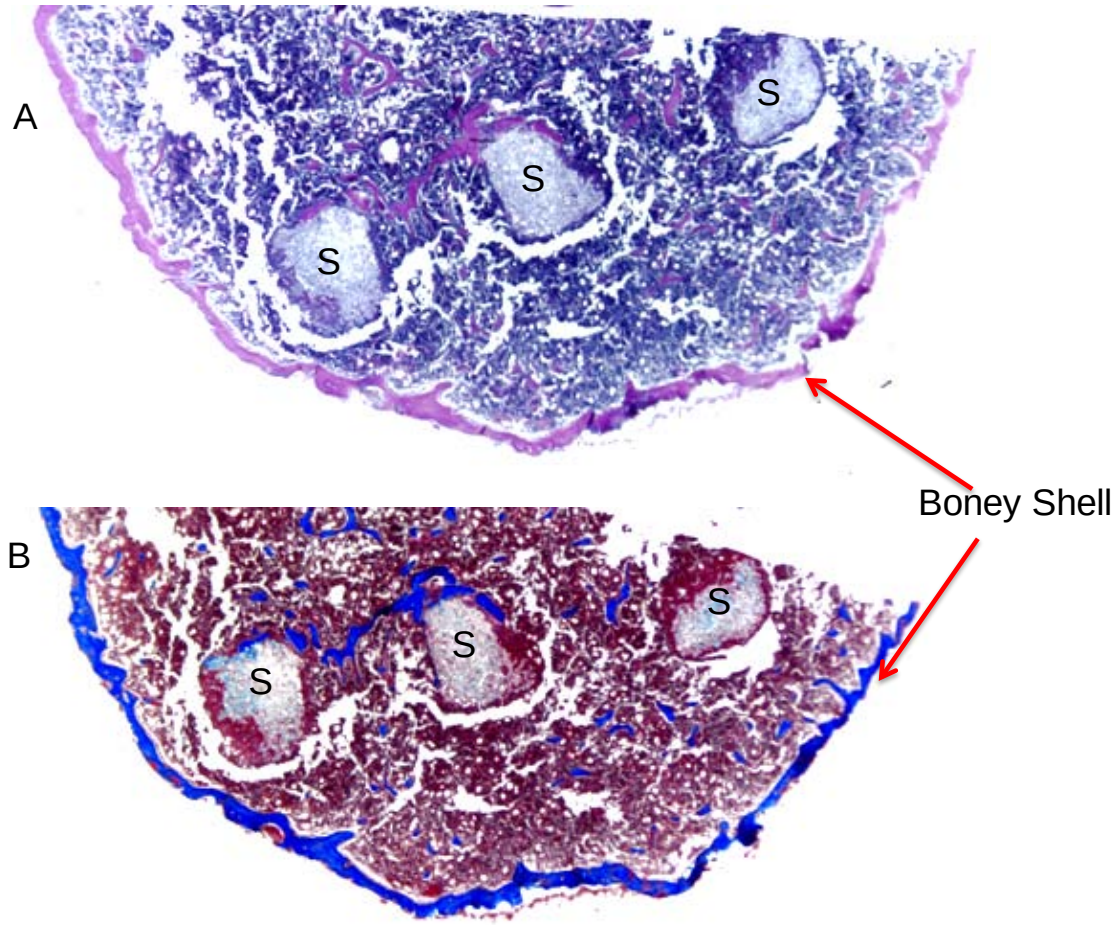


Figure 6.5: Persistence of a boney cortical shell in all histology sections. H&E [A] and Masson's Trichrome blue [B] stained histology section showing bone formation surrounding the scaffold [S]. In all cases, a boney cortical shell was seen surrounding the outer scaffold surface. Although the distance of the shell from the scaffold differed among samples, there did not seem to be any dependency on any of the factors tested in this model. H&E: bone stains pinkish-purple; Masson's trichrome: remodeled and lamellar bone is indicated by red, whereas blue indicates immature and freshly deposited bone.

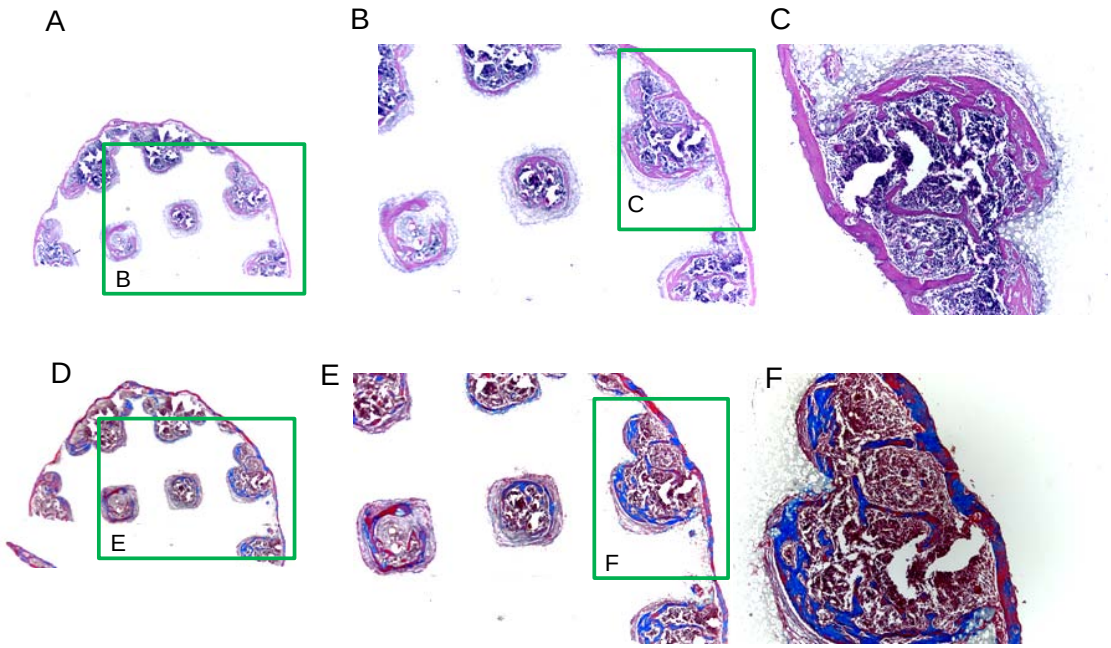


Figure 6.6: Bone regeneration occurred internal to the scaffold pores as well as external to the scaffold surface. H&E [A, B, C] and trichrome blue [D, E, F] stained histology sections showing bone formation within a high macroporosity design scaffold. In all cases, bone regeneration was both internal and external to the scaffold boundaries, with the formation of an outer cortical shell surrounding the scaffold surface; the distance of which, varied. Bone regeneration was also found aligning the scaffold pores [B,C, E,F]. H&E: bone stains pinkish-purple; Masson's trichrome: remodeled and lamellar bone is indicated by red, whereas blue indicates immature and freshly deposited bone.

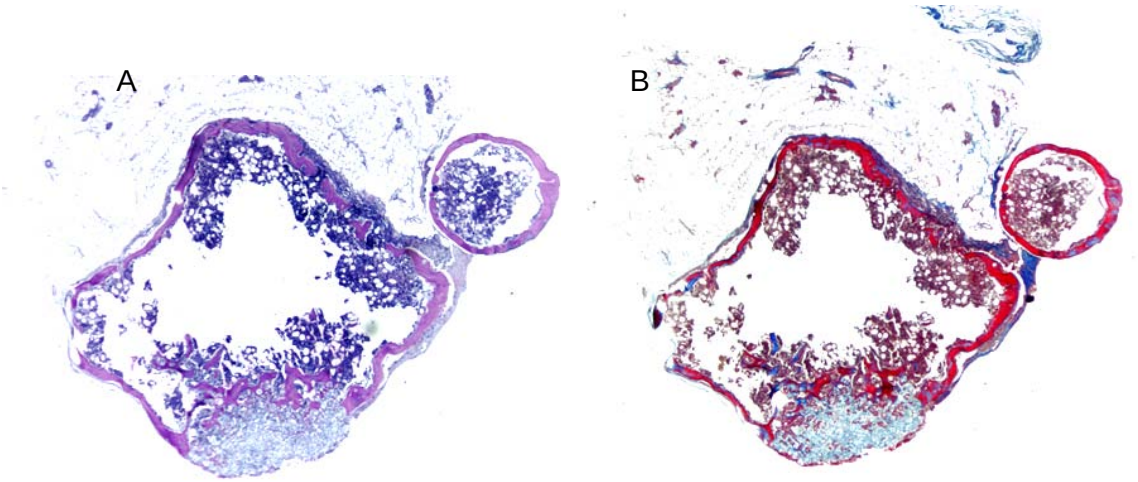


Figure 6.7: Bone regeneration within scaffold pores. H&E [A] and trichrome blue [B] stained histology section showing bone formation within the scaffold pores. In many cases, bone was seen aligning the pore surface. H&E: bone stains pinkish-purple; Masson's trichrome: remodeled and lamellar bone is indicated by red, whereas blue indicates immature and freshly deposited bone.

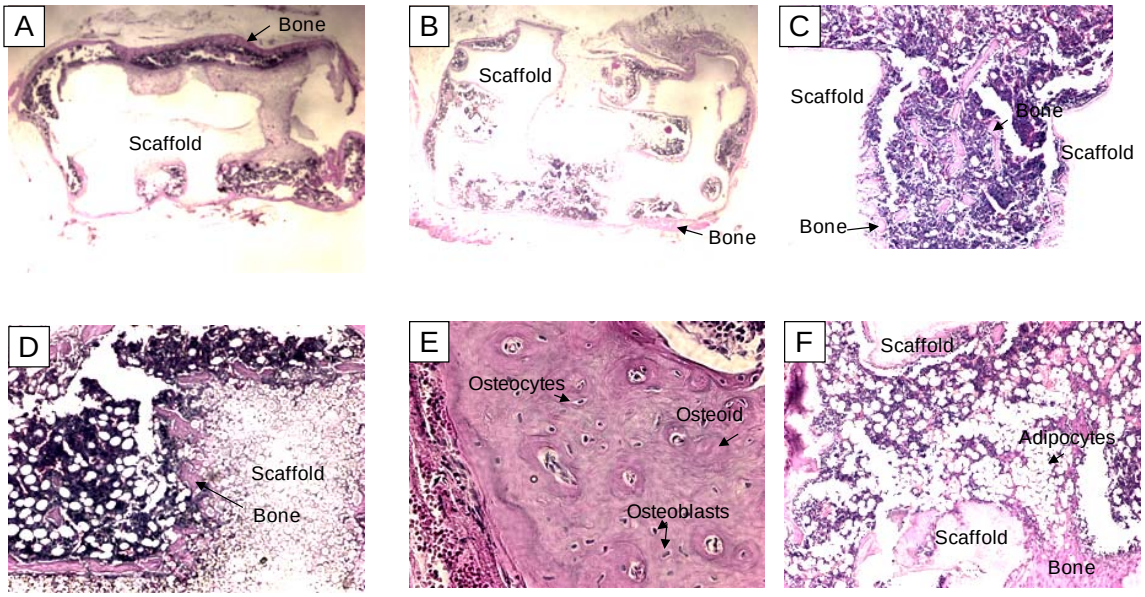


Figure 6.8: Regenerate bone is normal in appearance and demonstrates cellular markers for bone tissue; 4 week timepoint. H&E stained histology section of low macroporosity [A; 50BCP, 1100$^{o}$C, 2X magnification] and high macroporosity [B; TCP,1150$^{o}$C, 2X magnification ] design scaffolds, showing bone formation surrounding the scaffold perimeter. Bone ingrowth is also seen inside the pores aligning the scaffold surface [C: HA, low macroporosity design, 1150$^{o}$C, 10X magnification; D: TCP, low macroporosity, 1100$^{o}$C, 10X magnification]. The morphology of the neobone is normal in appearance, indicating the presence of osteoblasts, osteoid, osteocytes, marrow space, and mineralized bone tissue [E: BCP, high macroporosity design, 1100$^{o}$C, 40X magnification; F: TCP, low macroporosity design, 1150$^{o}$C, 10X magnification].

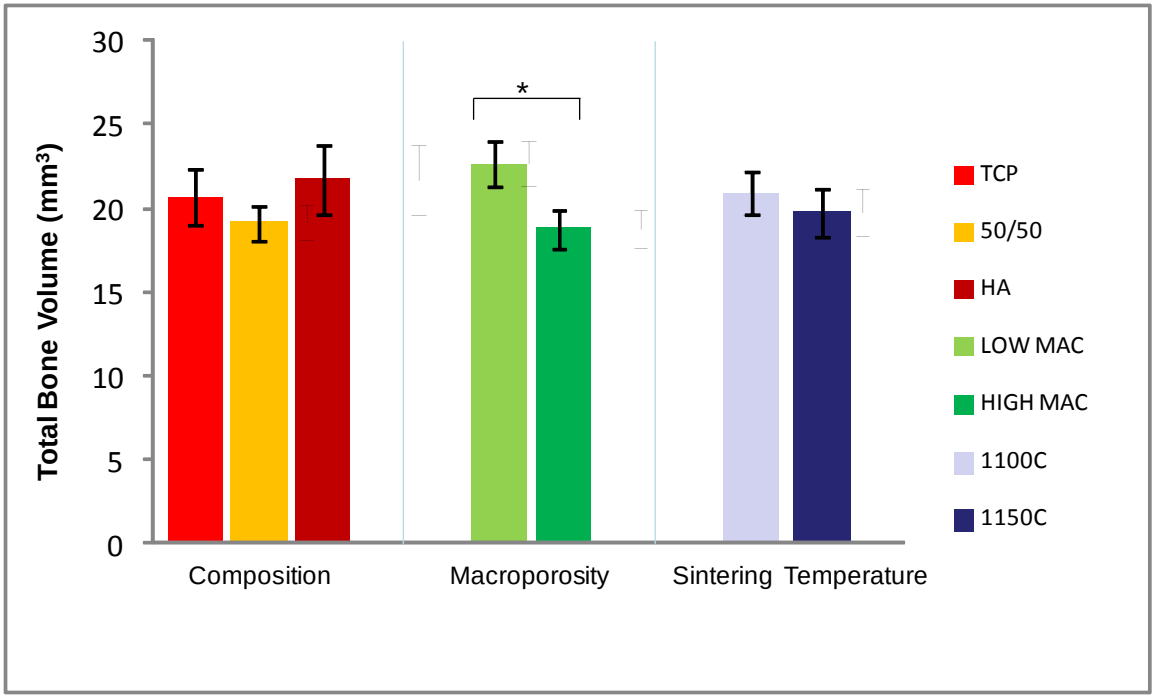


Figure 6.9: Total bone volume regenerated internal and external to scaffold boundaries. Total volume of bone (TBV; $mm^3$) regenerated internal and external to the scaffold boundaries at 4 weeks implantation; data is presented as a function of composition, macroporosity, and sintering temperature. Composition and sintering temperature had no effect on the TBV of bone produced, whereas macroporosity effects were significant for the low and high macroporosity designs. Values are expressed as arithmetic mean ± standard error. Statistical significance was at the $\alpha<0.05$ (*); $\alpha<0.01$ (**); $\alpha<0.001$ (***). Data tables are presented in Appendix 1.

.

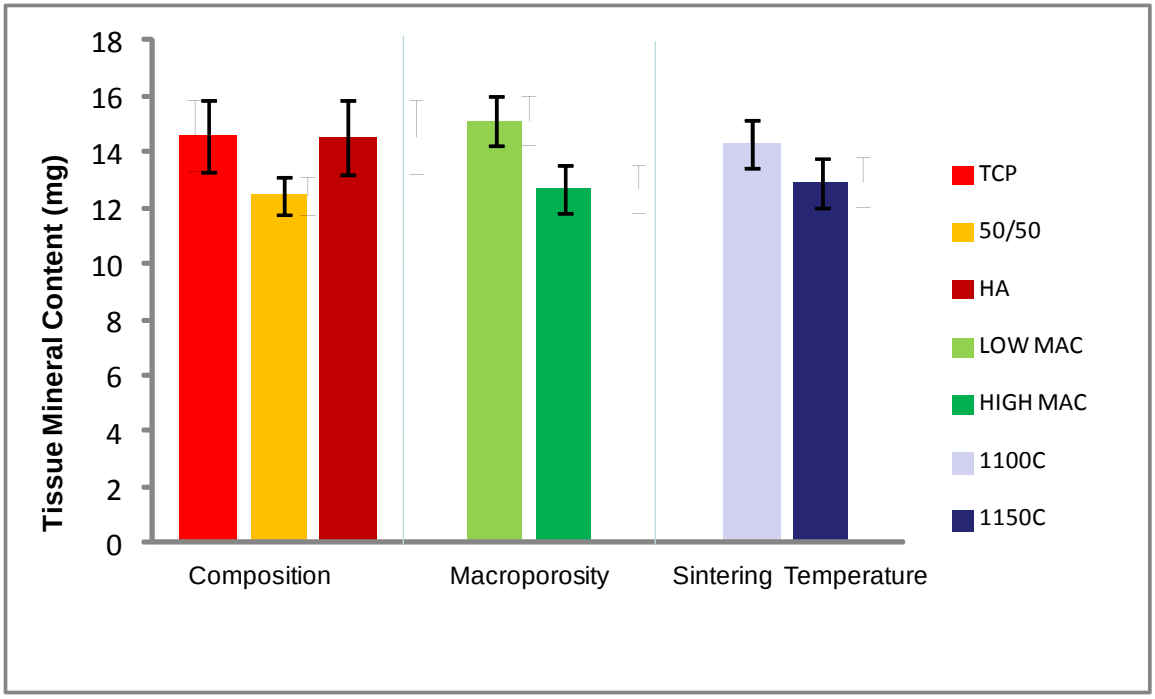


Figure 6.10: Tissue mineral content of regenerated bone internal and external to the scaffold boundaries Tissue mineral content (TMC; mg) of regenerated bone internal and external to the scaffold boundaries at 4 weeks implantation; data is presented as a function of composition, macroporosity, and sintering temperature. There was no effect of composition, macroporosity, or sintering temperature on the TMC of bone produced. Values are expressed as arithmetic mean ± standard error. Data tables are presented in Appendix 1.

.

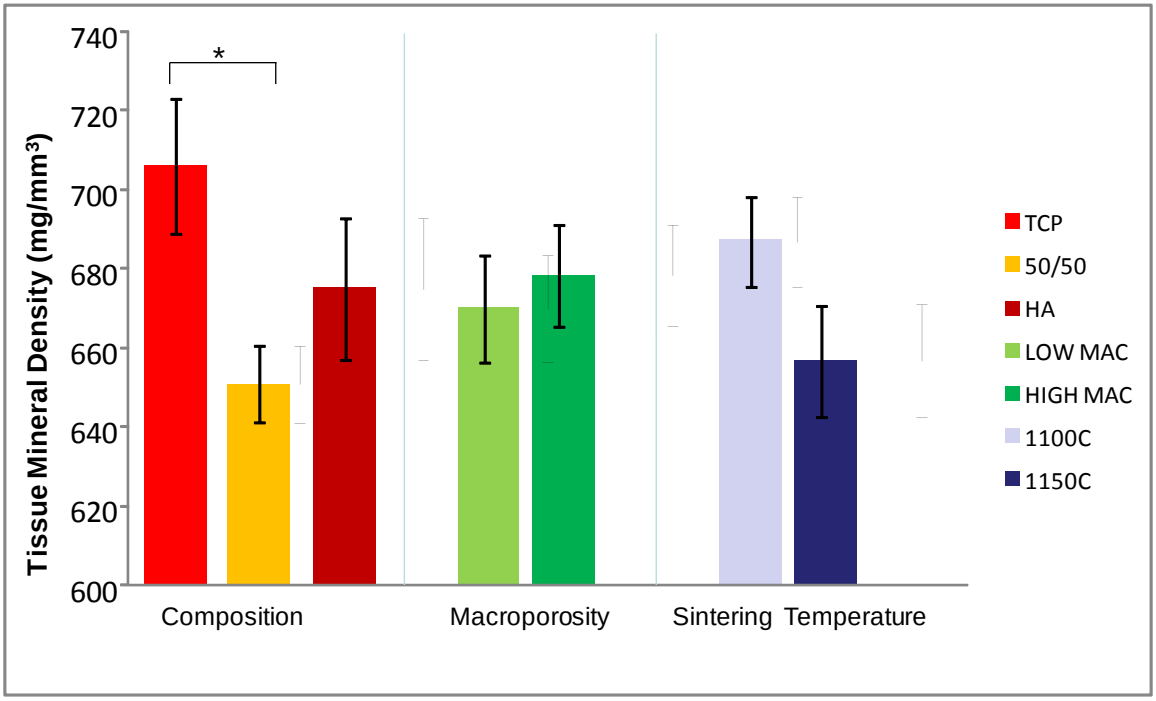


Figure 6.11: Tissue mineral density of regenerated bone internal and external to the scaffold boundaries. Tissue mineral density (TMD; mg/mm$^3$) of regenerated bone internal and external to the scaffold boundaries at 4 weeks implantation; data is presented as a function of composition, macroporosity, and sintering temperature. Macroporosity and sintering temperature had no effect on the TMD, whereas composition effects were significant for TCP and the 50/50 biphasic compositions. TMD values obtained were within the range for TMD values of human trabecular bone (500-800 mg/mm$^3$). Values are expressed as arithmetic mean ± standard error. Statistical significance was at the $\alpha$<0.05 (*); $\alpha$<0.01 (**); $\alpha$<0.001 (***). Data tables are presented in Appendix 1.

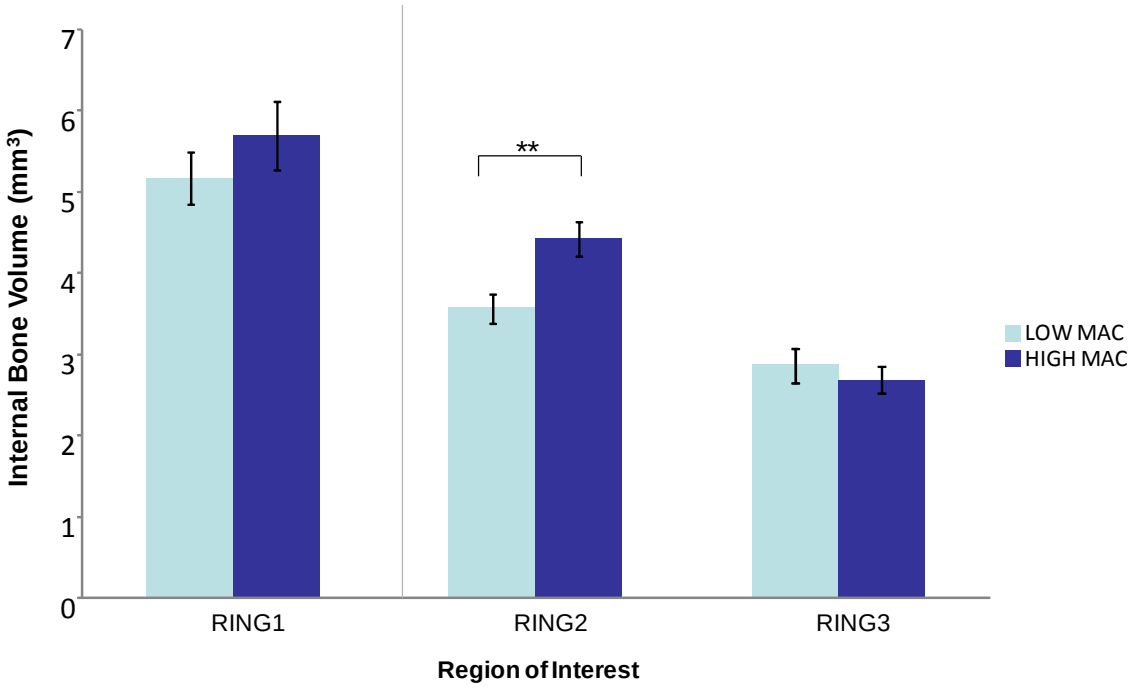


Figure 6.12: Assessment of penetration depth of internal bone volume as a function of macroporosity. At 4 weeks, the significance of macroporosity to penetration depth of regenerate bone is most evident in Ring 2. For the outer ring regions of interest, the high macroporosity scaffold design regenerated more bone than the low macroporosity design. Statistical significance was at the $\alpha<0.05$ (*); $\alpha<0.01$ (**); $\alpha<0.001$ (***). $Ring_1$: 0 - 0.71mm into the interior of scaffold; $Ring_2$: 0.71 - 1.42 mm into the interior of scaffold; $Ring_3$: 1.42 - 2.13 mm into the interior of scaffold.

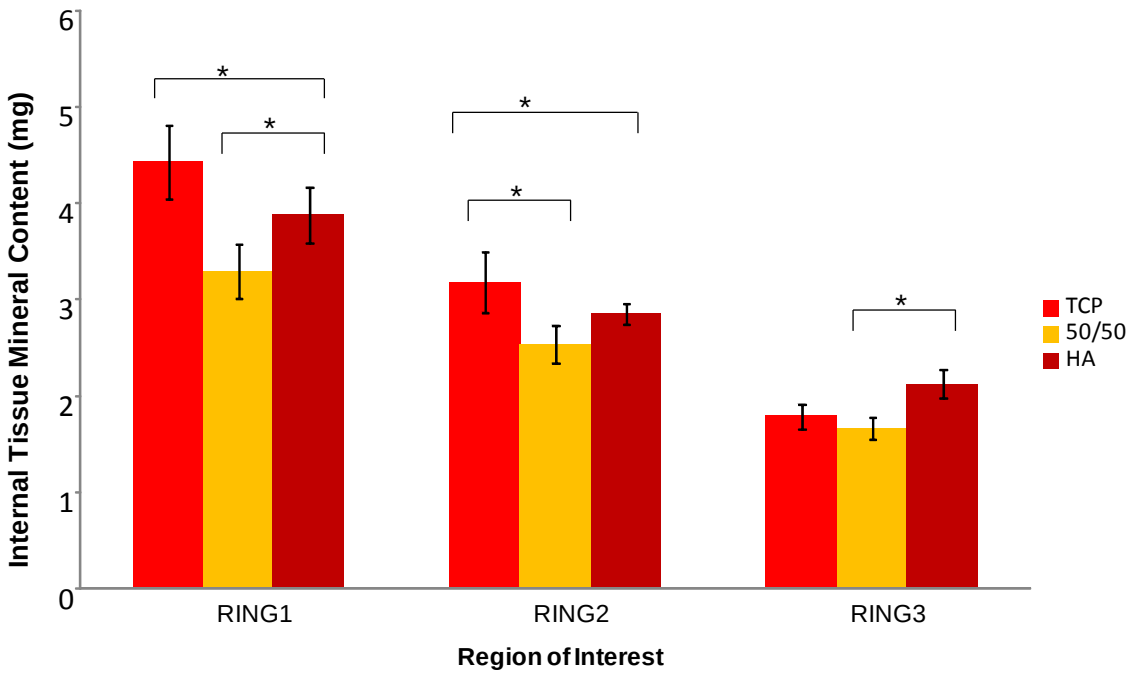


Figure 6.13: Assessment of internal tissue mineral content of bone volume within ring regions of interest as a function of composition. At 4 weeks, the significance of composition to internal tissue mineral content of regenerate bone is evident in all ring regions of interest, with TCP generating more mineral in the outer 1.42 mm of the scaffold. Statistical significance was at the $\alpha<0.05$ (*); $\alpha<0.01$ (**); $\alpha<0.001$ (***). $Ring_1$: 0 - 0.71mm into the interior of scaffold; $Ring_2$: 0.71 - 1.42 mm into the interior of scaffold; $Ring_3$: 1.42 - 2.13 mm into the interior of scaffold.

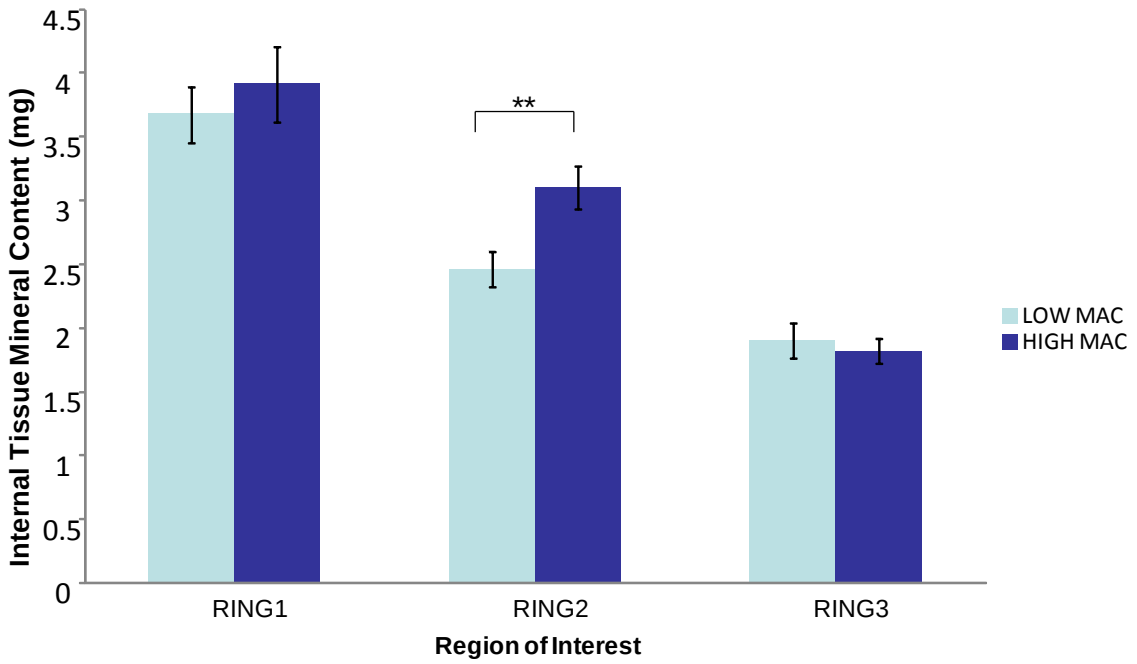


Figure 6.14: Assessment of internal tissue mineral content of bone volume within ring regions of interest as a function of macroporosity. At 4 weeks, data suggests a macroporosity dependence on internal tissue mineral content of regenerate bone: high macroporosity designs produce more mineral content in ring regions 1 and 2, with ring 2 demonstrating significance. TMC for region 3 is nearly identical. Statistical significance was at the $\alpha<0.05$ (*); $\alpha<0.01$ (**); $\alpha<0.001$ (***). $Ring_1$: 0 - 0.71mm into the interior of scaffold; $Ring_2$: 0.71 - 1.42 mm into the interior of scaffold; $Ring_3$: 1.42 - 2.13 mm into the interior of scaffold.

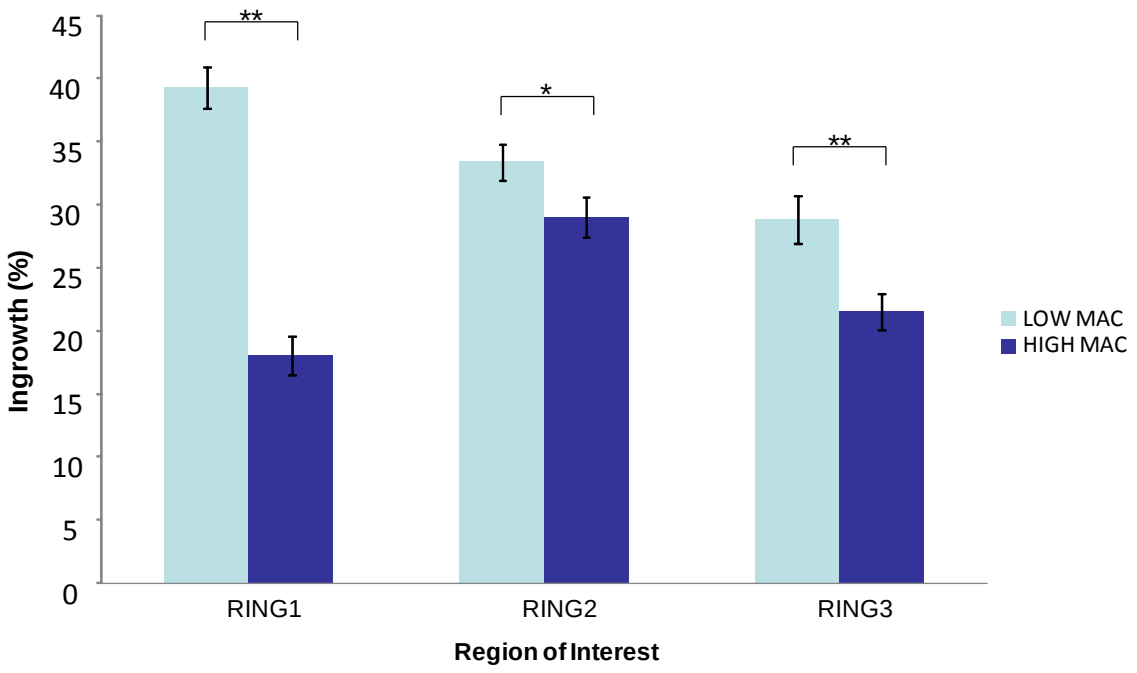


Figure 6.15 : Assessment of penetration depth of internal bone volume as a function of macroporosity. At 4 weeks, the significance of macroporosity to penetration depth of regenerate bone is most evident in Ring 2. For the outer ring regions of interest, the high macroporosity scaffold design regenerated more bone than the low macroporosity design. Statistical significance was at the $\alpha<0.05$ (*); $\alpha<0.01$ (**); $\alpha<0.001$ (***). $Ring_1$: 0 - 0.71mm into the interior of scaffold; $Ring_2$: 0.71 - 1.42 mm into the interior of scaffold; $Ring_3$: 1.42 - 2.13 mm into the interior of scaffold.

# CHAPTER 7
# A POST-HOC ANALYSIS OF THE INFLUENCE OF SURFACE AREA AND PERMEABILITY ON BONE REGENERATION AND MINERAL AND STRUCTURAL BONE QUALITY

*"All truths wait in all things; They neither hasten their own delivery, nor resist it."*
*-Walt Whitman, Leaves of Grass*

## 7.1 The Need for a *Post Hoc* Consideration of Surface Area

Numerous studies on the use and effectiveness of scaffolds for bone regeneration have recognized the individual contributions and importance of factors related to either scaffold material characteristics or design and processing specifications. For example, material-specific attributes, such as surface chemistry and surface roughness, often dictate the materials' osteoinductivity as well as the scaffold's osteoconductivity.[25, 42, 44, 261, 265-267] Design attributes, either architecture-dependent or fabrication-dependent, such as pore size, porosity, and permeability often control, direct, and influence the scaffold's ability to encourage infiltration, vascularization, and ultimately regeneration.[28, 35-36, 40, 52, 250, 268]

While the hierarchy of the two classes of design considerations (materials vs. architecture) may be unclear when we consider several different material types (polymers compared to metals or ceramics, for example), it may be more critical to establish this ranking within the boundaries of very similar materials groups, such as the CaP family of ceramic materials. While much has been done to establish the utility of these materials in osseous-focused applications,[38, 50, 173] there is still confusion or uncertainty in knowing which characteristics influence the quality of bone production best within this group. Furthermore, in an environment of limited resources, whether it is at the benchtop or in a clinical setting, the importance of knowing *a priori* how to maximize the effectiveness of scaffolds in order to overcome empirical shortcomings does not go unnoticed or underappreciated.[13, 27, 269-270]

The work presented in chapter six was aimed at helping to unlock this mystery. We studied the influence of materials-specific characteristics composition and microporosity due to sintering temperature; as well as the design characteristic, macroporosity, on bone regeneration and quality. What was determined was intriguing:

- *The amount of bone regenerated was dependent on the scaffold's macroporosity, and, counter to what is reported in literature:* ***lower macroporosity prevailed over higher in terms of the amount of bone ingrowth into the scaffold.***

- *The amount of regenerated bone was independent of the scaffold's composition or sintering temperature.*

- *The composition of the scaffold influences the mineralization of the developing tissue.*

- *The structural quality of the neo-bone was dependent on composition and sintering temperature.*

Moreover, the substantiation of a composition-macroporosity interaction effect is suggestive of an underlying effect of surface area; and, we believe, may explain the observed increase of bone ingrowth on lower levels of macroporosity. That is, the main effects of macroporosity, composition, and sintering temperature may be confounded by the interaction effect of surface area (see the discussion in chapter six). Although the conclusions drawn in chapter 6 are concrete, additional questions arise:

*Is surface area a consideration of importance, and can it explain our findings?*

*Are other design factors, permeability and macroporosity, equally as, or more, influential as surface area?*

*And finally, is there a manipulation of these factors that produces better bone growth?*

We approach the answers to these questions via a *post hoc* evaluation of data acquired from the aforementioned *in vivo* study. We assess the relative contributions of surface area and permeability to bone regeneration via the CaP scaffolds used in this model. Additionally, we seek to determine the most influential design factor (macroporosity, surface area, or permeability) in scaffold design specifications. As previously, micro-computed tomography is used to analyze the influences of these factors on the mineral and structural bone quality of implanted calcium phosphate scaffolds at the early time-point of four weeks. These evaluations are based on three compositions of calcium-based ceramics (hydroxyapatite, β-tricalcium phosphate, and a 50/50 biphasic combination of the two) and two sintering temperatures. In this fashion, variations in surface area[xi] are a result of materials properties and design, whereas permeability and macroporosity are largely the result of design, though shrinkage due to sintering may affect this variable as well.

[xi] The compositional and sintering effects on the scaffold's final surface area are addressed in chapter 4.

## 7.2 Materials and Methods

### 7.2.1 In vivo surgical procedures and post-surgical evaluation

Details regarding the experimentation and data analysis methodologies are previously reported (see Chapter 6, section 6.2). In short, CaP scaffolds with designed architecture having various fabrication parameters based on composition, sintering temperature, and macroporosity were imaged prior to implantation using a μCT and subcutaneously implanted in SCID mice. In this model, HGFs transfected with an adenovirus rendering the production of BMP-7 were seeded into scaffolds prior to implantation; empty scaffolds served as negative controls. Four weeks post-implantation, mice were euthanized, and retrieved scaffolds were again imagined using μCT. Regions of interest within the post-implantation scans were used to evaluate total bone volume, ingrowth, bone mineral density, and bone mineral content, and structural quality of newly regenerated tissue within the scaffolds with respect to composition, sintering temperature, and macroporosity. In a similar manner, a post-hoc analysis of the same post-implantation scans was performed by evaluating the bone mineral indices with respect to initial scaffold surface area, permeability, and macroporosity.

### 7.2.2 Surface Area and Permeability

The assessment of end-fabricated surface area and permeability is described in Chapter 4: Architectural Design and Characterization of Calcium Phosphate Scaffolds. In review, MicroView 2.1.2 software was used to determine the surface area of pre-

implanted scaffolds at time zero. A cylindrical ROI encompassing the entire scaffold region was employed, as was a uniform threshold value of 2500. Permeability was determined via a reservoir with continuous water flow and water level in equilibrium attached to an acrylic chamber, housing the scaffold, and a collector (Figure 4.3). The mass of the collector at variable time points was recorded using LabView (National Instruments, Austin, TX). Mass flow was calculated at stability and used to calculate permeability according to Bernoulli's equation and Darcy's Law:[183]

$$k = \frac{\Delta x}{A.M_s} \cdot \frac{2\pi^2 r^4}{\left(M_0/M_s\right)^2 - 1}$$

where $\Delta x$ corresponds to the scaffold's height, $A$ the scaffold's cross-sectional area, $r$ is the outlet radius and $M_s$ and $M_0$ are the mass flow rate with and without the scaffold, respectively.

### 7.2.3 Statistical analysis

Statistical calculations were performed using PASW18. A linear regression model was used to analyze all μCT data. The main effects of surface area, permeability, and macroporosity were evaluated. Data is reported as the arithmetic mean ± standard deviation; graphically represented as arithmetic mean ± standard error. Statistical significance was considered for p values ≤ 0.05.

## 7.3 Results

### 7.3.1 Surface Area and Permeability

Chapter 4 demonstrated that scaffold surface area was influenced by sintering temperature and not by macroporosity or composition. Further inspection demonstrates a relationship between scaffold design and surface to volume ratio (S:V). A look at the influence of surface area compared to that of S:V reveals that S:V is the most influential factor with regard to total regeneration ($p=0.045$, $p=0.024$), infiltrated regeneration ($p= 0.270$; $p=0.220$) and ingrowth ($p=0.022$; $p=0.000$) for surface area and S:V respectively ($n = 33$). Both factors demonstrate significance in the same areas and both within the conventional range, with S:V having slightly better values.

A t-test reveals that the mean S:V for the two designs, 30% and 50% macroporosity, differ by a factor of 1.86, and are significantly different ($p = 0.001$; $n= 33$) from one another. S:V is not influenced by either of the other factors, composition or sintering temperature. There is, however, a marginal significance of temperature on S:V ($p=0.0915$) and a partial influence in terms of composition, where HA significantly differs from TCP ($p=0.0263$). These p-values are suggestive of an interaction effect of temperature and design, and when taken into consideration reveal there are 4 distinct groups for the consideration of S:V—low macroporosity-low temperature, low macroporosity-high temperature, high macroporosity-low temperature, and high macroporosity-high temperature —all illustrative of the design-temperature interaction.

However, since the experimental design and the regression model do not allow for the consideration of more than three (or four) groups simultaneously, surface area influences on bone regeneration will be assessed with respect to surface-to-volume ratio, and not with respect to either of the four subgroups.

Scaffolds with higher permeability (n=18) under-performed the low permeability scaffolds (n = 14) in regard to total regeneration ($p=0.021$) and ingrowth ($p<0.005$), with no significant difference in the volume of infiltrated bone grown into the scaffold interior ($p=0.112$).

### 7.3.2 Effect on Regeneration and Bone Quality

Due to induced collinearity the regression model does not allow for the evaluation of permeability and macroporosity simultaneously. This finding is not at all in disagreement with the various studies that report, and sometimes incorrectly use the terms interchangeably, that permeability and macroporosity are nearly the same (further discussion to follow);[32] for this reason, analysis will consist of a comparison of the influence of two factors (surface-to-volume ratio and permeability) on regeneration and bone quality. As before, we evaluate bone regeneration from two perspectives: total bone regeneration, inclusive of all bony growth internal and external to the scaffold, and infiltrated bone regeneration, characterized by the amount of bone growth internal to the scaffold boundaries.

The total volume of bone produced, internal and external to the scaffold boundaries, was influenced by the scaffold's permeability, with the high permeability group producing statistically significant more bone than the low permeability group ($p = 0.041$). Whereas there was no comparative significance in the volume of bone as a function of S:V ($p=0.547$). Tissue mineral content of high permeability scaffolds was lower than that of low perm scaffolds ($p=0.027$), with S:V not providing a significant influence ($p=0.265$). Tissue mineral density was unaffected by permeability, and was marginally influenced by S:V ($p=0.08$).

The regeneration volume internal to the scaffold boundaries ($C_o$; infiltrated bone) was dependent on neither the permeability nor surface-to-volume ratio. TMC also remained unaffected by either factor, while TMD demonstrated a S:V dependency ($p=0.035$) and a suggested influence by permeability, the low perm prevailing over the high ($p=0.08$). Ingrowth was significantly influenced by permeability: the low permeability had statistically more ingrowth than the high permeability ($p < 0.001$), while S:V did not affect ingrowth by comparison ($p=0.426$).

We used directed measure calculations to assess the structural quality of the new bone: trabecular thickness (Tb.Th.), trabecular spacing (Tb.Sp.), and structure model

index (SMI). Permeability had no effect on trabecular thickness, trabecular spacing, or SMI (p=0.997, 0.289, and 0.373 respectively). By comparison, the S:V did not influence Tb.Th or SMI (p=0.379 and 0.835 respectively) but did contribute to the spacing of individual trabeculae (0.028). Neither factor had any significant effect on the structural quality of neo-bone internal to the scaffold region.

.

## 7.4 Discussion

The over-riding purpose of the current study was to determine if surface area played a role in the regeneration of bone from CaP scaffolds. And, if so, to what extent should it be a consideration in scaffold design. We reevaluated data from an earlier *in vivo* study designed to address the influence of composition, macroporosity, and sintering temperature of CaP scaffolds on the regeneration and structural quality of neo-bone. The experimental design of this work utilized three calcium phosphate compositions, differing in chemical phase amount of HA and TCP, two macrostructures, and two sintering temperatures. We relied on a previously established model of ectopic bone formation, in which BMP-7-producing HGFs were loaded unto scaffolds and subcutaneously implanted in immunocompromised mice. The results of the study highlighted macroporosity as the major influence in the amount of bone regeneration and surprisingly demonstrated a significant difference and inverse relationship of bone ingrowth to macroporosity. Other results showed the importance of composition and

sintering temperature to bone mineralization and structural quality respectively. Additionally, the influence of a composition-macroporosity interaction effect was demonstrated, and if exploited, is suggested to be a method to elicit increased regeneration. We hypothesized that the demonstrated relationship between macroporosity and bone ingrowth, as well as the presence of the composition-macroporosity interaction, may be rooted in the implant surface area.

Several studies have reported data regarding the benefit of surface area to biomaterials; though, for many, changes in surface area are oftentimes achieved via changes in microporosity or surface roughness.[9, 40] Few groups have discussed this phenomenon as it applies to the achievement of increased or reduced surface area via homogenous surfaces.[265] Nevertheless, the significance of surface area to biological performance cannot be overlooked. Improvements in surface area, or surface to volume ratio, have resulted in improvements in cellular morphology, adhesion, differentiation, and proliferation.[265] Poorer surfaces have been shown to produce non-tissues or tissues with substantially lower genetic material of interest compared to tissues generated from biomaterials of higher surface area.

The designed architectures utilized in this differ in surface area, notwithstanding the additional consideration of surface area due to microporosity or surface texture. A review of the data from this perspective should be a first step in delineating the

influence of available surface area from the influence of microporosity and roughness on regenerate bone. An evaluation of the data demonstrated the role of SA, and more specifically, surface-to-volume ratio (S:V), in the regeneration of new bone in and around these scaffolds. In this light, S:V was slightly more influential although significance levels for were well-within the desired range of confidence ($p=0.02$).

Another relevant consideration not accounted for in the original study is the influence of permeability. Permeability is addressed in this post-hoc analysis for two reasons: 1. It is a design specification proven to have a direct effect on bone regeneration, and 2) studies show that higher permeability improves boney ingrowth. The initial experimental design left to question the permeability difference of the scaffold designs as reasons for the ingrowth differences. Moreover we were faced with the question of importance, again, as related to scaffold design factors: what design and material features produce distinctive results, in terms of growth and quality, as it applies to this class of materials? This evaluation not only confirmed permeability differences between scaffold designs, it also paralleled the findings of others in that it gives the appearance[xii] that permeability and macroporosity are inextricable and can be either referred to interchangeably or considered the same design variable. However, Karande et al. explicitly points out that while it is true that the two factors run in the same direction (an increase in porosity leads to an increase in permeability) it is only so when there is a high degree of

[xii] As mentioned previously, the data is suggestive of collinearity between the variables permeability and macroporosity. This is true in the case of this study design, but is not necessarily true when interconnectivity is adjusted.

interconnectivity, as demonstrated by Agrawal et al.[32] More interesting than the permeability differences between the current study's scaffold designs is the finding that the low permeability scaffold produces more total regenerate bone and a higher degree of bony ingrowth than the high permeability scaffolds; counter to what has been demonstrated in the literature. This mirrors the results of macroporosity and further supports the influence of high connectivity within scaffold geometries.

Singularly we are able to demonstrate the effectiveness of permeability, surface area, and macroporosity in producing new and relevant tissue constructs. However, when analyzed with the intent to determine a hierarchy of importance, the individual contributions are either obfuscated or diminished; this is due to the original experimental design. For example, the linear regression model for bone growth (total bone volume, internal bone volume, and ingrowth) with macroporosity, S:V, and permeability as covariates cannot be determined because data, as presented, appear collinear. This means that, as designed, this study is not well-suited to truly address distinctions in permeability, macroporosity and surface area. A better study design (and certainly best if determined pre-experimentally) would include variations in the three cofactors while keeping others constant; taking the current study from a 12-group investigation to a minimally 48-group investigation. This lesson in statistics reveals, if nothing else, the importance of determining study parameters *a priori* to ensure data will unequivocally answer desired questions. All that said, an evaluation of the current data does allow for

a compromise: to look at the 2-factor interaction of surface area and permeability, without inclusion of the macroporosity, and determine its effect on bone regeneration as well as the relative significance of the two. For all reasons previously discussed, an evaluation of S:V-permeability influence mirrors an evaluation of S:V-macroporosity influence. Nonetheless, we believe the information was relevant and lessons were learned from such an inspection.

Data rendered demonstrates the individual significance of surface area, surface to volume ratio, permeability, and macroporosity in the regeneration of neo-bone. Collectively these factors form the “holy grail” for artificially-induced tissue regeneration in any anatomical defect site: large enough pores for the penetration of bone; sufficient surface area to encourage the attachment, spreading, and proliferation of osteoblasts; and enough connected space such that nutrient delivery and waste removal are effective enough to encourage healthy vascularized tissue. Furthermore, we can also choose a composition and fabrication profile that can influence both mineralization and structural bone quality.

Conversely, in the attempt to compare the influence of these individual factors and determine a hierarchy of significance, our efforts are not as valiant. This, too, is supported throughout literature. So many studies attempt to address separately macroporosity, microporosity, pore size, permeability, and interconnectedness. What

occurs does so in one of two ways: (we) discover the difficulty in isolating all of these factors for study, and come up with conclusions that are “binary by nature: “These factors are important to have; without them, no tissue growth occurs”. In trying to tease out the hierarchy we find 1. These factors are inter-related, and 2. We have no real ability to determine, isolate, or delineate one factor from another and test enough permutations in vivo to say for sure which is more important. What we can do, at best, is to understand our experimental limitations and decide within the realm of our available resources how to achieve better engineered constructs.

## 7.5 Chapter Summary and Conclusion

To the best of our understanding, no data has been reported in the literature specifically demonstrates, or addresses, the predictive influence of scaffold design parameters on neo-bone regeneration in calcium phosphate materials. In an earlier study, we evaluated the volume and mineral and structural quality of newly regenerated osseous tissue for its dependence on scaffold composition, macroporosity, and microporosity generated via sintering temperature. Data from this study revealed that macroporosity has the most influence on the volume of bone regenerated, while the mineral quality was most influenced by composition and structural quality by sintering temperature. Furthermore, we demonstrated although that TCP has the more desirable in vivo performance, due to interaction effects of composition and macroporosity, HA scaffolds

can surpass the regenerative potential of TCP if design modifications are considered. Although this work produced important results, several new questions needed to be considered regarding the importance of surface area and permeability in the collective determination of bone growth. The post-hoc evaluation of the aforementioned data was our attempt to answer those questions. Our conclusions follow:

- *This study demonstrated that the surface areas of the scaffolds are distinguishable and that available surface area is a significant factor in the regeneration of neo-bone, with surface area to volume ratio being a slightly more significant determinant.*
- *This study demonstrated that the scaffold permeabilities were distinctly (significantly) different, and that the lower permeability produces higher bone ingrowth, as in the initial study with respect to macroporosity, the amount of ingrowth was significantly higher for the lower permeability scaffold.*
- *The high degree of interconnectivity (100%) of both scaffold designs does not allow permeability and macroporosity to be distinguishable in terms of their individual influence on bone regeneration. Therefore, they cannot be treated as covariates in the linear regression equation.*
- *And, finally, when compared to surface area to volume ratio, the macroporosity-permeability influence is significantly more substantial than the available surface area in terms of overall bone regeneration and ingrowth.*

# CHAPTER 8
# CONCLUSIONS AND FUTURE WORK

*"I think and think for months and years. Ninety-nine times the conclusion is false. The hundredth time I am right"*
*-Albert Einstein*

## 8.1 General Discussion and Thesis Summary

The ability to design and fabricate effective scaffolds depends on our ability to identify and control important parameters related to scaffold architecture and its impact on tissue regeneration. Knowledge of a material's structural, mechanical, and degradation bulk properties a priori and the subsequent application of that knowledge to the fabrication of degradable scaffolds that match predetermined requirements is paramount. Similarly, knowledge of a tissue's growth rate and changes in mechanical property as a result of regeneration, for example, would aid in the production of a scaffold demonstrating tissue specificity.

How close are we to the realization of an ideal porous scaffold designed for the repair of bone? Tissue specificity dictates what is needed and what is important. For boney

tissue, osteoconductivity and mechanical integrity form the basic needs. Osteoconductivity, the umbrella requirement, describes several architectural features/needs, as well as covers “inherent functionality” of the construct. Included are requirements related to pore size, pore volume and macroporosity, interconnections with inherent functionality being related to scaffold permeability and its ability to induce vascularization, necessary for the development and survival of any newly regenerated tissue. The mechanical requirement is somewhat simpler: scaffolds need to be able to provide structural support that can withstand the mechanical demands of the tissue’s anatomical location for the duration of the regenerative period.

Requirements of ideal scaffolds however, are not limited to only these two, osteoconductivity and mechanics. There are far more considerations to make; these being of the inherent material nature. Given a choice of material, decisions regarding fabrication are also necessary. A choice affecting salient features such as microporosity, surface area, surface chemistry, surface attachment, pore orientation, surface roughness, and pore shape. Other factors worth considering are the material’s osteoinductivity and in the event of reduced osteoinductivity, delivery of biologics such as stem cells and growth factors. For any choice of material, for example, it has been shown that design features, and even processing methodologies, may overcome many of the inherent short comings and allow for the exploitation of its more positive or advantageous features. For example, the lack of osteoinductivity of several polymeric

materials can be addressed with HA coatings that encourage cellular and protein attachment; metal materials may be thermally coated or etched to achieve similar goals.

Calcium phosphate materials (CaP), materials chosen for this body of work, are commonly touted as materials having near perfect chemistry for the boney applications. These materials are highly favored as augmenting materials because of their innate ability to bond with bone and provide the requisite environment for favorable bone regeneration. This is because the mineral component of bone tissue, hydroxyapatite (HA), is so closely matched to the HA mineral component of CaP bioceramic compositions.

This dissertation targets the identification of critical scaffold properties that drive performance in terms of bone regeneration within the degrading calcium phosphate construct. Work done demonstrated that designed architectural features were more critical in facilitating bone regeneration from CaP scaffolding materials, but inherent materials attributes were more instrumental in producing quality tissue growth.

In chapter three, dense constructs were used to characterize composition and temperature effects on microstructure and initial mechanical properties. We established a relationship between sinterability, percent TCP, and sintering temperature. Constructs high in β-TCP (greater than 50% phase amount) were able to maintain composition,

whereas HA and 25% TCP biphasic groups demonstrated a phase shift to ~12-14% β-TCP, most likely the result of dehydroxylation of HA at low sintering temperatures. Furthermore, the densification of these constructs also varied with percent TCP and temperature. Increases in TCP scaled with higher densities and density increased with sintering temperature. This means that for compositions tested, the highest relative densities (lowest microporosities) were for 100% TCP pellets sintered at 1150$^{o}$C. Fracture strength of sintered disks were also evaluated for compositional and porosity influence. We demonstrated that compositions with higher fractions of β-TCP were stronger and that constructs high in microporosity were weaker. The 75/25 TCP/HA composition was an anomaly and may have been due to a combination of inefficient packing of agglomerated particles and microstructure developed due to sintering. We showed a porosity dependence of Weibull modulus and suggested a trend of high variability in Weibull modulus for microporosities greater than 37% and the achievement of a near-steady state for lesser microporosities. Finally, we were able to establish cathodoluminescence as an important and effective technique in the visualization and distinction of HA and β-TCP grains.

In chapter 4 we demonstrated the ability to design and fabricate porous scaffolds with targeted architecture and mechanical properties in the range of human trabecular bone. We analyzed the initial baseline mechanical properties as a function of macroporosity and composition. 50/50 HA/TCP biphasic compositions had higher overall fracture

strengths as compared to single-phase HA and TCP. Constructs highest in porosity were weakest.

Chapter 5 analyzed the mechanical behavior, specifically the ability to retain strength, due to degradation. Scaffolds were implanted in subcutaneous sites within a mouse model and evaluated for changes in strength and modulus post-implantation. Time periods ranged from zero to eight weeks. We determined that strength retention was lowest for biphasic compositions, and that of the factors affecting the moduli and strength of the scaffolds, macroporosity and sintering temperature were most important. We also established differences in significance of factors as a function of degradation period.

Chapter 6 focused on those parameters significant to the regeneration of bone. Ectopic mouse models with delivery of osteogenic cells were used in this study. Regeneration was assessed as a function of macroporosity, composition, and sintering temperature. We determined that macroporosity was most important for bone regeneration. Data from this study reveals several salient points: 1.) *the amount of bone regenerated was dependent on the scaffold's macroporosity, and, counter to what is reported in literature:* ***lower macroporosity prevailed over higher in terms of the amount of bone ingrowth into the scaffold;*** 2.) *the amount of regenerated bone was independent of*

*the scaffold's composition or sintering temperature; and* 3.) *The composition and sintering temperature of the scaffold influences the mineralization and structural quality of the developing tissue.* Furthermore, it can be inferred that TCP has the more desirable *in vivo* performance, but due to interaction effects of composition and macroporosity, HA scaffolds can surpass the regenerative potential of TCP if design modifications are considered.

Chapter 7 revaluated data from the in vivo study to determine if other design parameters, surface area and permeability, were explanatory in the results of Chapter 6, and ascertain the relative importance of these design parameters to macroporosity in the regeneration of bone from these materials. We demonstrated available surface area is a significant factor in the regeneration of neo-bone, with surface area to volume ratio being a slightly more significant determinant. We showed that highest scaffold permeability did not produce highest bone ingrowth, and postulate that it may not be as significant, comparatively speaking, as it is for non-osteoconductive surfaces. And finally, when compared to surface area to volume ratio, the macroporosity-permeability influence is significantly more substantial than the available surface area in terms of overall bone regeneration and ingrowth.

A driving motivation of work done in this thesis was to be able to determ

## 8.2 Future Directions

*“Science never solves a problem without creating ten more”.*

*-George Bernard Shaw*

.

Work done in this thesis was performed in an effort to determine if scaffold properties due to material properties were more significant than those due to designed architecture in the application of calcium phosphate bioceramics for bone tissue engineering. We demonstrated the significance of both: materials properties (due to material choice and fabrication or processing parameters) were important for the quality of bone regenerated, while designed architectural features were instrumental in the facilitation of bone regeneration. Future work as it relates to this idea can follow one of two directions: 1.) to further the understanding of degradation kinetics of the materials studied, and 2.) to further the understanding of degradation mechanics; both directions ultimately enhance clinical relevancy.

### 8.2.1 Understanding degradation mechanics

We examined the regeneration potential of the degrading CaP scaffolds in an ectopic environment, the benefit of which is to provide an “isolated” *in vivo* laboratory milieu, allowing for more rigorous control of experimental variables. This model is optimal for understanding mechanisms and pathways or isolating events in the much same way knockout models are prime for studying genetic deficiencies. As a result of the model used, we are able to understand osteoconductivity of our scaffolding materials, understand degradation in an *in vivo* environment sans bone ingrowth, and study scaffold architectural influences on bone regeneration. The disadvantage to studying bone-related events in this fashion is that the ectopic environment does not provide the totality of necessary physiological environment conducive to longer-term study of bone development or regeneration. Mechanically-mediated adaptation calls for the remodeling of bone as a function of physiological loading. Subcutaneous implantation does not provide the requisite mechanical loading to sustain bone regeneration for prolonged periods of time. In fact, the onset of resorption has been shown to occur with the 10-12 week post-implantation. To circumvent this issue, longer-term studies (on the order of 6-8 months) should be investigated in the orthotopic site. By doing so with larger-scale scaffolds, constructs are subject to necessary biologics and mechanical stimuli to affect both regeneration and degradation and impart higher clinical relevancy.

The understanding of the control of degradation for the CaP family is well-investigated and well-understood. Control of degradation rate, through the manipulation of composition, i.e. phase amount of stable CaP phases, has shown promise in controlling the duration of implant survival. As such, studies have demonstrated that these degrading materials can survive several months to years in the body with favorable regenerative (and degradative) results. What is not as well-understood is how the degradation of mechanical properties, and the control thereof, fares within this paradigm.

One of the primary objectives of this work was to establish the materials property degradation profile for degrading CaP materials; specifically to understand in what way, and how much, do they degrade or vary from the material's initial mechanical properties. The work performed in chapter 5 demonstrated that the maintenance or retention of mechanical properties is not as tied (linearly) to composition as is degradation, where, for instance in a biphasic composition, degradation rate falls between the rates of its constituent phases. Strength and modulus at various time points, or time point intervals, were not ranked with degradation rates. In the first interval (0-4weeks) biphasic compositions experienced the highest net loss in strength and stiffness. At the intermediate interval (4-8 weeks) , they experienced the lowest net

gain in both, and overall (0-8 weeks), they experienced the lowest gain in strength and the only net loss in stiffness.

We used a liner regression model to fit, and rank, the significance of the factors tested in the maintenance of mechanical function of the scaffolds. We determined that, of the factors studied (macroporosity, composition, sintering temperature, and microporosity), macroporosity was the most significant in the retention of strength and stiffness, with composition or microporosity as the least, for this class of materials. An interesting note was that if modeled at different points of degradation the relative significance of any of the factors may differ according to when in time the model is fit. More plainly, the factors of significance at time = 0 may not be significant, not at all or not in the same manner, as those significant at later time points. A next step in understanding the degradation behavior of these materials and, therefore understanding the design requirements of CaP scaffolds, should investigate how these influences change as a function of degradation, and using SFF methods, investigate how design attributes can accommodate for any loss in regenerative potential or mechanical function. To do so, time-dependent models need to be utilized. Furthermore, the models should allow for the investigation of several other structural and architectural factors, pore shape for instance, not critical for overall regeneration of bone, but critical in the fracture behavior of ceramic materials.

### 8.2.2 Understanding degradation kinetics

In Specific Aim 1, addressed in Chapter 3 of this work, we demonstrated that cathodoluminescence is an effective tool in the visualization of CaP granular material. It was established that, unlike conventional microscopy methodologies such as SEM and EPMA, CL has the ability to distinguish small differences in Ca/P ratios, and hence distinguish between the phases of calcium phosphate materials. A natural extension of this work would investigate the degradation kinetics of the materials used. Several studies have been conducted that speak to the stability of hydroxyapatite, such that it is considered non-degrading; and that regulation of its stability for the purpose of garnering a degradable scaffold employs the use of more degradable CaP phases such as β-TCP. This statement is true, but may need to be refined, in that it may only apply to HA sintered at temperatures above 1250$^{o}$C. Work done in Chapter 3 demonstrated that for the low sintering temperatures of 1100$^{o}$C and 1150$^{o}$C, HA composition transformed, due to the dehydroxylation of HA, into β-TCP into a biphasic 86/14 percent HA/TCP construct. Also, the microstructure due to sintering (the high level of microporosity and morphology of grains) implies that sintering may have only proceeded through stage one, and bonding of sintered particles may be penetrable. Truth to these ideas would mean that some degree of degradation may be imparted on HA materials processed in this way. CL may be an effective way to study changes in surface and composition of degrading CaP materials, thereby adding to the body of knowledge of the degradation kinetics of CaP materials.

# Appendix 1: Data Tables

| **Composition effects on BMD indices for total bone regenerated internal and external to the scaffold** | | | |
|---|---|---|---|
| | TCP<br>*n=9* | 50/50<br>*n=12* | HA<br>*n=11* |
| BV ($mm^3$) | 20.62 ± 4.92 | 19.10 ± 3.70 | 22.39 ± 7.52 |
| TMC (mg) | 14.57 ± 3.81 | 12.41 ± 2.38 | 14.90 ± 4.90 |
| TMD ($mg/mm^3$) | 670.81 ± 57.65 | 650.82 ± 34.21 | 705.81 ± 50.86 |

| Temperature effects on BMD indices for total bone regenerated internal and external to the scaffold | | |
|---|---|---|
| | 1100°C<br>n=19 | 1150°C<br>n=13 |
| BV ($mm^3$) | 21.31 ± 6.01 | 19.71 ± 5.02 |
| TMC (mg) | 14.54 ± 4.08 | 12.89 ± 3.29 |
| | | |
| TMD ($mg/mm^3$) | 684.46 ± 49.69 | 656.63 ± 51.66 |
| | | |

| Macroporosity effects on BMD indices for total bone regenerated internal and external to the scaffold | | |
|---|---|---|
| | 40%<br>n=14 | 65%<br>n=18 |
| BV ($mm^3$) | 23.19 ± 5.66 | 18.69 ± 4.83 |
| TMC (mg) | 15.43 ± 3.73 | 12.67 ± 3.51 |
| TMD ($mg/mm^3$) | 666.66 ± 44.43 | 678.21 ± 55.08 |

| Volume of bone ($mm^3$) infiltrated into various internal regions of the scaffold | | | |
|---|---|---|---|
| | TCP<br>*n=9* | 50/50<br>*n=12* | HA<br>*n=11* |
| $C_0$ | 13.75 ± 3.14 | 11.99 ± 3.29 | 13.77 ± 2.65 |
| $C_1$ | 7.74 ± 1.83 | 7.06 ± 1.96 | 8.17 ± 1.34 |
| $C_2$ | 3.44 ± 0.78 | 3.26 ± 0.96 | 4.05 ± 0.83 |
| $C_3$ | 0.93 ± 0.40 | 0.70 ± 0.39 | 0.85 ± 0.26 |

Values are expressed as arithmetic means ± standard deviation.

$C_0$: Entire interior of scaffold; $C_1$: 0.71mm into the interior of scaffold ; $C_2$: 1.42 mm into the interior of scaffold ; $C_3$: 2.13 mm into the interior of scaffold

| **Mineral content (mg) of tissue infiltrated into various internal regions of the scaffold** | | | |
|---|---|---|---|
| | TCP<br>*n=9* | 50/50<br>*n=12* | HA<br>*n=11* |
| $C_0$ | 10.09 ± 2.63 | 7.96 ± 2.00 | 9.47 ± 1.62 |
| $C_1$ | 5.67 ± 1.62 | 4.67 ± 1.24 | 5.59 ± 0.79 |
| $C_2$ | 2.49 ± 0.69 | 2.14 ± 0.59 | 2.74 ± 0.48 |
| $C_3$ | 0.70 ± 0.32 | 0.48 ± 0.25 | 0.62 ± 0.17 |

Values are expressed as arithmetic means ± standard deviation.

$C_0$: Entire interior of scaffold; $C_1$: 0.71mm into the interior of scaffold; $C_2$: 1.42 mm into the interior of scaffold; $C_3$: 2.13 mm into the interior of scaffold

| Mineral density (mg/mm$^3$) of tissue infiltrated into various internal regions of the scaffold | | | |
|---|---|---|---|
| | TCP<br>*n=9* | 50/50<br>*n=12* | HA<br>*n=11* |
| $C_0$ | 730.23 ± 49.30 | 667.97 ± 55.28 | 692.92 ± 73.92 |
| $C_1$ | 725.76 ± 52.75 | 663.76 ± 44.76 | 689.96 ± 78.08 |
| $C_2$ | 718.51 ± 50.68 | 658.00 ± 45.18 | 685.79 ± 78.98 |
| $C_3$ | 757.83 ± 57.16 | 695.90 ± 50.24 | 740.97 ± 109.68 |

Values are expressed as arithmetic means ± standard deviation.

$C_0$: Entire interior of scaffold; $C_1$: 0.71mm into the interior of scaffold; $C_2$: 1.42 mm into the interior of scaffold; $C_3$: 2.13 mm into the interior of scaffold

| Bone volume (mm3) infiltrated into various internal regions of the scaffold | | |
|---|---|---|
| | 1100°C (Low) *n = 19* | 1150°C (High) *n = 13* |
| $C_0$ | 13.07 ± 3.07 | 13.15 ± 3.19 |
| $C_1$ | 7.62 ± 1.83 | 7.66 ± 1.68 |
| $C_2$ | 3.58 ± 0.96 | 3.58 ± 0.88 |
| $C_3$ | 0.85 ± 0.37 | 0.76 ± 0.34 |

Values are expressed as arithmetic means ± standard deviation.

$C_0$: Entire interior of scaffold; $C_1$: 0.71mm into the interior of scaffold; $C_2$: 1.42 mm into the interior of scaffold; $C_3$: 2.13 mm into the interior of scaffold

| Mineral content (mm3) infiltrated into various internal regions of the scaffold | | |
|---|---|---|
| | 1100$^{o}$C (Low) *n = 19* | 1150$^{o}$C (High) *n = 13* |
| $C_0$ | 9.25 ± 2.23 | 8.83 ± 2.25 |
| $C_1$ | 5.36 ± 1.35 | 5.12 ± 1.23 |
| $C_2$ | 2.49 ± 0.64 | 2.38 ± 0.62 |
| $C_3$ | 0.63 ± 0.27 | 0.53 ± 0.23 |

Values are expressed as arithmetic means ± standard deviation.

$C_0$: Entire interior of scaffold; $C_1$: 0.71mm into the interior of scaffold; $C_2$: 1.42 mm into the interior of scaffold; $C_3$: 2.13 mm into the interior of scaffold

| Mineral density (mm3) infiltrated into various internal regions of the scaffold | | |
|---|---|---|
| | 1100°C (Low) *n = 19* | 1150°C (High) *n = 13* |
| $C_0$ | 710.36 ± 63.81 | 670.24 ± 50.05 |
| $C_1$ | 705.71 ± 67.88 | 667.55 ± 50.71 |
| $C_2$ | 700.04 ± 68.74 | 661.71 ± 47.97 |
| $C_3$ | 748.12 ± 90.34 | 700.59 ± 51.70 |

Values are expressed as arithmetic means ± standard deviation.

$C_0$: Entire interior of scaffold; $C_1$: 0.71mm into the interior of scaffold; $C_2$: 1.42 mm into the interior of scaffold; $C_3$: 2.13 mm into the interior of scaffold

| Bone volume (mm3) infiltrated into various internal regions of the scaffold | | |
|---|---|---|
| | 40% Macroporosity *n=14* | 65% Macroporosity *n=18* |
| $C_0$ | 12.12 ± 2.65 | 13.87 ± 3.22 |
| $C_1$ | 6.95 ± 1.59 | 8.17 ± 1.72 |
| $C_2$ | 3.39 ± 0.95 | 3.74 ± 0.88 |
| $C_3$ | 0.52 ± 0.21 | 1.05 ± 0.26 |

Values are expressed as arithmetic means ± standard deviation.

$C_0$: Entire interior of scaffold; $C_1$: 0.71mm into the interior of scaffold; $C_2$: 1.42 mm into the interior of scaffold; $C_3$: 2.13 mm into the interior of scaffold

| Mineral content (mm3) infiltrated into various internal regions of the scaffold | | |
|---|---|---|
| | 40% Macroporosity *n=14* | 65% Macroporosity *n=18* |
| $C_0$ | 8.44 ± 1.87 | 9.57 ± 2.37 |
| $C_1$ | 4.77 ± 1.16 | 5.66 ± 1.27 |
| $C_2$ | 2.30 ± 0.65 | 2.55 ± 0.59 |
| $C_3$ | 0.40 ± 0.19 | 0.74 ± 0.21 |

Values are expressed as arithmetic means ± standard deviation.

$C_0$: Entire interior of scaffold; $C_1$: 0.71mm into the interior of scaffold; $C_2$: 1.42 mm into the interior of scaffold; $C_3$: 2.13 mm into the interior of scaffold

| Mineral density (mm3) infiltrated into various internal regions of the scaffold | | |
|---|---|---|
| | 40% Macroporosity *n=14* | 65% Macroporosity *n=18* |
| $C_0$ | 697.70 ± 63.82 | 691.23 ± 60.64 |
| $C_1$ | 685.27 ± 66.84 | 694.04 ± 62.45 |
| $C_2$ | 681.13 ± 66.65 | 687.07 ± 62.31 |
| $C_3$ | 763.76 ± 85.08 | 701.63 ± 65.04 |

Values are expressed as arithmetic means ± standard deviation.

$C_0$: Entire interior of scaffold; $C_1$: 0.71mm into the interior of scaffold; $C_2$: 1.42 mm into the interior of scaffold; $C_3$: 2.13 mm into the interior of scaffold

| Volume of bone ($mm^3$) penetrated into various internal regions of the scaffold | | | |
|---|---|---|---|
| | TCP<br>*n=9* | 50/50<br>*n=12* | HA<br>*n=11* |
| Ring 1[a] | 6.01 ± 1.43 | 4.93 ± 1.64 | 5.61 ± 1.50 |
| Ring 2[b] | 4.30 ± 1.08 | 3.80 ± 1.04 | 4.12 ± 0.56 |
| Ring 3[c] | 2.51 ± 0.45 | 2.57 ± 0.66 | 3.19 ± 0.84 |

| Volume of bone ($mm^3$) penetrated into various internal regions of the scaffold | | |
|---|---|---|
| | 1100°C (Low) *n = 19* | 1150°C (High) *n = 13* |
| Ring 1[a] | 5.45 ± 1.54 | 5.49 ± 1.63 |
| Ring 2[b] | 4.04 ± 0.95 | 4.07 ± 0.89 |
| Ring 3[c] | 2.73 ± 0.72 | 2.82 ± 0.77 |

| Volume of bone ($mm^3$) penetrated into various internal regions of the scaffold | | |
|---|---|---|
| | 40% Macroporosity *n=14* | 65% Macroporosity *n=18* |
| Ring 1[a] | 5.17 ± 1.21 | 5.70 ± 1.77 |
| Ring 2[b] | 3.57 ± 0.68 | 4.43 ± 0.90 |
| Ring 3[c] | 2.87 ± 0.80 | 2.69 ± 0.68 |

| Mineral content of bone (mg) penetrated into various internal regions of the scaffold | | | |
|---|---|---|---|
| | TCP<br>*n=9* | 50/50<br>*n=12* | HA<br>*n=11* |
| Ring 1[a] | 4.42 ± 1.12 | 3.29 ± 0.95 | 3.88 ± 0.97 |
| Ring 2[b] | 3.18 ± 0.95 | 2.54 ± 0.68 | 2.85 ± 0.36 |
| Ring 3[c] | 1.79 ± 0.40 | 1.66 ± 0.39 | 2.11 ± 0.49 |

| Mineral content of bone (mg) penetrated into various internal regions of the scaffold | | |
|---|---|---|
| | 1100°C (Low) *n = 19* | 1150°C (High) *n = 13* |
| Ring 1[a] | 3.88 ± 1.09 | 3.70 ± 1.09 |
| Ring 2[b] | 2.87 ± 0.76 | 2.75 ± 0.66 |
| Ring 3[c] | 1.86 ± 0.43 | 1.85 ± 0.53 |

| Mineral content of bone (mg) penetrated into various internal regions of the scaffold | | |
|---|---|---|
| | 40% Macroporosity *n=14* | 65% Macroporosity *n=18* |
| Ring 1 | 3.68± 0.83 | 3.91 ± 1.25 |
| Ring 2 | 2.46 ± 0.54 | 3.10 ± 0.72 |
| Ring 3 | 1.90 ± 0.52 | 1.82 ± 0.43 |

| Ingrowth (%) penetrated into various internal regions of the scaffold: effect of composition | | | |
|---|---|---|---|
| | TCP<br>*n=9* | 50/50<br>*n=12* | HA<br>*n=11* |
| Ring 1[a] | 26.22 ± 10.57 | 25.96 ± 11.87 | 29.76 ± 14.78 |
| Ring 2[b] | 31.19 ± 4.01 | 30.04 ± 7.56 | 31.68 ± 7.15 |
| Ring 3[c] | 22.18 ± 4.12 | 24.34 ± 7.14 | 27.24 ± 9.13 |

| Ingrowth (%) penetrated into various internal regions of the scaffold: effect of sintering temperature | | |
|---|---|---|
| | 1100°C (Low) *n = 19* | 1150°C (High) *n = 13* |
| Ring 1[a] | 27.34± 12.49 | 27.33 ± 12.66 |
| Ring 2[b] | 30.21 ± 5.44 | 31.99 ± 7.79 |
| Ring 3[c] | 23.72 ± 6.47 | 26.21 ± 8.46 |

| Ingrowth (%) penetrated into various internal regions of the scaffold: effect of macroporosity | | |
|---|---|---|
| | 40% Macroporosity *n=14* | 65% Macroporosity *n=18* |
| Ring 1[a] | 39.28± 6.17 | 18.05 ± 6.36 |
| Ring 2[b] | 33.41 ± 5.29 | 29.00 ± 6.73 |
| Ring 3[c] | 28.82 ± 7.03 | 21.55 ± 5.95 |

# REFERENCES


**1.** Donati D, Zolezzi C, Tomba P, Vigano A. Bone grafting: historical and conceptual review, starting with an old manuscript by Vittorio Putti. *Acta Orthopaedica.* 2007;78(1):19-25.

**2.** Bose AC. *Hymns from the Vedas*. Bombay ; New York: Asia Pub. House; 1966.

**3.** Buxton R. *Complete world of Greek mythology*. New York: Thames & Hudson; 2004.

**4.** *The 1911 Bible. The Holy Bible*. New York, London [etc.]: Oxford University Press, American branch; H. Frowde; 1911.

**5.** Deboer HH. The History of Bone-grafts. *Clinical Orthopaedics and Related Research.* Jan 1988(226):292-298.

**6.** Gross TP, Cox QGN, Jinnah RH. History and Current Application of Bone Transplantation. *Orthopedics.* Aug 1993;16(8):895-900.

**7.** Urist MR. Bone: Formation by Autoinduction. *Science.* 1965;150(3698):893-899.

**8.** Brown KLB, Cruess RL. BONE AND CARTILAGE TRANSPLANTATION IN ORTHOPEDIC-SURGERY - A REVIEW. *Journal of Bone and Joint Surgery-American Volume.* 1982;64(2):270-279.

**9.** Habibovic P, Yuan HP, van der Valk CM, Meijer G, van Blitterswijk CA, de Groot K. 3D microenvironment as essential element for osteoinduction by biomaterials. *Biomaterials.* 2005;26(17):3565-3575.

**10.** Lane JM, Tomin E, Bostrom MPG. Biosynthetic bone grafting. *Clinical Orthopaedics and Related Research.* Oct 1999(367):S107-S117.

**11.** Cornell CN, Lane JM. Current understanding of osteoconduction in bone regeneration. *Clinical Orthopaedics and Related Research.* Oct 1998(355):S267-S273.

**12.** Damien CJ, Parsons JR. Bone-graft and Bone-graft Substitutes - A Review of Current Technology and Applications. *Journal of Applied Biomaterials.* 1991;2(3):187-208.

**13.** Guldberg RE, Boerckel JD, Dosier CR, et al. Translational approaches for engineering bone repair. *Translational Approaches in Tissue Engineering and Regenerative Medicine.* 2008:125-144.

**14.** Mastrogiacomo M, Papadimitropoulos A, Cedola A, et al. Engineering of bone using bone marrow stromal cells and a silicon-stabilized tricalcium phosphate bioceramic: Evidence for a coupling between bone formation and scaffold resorption. *Biomaterials.* 2007;28(7):1376-1384.

**15.** Prolo DJ, Rodrigo JJ. CONTEMPORARY BONE-GRAFT PHYSIOLOGY AND SURGERY. *Clinical Orthopaedics and Related Research.* 1985(200):322-342.

**16.** Younger EM, Chapman MW. Morbidity at bone graft donor sites. *J Orthop Trauma.* 1989 1989;3(3):192-195.

**17.** Urist MR, Silverman BF, Buring K, Dubuc FL, Rosenberg JM. The bone induction principle rabbit, rat. *Clin Orthop Related Resin Complications of Orthopaedic Surgery.* 1967 1967;53:243-281.

**18.** Habibovic P. *Properties and Clinical Relevance of Osteoinductive Biomaterials* [PhD Dissertation]. Bilthoven, The Netherlands, University of Twente; 2005.
**19.** Yanoso-Scholl L, Jacobson J, Bradica G, Lerner A, O'Keefe R, Schwarz E. Evaluation of dense polylactic acid/beta-tricalcium phosphate scaffolds for bone tissue engineering. *Journal of biomedical materials research. Part A.* 2010;95A(3):717-726.
**20.** Griffith LG, Grodzinsky AJ. Advances in biomedical engineering. *Jama-Journal of the American Medical Association.* 2001;285(5):556-561.
**21.** Bronzino JD. *The biomedical engineering handbook*. Boca Raton: CRC Press : IEEE Press; 1995.
**22.** Thomson RC, Mikos AG, Beahm E, et al. Guided tissue fabrication from periosteum using preformed biodegradable polymer scaffolds. *Biomaterials.* 1999;20(21):2007-2018.
**23.** Doll BA, Wenke JC, Hollinger J. Critically sized bone defects. *Translational Approaches in Tissue Engineering and Regenerative Medicine.* 2008:253-269.
**24.** Lin Y, Yelick PC. Dental and craniofacial tissue engineering. *Translational Approaches in Tissue Engineering and Regenerative Medicine.* 2008:181-194.
**25.** David B, Bensidhoum M, Potier E, Hannouche D, Logeart D, Petite H. Bone tissue engineering. *Translational Approaches in Tissue Engineering and Regenerative Medicine.* 2008:231-252.
**26.** Pettikiriarachchi J, Parish C, Shoichet M, Forsythe J, Nisbet D. Biomaterials for Brain Tissue Engineering. *Australian journal of chemistry.* 2010;63(8):1143-1154.
**27.** Atala A. Clinical requirements for bioengineered internal organs. *Translational Approaches in Tissue Engineering and Regenerative Medicine.* 2008:271-285.
**28.** Kim K, Yeatts A, Dean D, Fisher JP. Stereolithographic Bone Scaffold Design Parameters: Osteogenic Differentiation and Signal Expression. *Tissue Engineering Part B-Reviews.* 2010;16(5):523-539.
**29.** Gauthier O, Bouler JM, Aguado E, Pilet P, Daculsi G. Macroporous biphasic calcium phosphate ceramics: influence of macropore diameter and macroporosity percentage on bone ingrowth. *Biomaterials.* 1998;19(1-3):133-139.
**30.** Chang B-S, Lee iCKfC-K, Hong K-S, et al. Osteoconduction at porous hydroxyapatite with various pore configurations. *Biomaterials.* 2000;21(12):1291-1298.
**31.** Hutmacher DW. Scaffolds in tissue engineering bone and cartilage. *Biomaterials.* 2000;21(24):2529-2543.
**32.** Karande T, Ong J, Agrawal C. Diffusion in musculoskeletal tissue engineering scaffolds: Design issues related to porosity, permeability, architecture, and nutrient mixing. *Annals of Biomedical Engineering.* 2004;32(12):1728-1743.
**33.** Komlev V, Peyrin F, Mastrogiacomo M, Cedola A, Papadimitropoulos A, Rustichelli F. Kinetics of in vivo bone deposition by bone marrow stromal cells into porous calcium phosphate scaffolds: An X-ray computed microtomography study. *Tissue Engineering.* 2006;12(12):3449-3458.

**34.** van Lenthe GH, Hagenmüller H, Bohner M, Hollister SJ, Meinel L, Müller R. Nondestructive micro-computed tomography for biological imaging and quantification of scaffold-bone interaction in vivo. *Biomaterials.* 2007;28(15):2479-2490.
**35.** Hollister SJ. Porous scaffold design for tissue engineering. *Nature Materials.* 2005;4(7):518-524.
**36.** Uebersax L, Hagenmueller H, Hofmann S, et al. Effect of scaffold design on bone morphology in vitro. *Tissue Engineering.* 2006;12(12):3417-3429.
**37.** Zeltinger J, Sherwood JK, Graham DA, Mueller R, Griffith LG. Effect of pore size and void fraction on cellular adhesion, proliferation, and matrix deposition. *Tissue Eng.* Oct 2001;7(5):557-572.
**38.** Mastrogiacomo M, Scaglione S, Martinetti R, et al. Role of scaffold internal structure on in vivo bone formation in macroporous calcium phosphate bioceramics. *Biomaterials.* 2006;27(17):3230-3237.
**39.** Oliveira JFD, Aguiar PFD, Rossi AM, Soares GA. Effect of Process Parameters on the Characteristics of Porous Calcium Phosphate Ceramics for Bone Tissue Scaffolds. *Artificial Organs.* 2003;27(5):406-411.
**40.** Karageorgiou V, Kaplan D. Porosity of 3D biornaterial scaffolds and osteogenesis. *Biomaterials.* 2005;26(27):5474-5491.
**41.** Hutmacher DW. Scaffold design and fabrication technologies for engineering tissues - state of the art and future perspectives. *Journal of Biomaterials Science-Polymer Edition.* 2001;12(1):107-124.
**42.** Muschler GE, Nakamoto C, Griffith LG. Engineering principles of clinical cell-based tissue engineering. *J. Bone Joint Surg.-Am. Vol.* Jul 2004;86A(7):1541-1558.
**43.** Alsberg E, Anderson KW, Albeiruti A, Franceschi RT, Mooney DJ. Cell-interactive alginate hydrogels for bone tissue engineering. *J. Dent. Res.* Nov 2001;80(11):2025-2029.
**44.** Place ES, Evans ND, Stevens MM. Complexity in biomaterials for tissue engineering. *Nature Materials.* 2009;8(6):457-470.
**45.** Corsi KA, Schwarz EM, Mooney DJ, Huard J. Regenerative medicine in orthopaedic surgery. *Journal of Orthopaedic Research.* 2007;25(10):1261-1268.
**46.** Li XD, Jin L, Balian G, Laurencin CT, Anderson DG. Demineralized bone matrix gelatin as scaffold for osteochondral tissue engineering. *Biomaterials.* 2006;27(11):2426-2433.
**47.** Mauney JR, Jaquiéry C, Volloch V, Heberer M, Martin I, Kaplan DL. In vitro and in vivo evaluation of differentially demineralized cancellous bone scaffolds combined with human bone marrow stromal cells for tissue engineering. *Biomaterials.* 2005;26(16):3173-3185.
**48.** Woodard JR, Hilldore AJ, Lan SK, et al. The mechanical properties and osteoconductivity of hydroxyapatite bone scaffolds with multi-scale porosity. *Biomaterials.* 2007;28(1):45-54.
**49.** Komlev VS, Mastrogiacomo M, Pereira RC, Peyrin F, Rustichelli F, Cancedda R. Biodegradation of Porous Calcium Phosphate Scaffolds in an Ectopic Bone

Formation Model Studied by X-ray Computed Microtomography. *European Cells & Materials.* 2010;19:136-146.

**50.** Wilson CE, de Bruijn JD, van Blitterswijk CA, Verbout AJ, Dhert WJA. Design and fabrication of standardized hydroxyapatite scaffolds with a defined macro-architecture by rapid prototyping for bone-tissue-engineering research. *Journal of Biomedical Materials Research Part A.* 2004;68A(1):123-132.

**51.** Sanchez-Salcedo S, Izquierdo-Barba I, Arcos D, Vallet-Regi M. In vitro evaluation of potential calcium phosphate scaffolds for tissue engineering. *Tissue Engineering.* 2006;12(2):279-290.

**52.** Chu TMG, Halloran JW, Hollister SJ, Feinberg SE. Hydroxyapatite implants with designed internal architecture. *Journal of Materials Science-Materials in Medicine.* 2001;12(6):471-478.

**53.** Kim S, Kim SS, Lee SH, et al. In vivo bone formation from human embryonic stem cell-derived osteogenic cells in poly(D,L-lactic-co-glycolic acid)/hydroxyapatite composite scaffolds. *Biomaterials.* 2008;29(8):1043-1053.

**54.** Chesnutt BM, Viano AM, Yuan YL, et al. Design and characterization of a novel chitosan/nanocrystalline calcium phosphate composite scaffold for bone regeneration. *Journal of Biomedical Materials Research Part A.* 2009;88A(2):491-502.

**55.** Costa HS, Mansur AAP, Barbosa-Stancioli EF, Pereira MM, Mansur HS. Morphological, mechanical, and biocompatibility characterization of macroporous alumina scaffolds coated with calcium phosphate/PVA. *Journal of Materials Science.* 2008;43(2):510-524.

**56.** Park JB, Lakes RS. *Biomaterials An Introduction*. Second ed. New York: Plenum Press; 1992.

**57.** Baron R. General Principles of Bone Biology. In: Favus MJ, M.D., ed. *Primer on the Metabolic Bone Diseases and Disorders of Mineral Metabolism*. Washington, D.C.: The American Society for Bone and Mineral Research; 2003:1-8.

**58.** Ross MH, Pawlina W. *Histology: A Text and Atlas with correlated cell and molecular biology*. 5th Edition ed. Baltimore, MD: Lippincott Williams & Wilkins; 2006.

**59.** Fawcett DW, Jensh RP. *Bloom & Fawcett's Concise Histology*. 2nd Edition ed. London: Arnold, a member of the Hodder Headline Group; 2002.

**60.** Lian JB, Stein GS, Aubin JE. Bone Formation: Maturation and Functional Activities of Osteoblast Lineage Cells. In: Favus MJ, M.D., ed. *Primer on the Metabolic Bone Diseases and Disorders of Mineral Metabolism*. 5th ed. Washington, D.C.: The American Society for Bone and Mineral Research; 2003:13-28.

**61.** Vaughan J. *The Physiology of Bone*. Third ed. Oxford: Clarendon Press; 1981.

**62.** Recker RR, Barger-Lux MJ. Bone Biopsy and Histomorphometry in Clinical Practice. In: Favus MJ, M.D., ed. *Primer on Metabolic Bone Diseases and Disorders of Mineral Metabolism*. Washington, D.C.: The American Society for Bone and Mineral Research; 2003:213-219.

**63.** Nijweide PJ, Burger EH, Nulend JK, Van der Plas A. The Osteocyte. In: Bilezikian JP, Raisz LG, Rodan GA, eds. *Principles of Bone Biology*. San Diego: Academic Press; 1996:115-126.
**64.** Marks SC, Jr., Hermey DC. The Structure and Development of Bone. In: Bilezikian JP, Raisz LG, Rodan GA, eds. *Principles of Bone BIology*. San Diego: Academic Press; 1996:3-14.
**65.** Suda T, Udagawa N, Takahashi N. Cells of Bone: Osteoclast Generation. In: Bilezikian JP, Raisz LG, Rodan GA, eds. *Principles of Bone Biology*. San Diego: Academic Press; 1996:87-102.
**66.** Vaananen K. Osteoclast Function: Biology and Mechanisms. In: Bilezikian JP, Raisz LG, Rodan GA, eds. *Principles of Bone Biology*. San Diego: Academic Press; 1996:103-113.
**67.** Steiniche T, Hauge EM. Normal Structure and Function of Bone. In: An YH, Martin KL, eds. *Handbook of Histology Methods for Bone and Cartilage*. Totowa, New Jersey: Humana Press; 2003:59-72.
**68.** Mundy GR, Chen D, Oyajobi BO. Bone Remodeling. In: Favus MJ, M.D., ed. *Primer on the Metabloic Bone Diseases of Minerral Metabolism*. Washington. D.C.: The American Society for Bone and Minerral Research; 2003:46-58.
**69.** Frost HM. Skeletal structural adaptations to mechanical usage (SATMU): 2. Redefining Wolff's Law: The remodeling problem. *The Anatomical Record.* 1990;226(4):414-422.
**70.** Boskey AL. Matrix Proteins and Mineralization: An Overview. *Connect. Tissue Res.* 1996;35(1-4):357-363.
**71.** Boskey AL. Biomineralization: Conflicts, challenges, and opportunities. *J. Cell. Biochem.* 1998:83-91.
**72.** Young B, Lowe JS, Stevens A, Heath JW. *Wheater's Functional Histology. A Text and Colour Atlas*. 5th ed. Philadelphia: Churchill Livingstone Elsevier; 2006.
**73.** Katz JL. Mechanics of Hard Tissue. In: Bronzino JD, ed. *The Biomedical Engineering Handbook*. Boca Raton: CRC Press : IEEE Press; 1995:273-290.
**74.** Rho J-Y, Kuhn-Spearing L, Zioupos P. Mechanical properties and the hierarchical structure of bone. *Medical Engineering & Physics.* 1998;20(2):92-102.
**75.** Marieb EN. *Human Anatomy and Physiology*. Third Edition ed. Redwood City, California: The Benjamin/Cummings Publishing Co., Inc.; 1995.
**76.** Gibson LJ. THE MECHANICAL-BEHAVIOR OF CANCELLOUS BONE. *Journal of Biomechanics.* 1985 1985;18(5):317-&.
**77.** Bone cell lineage.
**78.** Bone Formation via Intramembraneous Ossification.
**79.** Bone Formation via Endochondrial Ossification.
**80.** Bone Modeling and Remodeling.
**81.** Gross Anatomy of a Long Bone: Benjamin Cummings.
**82.** Netter F. Structure of Trabecular Bone.
**83.** Structure of Cortical Bone.

**84.** Thangamani N, Chinnakali K, Gnanam FD. The effect of powder processing on densification, microstructure and mechanical properties of hydroxyapatite. *Ceramics International.* 2002;28(4):355-362.
**85.** Petrov OE, Dyulgerova E, Petrov L, Popova R. Characterization of calcium phosphate phases obtained during the preparation of sintered biphase Ca-P ceramics. *Materials Letters.* 2001;48(3-4):162-167.
**86.** Raynaud S, Champion E, Lafon JP, Bernache-Assollant D. Calcium phosphate apatites with variable Ca/P atomic ratio III. Mechanical properties and degradation in solution of hot pressed ceramics. *Biomaterials.* 2002;23(4):1081-1089.
**87.** Liu DM. Influence of porous microarchitecture on the in-vitro dissolution and biological behaviour of porous calcium phosphate ceramics. *Porous Materials for Tissue Engineering.* 1997;250:183-208.
**88.** Lin FH, Liao CJ, Chen KS, Sun JS, Lin CP. Petal-like apatite formed on the surface of tricalcium phosphate ceramic after soaking in distilled water. *Biomaterials.* 2001;22(22):2981-2992.
**89.** Ito A, Kawamura H, Miyakawa S, et al. Resorbability and solubility of zinc-containing tricalcium phosphate. *Journal of Biomedical Materials Research.* 2002;60(2):224-231.
**90.** Gauthier O, Bouler JM, Aguado E, Legeros RZ, Pilet P, Daculsi G. Elaboration conditions influence physicochemical properties and in vivo bioactivity of macroporous biphasic calcium phosphate ceramics. *Journal of Materials Science: Materials in Medicine.* 1999;10(4):199-204.
**91.** Ducheyne P. Bioceramics - Material Characteristics Versus InVivo Behavior. *Journal of Biomedical Materials Research-Applied Biomaterials.* 1987;21(A2):219-236.
**92.** Best S, Sim B, Kayser M, Downes S. The dependence of osteoblastic response on variations in the chemical composition and physical properties of hydroxyapatite. *Journal of Materials Science-Materials in Medicine.* 1997;8(2):97-103.
**93.** Legeros RZ, Lin S, LeGEros JP, Mijares D, Dimanno F, Serekian P. Effect of Firing Temperature on Properties of Biphasic Calcium Phosphates. Paper presented at: Society for Biomaterials 29th Annual Meeting Transactions2203; Reno, Nevada.
**94.** Bouslama N, Ben Ayed F, Bouaziz J. Effect of fluorapatite additive on densification and mechanical properties of tricalcium phosphate. *Journal of the Mechanical Behavior of Biomedical Materials.* 2010;3(1):2-13.
**95.** Winter M, Griss P, Degroot K, et al. Comparative Histocompatability Testing of 7 Calcium-Phosphate Ceramics. *Biomaterials.* 1981;2(3):159-&.
**96.** Ruys AJ, Wei M, Sorrell CC, Dickson MR, Brandwood A, Milthorpe BK. Sintering Effects on the Strength of Hydroxyapatite. *Biomaterials.* 1995;16(5):409-415.
**97.** Kivrak N, Tas AC. Synthesis of calcium hydroxyapatite-tricalcium phosphate (HA-TCP) composite bioceramic powders and their sintering behavior. *Journal of the American Ceramic Society.* 1998;81(9):2245-2252.

**98.** Cuneyt Tas A, Korkusuz F, Timucin M, Akkas N. An investigation of the chemical synthesis and high-temperature sintering behaviour of calcium hydroxyapatite (HA) and tricalcium phosphate (TCP) bioceramics. *Journal of Materials Science: Materials in Medicine.* 1997;8(2):91-96.
**99.** Evis Z, Ozturk F. Investigation of tensile strength of hydroxyapatite with various porosities by diametral strength test. *Materials Science and Technology.* 2008;24(4):474-478.
**100.** Diggs A. Sinterability of Wet Ball-Milled HA and β-TCP powders.2003.
**101.** Ben Ayed F, Chaari K, Bouaziz J, Bouzouita K. Frittage du phosphate tricalcique. *Comptes Rendus Physique.* 2006;7(7):825-835.
**102.** Enderle R, Götz-Neunhoeffer F, Göbbels M, Müller FA, Greil P. Influence of magnesium doping on the phase transformation temperature of β-TCP ceramics examined by Rietveld refinement. *Biomaterials.* 2005;26(17):3379-3384.
**103.** Ryu HS, Youn HJ, Hong KS, Chang BS, Lee CK, Chung SS. An improvement in sintering property of beta-tricalcium phosphate by addition of calcium pyrophosphate. *Biomaterials.* 2002;23(3):909-914.
**104.** Raynaud S, Champion E, Bernache-Assollant D, Thomas P. Calcium phosphate apatites with variable Ca/P atomic ratio I. Synthesis, characterisation and thermal stability of powders. *Biomaterials.* 2002;23(4):1065-1072.
**105.** Lukić M, Stojanović Z, Škapin SD, et al. Dense fine-grained biphasic calcium phosphate (BCP) bioceramics designed by two-step sintering. *Journal of the European Ceramic Society.* 2011;31(1–2):19-27.
**106.** Raynaud S, Champion E, Bernache-Assollant D. Calcium phosphate apatites with variable Ca/P atomic ratio II. Calcination and sintering. *Biomaterials.* 2002;23(4):1073-1080.
**107.** Yang XH, Wang ZH. Synthesis of biphasic ceramics of hydroxyapatite and beta-tricalcium phosphate with controlled phase content and porosity. *Journal of Materials Chemistry.* 1998;8(10):2233-2237.
**108.** Ginebra MP, Driessens FCM, Planell JA. Effect of the particle size on the micro and nanostructural features of a calcium phosphate cement: a kinetic analysis. *Biomaterials.* 2004;25(17):3453-3462.
**109.** Li X, van Blitterswijk CA, Feng Q, Cui F, Watari F. The effect of calcium phosphate microstructure on bone-related cells in vitro. *Biomaterials.* 2008;29(23):3306-3316.
**110.** dos Santos EA, Farina M, Soares GA, Anselme K. Chemical and topographical influence of hydroxyapatite and beta-tricalcium phosphate surfaces on human osteoblastic cell behavior. *Journal of Biomedical Materials Research Part A.* May 2009;89A(2):510-520.
**111.** Rouahi M, Gallet O, Champion E, Dentzer J, Hardouin P, Anselme K. Influence of hydroxyapatite microstructure on human bone cell response. *Journal of Biomedical Materials Research Part A.* 2006;78A(2):222-235.

**112.** Okuda T, Ioku K, Yonezawa I, et al. The effect of the microstructure of beta-tricalcium phosphate on the metabolism of subsequently formed bone tissue. *Biomaterials.* Jun 2007;28(16):2612-2621.
**113.** Gross KA, Muller D, Lucas H, Haynes DR. Osteoclast resorption of thermal spray hydoxyapatite coatings is influenced by surface topography. *Acta Biomaterialia.* 2012;8(5):1948-1956.
**114.** Isaac J, Hornez J-C, Jian D, Descamps M, Hardouin P, Magne D. β-TCP microporosity decreases the viability and osteoblast differentiation of human bone marrow stromal cells. *Journal of Biomedical Materials Research Part A.* 2008;86A(2):386-393.
**115.** Dorozhkin SV. Calcium Orthophosphates as Bioceramics: State of the Art. *Journal of Functional Biomaterials.* 2010;1(1):22-107.
**116.** Pecqueux F, Tancret F, Payraudeau N, Bouler JM. Influence of microporosity and macroporosity on the mechanical properties of biphasic calcium phosphate bioceramics: Modelling and experiment. *Journal of the European Ceramic Society.* 2010;30(4):819-829.
**117.** Benaqqa C, Chevalier J, Saädaoui M, Fantozzi G. Slow crack growth behaviour of hydroxyapatite ceramics. *Biomaterials.* 2005;26(31):6106-6112.
**118.** Kwon SH, Jun YK, Hong SH, Lee IS, Kim HE, Won YY. Calcium phosphate bioceramics with various porosities and dissolution rates. *Journal of the American Ceramic Society.* 2002;85(12):3129-3131.
**119.** Degroot K. Bioceramics Consisting of Calcium-Phosphate Salts. *Biomaterials.* 1980;1(1):47-50.
**120.** Daculsi G, Legeros RZ, Heughebaert M, Barbieux I. Formation of Carbonate-Apatite Crystals After Implantation of Calcium-Phosphate Ceramics. *Calcified Tissue International.* 1990;46(1):20-27.
**121.** Porter NL, Pilliar RM, Grynpas MD. Fabrication of porous calcium polyphosphate implants by solid freeform fabrication: A study of processing parameters and in vitro degradation characteristics. *Journal of Biomedical Materials Research.* 2001;56(4):504-515.
**122.** Barbarand J, Pagel M. Cathodoluminescence study of apatite crystals. *American Mineralogist.* Apr 2001;86(4):473-484.
**123.** Kempe U, Gotze J. Cathodoluminescence (CL) behaviour and crystal chemistry of apatite from rare-metal deposits. *Mineralogical Magazine.* Feb 2002;66(1):151-172.
**124.** Leichmann J, Broska I, Zachovalova K. Low-grade metamorphic alteration of feldspar minerals: a CL study. *Terra Nova.* Apr 2003;15(2):104-108.
**125.** Gross KA, Phillips MR. Identification and mapping of the amorphous phase in plasma-sprayed hydroxyapatite coatings using scanning cathodoluminescence microscopy. *Journal of Materials Science-Materials in Medicine.* Dec 1998;9(12):797-802.
**126.** Gross KA, Phillips MR, Suetsugu Y. Cathodoluminescence emission for differentiating the degree of carbonation in apatites. In: Giannini S, Moroni A,

eds. *Bioceramics.* Vol 192-1. Zurich-Uetikon: Trans Tech Publications Ltd; 2000:179-182.

**127.** Gotze J, Heimann RB, Hildebrandt H, Gburek U. Microstructure investigation into calcium phosphate biomaterials by spatially resolved cathodoluminescence. *Materialwiss. Werkstofftech.* Feb 2001;32(2):130-136.

**128.** Fahad MK. Stresses and failure in the diametral compression test. *Journal of Materials Science.* 1996;31(14):3723-3729.

**129.** Elliott JC. *Structure and chemistry of the apatites and other calcium orthophosphates*. Amsterdam [The Netherlands] : New York: Elsevier; 1994.

**130.** Nilen R, Richter P. The thermal stability of hydroxyapatite in biphasic calcium phosphate ceramics. *Journal of Materials Science: Materials in Medicine.* 2008;19(4):1693-1702.

**131.** Liao C-J, Lin F-H, Chen K-S, Sun J-S. Thermal decomposition and reconstitution of hydroxyapatite in air atmosphere. *Biomaterials.* 1999;20(19):1807-1813.

**132.** Muralithran G, Ramesh S. The effects of sintering temperature on the properties of hydroxyapatite. *Ceramics International.* 2000;26(2):221-230.

**133.** Wang PE, Chaki TK. Sintering behaviour and mechanical properties of hydroxyapatite and dicalcium phosphate. *Journal of Materials Science: Materials in Medicine.* 1993;4(2):150-158.

**134.** Diggs A, Hollister S, Chu TM. Fabrication and Characterization of 3-D Biphasic Ceramic Scaffolds Composed of Hydroxyapatite and β-Tricalcium Phosphate. Paper presented at: Society for Biomaterials 29th Annual Meeting 2003; Reno, Nevada.

**135.** Barsoum MW. *Fundamentals of ceramics*. New York: McGraw Hill; 1997.

**136.** Fan X, Case ED, Ren F, Shu Y, Baumann MJ. Part I: Porosity dependence of the Weibull modulus for hydroxyapatite and other brittle materials. *Journal of the Mechanical Behavior of Biomedical Materials.* Apr 2012;8:21-36.

**137.** Murray MGS, Wang J, Ponton CB, Marquis PM. AN IMPROVEMENT IN PROCESSING OF HYDROXYAPATITE CERAMICS. *Journal of Materials Science.* Jun 1995;30(12):3061-3074.

**138.** Cordell JM, Vogl ML, Johnson AJW. The influence of micropore size on the mechanical properties of bulk hydroxyapatite and hydroxyapatite scaffolds. *Journal of the Mechanical Behavior of Biomedical Materials.* 2009;2(5):560-570.

**139.** Diggs AB, Halloran J, Hollister SJ. Cathodoluminescence as a method of microstructure characterization of biphasic ceramics composed of hydroxyapatite and beta-tricalcium phosphate. In: Li P, Zhang K, Colwell CW, eds. *Bioceramics 17.* Vol 284-286. Zurich-Uetikon: Trans Tech Publications Ltd; 2005:333-336.

**140.** Sundelacruz S, Kaplan DL. Stem cell- and scaffold-based tissue engineering approaches to osteochondral regenerative medicine. *Semin. Cell Dev. Biol.* Aug 2009;20(6):646-655.

**141.** Bohner M, Loosli Y, Baroud G, Lacroix D. Commentary: Deciphering the link between architecture and biological response of a bone graft substitute. *Acta Biomaterialia.* 2011;7(2):478-484.

**142.** Wong DY, Krebsbach PH, Hollister SJ. Brain cortex regeneration affected by scaffold architectures. *Journal of Neurosurgery.* 2008;109(4):715-722.
**143.** Wong DY, Leveque JC, Brumblay H, Krebsbach PH, Hollister SJ, LaMarca F. Macro-architectures in spinal cord scaffold implants influence regeneration. *Journal of Neurotrauma.* Aug 2008;25(8):1027-1037.
**144.** Miot S, Woodfield T, Daniels AU, et al. Effects of scaffold composition and architecture on human nasal chondrocyte redifferentiation and cartilaginous matrix deposition. *Biomaterials.* May 2005;26(15):2479-2489.
**145.** Kemppainen JM, Hollister SJ. Differential effects of designed scaffold permeability on chondrogenesis by chondrocytes and bone marrow stromal cells. *Biomaterials.* Jan 2010;31(2):279-287.
**146.** Malda J, Woodfield TBF, van der Vloodt F, et al. The effect of PEGT/PBT scaffold architecture on the composition of tissue engineered cartilage. *Biomaterials.* Jan 2005;26(1):63-72.
**147.** Jeong CG, Hollister SJ. A comparison of the influence of material on in vitro cartilage tissue engineering with PCL, PGS, and POC 3D scaffold architecture seeded with chondrocytes. *Biomaterials.* 2010;31(15):4304-4312.
**148.** Freed LE, Marquis JC, Nohria A, Emmanual J, Mikos AG, Langer R. NEOCARTILAGE FORMATION INVITRO AND INVIVO USING CELLS CULTURED ON SYNTHETIC BIODEGRADABLE POLYMERS. *Journal of Biomedical Materials Research.* Jan 1993;27(1):11-23.
**149.** Li WJ, Tuli R, Okafor C, et al. A three-dimensional nanofibrous scaffold for cartilage tissue engineering using human mesenchymal stem cells. *Biomaterials.* Feb 2005;26(6):599-609.
**150.** Liao E, Yaszemski M, Krebsbach P, Hollister S. Tissue-engineered cartilage constructs using composite hyaluronic acid/collagen I hydrogels and designed poly(propylene fumarate) scaffolds. *Tissue Engineering.* Mar 2007;13(3):537-550.
**151.** Hing KA. Bioceramic bone graft substitutes: Influence of porosity and chemistry. *Int. J. Appl. Ceram. Technol.* 2005;2(3):184-199.
**152.** LeGeros RZ. Properties of Osteoconductive Biomaterials: Calcium Phosphates. *Clinical Orthopaedics and Related Research.* 2002;395:81-98.
**153.** Sun LM, Berndt CC, Grey CP. Phase, structural and microstructural investigations of plasma sprayed hydroxyapatite coatings. *Mater. Sci. Eng. A-Struct. Mater. Prop. Microstruct. Process.* Nov 2003;360(1-2):70-84.
**154.** Sun L, Berndt CC, Gross KA, Kucuk A. Material fundamentals and clinical performance of plasma-sprayed hydroxyapatite coatings: A review. *Journal of Biomedical Materials Research.* 2001;58(5):570-592.
**155.** Ducheyne P, Radin S, Heughebaert M, Heughebaert JC. Calcium phosphate ceramic coatings on porous titanium: effect of structure and composition on electrophoretic deposition, vacuum sintering and in vitro dissolution. *Biomaterials.* 1990;11(4):244-254.
**156.** Witte F, Fischer J, Nellesen J, et al. In vivo corrosion and corrosion protection of magnesium alloy LAE442. *Acta Biomaterialia.* May 2010;6(5):1792-1799.

**157.** Ryan G, Pandit A, Apatsidis DP. Fabrication methods of porous metals for use in orthopaedic applications. *Biomaterials.* May 2006;27(13):2651-2670.
**158.** Bansiddhi A, Sargeant TD, Stupp SI, Dunand DC. Porous NiTi for bone implants: A review. *Acta Biomaterialia.* Jul 2008;4(4):773-782.
**159.** Williams JM, Adewunmi A, Schek RM, et al. Bone tissue engineering using polycaprolactone scaffolds fabricated via selective laser sintering. *Biomaterials.* Aug 2005;26(23):4817-4827.
**160.** Di Martino A, Sittinger M, Risbud MV. Chitosan: A versatile biopolymer for orthopaedic tissue-engineering. *Biomaterials.* Oct 2005;26(30):5983-5990.
**161.** Wahl DA, Czernuszka JT. Collagen-hydroxyapatite composites for hard tissue repair. *European Cells & Materials.* Jan-Jun 2006;11:43-56.
**162.** Yang SF, Leong KF, Du ZH, Chua CK. The design of scaffolds for use in tissue engineering. Part 1. Traditional factors. *Tissue Engineering.* 2001;7(6):679-689.
**163.** Stevens B, Yang Y, MohandaS A, Stucker B, Nguyen KT. A review of materials, fabrication to enhance bone regeneration in methods, and strategies used engineered bone tissues. *Journal of Biomedical Materials Research Part B-Applied Biomaterials.* May 2008;85B(2):573-582.
**164.** Leong KF, Cheah CM, Chua CK. Solid freeform fabrication of three-dimensional scaffolds for engineering replacement tissues and organs. *Biomaterials.* Jun 2003;24(13):2363-2378.
**165.** Yang SF, Leong KF, Du ZH, Chua CK. The design of scaffolds for use in tissue engineering. Part II. Rapid prototyping techniques. *Tissue Engineering.* 2002;8(1):1-11.
**166.** Taboas JM, Maddox RD, Krebsbach PH, Hollister SJ. Indirect solid free form fabrication of local and global porous, biomimetic and composite 3D polymer-ceramic scaffolds. *Biomaterials.* Jan 2003;24(1):181-194.
**167.** Hollister SJ, Maddox RD, Taboas JM. Optimal design and fabrication of scaffolds to mimic tissue properties and satisfy biological constraints. *Biomaterials.* 2002;23(20):4095-4103.
**168.** Hollister SJ, Guldberg RE, Kuelske CL, Caldwell NJ, Richards M, Goldstein SA. Relative effects of wound healing and mechanical stimulus on early bone response to porous-coated implants. *Journal of Orthopaedic Research.* Jul 1996;14(4):654-662.
**169.** Hollister SJ, Chu TM, Guldberg RE, et al. Image based design and manufacture of scaffolds for bone reconstruction. In: Pederson P, Bendsoe M, eds. *IUTAM Synthesis in Biosolid Mechanics*: Kluwek Press; 1998
163-174.
**170.** Hollister SJ, Levy RA, Chu TM, Halloran JW, Feinberg SE. An image-based approach for designing and manufacturing craniofacial scaffolds. *International Journal of Oral and Maxillofacial Surgery.* 2000;29(1):67-71.
**171.** Hollister SJ, Chu TM, Halloran JW, Feinberg SE. Design and Manufacture of Bone Replacement Scaffolds. In: Cowin S, ed. *Bone Mechanics Handbook*. Second ed: CRC Press; 2001.

**172.** Mikos AG, Sarakinos G, Lyman MD, Ingber DE, Vacanti JP, Langer R. PREVASCULARIZATION OF POROUS BIODEGRADABLE POLYMERS. *Biotechnology and Bioengineering.* Sep 1993;42(6):716-723.
**173.** Chu TMG, Orton DG, Hollister SJ, Feinberg SE, Halloran JW. Mechanical and in vivo performance of hydroxyapatite implants with controlled architectures. *Biomaterials.* 2002;23(5):1283-1293.
**174.** Lee JTY, Chow KL, Wang K, Tsang W-H. Is Macroporosity Absolutely Required for Preliminary in Vitro Bone Biomaterial Study? A Comparison Between Porous Materials and Flat Materials. *Journal of Functional Biomaterials.* 2011;2(4):308-337.
**175.** Ramay HR, Zhang M. Preparation of porous hydroxyapatite scaffolds by combination of the gel-casting and polymer sponge methods. *Biomaterials.* 2003;24(19):3293-3302.
**176.** Chen QZ, Thompson ID, Boccaccini AR. 45S5 Bioglass®-derived glass–ceramic scaffolds for bone tissue engineering. *Biomaterials.* 2006;27(11):2414-2425.
**177.** Callcut S, Knowles JC. Correlation between structure and compressive strength in a reticulated glass-reinforced hydroxyapatite foam. *Journal of Materials Science-Materials in Medicine.* May 2002;13(5):485-489.
**178.** Sepulveda P, Ortega FS, Innocentini MDM, Pandolfelli VC. Properties of highly porous hydroxyapatite obtained by the gelcasting of foams. *Journal of the American Ceramic Society.* Dec 2000;83(12):3021-3024.
**179.** Sepulveda P, Bressiani AH, Bressiani JC, Meseguer L, Konig B. In vivo evaluation of hydroxyapatite foams. *Journal of Biomedical Materials Research.* Dec 15 2002;62(4):587-592.
**180.** Sepulveda P, Binner JGP, Rogero SO, Higa OZ, Bressiani JC. Production of porous hydroxyapatite by the gel-casting of foams and cytotoxic evaluation. *Journal of Biomedical Materials Research.* Apr 2000;50(1):27-34.
**181.** Freyman TM, Yannas IV, Gibson LJ. Cellular materials as porous scaffolds for tissue engineering. *Progress in Materials Science.* 2001 2001;46(3-4):273-282.
**182.** Dias MR, Fernandes PR, Guedes JM, Hollister SJ. Permeability analysis of scaffolds for bone tissue engineering. *Journal of Biomechanics.* 2012;45(6):938-944.
**183.** Li JS, Mak AFT. Hydraulic permeability of polyglycolic acid scaffolds as a function of biomaterial degradation. *J. Biomater. Appl.* Jan 2005;19(3):253-266.
**184.** Jongpaiboonkit L, Lin CY, Krebsbach PH, Hollister SJ, Halloran JW. Mechanical behavior of complex 3D calcium phosphate cement scaffolds fabricated by indirect solid freeform fabrication in vivo. In: Nakamura T, Yamashita K, Neo M, eds. *Bioceramics 18, Pts 1 and 2.* Vol 309-311. Zurich-Uetikon: Trans Tech Publications Ltd; 2006:957-960.
**185.** Dellinger JG, Wojtowicz AM, Jamison RD. Effects of degradation and porosity on the load bearing properties of model hydroxyapatite bone scaffolds. *Journal of Biomedical Materials Research Part A.* 2006;77A(3):563-571.
**186.** Dellinger JG, Cesarano J, III, Jamison RD. Robotic deposition of model hydroxyapatite scaffolds with multiple architectures and multiscale porosity for

bone tissue engineering. *Journal of Biomedical Materials Research Part A.* Aug 2007;82A(2):383-394.

**187.** Roy TD, Simon JL, Ricci JL, Rekow ED, Thompson VP, Parsons JR. Performance of hydroxyapatite bone repair scaffolds created via three-dimensional fabrication techniques. *Journal of Biomedical Materials Research Part A.* Dec 2003;67A(4):1228-1237.

**188.** Guo D, Xu K, Han Y. The in situ synthesis of biphasic calcium phosphate scaffolds with controllable compositions, structures, and adjustable properties. *Journal of Biomedical Materials Research Part A.* Jan 2009;88A(1):43-52.

**189.** An S-H, Matsumoto T, Miyajima H, Nakahira A, Kim K-H, Imazato S. Porous zirconia/hydroxyapatite scaffolds for bone reconstruction. *Dental Materials.* 2012;28(12):1221-1231.

**190.** Bignon A, Chouteau J, Chevalier J, et al. Effect of micro- and macroporosity of bone substitutes on their mechanical properties and cellular response. *Journal of Materials Science: Materials in Medicine.* 2003;14(12):1089-1097.

**191.** Schumacher M, Deisinger U, Detsch R, Ziegler G. Indirect rapid prototyping of biphasic calcium phosphate scaffolds as bone substitutes: influence of phase composition, macroporosity and pore geometry on mechanical properties. *Journal of Materials Science-Materials in Medicine.* Dec 2010;21(12):3119-3127.

**192.** Elliott JC. Calcium Phosphate Biominerals. *Reviews in Mineralogy and Geochemistry.* January 1, 2002 2002;48(1):427-453.

**193.** Bohner M, van Lenthe GH, Grünenfelder S, Hirsiger W, Evison R, Müller R. Synthesis and characterization of porous [beta]-tricalcium phosphate blocks. *Biomaterials.* 2005;26(31):6099-6105.

**194.** Hing KA, Best SM, Bonfield W. Characterization of porous hydroxyapatite. *Journal of Materials Science: Materials in Medicine.* 1999;10(3):135-145.

**195.** Best SM, Porter AE, Thian ES, Huang J. Bioceramics: Past, present and for the future. *Journal of the European Ceramic Society.* 2008;28(7):1319-1327.

**196.** Blokhuis TJ, Termaat MF, den Boer FC, Patka P, Bakker FC, Haarman H. Properties of calcium phosphate ceramics in relation to their in vivo behavior. *Journal of Trauma-Injury Infection and Critical Care.* 2000;48(1):179-186.

**197.** Daculsi G, Legeros RZ, Nery E, Lynch K, Kerebel B. TRANSFORMATION OF BIPHASIC CALCIUM-PHOSPHATE CERAMICS INVIVO - ULTRASTRUCTURAL AND PHYSICOCHEMICAL CHARACTERIZATION. *Journal of Biomedical Materials Research.* Aug 1989;23(8):883-894.

**198.** Kurashina K, Kurita H, Wu Q, Ohtsuka A, Kobayashi H. Ectopic osteogenesis with biphasic ceramics of hydroxyapatite and tricalcium phosphate in rabbits. *Biomaterials.* 2002;23(2):407-412.

**199.** Koc N, Timucin M, Korkusuz F. Fabrication and characterization of porous tricalcium phosphate ceramics. *Ceramics International.* 2004 2004;30(2):205-211.

**200.** Matsushita N, Terai H, Okada T, et al. A new bone-inducing biodegradable porous beta-tricalcium phosphate. *Journal of Biomedical Materials Research Part A.* Sep 1 2004;70A(3):450-458.

**201.** Urist MR, Lietze A, Dawson E. Beta-Tricalcium Phosphate Delivery System for Bone Morphogenetic Protein. *Clinical Orthopaedics and Related Research.* 1984(187):277-280.
**202.** Wilson C, van Blitterswijk C, Verbout A, Dhert W, de Bruijn J. Scaffolds with a standardized macro-architecture fabricated from several calcium phosphate ceramics using an indirect rapid prototyping technique. *Journal of Materials Science: Materials in Medicine.* 2011;22(1):97-105.
**203.** Gauthier O, Muller R, von Stechow D, et al. In vivo bone regeneration with injectable calcium phosphate biomaterial: A three-dimensional micro-computed tomographic, biomechanical and SEM study. *Biomaterials.* Sep 2005;26(27):5444-5453.
**204.** Bandyopadhyay A, Withey EA, Moore J, Bose S. Influence of ZnO doping in calcium phosphate ceramics. *Materials Science & Engineering C-Biomimetic and Supramolecular Systems.* Jan 2007;27(1):14-17.
**205.** Silva VV, Lameiras FS, Domingues RZ. Microstructural and mechanical study of zirconia-hydroxyapatite (ZH) composite ceramics for biomedical applications. *Composites Science and Technology.* 2001 2001;61(2):301-310.
**206.** Kim HW, Knowles JC, Kim HE. Hydroxyapatite/poly(epsilon-caprolactone) composite coatings on hydroxyapatite porous bone scaffold for drug delivery. *Biomaterials.* Mar-Apr 2004;25(7-8):1279-1287.
**207.** Zhao F, Yin YJ, Lu WW, et al. Preparation and histological evaluation of biomimetic three-dimensional hydroxyapatite/chitosan-gelatin network composite scaffolds. *Biomaterials.* Aug 2002;23(15):3227-3234.
**208.** Swetha M, Sahithi K, Moorthi A, Srinivasan N, Ramasamy K, Selvamurugan N. Biocomposites containing natural polymers and hydroxyapatite for bone tissue engineering. *International Journal of Biological Macromolecules.* 2010;47(1):1-4.
**209.** Zhang R, Ma PX. Poly(α-hydroxyl acids)/hydroxyapatite porous composites for bone-tissue engineering. I. Preparation and morphology. *Journal of Biomedical Materials Research.* 1999;44(4):446-455.
**210.** Wei GB, Ma PX. Structure and properties of nano-hydroxyapatite/polymer composite scaffolds for bone tissue engineering. *Biomaterials.* Aug 2004;25(19):4749-4757.
**211.** Shor L, Guceri S, Wen XJ, Gandhi M, Sun W. Fabrication of three-dimensional polycaprolactone/hydroxyapatite tissue scaffolds and osteoblast-scaffold interactions in vitro. *Biomaterials.* Dec 2007;28(35):5291-5297.
**212.** Malard O, Bouler JM, Guicheux J, et al. Influence of biphasic calcium phosphate granulometry on bone ingrowth, ceramic resorption, and inflammatory reactions: Preliminary in vitro and in vivo study. *Journal of Biomedical Materials Research.* Jul 1999;46(1):103-111.
**213.** Ke S, Gibson IR, Hing KA. Characterisation of mono- and biphasic calcium phosphates granules. *Bioceramics 14.* 2002;218-2:625-628.
**214.** Legeros RZ, Lin S, LeGEros JP, Mijares D, Dimanno F, Serekian P. Effect of Firing Temperature on Properties of Biphasic Calcium Phosphates. Paper

presented at: Society for Biomaterials 29th Annual Meeting Transactions2003; Reno, Nevada.

**215.** Daculsi G, Laboux O, Malard O, Weiss P. Current state of the art of biphasic calcium phosphate bioceramics. *Journal of Materials Science-Materials in Medicine.* Mar 2003;14(3):195-200.

**216.** LeGeros RZ, Lin S, Rohanizadeh R, Mijares D, LeGeros JP. Biphasic calcium phosphate bioceramics: preparation, properties and applications. *Journal of Materials Science: Materials in Medicine.* 2003;14(3):201-209.

**217.** Mayr H, Schluefter S, Detsch R, Ziegler G. Influence of phase composition on degradation and resorption of biphasic calcium phosphate ceramics. In: Daculsi G, Layrolle P, eds. *Bioceramics, Vol 20, Pts 1 and 2.* Vol 361-3632008:1043-1046.

**218.** Toquet J, Rohanizadeh R, Guicheux J, et al. Osteogenic potential in vitro of human bone marrow cells cultured on macroporous biphasic calcium phosphate ceramic. *Journal of Biomedical Materials Research.* 1999;44(1):98-108.

**219.** Hannink G, Arts JJC. Bioresorbability, porosity and mechanical strength of bone substitutes: What is optimal for bone regeneration? *Injury.* 2011;42, Supplement 2(0):S22-S25.

**220.** Ignatius AA, Wolf S, Augat P, Claes LE. Composites made of rapidly resorbable ceramics and poly(lactide) show adequate mechanical properties for use as bone substitute materials. *Journal of Biomedical Materials Research.* Oct 2001;57(1):126-131.

**221.** Baradararan S, Hamdi M, Metselaar IH. Biphasic calcium phosphate (BCP) macroporous scaffold with different ratios of HA-TCP by combination of gel casting and polymer sponge methods. *Advances in applied ceramics.* 2012;111(7):367-373.

**222.** Impens S, Schelstraete R, Luyten J, et al. Production and characterisation of porous calcium phosphate structures with controllable hydroxyapatite-tricalcium phosphate ratios. *Advances in applied ceramics.* 2009;108(8):494-500.

**223.** Ranito CMS, Oliveira FAC, Borges JP. Hydroxyapatite foams for bone replacement. In: Li P, Zhang K, Colwell CW, eds. *Bioceramics, Vol 17.* Vol 284-286. Zurich-Uetikon: Trans Tech Publications Ltd; 2005:341-344.

**224.** Vallet-Regí M, González-Calbet JM. Calcium phosphates as substitution of bone tissues. *Progress in Solid State Chemistry.* 2004;32(1–2):1-31.

**225.** Catagne JF, Chamousset J, Minois LM, Ponsinet A, Bouler JM, Tancret F. Mechanical properties of macroporous biphasic calcium phosphate bioceramics fabricated using a porogen. In: Pan W, Gong JH, Ge CC, Li JF, eds. *High-Performance Ceramics Iii, Pts 1 and 2.* Vol 280-2832005:1549-1553.

**226.** Tancret F, Bouler JM, Chamousset J, Minois LM. Modelling the mechanical properties of microporous and macroporous biphasic calcium phosphate bioceramics. *Journal of the European Ceramic Society.* 2006 2006;26(16):3647-3656.

**227.** Dellinger JG, Eurell JAC, Jamison RD. Bone response to 3D periodic hydroxyapatite scaffolds with and without tailored microporosity to deliver bone

morphogenetic protein 2. *Journal of Biomedical Materials Research Part A.* Feb 2006;76A(2):366-376.

**228.** Chen YH, Zhou SW, Li Q. Microstructure design of biodegradable scaffold and its effect on tissue regeneration. *Biomaterials.* Aug 2011;32(22):5003-5014.

**229.** Diggs A, Halloran J, Hollister S. In-vitro Degradation to Assess the Effect of Aging on the Mechanical Properties of Biphasic Calcium Phosphate Scaffolds. . *Oral Presentation, Presented at the107th Annual Meeting & Exposition of The American Ceramics Society*. Baltimore, MD.

**230.** Gibson LJ, Ashby MF. *Cellular solids: structure and properties*. Cambridge ; New York: Cambridge University Press; 1999.

**231.** Diggs AB, Bae CJ, Tseng WJ, Flanagan CL, Halloran JW, Hollister SJ. Assessing in vitro Degradation of beta-Tricalcium Phosphate Ceramics via Micro-Computed Tomography. In: Prado M, Zavaglia C, eds. *Bioceramics 21.* Vol 396-3982009:637-640.

**232.** Triantafillou TC, Gibson LJ. Multiaxial failure criteria for brittle foams. *International Journal of Mechanical Sciences.* 1990;32(6):479-496.

**233.** Kretlow JD, Young S, Klouda L, Wong M, Mikos AG. Injectable Biomaterials for Regenerating Complex Craniofacial Tissues. *Advanced Materials.* Sep 4 2009;21(32-33):3368-3393.

**234.** Qiu H, Yang J, Kodali P, Koh J, Ameer GA. A citric acid-based hydroxyapatite composite for orthopedic implants. *Biomaterials.* Dec 2006;27(34):5845-5854.

**235.** Frayssinet P, Conte P, Tourenne F, Rouquet N. Influence of the Crystallinity of Plasma Sprayed HA-Coatings on Their Osseointegration. In: Brown PW, Constantz B, eds. *Hydroxyapatite and Related Materials*. Boca Raton: CRC Press; 1994:237-242.

**236.** Costa N, Maquis PM. Biomimetic processing of calcium phosphate coating. *Medical Engineering & Physics.* Nov 1998;20(8):602-606.

**237.** Choi JM, Kim HE, Lee IS. Ion-beam-assisted deposition (IBAD) of hydroxyapatite coating layer on Ti-based metal substrate. *Biomaterials.* Mar 2000;21(5):469-473.

**238.** Jinno T, Davy DT, Goldberg VM. Comparison of hydroxyapatite and hydroxyapatite tricalcium-phosphate coatings. *Journal of Arthroplasty.* Oct 2002;17(7):902-909.

**239.** Chang E, Chang WJ, Wang BC, Yang CY. Plasma spraying of zirconia-reinforced hydroxyapatite composite coatings on titanium .1. Phase, microstructure and bonding strength. *Journal of Materials Science-Materials in Medicine.* Apr 1997;8(4):193-200.

**240.** Teng YD, Lavik EB, Qu XL, et al. Functional recovery following traumatic spinal cord injury mediated by a unique polymer scaffold seeded with neural stem cells. *Proc. Natl. Acad. Sci. U. S. A.* Mar 2002;99(5):3024-3029.

**241.** Ellis-Behnke RG, Liang YX, You SW, et al. Nano neuro knitting: Peptide nanofiber scaffold for brain repair and axon regeneration with functional return of vision. *Proc. Natl. Acad. Sci. U. S. A.* Mar 2006;103(13):5054-5059.

**242.** Park KI, Teng YD, Snyder EY. The injured brain interacts reciprocally with neural stem cells supported by scaffolds to reconstitute lost tissue. *Nature Biotechnology.* Nov 2002;20(11):1111-1117.
**243.** Nerem RM, Seliktar D. Vascular tissue engineering. *Annu. Rev. Biomed. Eng.* 2001;3:225-243.
**244.** Zong XH, Bien H, Chung CY, et al. Electrospun fine-textured scaffolds for heart tissue constructs. *Biomaterials.* Sep 2005;26(26):5330-5338.
**245.** Xu CY, Inai R, Kotaki M, Ramakrishna S. Aligned biodegradable nanotibrous structure: a potential scaffold for blood vessel engineering. *Biomaterials.* Feb 2004;25(5):877-886.
**246.** Kim WS, Vacanti JP, Cima L, et al. Cartilage Engineered In Predetermined Shapes Employing Cell Transplantation on Synthetic Biodegradable Polymers. *Plastic and Reconstructive Surgery.* Aug 1994;94(2):233-237.
**247.** Mitsak AG, Kemppainen JM, Harris MT, Hollister SJ. Effect of Polycaprolactone Scaffold Permeability on Bone Regeneration. *Tissue engineering. Part A.* 2011;17(13-14):1831-1839.
**248.** Li S, de Wijn J, Li J, Layrolle P, de Groot K. Macroporous biphasic calcium phosphate scaffold with high permeability/porosity ratio. *Tissue Engineering.* 2003;9(3):535-548.
**249.** Roosa S, Kemppainen J, Moffitt E, Krebsbach P, Hollister S. The pore size of polycaprolactone scaffolds has limited influence on bone regeneration in an in vivo model. *Journal of biomedical materials research. Part A.* 2010;92A(1):359-368.
**250.** Jones A, Arns C, Hutmacher D, Milthorpe B, Sheppard A, Knackstedt M. The correlation of pore morphology, interconnectivity and physical properties of 3D ceramic scaffolds with bone ingrowth. *Biomaterials.* 2009;30(7):1440-1451.
**251.** Galois L, Mainard D. Bone ingrowth into two porous ceramics with different pore sizes: an experimental study. *Acta orthopaedica Belgica.* 2004-Dec 2004;70(6):598-603.
**252.** Kasten P, Beyen I, Niemeyer P, Luginbuehl R, Bohner M, Richter W. Porosity and pore size of beta-tricalcium phosphate scaffold can influence protein production and osteogenic differentiation of human mesenchymal stem cells: An in vitro and in vivo study. *Acta Biomaterialia.* Nov 2008;4(6):1904-1915.
**253.** D'Lima DD, Lemperle SM, Chen PC, Holmes RE, Colwell Jr CW. Bone response to implant surface morphology. *The Journal of Arthroplasty.* 1998;13(8):928-934.
**254.** Wang CY, Duan YR, Markovic B, et al. Proliferation and bone-related gene expression of osteoblasts grown on hydroxyapatite ceramics sintered at different temperature. *Biomaterials.* Jul 2004;25(15):2949-2956.
**255.** Liu DM. Influence of Porous Microarchitecture on the In-Vitro Dissolution and Biological Behavior of Porous Calcium Phosphate Ceramics. *Materials Science Forum.* 1997;250:183-208.
**256.** Krebsbach PH, Gu K, Franceschi RT, Rutherford RB. Gene therapy-directed osteogenesis: BMP-7-transduced human fibroblasts form bone in vivo. *Human Gene Therapy.* 2000;11(8):1201-1210.

**257.** Rutherford RB, Moalli M, Franceschi RT, Wang D, Gu K, Krebsbach PH. Bone morphogenetic protein-transduced human fibroblasts convert to osteoblasts and form bone in vivo. *Tissue Engineering.* Jun 2002;8(3):441-452.
**258.** Hutmacher DW, Schantz JT, Lam CXF, Tan KC, Lim TC. State of the art and future directions of scaffold-based bone engineering from a biomaterials perspective. *Journal of Tissue Engineering and Regenerative Medicine.* 2007;1(4):245-260.
**259.** Hing KA, Best SM, Tanner KE, Bonfield W, Revell PA. Quantification of bone ingrowth within bone-derived porous hydroxyapatite implants of varying density. *Journal of Materials Science-Materials in Medicine.* Oct-Nov 1999;10(10-11):663-670.
**260.** Hing KA, Best SM, Tanner KE, Bonfield W, Revell PA. Mediation of bone ingrowth in porous hydroxyapatite bone graft substitutes. *Journal of Biomedical Materials Research Part A.* Jan 1 2004;68A(1):187-200.
**261.** Habibovic P, Sees TM, van den Doel MA, van Blitterswijk CA, de Groot K. Osteoinduction by biomaterials - Physicochemical and structural influences. *Journal of Biomedical Materials Research Part A.* Jun 15 2006;77A(4):747-762.
**262.** Arinzeh TL, Tran T, McAlary J, Daculsi G. A comparative study of biphasic calcium phosphate ceramics for human mesenchymal stem-cell-induced bone formation. *Biomaterials.* Jun 2005;26(17):3631-3638.
**263.** Yuan HP, Van den Doel M, Li SH, Van Blitterswijk CA, De Groot K, De Bruijn JD. A comparison of the osteoinductive potential of two calcium phosphate ceramics implanted intramuscularly in goats. *Journal of Materials Science-Materials in Medicine.* 2002;13(12):1271-1275.
**264.** Yuan HP, Van Blitterswijk CA, De Groot K, De Bruijn JD. Cross-species comparison of ectopic bone formation in biphasic calcium phosphate (BCP) and hydroxyapatite (HA) scaffolds. *Tissue Eng.* Jun 2006;12(6):1607-1615.
**265.** Mitragotri S, Lahann J. Physical approaches to biomaterial design. *Nature Materials.* 2009;8(1):15-23.
**266.** Habibovic P, Yuan HP, Van den Doel M, Sees TM, Van Blitterswiik CA, De Groot K. Relevance of osteoinductive biomaterials in critical-sized orthotopic defect. *Journal of Orthopaedic Research.* May 2006;24(5):867-876.
**267.** Green D, Walsh D, Mann S, Oreffo ROC. The potential of biomimesis in bone tissue engineering: Lessons from the design and synthesis of invertebrate skeletons. *Bone.* Jun 2002;30(6):810-815.
**268.** Otsuki B, Takemoto M, Fujibayashi S, Neo M, Kokubo T, Nakamura T. Pore throat size and connectivity determine bone and tissue ingrowth into porous implants: Three-dimensional micro-CT based structural analyses of porous bioactive titanium implants. *Biomaterials.* Dec 2006;27(35):5892-5900.
**269.** Ahsan T, Bellamkonda R, Nerem RM. Tissue engineering and regenerative medicine: Advancing toward clinical therapies. *Translational Approaches in Tissue Engineering and Regenerative Medicine.* 2008:3-16.

**270.** Williams DJ, Sebastine IM. Tissue engineering and regenerative medicine: manufacturing challenges. *IEE Proceedings Nanobiotechnology.* Dec 2005;152(6):207-210.